2019

Near-Infrared High Efficiency Organic Dye Sensitized Solar Cells (DSCs) and Biological Fluorescent Imaging Dyes

Yanbing Zhang
University of Mississippi

NEAR-INFRARED HIGH EFFICIENCY ORGANIC DYE SENSITIZED SOLAR CELLS (DSCS) AND BIOLOGICAL FLUORESCENT IMAGING DYES

A Dissertation
presented in partial fulfillment of requirements
for the degree of Doctor of Philosophy
in the Department of Chemistry and Biochemistry
The University of Mississippi

By

YANBING ZHANG

May 2019

ABSTRACT

With the energy consumption increase every year, the non-renewable energy sources such as fossil fuels, natural gas, and coal will not sustain forever. In this case, searching for a way to develop a renewable energy source is an emergency. For decades, dye-sensitized solar cells (DSCs) have received intensive attention due to their high power conversion efficiency and low material cost. This dissertation describes efforts to design and synthesize near-infrared organic dyes to apply to two systems: first, for use in the improvement of DSCs by the optimization of electron rich components such as ullazine and cross-conjugated π-bridges to increase photon-to-electricity conversion and second, as a way to manipulate the UV-vis absorption and emission of the near-infrared organic dyes to use lower energy photons with wavelength ranges in the therapeutic window (700 nm-1000 nm).

DEDICATION

This dissertation is dedicated to everyone who helped me towards the goal of achieving my doctorate. I want to especially thank to my parents and my friend, Lizhu Chen, whose love and support made this achievement possible.

ACKNOWLEDGEMENTS

I extend all the grateful appreciation to my advisor Dr. Jared Delcamp, who lead me to the fantastic science world. He not only taught me the technique skills but also more valuable things in regular life. I would also like to thank my committee members Dr. Daniell Mattern, Dr. Nathan Hammer, Dr. Davita Watkins, and Dr. David Colby for their time, advice, and collaboration.

I would also like to thank my graduate student colleagues that helped, collaborated with, and support me along the way. Finally, I'd like to thank the sources of funding that allowed me to research full time during 3 years in my graduate school career. Specifically, I gratefully acknowledge financial support from the US National Science Foundation (Awards: NSF-1455167 & NSF-1539035) for funding DSC related research.

TABLE OF CONTENTS

LIST OF FIGURES

LIST OF TABLES

LIST OF SCHEMES

CHAPTER 1

INTRODUCTION

1.1 INTRODUCTION TO NEAR-INFRARED ORGANIC DYES FOR DYE-SENSITIZED SOLAR CELLS AND EMISSIVE APPLICATIONS AND PROGRESS OF RESEARCH

Dye-sensitized solar cells (DSCs) have attracted increasing attention since 1991 when the modern DSC was developed by Grätzel and O'Regan with 7.1% efficiency.[1] DSCs operate through light absorption by the sensitizers or dyes anchored to the semiconductor, by exciting electrons from the ground-state to the excited-state of the dye, followed by transferring of the electron to the semiconductor, collection of the electron by a redox shuttle at a counter electrode after it has traveled an external circuit, and return of the electron to the oxidized dye by the redox shuttle.[2] (Figure 1)

The DSC can be evaluated by the equation (1) below.

$$PCE = J_{sc}V_{oc}FF/I_0 \qquad \text{equation (1)}$$

PCE represents the photon conversion efficiency, J_{sc} stands for the short-circuit current density, V_{oc} shows the open-circuit voltage, FF is the fill factor and I_0 means the intensity of sunlight. The dye is primarily responsible for influencing J_{sc} which depends on the number of photons absorbed by the dye, and V_{oc} which represents the energy difference between the conduction band of semiconductor and the redox potential of the redox shuttle. Recently, some representative dyes have been published such as Ru-based sensitizers,[3] porphyrin-based sensitizers,[4] and metal-free

sensitizers[5–8] demonstrating attractive power conversion efficiencies ranging from 11.5%-14% PCE. **SM315**[4] is the leader in metal-based dyes and has shown up to 13% PCE for a single dye cell. Yet for multi-dye cells (**ADEKA-1** co-sensitized with **LEG4**) the power conversion efficiency increased to 14% which broke the top efficiency for organic dyes set by **SM315**.

Ullazine dyes with heterocyclic electron rich donor have been designed and synthesized during my Ph.D. progress. **YZ7, YZ12, YZ14**, and **YZ15** have been tested to show further photon harvest up to 800 nm with better performance than **C218** under the same condition which has been published in *Chem. Eur. J.* [2] (Figure 2) In addition, cross-conjugated electron rich bridges have been developed based on the **C218**'s bridge. As these dyes have extended the bridge by C=C linked to phenyl, these dyes showed broader photon coverage in the high energy region than the original CPDT bridge and exhibited better efficiency than the **C218** under same condition.[9] (Figure 2) Meanwhile, collaborations between groups were conducted by making solar cells devices and data analysis.

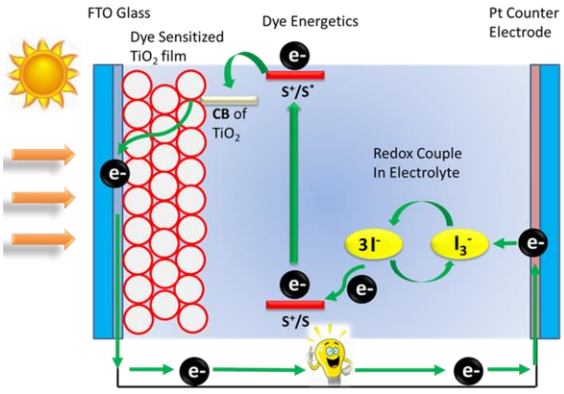

Figure 1. Schematic of a DSC devices, containing a semiconductor, sensitizer and redox shuttle (The figure was remade with inspiration from Grätzel, M. et al. *Nature* 2001, *414*, 338).

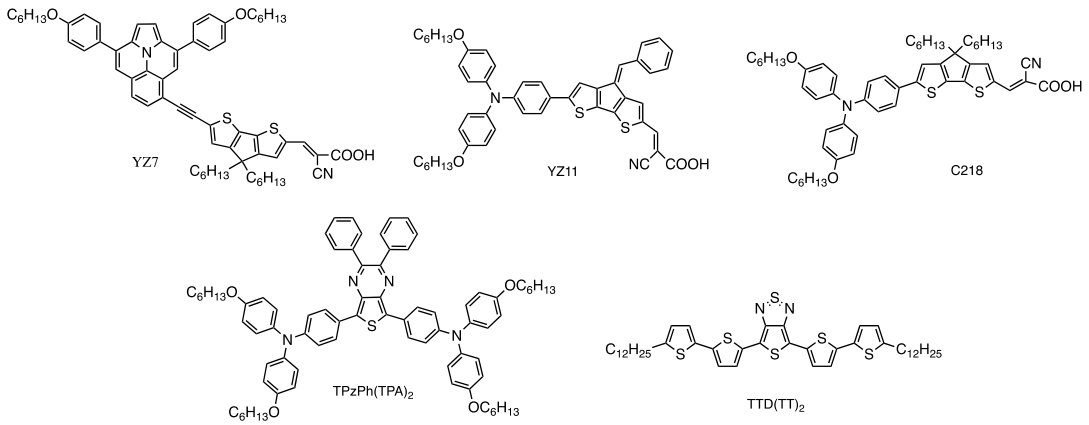

Figure 2. Representative structures of YZ7, YZ11, TPzPh(TPA)$_2$ and TTD(TT)$_2$, C218 in research progress.[2,9,10]

Around 20 years ago, scientists demonstrated small fluorescent dyes can render biological molecules visible. These small fluorescent dyes can absorb and emit photons in the therapeutic window of 650 nm to 1400 nm (depending on tissue present), where the absorption and auto-fluorescence of the biological matrix is the lowest, leading to the deepest penetration depth. Higher resolution in this region is desirable and is directly related to increased Stokes shifts (change in energy between absorption and emission curves), high fluorescence quantum yields (ratio of number of photons emitted to the number of photon absorbed), and absorption as well as emission within the therapeutic window. Based on these particular features, TTD and TPzPh series dyes were designed and synthesized. These dyes showed better photostability than indocyanine green (ICG), a dye has been approved by FDA for clinic use. (Figure 2) Additionally, these series of dyes have successfully shifted their absorption and emission into the therapeutic window. With these characteristics, this project has been published in the Journal of Organic Chemistry.[10]

CHAPTER 2

2.1 NEAR-INFRARED FLUORESCENT THIENOTHIADIAZOLE DYES WITH LARGE STOKES SHIFTS AND HIGH PHOTOSTABILITY

Adapted with the permission from **Yanbing Zhang**; Shane A. Autry, Louis E. McNamara, Suong T. Nguyen, Ngoc Le, Phillip Brogdon, Davita L. Watkins, Nathan I. Hammer, and Jared H. Delcamp.; *J. Org. Chem.* **2017**, *82*, 5597. Copyright (2019) American Chemical Society.

(See appendix for permission license.)

This project also a collaborative project between Dr. Delcamp's group, Dr. Hammer's group, and Dr. Watkins's group, where Shane Autry and Dr. Louis McNamara contributed to the work by measuring the emission and quantum yield of the organic dyes, Suong Nguyen and Ngoc Le contributed to the project by synthesizing the furan-furan and thiophen-furan building blocks and Philip Brogdon contributed to the project by making $TTD(T)_2$.

ABSTRACT

A series of near-infrared (NIR) organic emissive materials were synthesized and the photophysical properties analyzed. The donor-acceptor-donor (D-A-D) materials were designed with thienopyrazine and thienothiadiazole acceptor groups with thiophene, furan, and triphenylamine-based donor groups. The absorption and emission spectra were found to be widely tunable based on the donor and acceptor groups selected. Computational analysis confirms these

materials undergo an intramolecular charge transfer event upon photoexcitation. Large Stokes shifts of ~150 nm was observed and rationalized by computational analysis of geometry changes in the excited-state. Fluorescence studies on the dye series reveal maximum peak emission wavelengths near 900 nm and a quantum yield exceeding 16% for $TTD(T)_2$. Additionally, several dyes were found to have reasonable quantum yields within this NIR region (>1%) with emission wavelengths reaching 1000 nm at the emission curve onset. Photostability studies were conducted on these materials in an ambient oxygen environment, revealing excellent stability in the presence of oxygen from all the dyes studied relative to a benchmark cyanine dye (ICG) during photoexcitation with exceptional photostability from the $TTD(TT)_2$ derivative.

INTRODUCTION

A wide array of applications exists for emissive materials with research interest recently increasing regarding materials in the NIR region. Among potential applications for these materials, optical biological imaging is becoming a prosperous field due to the high sensitivity and resolution without invasive measures.[11] This technique can use small organic molecules to absorb and emit photons in the therapeutic window of 650 nm to 1400 nm (depending on tissue present), where the absorption and auto-fluorescence of the biological matrix is the lowest, leading to the deepest penetration depth.[12,13] Higher resolution in this region is desirable and is directly related to increased Stokes shifts (change in energy between absorption and emission curves), high fluorescence quantum yields (ratio of number of photons emitted to the number of photon absorbed), and absorption as well as emission within the therapeutic window. Materials with these properties could offer new advances in emissive materials applications such as biological imaging.[12-33] One of the most intriguing dyes for imaging applications is based on a donor-acceptor-donor (D-A-D) design with a benzobisthiadiazole acceptor and two triphenylamine donor

groups (CH1055-PEG) which emits in the NIR II window (Figure 3); however, the fluorescence quantum yield can still be improved upon (ϕ = 0.3%).[36] Further understanding of the fundamental photophysical properties of NIR conjugated systems is needed in order to rationally design future generations of applied materials with tailored emissive properties for numerous applications including biological imaging.

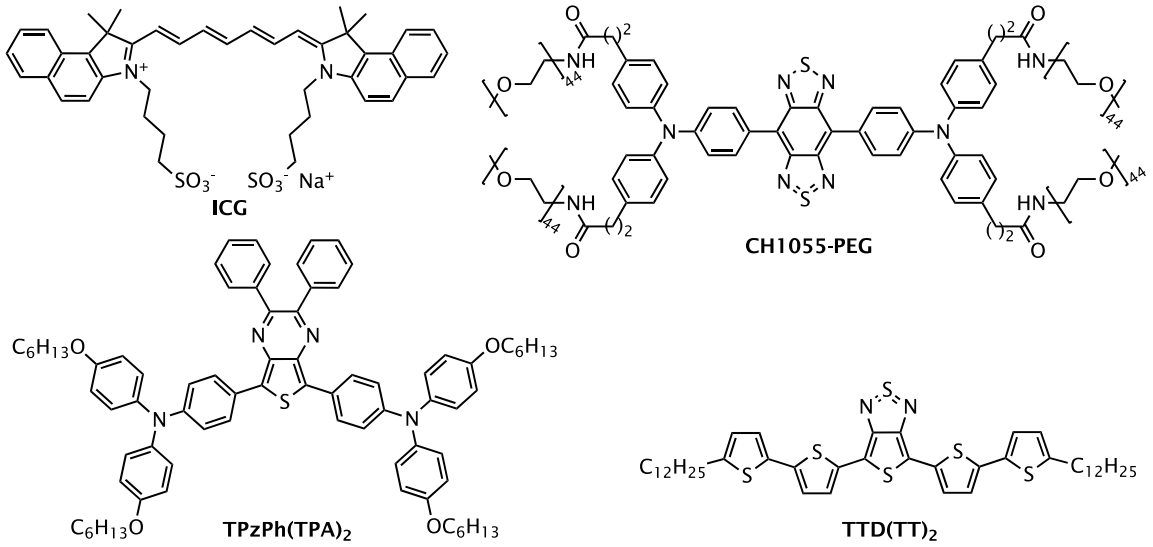

Figure 3. Known ICG,[12-33] CH1055-PEG,[36] and TPzPh(TPA)$_2$[37] NIR emissive material structures compared to target dye TTD(TT)$_2$.

Recently, our groups evaluated a thienopyrazine (TPz) based D-A-D dye series(Figure 3),[37] which has large Stokes shifts when compared to many common NIR dyes, such as those based on cyanine (ICG), of up to 200 nm with a 4% quantum yield (Figure 3). Due to steric interactions between the thienopyrazine ring and triarylamine rings, significant reorganization energy is needed upon photoexcitation to reach the lowest energy excited-state geometry. This high reorganization energy results in a large Stokes shift. Despite these impressive metrics, these dyes can be improved upon by a shifting of the absorption and emission profiles further into the NIR region as is needed

for many applications.[11,13] Herein, we report a fundamental study in tuning the photophysical properties of D-A-D dyes by designing a new series of NIR dyes aimed at maintaining the desired properties of the prior TPz series while accessing lower energy photons.

The low energy absorption band of the TPz-based dyes results from the transfer of electron density from the donor (D) regions to the acceptor (A) region within the D-A-D framework. We reasoned this band could be shifted toward longer wavelengths by: (1) using a stronger accepting motif, (2) reducing the acceptor-donor dihedral angle, and (3) increasing conjugation length with weaker donors in place of stronger donors with shorter conjugation lengths. The thienothiadiazole (TTD) building block was evaluated as a stronger acceptor with reduced steric repulsion between the donor and acceptor as a result of introducing a 5,5-fused ring system in place of the 5,6-fused TPz (Figure 4). We reasoned the release of ring strain energy from the thiadiazole ring by significantly elongating bonds in this ring would maintain significant Stokes shifts. Additionally, we sought to evaluate the effects of replacing the previously studied triphenylamine donor with furan and thiophene linkages to both the TPz and TTD acceptors. The triphenylamine donor is a strong electron donating group with increased steric interactions at the D-A bond, while the furan and thiophene groups are weaker electron donors with reduced sterics. While increasing the strength of donor and acceptor groups commonly leads to lower energy absorptions in small molecules, we reasoned that reduced sterics, elimination of highly resonance stabilized benzene rings, and increased conjugation length could result in lower energy absorptions from weaker donor building blocks.

To analyze our hypotheses, we selected a series of systematically targeted dyes for comparing the effects of varying donor groups on an identical thienopyrazine core. Dithiophene and furan-thiophene based donors ($TPzPh(TT)_2$ and $TPzPh(FT)_2$) were chosen to increase

planarity as well as conjugation length to allow for lower energy photon absorption when compared to the previously reported TPzPh(TPA)$_2$. However, the Stokes shift is predicted to be significantly reduced with higher planarity dyes.[37] As the Stokes shift represents the reorganization of the dye in the excited-state, varying the acceptor core to a building block with strain that can be released in the excited-state can still provide a large Stokes shift without reducing dye planarity as is needed to reach longer wavelengths. To provide a desirable reorganization energy and further shift the absorption and emission spectrum into the optical therapeutic window, TTD was substituted in place of the TPzPh acceptor since thienothiadiazole is more electron deficient than thienopyrazine due in part to the inclusion of a hypervalent sulfur atom.[38] For a direct comparison of these functionalities, TTD(TT)$_2$ and TTD(TPA)$_2$ are valuable target dyes. To assess the importance of the second thiophene with TTD(TT)$_2$, TTD(T)$_2$ is targeted to analyze the resulting photophysical properties.

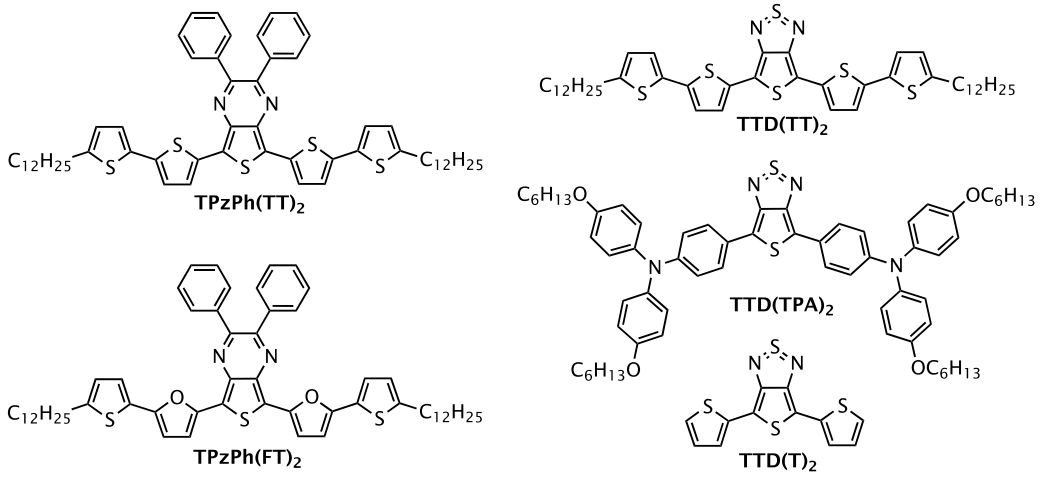

Figure 4. Target NIR emissive compounds TPzPh(TT)$_2$, TPzPh(FT)$_2$, TTD(TT)$_2$, TTD(TPA)$_2$, and TTD(T)$_2$.

SYNTHESIS

All of the target NIR dyes are readily accessible through traditional transition metal cross-coupling synthetic routes. Synthetic routes to the five target dyes can be been carried out in 5 or fewer linear steps from commercially available materials (Scheme 1). Several synthetic analogs of the TPzPh[39–42] and TTD[42–47] target dyes are known primarily in polymer literature as monomer precursors for alternative applications. The synthesis of the TPzPh based dyes began with known 5,7-dibromo-2,3-diphenylthieno[3,4-b]pyrazine (**1**), which undergoes Stille coupling with stannylTT (**2**) or stannylFT (**3**) (Scheme 1).[35,46-47] **3** is available in two steps beginning from bromothiophene derivative **4** and 2-tributylstannyl furan and then lithiation with butyllithium and quenching with tributyltin chloride to give **3**. Due to purification challenges associated with chromatographically separating the desired product from the homocoupled stannyl reagent, recrystallization was used as the final purification technique to give a 11-12% yield of the final pure desired dyes TPzPh$(TT)_2$ and TPzPh$(FT)_2$. The furan-based dye demonstrates limited stability and needs to be kept under nitrogen in the dark to reduce decomposition. The synthetic route for TTD$(T)_2$ is known and was easily repeated.[46] The remaining TTD based dyes followed a similar route beginning from known 2,5-dibromo-3,4-dinitrothiophene (**6**) which underwent Stille coupling with Bu_3SnTT to generate **7** (x = TT). Analogously, the triphenylamine donors were installed via Suzuki coupling of **6** with TPApinacol boronic ester to give **7** (x = TPA). The dinitro interemediates **7** underwent quantitative reduction with $SnCl_2$ to give the diamine intermediates **8**, which were converted to the desired final dyes with thionylaniline and TMSCl. Attempts to synthesize the TTD$(FT)_2$ analogue of TTD$(TT)_2$ were not successful as the diamine intermediate **8** (x = FT) had significantly lower stability and could not be successfully isolated.

RESULTS AND DISCUSSION

With the target dyes synthesized, the optical properties of the D-A-D NIR dyes were

measured to reveal the effect of the different donors and acceptors on the molar absorptivity and optical band gap. The λ_{max} range for the dye series varied from 629 nm to 717 nm due to what appears to be a single, broad intramolecular charge transfer band (Figure 5, Table 1). Comparison of the donor group on dye optical properties is possible through a comparison of the previously characterized TPzPh(TPA)$_2$ and the newly reported dyes TPzPh(TT)$_2$ and TPzPh(FT)$_2$.

Scheme 1. Synthetic route to TPzPh(TT)$_2$, TPzPh(FT)$_2$, TTD(TT)$_2$, and TTD(TPA)$_2$.

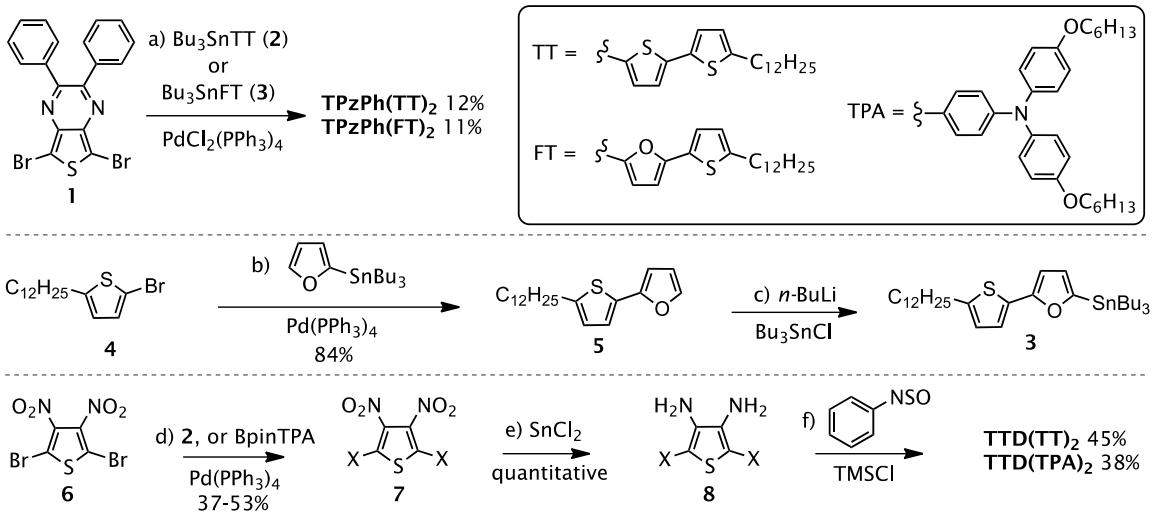

a) 10% $PdCl_2(PPh_3)_2$, 50°C, overnight, 11-12%; b) 10% $Pd(PPh_3)_4$, toluene:DMF, reflux, overnight, 84%; c) *n*-BuLi (1.5 equiv.), Bu_3SnCl (0.4 equiv.), 0.1 M THF, -78°C, overnight, quantitative; d) 10% $Pd(PPh_3)_4$, toluene or dioxane, 24 hours, 37%-53%; e) $SnCl_2$ (10 equiv.), 1.4 M conc. HCl, 1.0 M EtOH, 0.01 M DCM, room temperature 3 days, 100%; f) thionyl aniline (2.0 equiv.), TMSCl (7.0 equiv.), 0.2 M pyridine, room temperature, overnight, 38-68%.

Interestingly, despite the lower electron donating strength of thiophene and furan when compared with triphenylamines, the newly synthesized dyes with thiophene and furan donors are red-shifted by 29 and 33 nm, respectively, when compared with the parent dye TPzPh(TPA)$_2$.

Reduced steric repulsion between the acceptor and a 5-membered thiophene or furan ring when compared to the same interaction between acceptor and a 6-membered benzene promotes dye planarity enough to desirably red-shift the absorption maximum. Additionally, conjugation length is increased through the use of two aromatic heterocycles per donor in place of the single benzene in triphenylamine, further causing a bathochromic shift. The molar absorptivity is only modestly affected by the change in donor group, with TPzPh(TPA)$_2$ having a molar absorptivity of 14,000 $M^{-1}cm^{-1}$ while the TT and FT substituted analogues have molar absorptivities of 12,000 $M^{-1}cm^{-1}$. Little difference is observed in the absorption spectrum for TPzPh(TT)$_2$ and TPzPh(FT)$_2$ in the low energy region (450-750 nm); however, at the higher energy region (350-450 nm) a significantly stronger absorption is observed for the furan derivative. TTD(TPA)$_2$ and TTD(TT)$_2$ offer a direct comparison of the thienothiadiazole with the thienopyrazine group of TPzPh(TPA)$_2$ and TPzPh(TT)$_2$. A near 100 nm red-shift of the λ_{max} and λ_{onset} values in toluene is observed for the thienothiadiazole derivatives. Additionally, an increase in molar absorptivity is observed for each thienothiadiazole derivative (14,000 to 19,000 $M^{-1}cm^{-1}$ for the TPA derivatives; and 12,000 to 15,000 $M^{-1}cm^{-1}$ for the TT derivatives). Otherwise, the charge transfer low-energy absorption peaks have similar shapes and widths for the two derivatives. The enhanced molar absorptivity and absorption of lower energy photons when using the thienothiadiazole bridge is indicative of a more planarized π-conjugated system and an enhanced electron withdrawing strength. Removal of a thiophene from the TTD(TT)$_2$ structure to give TTD(T)$_2$ resulted in a 110 nm blue-shift of the absorption spectrum onset, which clearly highlights the importance of the added electron density of the second thiophene group when developing dyes to access low energy photons in the NIR region.

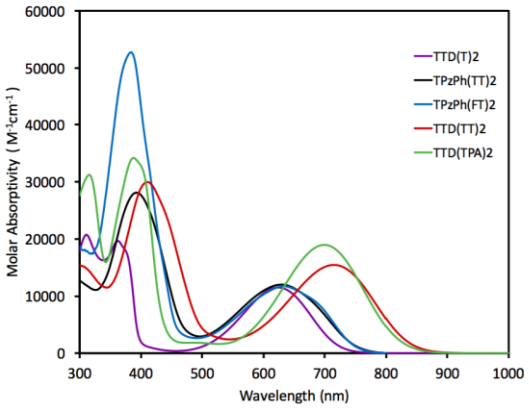

Figure 5. Absorption curves of $TTD(T)_2$, $TPzPh(TT)_2$, $TPzPh(FT)_2$, $TTD(TT)_2$, $TTD(TPA)_2$ in toluene.

Table 1. Photophysical properties of TPzPh, TTD and ICG series dyes measured in toluene.

dye	λ_{abs}^{max} (nm)	λ_{abs}^{onset} (nm)	ε ($M^{-1}cm^{-1}$)	λ_{emis}^{max} (nm)	Stokes shift (nm; eV)	ϕ (%)	τ (ns)
$TPzPh(TPA)_2$[a]	600	730	14,000	748	148; 0.41	4.3	1.2
$TPzPh(TT)_2$	629	770	12,000	765	136; 0.35	1.2	0.9
$TPzPh(FT)_2$	633	765	12,000	764	131; 0.34	4.1	0.6
$TTD(TPA)_2$	698	830	19,000	875	177; 0.36	1.1	1.1
$TTD(TT)_2$	717	850	15,000	877	160; 0.32	1.0	0.8
$TTD(T)_2$	624	740	12,000	765	141; 0.37	16.8	2.1
ICG[b]	816	870	141,000	819	3; <0.01	9.0	0.7

[a]Previously reported.[37] [b]Measured in toluene:methanol (2:1). Note: When comparing Stokes shifts of dyes, the energy comparison we focus on is in terms of eV whereas small perturbations to dye structures often leads to larger shifts in nm values in the NIR region compared to the higher energy regions. However, these large changes in energy in terms of nm numerical values in the NIR region are represented by relatively small energy changes in terms of eV.

COMPUTATIONAL RESULTS

To better understand the optical properties of these dyes, density functional theory (DFT) and time-dependent density functional theory (TD-DFT) computational studies were undertaken

to analyze the orbital arrangement, planarity, and intramolecular charge transfer (ICT) characteristics of the dyes. The geometry of the dyes was first optimized with the B3LYP functional and 6-311G(d,p) basis set (Figure 6, Table 2). The highest occupied molecular orbital (HOMO) and lowest unoccupied molecular orbital (LUMO) orientations are shown in Figure 5. The HOMO is delocalized across the dye from each donor and includes the thiophene region of the acceptor groups. Specifically, in the case of the TPA based dyes, the HOMO is only substantially present on the benzene ring in conjugation with the acceptor while the two remaining TPA rings out of conjugation do not have substantial HOMO contribution. This is in contrast to the TT and FT based donors where the HOMO is delocalized across the entire dye, with contributions from both rings of each donor. This observation suggests conjugation length changes may significantly affect the lowest absorption wavelengths of these dyes. The LUMO is heavily localized on the whole acceptor building block, and substantial orbital overlap is observed on the thiophene of each acceptor. For the thienopyrazine based dyes, the LUMO does show some orbital density on the donor region while the thienothiadiazole shows LUMO orbital density only on the acceptor region at the same iso values. This comparison highlights the stronger electron accepting ability of the TTD donor and results in a lower energy ICT absorption for these dyes with analogous donor groups. As previously noted, a reduction in sterics is expected when changing from the TPA to TT or FT donor groups. For the TPz acceptor based dyes, this change in sterics from the donor is apparent as the TPA-TPz dihedral angle is 20^{o} and the dihedral angle at the TT-TPz and TF-TPz bonds are 3.7^{o}-7.7^{o} after geometry optimization. Changing the acceptor building block also leads to a significant reduction in sterics at the D-A bond, giving a TPA-TTD dihedral angle of 0.0^{o} after geometry optimization. These results support the conclusion that reduced steric interactions play an important role in shifting the UV-Vis-NIR absorption values for these dyes as

changing the donor from TPA to TT or FT dramatically lowers the dihedral angle value while simultaneously absorbing lower energy wavelengths.

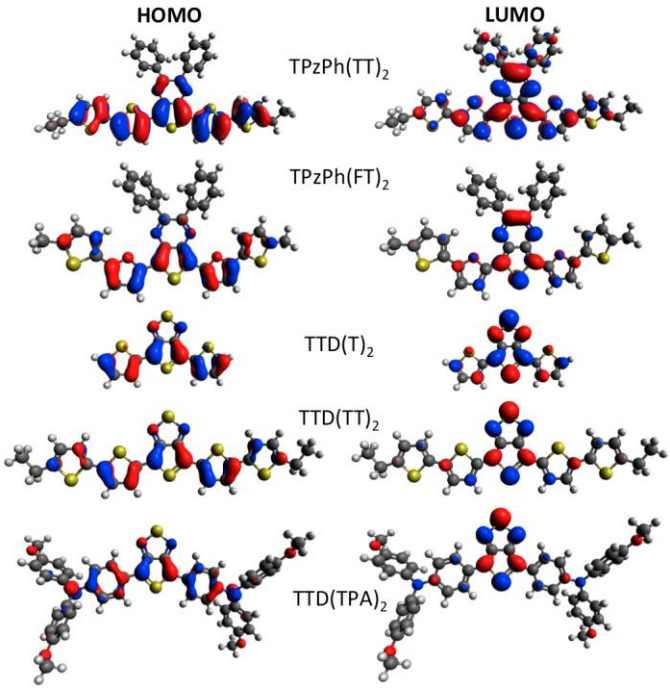

Figure 6. HOMO (left) and LUMO (right) orbitals of $TPzPh(TT)_2$, $TPzPh(FT)_2$, $TTD(T)_2$, $TTD(TT)_2$, $TTD(TPA)_2$. Iso values were set to 0.04.

TD-DFT analysis with the B3LYP functional and 6-311G(d,p) basis set was used to analyze the predicted 10 lowest energy vertical transitions of the dyes in isolation from the optimized ground-state geometry in order to identify the orbitals contributing to the absorption bands observed (Table 2). The lowest-energy vertical transition trends match the experimental λ_{max} trends based on acceptor building block choice. However, for the donor groups TD-DFT predicts similar values for vertical transition energies. Given how close in energy the experimental absorption spectrum maxima are for the TPzPh dyes and the similar absorption spectra of the

$TTD(TPA)_2$ and $TTD(TT)_2$ dyes, predicting the changes in energy with TD-DFT is challenging as only a ≤0.06 eV difference separates each dye set. The oscillator strength values are close for each of the dyes, which indicates the molar absorptivity values should be relatively close in value for each of the dyes as is observed from solution measurements. In all cases, the TD-DFT results show the lowest-energy vertical transitions are dominated by HOMO-LUMO transition (>99%) with the nearest significant vertical transition substantially higher in energy by >250 nm. These results suggest the absorption bands of these dyes extending into the NIR region is predominantly resulting from a strong ICT from a donor to acceptor region.

Table 2. Computational Results of TPz, TTD series from DFT and TD-DFT Analysis.

dye	D-A dihedral angle	vert. trans. (nm; eV)	Oscillator strength
$TPzPh(TPA)_2$[a]	20	706; 1.76	0.41
$TPzPh(TT)_2$	3.7	725; 1.71	0.56
$TPzPh(FT)_2$	7.7	699; 1.77	0.49
$TTD(TPA)_2$	4.6	891; 1.39	0.50
$TTD(TT)_2$	1.0	887; 1.40	0.54
$TTD(T)_2$	0.0	725; 1.71	0.21

[a] Previously reported.[37]

EMISSIVE PROPERTIES

Having established the strong absorption of these dyes into the NIR spectral region, the emissive properties of the dyes were evaluated in toluene solutions (Figure 7, Table 1). All dyes were found to emit within the desired wavelength range with λ_{emis} maxima ranging from 748-877 nm and emission curve onset values from 900-1000 nm. An additional requirement for biological imagining purposes is a large Stokes shift to reduce overlap of the excitation energy and emission energy as scattered excitation photons from the laser source dramatically reduce image resolution in the absence of significant energy separation. Large Stokes shifts of 131-177 nm (0.32-0.41 eV)

in toluene were observed for the dye series. Prior studies have shown the Stokes shift of $TPzPh(TPA)_2$ to originate from a substantial shift in ground-state and excited-state geometries with a dramatic change at the donor group-acceptor group dihedral angle. The Stokes shift is hypothesized to be reduced as a result of lowering steric interactions at the donor-acceptor (D-A) group bond. For the largest acceptor group, TPzPh, the following trend of Stokes shifts was observed $TPzPh(TPA)_2$ > $TPzPh(TT)_2$ > $TPzPh(FT)_2$ which is in agreement with the predicted steric influence. The smaller acceptor group, TTD should have a similar trend among the donor group substituents, only with a

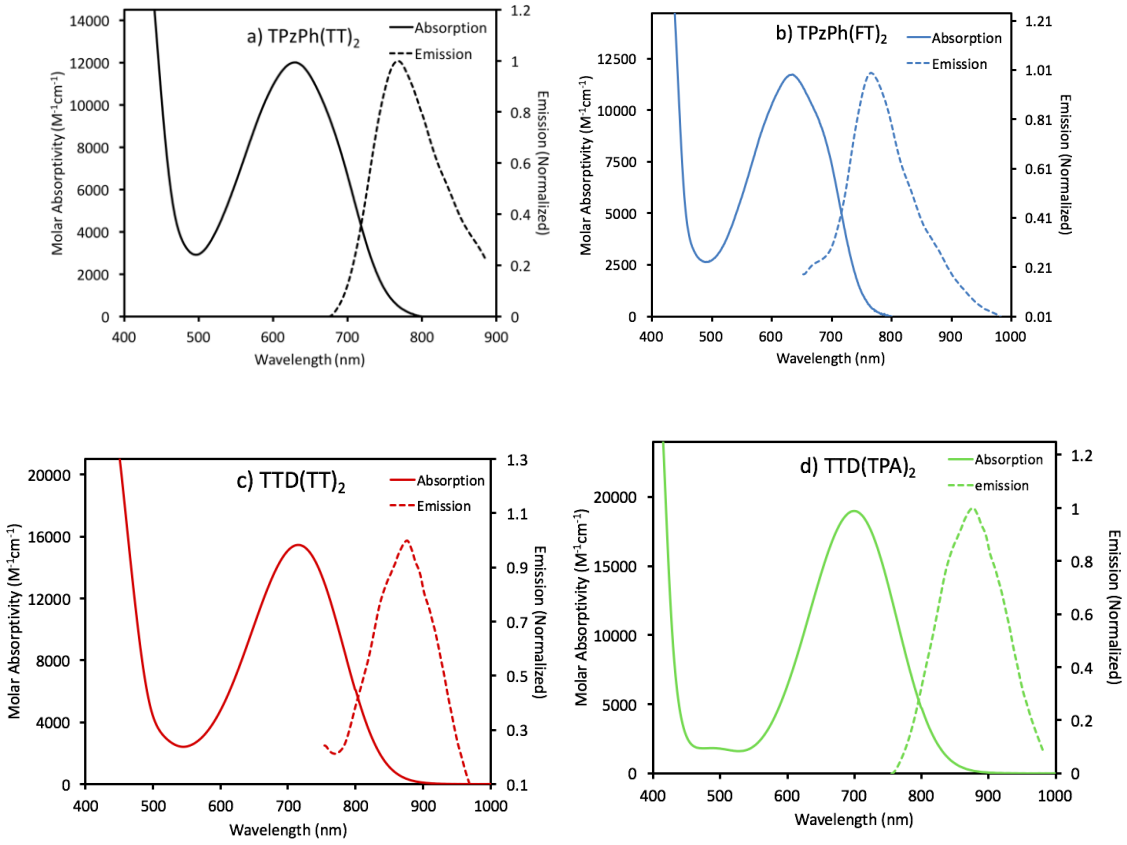

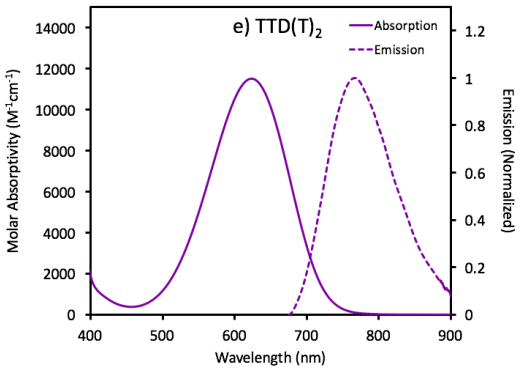

Figure 7. Absorption and emission curves of a) $TPzPh(TT)_2$ b) $TPzPh(FT)_2$ c) $TTD(TT)_2$ d) $TTD(TPA)_2$ e) $TTD(T)_2$ in toluene.

lesser extent of Stokes shifts changes. This prediction was observed as the Stokes shift of $TTD(TPA)_2$ was greater than that of $TTD(FT)_2$, but lower than $TPzPh(TPA)_2$. Interestingly, $TTD(T)_2$ was found to have one of the largest Stokes shifts in the series in terms of eV units at 0.37 eV using the smallest accepting group, and a 0.05 eV larger Stokes shift than is observed for the $TTD(TT)_2$ derivative. This implies the $TTD(T)_2$ has a greater reorganization energy than the $TTD(TT)_2$ derivative. Solvatochromic effects were evaluated via absorption and emission spectroscopy with $TTD(T)_2$ to examine the effects of solvent polarity on the ground-state and excited-state (Figure 42, Appendix). The absorption maxima varied by 0.05 eV (14 nm) over 12 solvents with widely varied polarities. This negligible change of the absorption spectrum suggests the conformation of the molecule in the ground-state is relatively unaffected by solvent polarity. Interestingly, the emission maxima energy varied to a great extent by 0.14 eV (73 nm) over the same 12 solvents. This change is more significant and suggests a substantial reorganization of the $TTD(T)_2$ dye in the excited-state. For the most polar solvent that $TTD(T)_2$ was appreciably soluble in (DMSO), the largest Stokes-shift was observed at 0.52 eV (220 nm). To better understand the origin of the Stokes-shift for these dyes, computational chemistry was used to analyze the excited-

state geometry changes. Interestingly, unlike other biological imaging dyes having large Stokes shift resulting from dihedral angle changes between donor and acceptor rings, $TPzPh(TT)_2$, $TPzPh(FT)_2$, $TTD(TT)_2$, $TTD(FT)_2$, and $TTD(T)_2$ have substantial Stokes shifts but no substantial change in dihedral angle has been observed as this value is already near 0^o for these dyes. To probe this expectation, computational studies were carried out to optimize the first excited-state geometry.

$TTD(TT)_2$ was closely analyzed as an example dye to evaluate the origin of the observed Stokes shifts based on geometry changes in the ground-state (S_0) and lowest excited-state (S_1, Figure 8, Table 3). In a straightforward manner, valence bond theory suggests that bonds 1 and 2 will be shortened upon excitation to the excited-state as double-bond character is increased upon ICT. Conversely, bond 5 should be elongated due to an increase in single bond character upon intramolecular charge transfer. Upon careful examination of the calculated excited-state geometry, bond length changes in the dyes were found to be the primary reorganization event with the largest effects seen at the TTD building block (Table 3). The lengths of bond 1 and bond 2 decrease by 0.01 and 0.02 Å, respectively, while the length of bond 5 shows the largest change by elongating 0.06 Å as predicted by valence bond theory. Interestingly, bonds 3 (0.02 Å lengthening) and 4 (0.03 Å shortening) both change significantly according to computational analysis for the ground- and excited-states. We rationalize the change in bond 3 length as occurring due to the loss of local aromaticity (and thus less homogenous bond lengths) at the center thiophene ring upon ICT. Bond 4 in the ground-state is significantly longer than that of the remaining thiophenes in the $TTD(TT)_2$ dye (1.46 Å versus 1.41 Å, respectively). We attribute this to the hypervalent sulfur (assuming a similar geometry preference to SO_2 with an AX_2N geometry) and both sp^2 hybridized nitrogens attached to the sulfur atom all preferring bond angles of 120^o, which would significantly elongate

bond 4 in the ground-state. In the excited-state some of this ring strain is released, presumably due to a partial rehybridization of the hypervalent sulfur to more of an AX_2N_2 geometry (~110° for non-cyclic systems) which better matches the ring strain free five member ring geometry at ~110°.

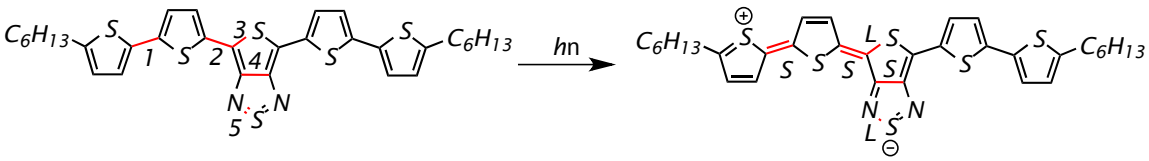

Figure 8. TTD(TT)$_2$ ground-state and excited-state bond length changes.

Table 3. Comparison of C-C bond lengths of TTD(T)$_2$ in ground-state (S_0), excited-state (S_1) and the length changes (ΔR).

Bond	S_0 (Å)	S_1 (Å)	ΔR (Å)
1	1.442	1.432	-0.01
2	1.425	1.402	-0.02
3	1.748	1.770	+0.02
4	1.455	1.427	-0.03
5	1.638	1.694	+0.06

In addition to inducing large Stokes shifts for better imaging resolution, high fluorescence quantum yields are important for either allowing lower dye quantities to be administered for imaging applications, or enhanced resolution at larger tissue depths with equal dye amounts administered when compared with lower fluorescence quantum yield dyes.[37] For this series, despite large Stokes shifts, the target dyes maintain a >1% quantum yield which improves on the current state of the art emissive dye quantum yields of materials with similar Stokes shifts near this spectral region (e.g. CH1055-PEG: ϕ = 0.3%). TTD(TT)$_2$ and TTD(TPA)$_2$ both have emission spectrum reaching >950 nm. In this range, a QY greater than 1% (as both of these dyes show) is notable. TPzPh(TT)$_2$, TTD(TT)$_2$ and TTD(TPA)$_2$ all demonstrated roughly similar fluorescence quantum yields of ~1% despite significantly different emission ranges with $\lambda_{emis\ max}$ varying by 112 nm

(0.21 eV). The energy gap law generally dictates that the non-radiative excited-state decay rate increases exponentially as the emission energy decreases leading to dramatically lower quantum yields as ($\phi = k_r/(k_r + k_{nr})$), where k_r is the radiative decay rate and k_{nr} is the sum of all non-radiative decay rates.[27,50–56] This suggests the energy gap law is not the primary factor controlling the relative quantum yields of these materials since as k_{nr} increases exponentially an inverse effect is expected to be observed on ϕ.[27,50] To indirectly evaluate the change in k_{nr} of these dyes, fluorescent lifetimes of these materials were measured through time correlated single photon counting (TCSPC) experiments where $\tau = 1/(k_r + k_{nr})$ and τ is found through the fluorescence decay curve fit (Figure 9).

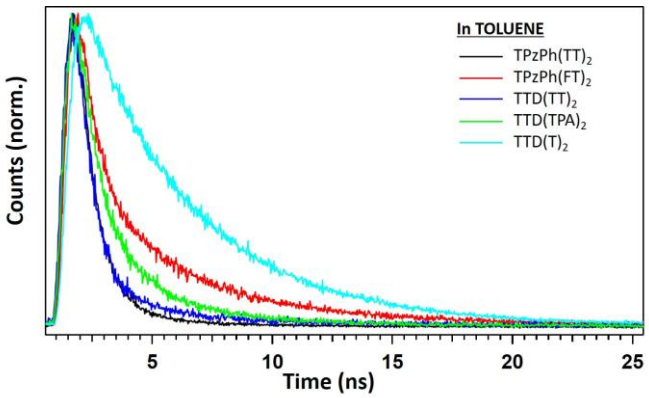

Figure 9. TCSPC fluorescent decay curves for $TPzPh(TT)_2$, $TPzPh(FT)_2$, $TTD(TPA)_2$, $TTD(TT)_2$, and $TTD(T)_2$.

Fluorescence lifetimes for the dyes are all close with a range from 2.1 ns to 0.6 ns. Since the measured ϕ and τ values are similar for each of the dyes, this suggests the summed rate of non-radiative decay events is remaining near constant for these dyes as the emission energies shift to lower energy values. Substantially, higher fluorescence quantum yields were observed for $TTD(T)_2$ (16.8%) and $TPzPh(FT)_2$ (4.1%). Both materials have emission maximum at similar

energies (1 nm difference in energy) which eliminates energy gap law concerns for explaining the drastic difference in ϕ. Comparison of fluorescence lifetimes shows a 3.5x increase in τ value for $TTD(T)_2$ when compared with $TPzPh(FT)_2$. Given the 4.1x increase in quantum yield for $TTD(T)_2$, and the equation $k_r = \phi / \tau$ derived from the above equations, essentially no substantial change has occurred in the k_r term for either of the dyes. This suggests the dramatically improved fluorescence quantum yield of $TTD(T)_2$ comes from reducing the non-radiative decay rate by roughly 4 times that of $TPzPh(FT)_2$. This decrease in k_{nr} is potentially due to fewer thermal deactivation pathways in the more concise $TTD(T)_2$ structure. It should be noted that the ϕ of $TTD(T)_2$ is exceptionally high for a material emitting photons at >750 nm.

PHOTOSTABILITY

A common challenge with many NIR emissive materials is low photostability of dyes during prolonged irradiation in the presence of oxygen.[57] To evaluate the photostability of these dyes, they were dissolved in toluene at a concentration of 1×10^{-5} M to maintain consistency with absorption and fluorescent quantum yield studies. The samples were then irradiated with a 150 W Xe lamp (AM 1.5 filter) at distance of 25 cm (94.8 mW/cm^2) with a cutoff filter to remove photons higher in energy than 400 nm (Figure 10).[58] No precautions were taken for the removal of oxygen from the dye solution to evaluate the stability of the

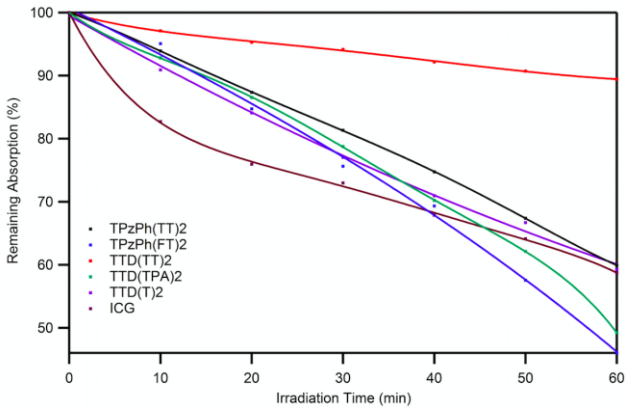

Figure 10. Photostability behavior of $TPzPh(TT)_2$, $TPzPh(FT)_2$, $TTD(TT)_2$, $TTD(TPA)_2$, $TTD(T)_2$ in toluene and ICG in toluene:methanol (2:1)

dyes under ambient conditions. The dye solutions were placed in front of the lamp for the indicated time and then absorption spectra were taken to evaluate the percent change in λ_{max} as a result of irradiation. The data is plotted in Figure 10 as the percent of the λ_{max} absorbance remaining after irradiation.

All dyes show reasonable stability over the course of a continuous hour of irradiation and maintain ~50% to >90% of the original dye concentration. The dye stability in order from most stable to least is: $TTD(TT)_2 > TPzPh(TT)_2 = TTD(T)_2 > TTD(TPA)_2 > TPzPh(FT)_2$ after 1 hour of irradiation. Interestingly, among the TTD series the thiophene donor based dyes were significantly more stable than the TPA based dye. By a considerable amount, the $TTD(TT)_2$ dye was the most stable and maintained >90% dye concentration after being irradiated continuously for one hour. When comparing the TPzPh and TTD acceptor with the TT donor group, a significantly higher stability is observed for the TTD acceptor, which suggests the decomposition pathways for the TPzPh acceptor are more facile than the TTD acceptor. When comparing the highest stability of the TT donor and the FT donor, a greater stability for the TT donor is clearly observed as was

noted qualitatively during the synthesis of these materials. This correlates to what would be predicted based on the lower resonance stabilization energy of furan when compared with thiophene (16 kcal/mol vs. 29 kcal/mol) which likely plays a role in the rate of decomposition. The high photostability of $TTD(TT)_2$ is in stark contrast to the cyanine dye ICG.[59] The key structural elements for introducing high photostability were: (1) the addition of a strong electron withdrawing group, and (2) the use of planarizing, weaker donating functionality.

CONCLUSION

These results suggest the D-A-D design for NIR dyes can be used as a low energy absorbing and emitting dye design with good photostability and high fluorescence quantum yields. All target dyes studied were synthesized in 5 reproducible steps. UV-Vis-NIR spectrometry, computational studies, photostability and emissive studies were undertaken to analyze photophysical property changes of these dye designs. The series of 5 dyes synthesized in this manuscript all absorb and emit within NIR region with Stokes shifts from 136 nm to 177 nm (λ^{abs}_{onset} 730 nm to 850 nm, λ^{emis}_{onset} = 950 nm to 1000 nm). Encouragingly, the fluorescence quantum yields of all the dyes were observed at >1% (reaching 16.8%), which is particularly intriguing as the energy gap law suggests greatly diminished fluorescence quantum yield in this spectral region. Photostability experiments indicated all the dyes exhibit reasonable stabilities in the presence of ambient oxygen during continuous irradiation, with $TTD(TT)_2$ showing exceptional photostability. These characteristics suggest the π-conjugated dye systems are promising candidates for future NIR emissive material applications including biological system fluorescence imaging studies with several functional positions for tuning dyes to specific application needs.

EXPERIMENTAL SECTION

Materials. All commercially obtained reagents and solvents were used as received without further purification. 4,6-Bis(2-thienyl)thieno[3,4-c][1,2,5]thiadiazole,[43] 4,6-Bis(5-bromo-2-thienyl)thieno[3,4-c][1,2,5]thiadiazole,[46] 5,7-dibromo-2,3-diphenylthieno[3,4-b]pyrazine,[37] 2,5-dibromo-3,4-dinitrothiophene,[37] tributyl(5'-dodecyl-[2,2'-bithiophen]-5-yl)stannane,[60] and 2-bromo-5-dodecylthiopheneade[60] were prepared according to literature. Thin-layer chromatography (TLC) was conducted with Silica Gel XHL TLC Plates from Sorbent Technologies and visualized with UV and potassium permanganate staining. Flash column chromatography was performed using Sorbent Tech P60, 40–63 μm (230–400 mesh) silica gel. ^{1}H NMR spectra were recorded on Bruker Avance-300 (300 MHz) and Bruker Avance DRX-500 (500 MHz) spectrometers and are reported in ppm using solvent as an internal standard ($CDCl_3$ at 7.28 ppm). NMR data is reported as s = singlet, d = doublet, t = triplet, q = quartet, p = pentet, m = multiplet, b = broad, ap = apparent, dd = doublet of doublets, and coupling constant(s) are in Hertz, followed by integration information. UV−Vis-NIR spectra were measured with a Cary 5000 instrument. HRMS spectra were obtained with a QTOF HRMS utilizing nanospray ionization. The mass analyzer was set to the 400−2000 Da range. Photostabiltiy studies were performed with a Xe-lamp (SF-150-C, 150W, Xe lamp, AM 1.5 filter, ScienceTech solar simulator) and a cutoff filter blocking light <400 nm from ThorLabs. Solution-phase fluorescent quantum yields were obtained using the optically dilute method described by Crosby and Demas.[61] All sample concentrations were on the order of 10^{-5} M to reduce reabsorption. The 647 nm line of a Kr^+/Ar^+ ion laser was used as the excitation source, and zinc phthalocyanine (φ = 0.30 in 1% pyridine in toluene)[62] was used as a reference. Fluorescent lifetimes were obtained by exciting with the 485 nm line of a pulsed diode laser (fwhm <100 ps) and detecting with an avalanche photodiode. Infrared spectra were recorded with an Agilent Cary 660 ATR-FTIR.

2-(5-Dodecylthiophen-2-yl)furan (5). To a degassed mixture of **4** (4.4 g, 13.24 mmol) and $Pd(PPh_3)_4$ (1.6 g, 1.4 mmol) was added the dry toluene (60 mL) and dry *N*,*N*-dimethylformamide (60 mL). The solution was stirred at room temperature for 30 min before 2-tri-*n*-butylstannylfuran (4.6 mL, 14.5 mmol) was added. The mixture was stirred at room temperature for another 30 minutes before being heated to reflux for 48 hours. After being cooled to room temperature and diluted with dichloromethane, the product was extracted with deionized water. The organic layers were combined, dried over $MgSO_4$, and concentrated under reduced pressure. The product was purified by flash column chromatography (petroleum ether) and obtained as light beige oil in 84 % yield (3.5 g). ^{1}H NMR (300 MHz, $CDCl_3$) δ 7.37 (s, 1H), 7.05 (d, J = 3.6 Hz, 1H), 6.70 (d, J = 3.6 Hz, 1H), 6.46 – 6.37 (m, 2H), 2.80 (t, J = 7.6 Hz, 2H), 1.68 (m, 2H), 1.48 – 1.31 (m, 18H), 0.89 (t, J = 6.9 Hz, 3H). ^{13}C NMR (75 MHz, $CDCl_3$) δ 149.9, 145.3, 141.3, 131.3, 124.7, 122.4, 111.7, 104.3, 32.1, 31.8, 30.2, 29.8, 29.7, 29.5, 29.2, 22.9, 14.3. HRMS (ESI) m/z calculated for $C_{20}H_{30}OS$ $[M + Cs]^+$ 451.1072, found 451.1091.

Tributyl(5-(5-dodecylthiophen-2-yl)furan-2-yl)stannane (3). Under argon, *n*-butyllithium in hexane (2.5 M, 2.4 mL, 6.0 mmol) was added to a solution of **5** (1.3 g, 4.0 mmol) in dry THF (40 mL) at –10 ^{o}C and the mixture was stirred at this temperature for 30 minutes. Tributyltin chloride (1.6 mL, 1.6 mmol) was added, and the reaction mixture was warmed to room temperature and stirred for an additional 12 hours. The reaction was then quenched with brine (50 mL) and the product was extracted with ethyl acetate. The organic layers were combined, washed with water, dried over $MgSO_4$, and concentrated under reduced pressure. The crude product was used directly without further purification. ^{1}H NMR (500 MHz, $CDCl_3$) δ 7.05 (d, J = 3.5 Hz, 1H), 6.70 (d, J = 3.5 Hz, 1H), 6.58 (d, J = 3.0 Hz, 1H), 6.45 (d, J =3.1 Hz, 1H), 2.82 (t, J = 7.5 Hz, 2H), 1.72-1.59

(m, 8H), 1.53-1.47 (m, 6H), 1.42-1.30 (m, 24 H), 1.14-1.10 (m, 9H), 0.84-0.82 (m, 3H). HRMS (ESI) m/z calculated for $C_{32}H_{56}OSSnCs$ $[M + Cs]^+$ 741.2128, found 741.2147.

5,7-bis(5'-dodecyl-[2,2'-bithiophen]-5-yl)-2,3-diphenylthieno[3,4-b]pyrazine (TPzPh(TT)$_2$). To a flame-dried sealed tube was added **1** (25 mg, 0.056 mmol), tributyl(5'-dodecyl-[2,2'-bithiophen]-5-yl)stannane (71.3 mg, 0.112 mmol), dimethylformamide (0.3 ml, 0.2 M) degassed for 20 minutes, and $PdCl_2(PPh_3)_2$ (0.014 mg, 0.006 mmol). The whole reaction was heated under N_2 while stirring at 50^{o}C for 48 hours. The reaction mixture was poured into ether, extracted with water, and dried with anhydrous Na_2SO_4. The product was purified through recrystallization with hot hexanes to give a green color crystalline solid (6.4 mg, 12.0%). ^{1}H NMR (300 MHz, $CDCl_3$) δ 7.59 (d, J = 7.7 Hz, 6H), 7.39-7.35 (m, 6H), 7.09 (d, J = 3.7 Hz, 2H) 7.06 (d, J = 3.6 Hz, 2H), 6.71 (d, J = 3.5 Hz, 2H), 2.79 (t, J = 7.4 Hz, 4H), 1.72-1.67 (m, 4H), 1.34-1.27 (m, 36H), 0.92-0.86 (m, 6H). HRMS (ESI) m/z calculated for $C_{58}H_{68}N_2S_5Cs$ $[M + Cs]^+$ 1085.3041, found 1085.3046. IR (neat, cm^{-1}) 2953.4, 2920.3, 2852.2, 1723.4, 1459.3, 1377.4, 1260.3, 1094.2, 1019.2. Melting Point: 130.0-132.4 ^{o}C.

5,7-bis(5-(5-dodecylthiophen-2-yl)furan-2-yl)-2,3-diphenylthieno[3,4-b]pyrazine (TPzPh(FT)$_2$). To a flame-dried sealed tube was added **1** (25 mg, 0.056 mmol), tributyl(5-(5-dodecylthiophen-2-yl)furan-2-yl)stannane (69.5 mg, 0.112 mmol), dimethylformamide (0.3 ml, 0.2 M) degassed for 20 min, and $PdCl_2(PPh_3)_2$ (0.014 mg, 0.006 mmol). The reaction was heated under N_2 with a sealed tube stirring at 50^{o}C for 48 hours. The reaction mixture was poured into ether, extracted with water, dried with anhydrous Na_2SO_4. The product was purified through recrystallization with hot hexane to give a green color crystalline solid (5.8 mg, 11.0%). ^{1}H NMR (500 MHz, acetone-d_6) δ 7.64 (d, J = 7.0 Hz, 4H), 7.53 (d, J = 5.0 Hz, 2H), 7.46-7.40 (m, 6H), 7.36 (d, J = 5.0 Hz, 2H), 6.91 (d, J = 3.6 Hz, 2H), 6.88 (d, J = 3.6 Hz, 2H), 2.93 (t, J = 8.9 Hz,

4H), 1.79-1.74 (m, 4H), 1.47-1.32 (m, 36H), 0.90-0.88 (m, 6H). MS (ESI) m/z calculated for $C_{58}H_{68}N_2O_2S_3Cs$ $[M + Cs]^+$ 1053.3497, found 1053.3505. IR (neat, cm^{-1}) 2951.5, 2924.1, 2854.2, 1092.9, 1018.7. Melting Point: 126.0-129.4 ^oC.

5,5''''-didodecyl-3'',4''-dinitro-2,2':5',2'':5'',2''':5''',2''''-quinquethiophene (7, x = TT). To a flame-dried round bottom flask was added **6** (50 mg, 0.15 mmol), **2** (303 mg, 0.36 mmol), toluene (4.5 ml, 0.03 M), and $Pd(PPh_3)_4$ (4.5 mg, 0.004 mmol) under N_2. The reaction was sealed and heated with stirring 24 hours at 100^{o}C. The reaction mixture was extracted with DCM and water. The product was filtered through a pad of silica gel, and recrystallized with hexane to give a red solid (46 mg, 37%). ^{1}H NMR (500 MHz, $CDCl_3$) δ 7.47 (d, J = 7.0 Hz, 2H), 7.14 (ap t, J = 3.9 Hz, 4H), 6.75 (d, J = 3.6 Hz, 2H), 2.83 (t, J = 7.6 Hz, 4H), 1.73-1.70 (m, 4H), 1.45-1.23 (m, 36H), 0.92-0.90 (m, 6H).^{13}C NMR (125 MHz, $CDCl_3$) δ 147.9, 144.2, 135.2, 133.4, 132.9, 132.1, 125.7, 125.3, 125.2, 123.7, 31.9, 31.5, 30.3, 29.8, 29.7, 29.6, 29.5, 29.4, 29.3, 29.1, 22.7, 14.1. HRMS (ESI) m/z calculated for $C_{44}H_{58}N_2O_4S_5Cs$ $[M + Cs]^+$ 971.2054, found 971.2083. IR (neat, cm^{-1}) 2920.7, 2852.2, 1535.4, 1464.0. Melting Point: 111.6-114.1 ^{o}C.

5,5''''-didodecyl-[2,2':5',2'':5'',2''':5''',2''''-quinquethiophene]-3'',4''-diamine (8, x = TT). To a N_2 filled round bottom flask was added **7** (x = TT, 46 mg, 0.055 mmol), ethanol (0.34 ml, 0.16 M), DCM (0.34 ml, 0.16 M), and a solution of tin (II) chloride dihydrate (124 mg, 0.55 mmol) in ethanol (0.55 ml, 1.0 M) and concentrated HCl (0.41 ml, 1.35 M). The reaction was stirred 3 days at 30^{o}C. The reaction mixture was quenched by 25% NaOH (aq.) and extracted with DCM. The product was used immediately, crude without further purification. ^{1}H NMR (300 MHz, $CDCl_3$) δ 7.07 (d, J = 3.7 Hz, 2H), 6.98 (ap d, J = 3.5 Hz, 4H), 6.70 (d, J = 3.4 Hz, 2H). 2.81 (t, J = 7.3 Hz, 4H), 1.94-1.86 (m, 4H), 1.78-1.68 (m, 4H), 1.67-1.52 (m, 36H), 1.19-1.03 (m, 6H).

1,3-bis(5'-dodecyl-[2,2'-bithiophen]-5-yl) thieno[3,4-c][1,2,5]thiadiazole (TTD(TT)$_2$). To a flame-dried round bottom flask was added **8** (x = TT, 17.5 mg, 0.022 mmol), pyridine (0.12 ml, 0.18 M), TMSCl (0.012 ml, 0.154 mmol), thionylaniline (0.003 ml, 0.044 mmol) sequentially under N_2. The reaction was stirred at room temperature overnight. The reaction was quenched with 1.0 M HCl (aq.) and extracted with DCM. The product was purified through recrystallization with hot hexane to give a bright green solid. (8.0 mg, 45%). ^{1}H NMR (500 MHz, $CDCl_3$) δ 7.47 (d, *J* = 3.6 Hz, 2H), 7.12 (d, *J* = 3.9 Hz, 2H), 7.08 (d, *J* = 3.3 Hz 2H), 6.73 (d, *J* = 3.4 Hz, 2H). 2.83 (t, *J* = 7.5 Hz, 4H), 1.74-1.68 (m, 4H), 1.44-1.31 (m, 36H), 0.92-0.89 (t, *J* = 6.5 Hz, 6H). HRMS (ESI) m/z calculated for $C_{44}H_{58}N_2S_6$ $[M]^+$ 806.2924, found 806.2903. IR (neat, cm^{-1}) 2953.3, 2917.3, 2849.6, 1462.3, 1258.5, 1020.5. Melting Point: 117.8-123.9 ^{o}C.

4,4'-(3,4-dinitrothiophene-2,5-diyl)bis(N,N-bis(4-(hexyloxy)phenyl)aniline) (7, x = TPA) To a flame-dried round bottom flask was added **6** (40.0 mg, 0.12 mmol), TPA-Bpin (172.0 mg, 0.30 mmol), dioxane (20.0 ml, 0.006 M), K_2CO_3 (4.0 ml, 1.0 M), then $Pd(PPh_3)_4$ (70.7 mg, 0.061 mmol) was added under N_2. The reaction was heated to 90 ^{o}C and stirred overnight. The reaction was extracted with DCM and H_2O. The organic layer was then dried with sodium sulfate. The product was purified through column chromatography with 40% DCM:hexane to give a red solid (76.0 mg, 60%) ^{1}H NMR (500 MHz, $CDCl_3$) δ 7.62 (d, *J* = 8.2 Hz, 4H), 7.07 (d, *J* = 8.2 Hz, 8H), 6.88 (d, *J* = 8.0 Hz, 4H), 6.83 (d, *J* = 8.9 Hz, 4H), 3.95 (t, *J* = 6.5 Hz, 8H), 1.83-1.78 (m, 8H), 1.52-1.46 (m, 8H), 1.38-1.35 (m, 16H), 0.93 (t, *J* = 6.8 Hz, 12H). ^{13}C NMR (125 MHz, $CDCl_3$) δ 155.8, 151.5, 140.2, 135.8, 127.1, 119.2, 118.6, 115.4, 115.3, 83.4, 68.2, 31.6, 25.8, 24.9 22.7, 14.1. HRMS (ESI) m/z calculated for $C_{64}H_{75}N_4SO_8Cs$ $[M + Cs]^+$ 1193.4438, found 1193.4442. IR (neat, cm^{-1}) 2928.7, 2861.4, 1718.4, 1600.9, 1503.3, 1240.5. Melting Point: 124.1-128.2 ^{o}C.

2,5-bis(4-(bis(4-(hexyloxy)phenyl)amino)phenyl)thiophene-3,4-diamine (8, x = TPA). 7 (x = TPA, 10 mg, 0.01 mmol) was dissolved in ethanol (0.06 ml, 0.16 M) and DCM (0.06 ml, 0.16 M) in a round bottom flask under N_2. Tin (II) chloride dihydrate (22.6 mg, 0.1 mmol) was added as a solution in ethanol (0.1 ml, 1.0 M) and concentrated HCl (0.074 ml, 1.35 M) to the reaction mixture. The reaction was stirred 3 days at 30°C. The reaction was quenched with 25% NaOH (aq.) and extracted with DCM to give a yellow oil. The crude product was directly used immediately in the next reaction without further purification. ^{1}H NMR (300 MHz, DMSO-d_6) δ 7.32 (d, J = 8.6 Hz, 4H), 6.99 (d, J = 8.7 Hz, 8H), 6.88 (d, J = 8.9 Hz, 8H), 6.79 (d, J = 8.7 Hz, 4H), 4.63 (s, 4H), 3.92 (t, J = 6.5 Hz, 8H), 1.72-1.67 (m, 8H), 1.41-1.23 (m, 24H), 0.88 (m, 12H).

4,4'-(thieno[3,4-c][1,2,5]thiadiazole-1,3-diyl)bis(N,N-bis(4(hexyloxy)phenyl)aniline) (TTD(TPA)$_2$). To a flame-dried round bottom flask was added 8 (x = TPA, 43 mg, 0.04 mmol), N-thionylaniline (0.01 ml, 0.086 mmol), TMSCl (0.04 ml, 0.301 mmol), and pyridine (0.24 ml, 0.18 M) under N_2. The reaction was stirred at room temperature overnight. The reaction was quenched with 1M HCl (aq.) and extracted with DCM to give green solid. The product was purified through silica gel chromatography column with 40% DCM:hexane. (17 mg, 39 %). ^{1}H NMR (500 MHz, DMSO-d_6) δ 7.89 (d, J = 8.7 Hz, 4H), 7.06 (d, J = 8.9 Hz, 8H), 6.93 (d, J = 8.9 Hz, 8H), 6.86 (d, J = 8.7 Hz, 4H), 3.95 (t, J = 6.5 Hz, 8H), 1.73-1.70 (m, 8H), 1.46-1.39 (m, 8H), 1.34-1.21 (m, 24H), 0.91-0.86 (m, 12H). HRMS (ESI) m/z calculated for $C_{64}H_{76}N_4O_4S_2$ $[M + Cs]^+$ 1161.4363, found 1161.4347. IR (neat, cm^{-1}) 2924.9, 2856.7, 1600.8, 1505.3, 1480.5, 1240.1, 1030.6.

CHAPTER 3

3.1 ULLAZINE DONER-π BRIDGE-ACCEPTOR ORGANIC DYES FOR DYE-SENSITIZED SOLAR CELLS

Adapted with the permission from **Yanbing Zhang,**; Hammad Cheema,; Louis McNamara,; Leigh Hunt,; Nathan I. Hammer,; Delcamp, J. H. *Chem. Eur. J*. **2018**, *24*, 5939. Copyright (2019) Wiley Online Library.

(See appendix for permission license)

This project is a collaborative project between Dr. Delcamp group and Dr. Hammer group. Dr. Hammad Cheema equally contributed to the work by making and analyzing all the devices, Dr. Louis McNamara and Leigh Hunt contributed to the project by measuring the lifetime of the solid-state of the dyes.

ABSTRACT

A series of 4 ullazine-donor based donor-π bridge-acceptor (D-π-A) dyes have been synthesized and compared to a prior ullazine donor-acceptor (D-A) dye as well as a triphenylamine donor with an identical π-bridge and acceptor. The D-π-A ullazine series demonstrates an unusually uniform-in-intensity panchromatic UV-Vis absorption spectrum throughout the visible region. This is in part due to the introduction of strong high-energy bands through incorporation of the ullazine building block as shown by computational analysis. The dyes were characterized

on TiO_2 films and in DSC devices. Performances of 5.6% power conversion efficiency were obtained with IPCE onsets reaching 800 nm.

INTRODUCTION

Dye-sensitized solar cells (DSCs) have attracted increasing attention since 1991 due to low manufacturing costs, affordable solar cell materials, easy integration into building materials and the potential to meet energy production needs.[63–65] DSCs operate through light absorption by a sensitizer or dye anchored to a semiconductor, electron transfer from the excited-state dye to the semiconductor, collection of the electron by a redox shuttle at a counter electrode after it has traveled an external circuit, and return of the electron to the oxidized dye by the redox shuttle. The sensitizer component of the DSC devices plays a critical role in controlling light absorption and subsequent electron transfers. Organic sensitizers based on the conjugated donor-π-acceptor (D-π-A) framework offer a modular synthesis, high molar extinction coefficient, and tunable molecular design which has furnished organic dyes outperforming precious metal containing sensitizer with power conversion efficiencies (PCEs) of over 13%.[4,6,66] Additional improvements to organic sensitizers are possible by extending the absorption range with precise control of the sensitizer energy levels. A key functionality needed for many D-π-A dye systems to extend their absorption spectrum is the donor building block.[67–71] Frequently, organic dyes do not have ground-state oxidation potentials well positioned for minimal energy loss as a result of the limited availability of stable, strong electron donating functionality.[72] Typically, phenyl amine organic molecular building blocks such as coumarin, indoline, triphenylamine, or carbazole are employed as donors.[66,73] However, these donors often lack planarization of the nitrogen lone pair with the dye π-system, conjugation of all p-orbitals on the donor building block, and the ability to add additional electron donating groups in conjugation with the dye π-system.[68] These inherent challenges have

led to the extensive evaluation of various electron rich π-bridges to compensate for the lack of desired donor strength. The use of a planarized *peri*-fused nitrogen containing building blocks such as ullazine offers a potential solution to each of these challenges.

Ullazine is a 16 π-electron planar nitrogen containing *peri*-fused heterocyclic system which is isoelectronic with pyrene.[65,67,72-81] Ullazine is fully conjugated with a number of substitutable positions for modulating donor strength and tuning dye morphologies. Ullazine has a charge separated anionic 14 π-electron aromatic annulene resonance structure around the periphery which enhances the donation strength of the nitrogen lone pair by favoring charge separation (Figure 11). This charge-separated state can be used to promote intramolecular charge transfer (ICT) at lower energies. Additionally, upon ICT, an aromatic ring arises on ullazine in the excited-state. This proaromatic pyridinium ring serves to lower the energy necessary for ICT by aromatically stabilizing the excited-state.[68,70,84] These desirable attributes have been shown to shrink optical band gap by ~ 0.7 eV when compared with an analogous triarylamine donor based dye.[69] Ullazine is also known to be stable during redox processes as is desirable within a solar cell device.[82] Due to these properties, ullazine has recently attracted interest in donor-acceptor dyes and as a donor for porphyrin sensitizers in DSC devices.[69,76] However, to date ullazine has only been evaluated once in metal-free donor-π bridge-acceptor sensitizers despite the potential for robust, panchromatic organic dyes which are desperately needed in DSCs.[75]

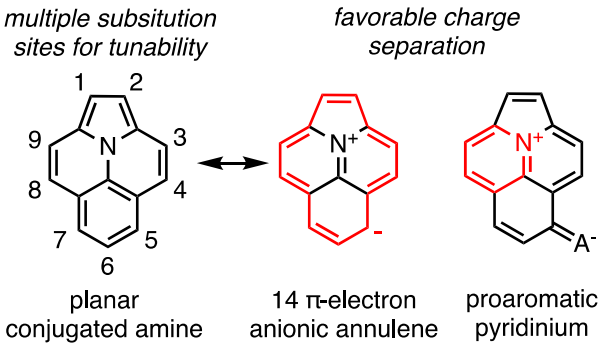

Figure 11. Ullazine building block with resonance structures drawn to illustrate favorable ICT.

RESULTS AND DISCUSSION

Given the promising known properties of ullazine, a series of novel D-π-A based ullazine dyes were targeted for synthesis (Figure 12). This series focused on the incorporation of two different aryl groups on ullazine with either a *para*-alkoxy group to maintain a highly electron rich donor (**YZ7** and **YZ12**) or di-*ortho*-alkoxy groups extending over the ullazine π-face to disrupt any potential π-stacking based aggregation (**YZ14** and **YZ15**). Given the two strongest donating positions (the 4 and 5 positions) of ullazine are ortho substituted, an alkyne was chosen to link the donor to the π-bridge in order to enable access to a fully planarized π-system conformation. The dyes with identical aryl substituents vary in position of an alkyne linking group either at the meta position relative to the nitrogen substituent on the fused benzene ring (5 position) or at the position adjacent to the aryl group (4 position). Cyclopentadithiophene (CPDT) was chosen as an electron rich π-bridge since DSC dyes typically have considerable energy losses due to lack of electrons with high enough potential energy in the ground state of the dye to reach ideal energetics. Additionally, CPDT is a well-established π-bridge in high efficiency DSCs which allows for a straight forward comparison of a ullazine-alkyne donor to common amine donors such as triphenylamines (TPAs).[85–87] All dyes utilize the ubiquitous cyanoacrylic acid acceptor.

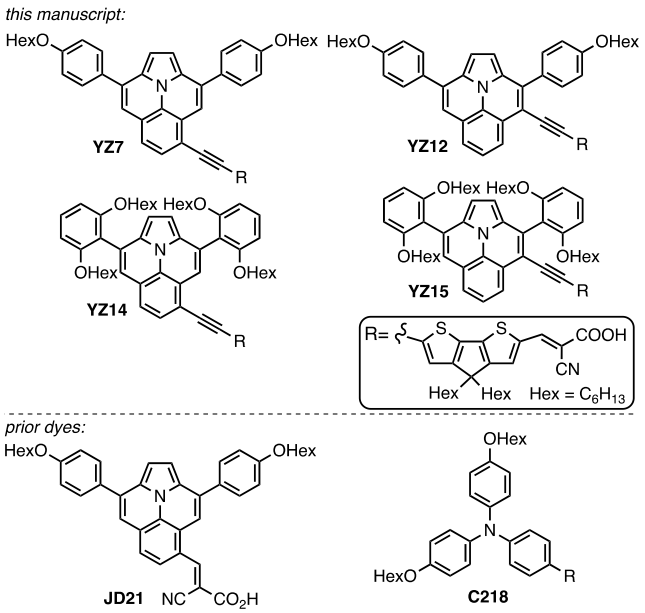

Figure 12. Structure of ullazine-based dyes **YZ7, YZ12, YZ14, YZ15,** and **JD21** as well as TPA dye **C218**.

The synthesis of **YZ7**, **YZ12**, **YZ14** and **YZ15** is briefly described here from known intermediates (Scheme 2). The ullazine heterocycle with two di-*ortho*-hexyloxyphenyl groups was synthesized similar to prior analogs.[69] Briefly, the di-*ortho*-hexyloxyphenyl alkyne (**2b**) was synthesized from the corresponding aryl aldehyde (**1b**) via treatment with TMS-diazomethane and LDA in 91% yield. Alkyne **2b** was coupled to dibromophenyl pyrrole **3** via a Sonogashira reaction in 83% yield. $InCl_3$ catalyzed cyclization furnished parent ullazine **5b** in 29% yield. Formyl groups were installed via Vilsmeyer-Haack reaction to give the two desired isomers **6b** and **7b**, which were separated via silica gel chromatography and carried forward.[69] The aldehydes **6a, 6b, 7a** and **7b** were subjected to modified Corey-Fuchs reaction conditions to give desired alkynes **8a**, **8b**, **9a**, and **9b** in high yield except for derivative **9b** presumably due to sterics. For aldehyde precursors to final dyes **YZ7**, **YZ12** and **YZ14**, Sonogashira cross couplings with 6-bromo-4,4-dihexyl-4H-cyclopenta[2,1-b:3,4-b']dithiophene-2-carbaldehyde **10** and intermediates **8a**, **8b**, or **9a** were

carried out in low to high yields. Alkyne **9b**, a precursor to **YZ15**, gave no desired product under similar

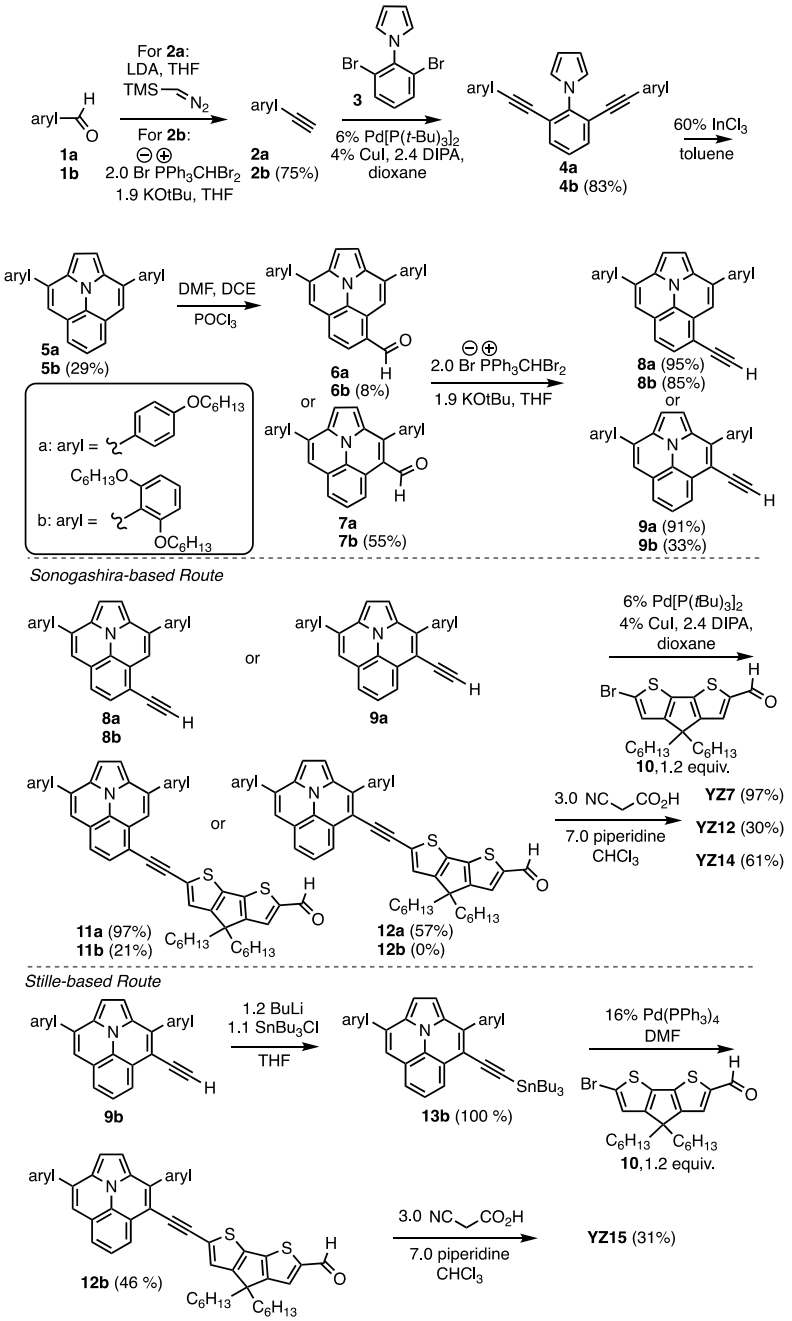

Scheme 2. Synthetic route to **YZ7**, **YZ12**, **YZ14** and **YZ15**. Yields are only listed for compounds which are novel to this manuscript.

conditions, thus an alternative alkyne-stannylation/Stille coupling route was used to furnish the desired aldehyde **12b** in 46% yield. Knoevenagel condensation on the resulting aldehydes (**11a**, **11b**, **12a**, or **12b**) furnished the desired dye series.

With the desired dyes in hand, the absorption properties of the **YZ** dyes were examined to determine the suitability of these dyes in DSC devices and to better understand the effects of the ullazine-donor group on ICT. The ullazine-based dyes have a broad absorbance from 400-700 nm with high molar absorptivities of (26,000-29,000 $M^{-1}cm^{-1}$, Figure 13, Table 4). The absorption spectra of **YZ7-YZ15** exhibit an intense peak at around 535 nm, which is due to the HOMO-LUMO transition of the conjugated molecule (discussion below). The introduction of the alkyne-CPDT π-system to give a D-π-A structure led to a red-shift of the absorption spectrum relative to D-A ullazine-cyanoacrylic acid dye **JD21** (Figure 12).[69] Additionally, the D-π-A structure broadened the absorption spectrum relative to the simple D-A dye and led to the introduction of a strong high-energy absorption band. This high-energy transition band is unique to ullazine D-π-A CPDT bridged dyes as triphenylamine analogues such as **C218** only have a single strong absorption band in the visible region.[88] This is important as the introduction of high-energy bands in the absorption spectrum has been related to higher performing DSC devices due to a more uniform absorption of the solar spectrum.[89] The molar absorptivities of these high energy bands are comparable to that of the ICT low energy band ranging from about 15,000-30,000 $M^{-1}cm^{-1}$. Dyes with strong absorption across the full visible spectrum are desirable and rare in DSC reports. Comparing the effects within the proposed series, only a modest shift (10 nm) of the absorption maximum is observed based on the substitution

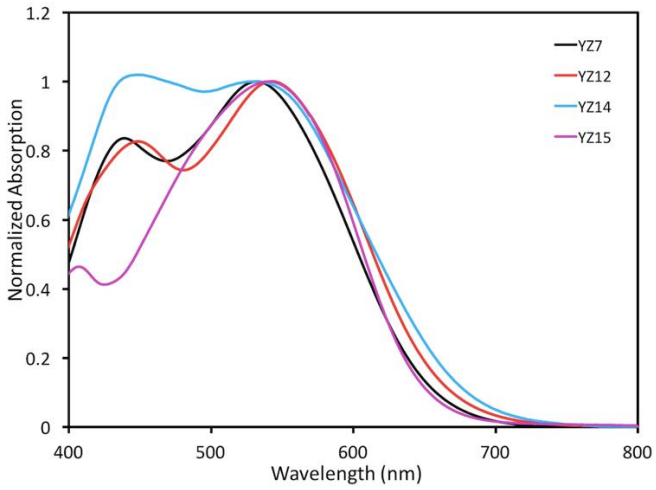

Figure 13. Absorption of **YZ7** (black line), **YZ12** (red line), **YZ14** (blue line), **YZ15** (purple line) measured in CH_2Cl_2.

position of the alkyne on ullazine with the position closest to the aryl group (4 position) giving the most red-shifted values. The ullazine-phenyl group substituent selection had little effect on the position of the absorption maximum.

Having established a desirable broad absorption spectrum for use in DSC devices, the dye energy levels were analyzed to evaluate the thermodynamic suitability of these dyes for DSCs. Cyclic voltammetry was used to measure the ground-state oxidation potentials ($E_{(S+/S)}$) (Table 4). The $E_{(S+/S)}$ values were measured within a range of 0.71-0.90 V versus NHE which are significantly more positive than the iodide/triiodide redox shuttle (0.35 V versus NHE). This indicates neutral dye regeneration is favorable with a driving force of 360-550 mV. The ground-state oxidation potential is similar or higher in energy for

Table 4. Optical and electrochemical data for ullazine dyes **YZ7, YZ12, YZ14, YZ15**, **JD21**, and a TPA analogue **C218.** *See experimental for detailed energy measurements and calculations

dye	λ_{max} (nm)	ε ($M^{-1}cm^{-1}$)	$E_{(S+/S)}$ (V)	$E_{(S+/S^*)}$ (V)	E_g^{opt} (eV)
YZ7	532	29,000	0.90	-0.98	1.88
YZ12	543	28,000	0.90	-0.94	1.84
YZ14	537	28,000	0.71	-1.08	1.79
YZ15	549	26,000	0.84	-1.05	1.89
JD21	582	28,000	1.09	-0.94	2.03
C218	550	21,000	0.89	-1.06	1.95

these dyes relative to a triphenylamine analogue (**C218**), which we attribute to the strong donation strength of the ullazine donor. The decrease in overpotential used to regenerate the dye is important to maximizing DSC device efficiencies, and maintaining high energy $E_{(S+/S)}$ values with NIR absorbing materials is critical for efficient solar-to-electric conversion at low energy with TiO_2 based DSC devices. The ullazine aryl substituents were found to have a significant effect on the dye ground state oxidation potential with the

relative to the di-*ortho*-alkyoxyphenyl substituted dyes (**YZ14** and **YZ15**). This highlights that the ullazine-phenyl group plays a key role in tunably tailoring $E_{(S+/S)}$ values. For favorable electron transfer to TiO_2 the dye excited-state oxidation potential ($E_{(S+/S^*)}$) should be higher in energy than -0.5 V versus NHE. The dye $E_{(S+/S^*)}$ values were calculated by subtracting the optical band gap (E_g^{opt}) found at the absorption onset from $E_{(S+/S)}$. $E_{(S+/S^*)}$ values for the dye series were found to be between -0.94 and -1.08 V versus NHE, which provides enough overpotential for injecting an electron from the photo-excited dye to the TiO_2 conduction band.

In addition to the suitable energetics found for each of the dyes, well positioned orbitals are required for efficient DSC devices. The dye lowest unoccupied molecular orbital (LUMO) should be positioned near the TiO_2 surface for efficient electron transfer from the dye to TiO_2. Additionally, the highest occupied molecular orbital (HOMO) should be positioned away from the TiO_2 surface to diminish back electron transfer from TiO_2 to the oxidized dye. Computational

studies via density functional theory (DFT) were carried out to examine the position of the HOMO and LUMO at the B3LYP and 6-311G(d,p) level (**YZ7:** Figure 14; **YZ12**, **YZ14**, **YZ15**: Figure 43 in Appendix). The HOMOs of the four ullazine-based dyes are primarily positioned on the ullazine motif with some delocalization onto the CPDT π-bridge. This position is ideal for good separation of the HOMO from the TiO_2 surface in space as the ullazine-donor is at the opposite end of the dyes relative to the anchor. The LUMO is partially delocalized over the CPDT bridge and primarily positioned on the acceptor/anchor. The position of both the HOMO and LUMO suggests these ullazine-based dyes can perform efficiently in DSC devices, and also suggests the ullazine-based D-π-A dyes are absorbing light via ICT.

Time-dependent DFT (TD-DFT) calculations were carried out to access the orbital contributions to each of the transitions observed in the absorption spectrum. For the ullazine D-π-A dyes, TD-DFT indicates the low energy transition band centered at ~530 nm is dominated by a HOMO to LUMO transition (99%) which confirm the ICT nature of these dyes (see Figure 14 for orbitals, see Table 13, Appendix, for TD-DFT results). The high energy transition band at ~430 nm which led to a true panchromatic absorption in the UV-Vis-NIR absorption spectrum is attributed to a combination of transitions from the HOMO-1 to LUMO (62%) and HOMO to LUMO+1 (36%). The HOMO-1 and LUMO+1 both have substantial involvement from the ullazine building block showing the importance of this building block in adding these strongly absorbing higher energy bands.

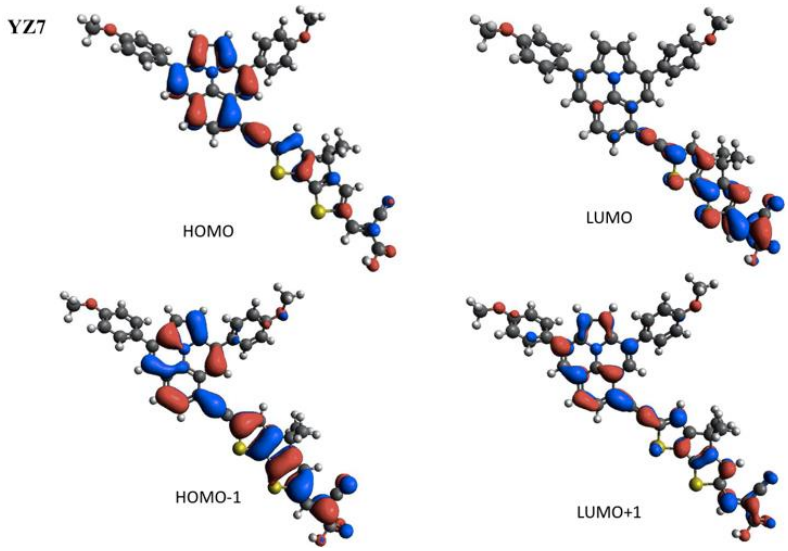

Figure 14. HOMO, LUMO, HOMO-1, LUMO+1 orbitals for dye **YZ7** given by DFT calculations at the B3LYP/6-311G(d,p) level.

YZ7, **YZ12**, **YZ14** and **YZ15** were found to have a panchromatic solution absorption, properly positioned energy levels and properly positioned orbitals to perform well in DSC devices. Thus, devices were fabricated with the ullazine D-π-A dyes using TiO_2 as the semiconductor and iodine/triiodide as the redox shuttle (Figure 15 and Table 5). Sensitization of TiO_2 films is commonly done with EtOH:THF solutions for many organic dyes; however, the dyes examined in this report were not fully soluble at the desired 0.3 mM concentration. The addition of DMF to give a 4:1:2 (EtOH:THF:DMF) solution gave higher solubility and films were sensitized from this mixture. Initially the dyes were found to have PCE values of 2.1-4.4% with **YZ7** and **YZ15** having the highest performance according to the equation PCE = (J_{sc} x V_{oc} x FF)/I_0 where J_{sc} is the short circuit current density, V_{oc} is the open circuit voltage, *FF* is the fill factor, and I_0 is the sun intensity (Table 5, Figure 15). The dyes show similar *FF* values (0.68-0.70) and similar V_{oc} values (543-568 mV, except **YZ14** with 477 mV). The V_{oc} values were low in part due to significant LiI needing to be added to the cell electrolyte to increase J_{sc} values.

The largest change in dye performance was from the J_{sc} parameter, which ranged from 6.2-11.3 mA/cm^2. Such a broad variation in this parameter is somewhat surprising given the similarity of the dye orbital properties and dye energetics. Additionally, the two highest J_{sc} value dyes were **YZ7** and **YZ15,** which vary structurally the most in the series with a change at the position of the bridge-acceptor substitution and at the substituents on the aryl groups. To better understand this large variation in J_{sc} values, incident photon-to-current conversion efficiency (IPCE) measurements were undertaken. All of the dyes show a broad IPCE spectrum from 350 nm to approximately 800 nm, however the height of the IPCE spectrum varies dramatically with peak IPCE values in the following order **YZ14** (35%) < **YZ12** (55%) < **YZ15** (65%) = **YZ7** (65%). A slight increase in the high-energy region breadth explains the higher current from **YZ7** compared to **YZ15** observed from the IV curve measurements.

Table 5. DSC device parameters for **YZ7, YZ12, YZ14** and **YZ15**.

Dye	Voc/mV	*J*sc/ mA cm^{-2}	FF	PCE (%)
YZ7	551	11.3	0.68	4.4
YZ12	543	9.6	0.70	3.8
YZ14	477	6.2	0.70	2.1
YZ15	568	10.9	0.69	4.4
YZ7*	559	14.1	0.67	5.6

See experimental for device details. *Indicates **YZ7** optimized device conditions.

The highest performing dye in the series (**YZ7**) was subjected to time correlated single photon counting (TCSPC) excited-state lifetime analysis to evaluate electron injection efficiency. **YZ7** shows excited-state lifetimes shorter than our instrument response time of 150 ps, both on TiO_2 and Al_2O_3 films, compared to 1.25 ns in DCM (Figure 16). This is surprising as a decrease

in excited-state lifetime on TiO_2 is commonly thought to correlate with electron injection; however, electron injection is not possible with Al_2O_3 as it is an insulator. Yet, Al_2O_3 shows a dramatic decrease in excited-state lifetime. A possible rationale for this observation is heavy aggregation of the dye on film surfaces which diminishes excited-state lifetimes.

To evaluate this hypothesis, solid film UV-Vis absorption measurements were made for comparison to solution measurements for **YZ7** (Figure 17). Compared to solution measurements, the strength of the low energy and high energy transitions are reversed on the film. The results support our aggregation hypothesis as **YZ7** appears to aggregate heavily on solid films of TiO_2. CDCA is commonly used to disrupt aggregation and at very high loadings (100:1 CDCA:dye), the film absorption spectrum begins to look more like the solution spectrum in terms of relative transition intensity. Thus, the shorter excited state lifetime

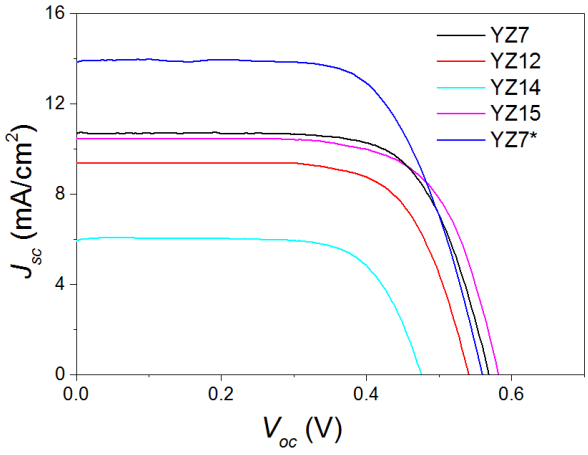

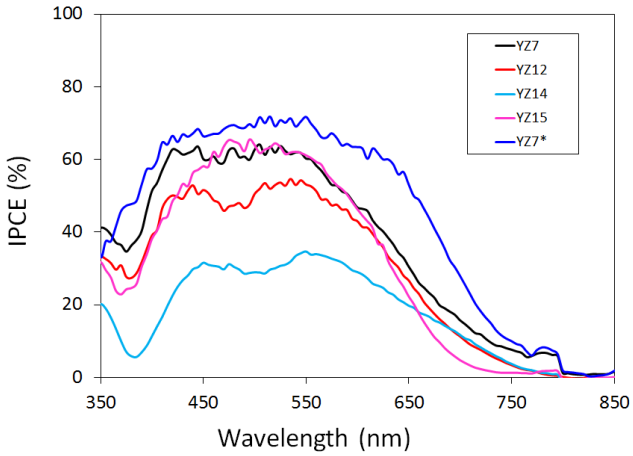

Figure 15. *J-V* curves (top) and IPCE (bottom) for DSC devices with **YZ7, YZ12, YZ14** and **YZ15.** *Indicates different dye sensitization solution was used (see Table 5 for details).

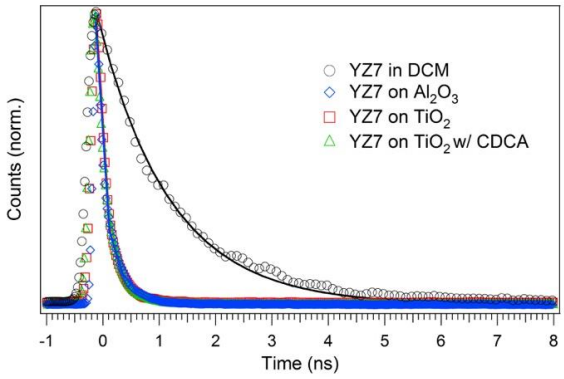

Figure 16. Time correlated single photon counting graph with **YZ7** in DCM solution, **YZ7** on Al_2O_3, **YZ7** on TiO_2 and **YZ7** on TiO_2 with CDCA.

in the solid-state and the appearance of aggregation induced absorption may explain the need for higher LiI loading to achieve a higher injection free energy from the aggregates to TiO_2 by lowering TiO_2 conduction band (Table 14 in Appendix).

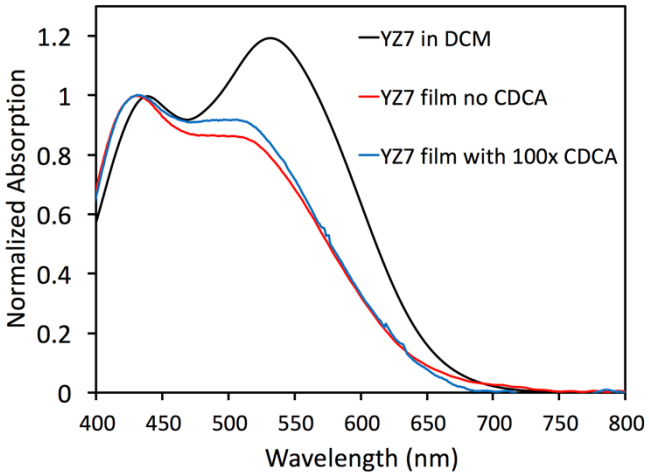

Figure 17. Normalized UV-Vis absorption of **YZ7** in DCM, and TiO_2 film absorption of **YZ7** with no CDCA and 100:1 CDCA:dye.

Given the similar energetics and absorption breadths, aggregation of these dyes on the TiO_2 surface is a potential PCE diminishing factor in this series. Evidence for this includes: (1) the IPCE spectrum onsets at a 100 nm longer wavelength than that of the DCM solution, (2) the absorption spectrum of the dye on TiO_2 shows the higher energy absorption band as the strongest transition while the solution absorption spectrum shows the lower energy absorption band as the strongest, (3) TCSPC studies show Al_2O_3 films decrease excited-state lifetimes dramatically compared to solution measurements, and (4) the addition of a co-sensitizer (**D35**) increased the IPCE intensity of **YZ7** in a region of the spectrum where **D35** does not absorb which implies disruption of aggregates (Figure 44, Appendix). Attempts to diminish aggregation through addition of CDCA to the dye-deposition solution only showed a modest change in the dye-TiO_2 film absorption spectrum and no significant enhancement of device performance. To evaluate the effects of deposition solvent with the best performing dye, **YZ7**, a series of solvents were examined (Table 15, Figure 45, Appendix). The PCE efficiency varied substantially with deposition solvent from 3.4-5.6% PCE. The best conditions were found to be deposition of **YZ7** from acetonitrile:*tert*-butanol:chlorobenzene (1:1:1.2,v/v/v) with 10:1 CDCA:dye. The IPCE curve of **YZ7** under

optimized conditions shows an increase in percent intensity from 350 nm to 800 nm with a peak value of 75%. The integrated current under the IPCE curve is in good agreement with the short-circuit current density (J_{sc}) of 14.1 mA/cm^2 measured under AM 1.5 conditions. The measured J_{sc} combined with an open-circuit voltage (V_{oc}) of 559 mV and fill factor (FF) of 0.67 gives the highest power conversion efficiency (PCE) of the series at 5.6%. These results show that the Ullazine donor is exceptional at the introduction of desirable dye properties (panchromatic light absorption, multiple transitions in the UV-Vis spectrum, and maintaining high energy oxidation potentials); however, in the solid state the aggregation of these dyes leads to diminished device performances which must be carefully optimized to increase IPCE response and device PCE.

CONCLUSIONS

In summary, we have designed and synthesized a series of metal-free ullazine based D-π-A dyes for the first time. These dyes were characterized by UV-Vis-NIR absorption spectroscopy, cyclic voltammetry, and computational analysis, which reveal suitable characteristics for use in DSC devices. The broad, near uniform solution absorption intensity from 350-700 nm is particularly desirable for DSC applications. This dramatic change in absorption spectrum from the prior reports on D-A ullazine sensitizers with relatively narrow absorption spectrum response is encouraging. A PCE of 5.6% was obtained for the highest performing dye in the series (**YZ7**) with an IPCE onset of 800 nm. Given the relatively few metal-free dyes reaching 800 nm in an IPCE spectrum this dye-design warrants further investigation. TCSPC studies and film absorption measurements show substantial aggregation of the dyes on the TiO_2 surface. This strongly suggests the diminishment in IPCE peak value (75% with a maximum of 90%) is the result of surface aggregation. Future dye designs will focus added substituents to the ullazine building block which are known to dramatically reduce dye aggregation.

EXPERIMENTAL SECTION

General Information. All commercially obtained reagents were used as received. 3,9-bis(4-(hexyloxy)phenyl) indolizino[6,5,4,3-ija]quinoline-5-carbaldehyde (**6a**) and 3,9-bis(4-(hexyloxy)phenyl)indolizino[6,5,4,3-ija]quinoline-4-carbaldehyde (**7a**) were made according to literature.[69] 6-bromo-4,4-dihexyl-4H-cyclopenta[2,1-b:3,4-b']dithiophene-2-carbaldehyde (**10**) was prepared according to literature procedure.[90] 1-(2,6-dibromophenyl)-1H-pyrrole (**3**) was prepared according to literature procedure.[69] Thin-layer chromatography (TLC) was conducted with Sorbtech silica XHL TLC plates and visualized with UV. Flash column chromatography was performed with Silicycle ultrapure silica gel P60, 40-63 μm (230-400 mesh). Reverse phase column chromatography was performed with premium grade C18 silica gel from Sorbent technologies. ^{1}H NMR spectra were recorded on Bruker Avance-300 (300 MHz) and Bruker Avance DRX-500 (500 MHz) spectrometers and are reported in ppm using solvent as an internal standard ($CDCl_3$ at 7.28 ppm). NMR data is reported as s = singlet, d = doublet, t = triplet, q = quartet, p = pentet, m = multiplet, br = broad, ap = apparent, dd = doublet of doublets, and coupling constant(s) are in Hertz, followed by integration information. UV−Vis-NIR spectra were measured with a Cary 5000 instrument. HPLC measurements were taken using an Agilent 1100A HPLC instrument, equipped with an Agilent Eclipse Plus C18 column and UV-Vis detector. 90% isopropanol: 10% water was used as the mobile phase at 0.3 ml/min for all the measurement. HRMS spectra were obtained with a QTOF HRMS utilizing nanospray ionization. The mass analyzer was set to the 400−2000 Da range. CV data was collected with a CH Instruments CHI600E instrument.

Electrochemical Characterization. Cyclic voltammetry was measured with a 0.1 M Bu_4NPF_6 in CH_2Cl_2 solution using a glassy carbon working electrode, platinum reference electrode,

and platinum counter electrode with ferrocene as an internal standard. Values are reported versus NHE with ferrocene taken as 0.70 V vs NHE. $E_{(S+/S^*)}$ is calculated from the equation $E_{(S+/S^*)} = E_{(S+/S)} - E_g^{opt}$. E_g^{opt} is estimated from the onset of the absorption spectrum and converted from nanometers to eV with the equation: $E_g^{opt} = 1240/\lambda_{onset.}$

Computational Protocol. MM2 energy minimization in ChemBio3D Ultra (version:13.0.2.3021) was used for the initial energy minimization of the four dyes. Dihedral angles for the relevant groups were set to values between the global minimum and the next local minimum on the conformation energy diagram as calculated by ChemBio3D. Accurate geometry optimizations were performed sequentially by density functional theory (DFT) using Guassian09 with the B3LYP functional with the following basis sets: first 3-21g, second 6-31g (d,p) and finally 6-311g (d,p). No imaginary frequencies were observed for the optimized geometries. Time-dependent density functional theory (TD-DFT) computations were performed with optimized geometries and with the B3LYP functional and 6-311g (d.p) basis set to compute the lowest energy 10 vertical transitions and oscillator strengths. Orbital images were prepared with Avogadro 1.0.3 with an iso value of 0.30.

Time Correlated Single Photon Counting (TCSPC) Measurements: Fluorescence lifetime curves were obtained using the 485 nm line of an LDH series 485B pulsed diode laser (pulse width approx. 100 ps) as the excitation source and emission was detected using a PicoQuant PDM series single photon avalanche diode (time resolution approx. 50 ps) and TimeHarp 260 time correlated single photon counter (25 ps resolution). The alumina paste was prepared by following the reported procedure with the following modifications.[91] 167 mg of Al_2O_3 NPs (particle size ~ 150 mesh, pore size = 58 Å, surface area = 155 m^2/g, SigmaAldrich) was dispersed in a 5 mL solution containing α-terpineol/ethylcellulose (Sigma aldrich # 46080, 48.0-49.5% (w/w) ethoxyl

basis) (ethylcellulose content: 6 wt % of α-terpineol, 280 mg) with 5 ml of acetone. The suspension was kept under stirring conditions over a period of 2 days, after which the remaining acetone was removed by rotary evaporator. The α-terpineol/ethylcellulose mixture was first prepared by completely dissolving ethylcellulose in α-terpineol in the presence of 5 ml ethanol, once dissolved excess ethanol was removed by rotary evaporator. The prepared paste was then used to screen print films with a Sefar screen (54/137–64W) resulting in 1 µm thick films on TEC 15 FTO glass. Before its use, the TEC 15 was cleaned by submerging in a 0.2% Deconex 21 aqueous solution and sonicated for 15 minutes at room temperature. The FTO glass was rinsed with water and sonicated in acetone 10 minutes followed by sonication in ethanol for 10 minutes. Finally, after paste printing and drying on a hot plate for 7 minutes at 125^{o}C, substrates were then sintered with progressive heating from 125^{o}C (5 minute ramp from r.t., 5 minute hold) to 325^{o}C (15 minute ramp from 125oC, 5 minute hold) to 375^{o}C (5 minute ramp from 325^{o}C, 5 minute hold) to 450^{o}C (5 minute ramp from 375^{o}C, 15 minute hold) to 500^{o}C (5 minute ramp from 450^{o}C, 15 minute hold) using a programmable furnace (Vulcan® 3-Series Model 3-550). After cooling to room temperature, the electrodes were dipped in the 0.3 mM dye solution for 16 hours and used as it is for TCSPC measurements.

Photovoltaic Measurements: Current-Voltage curve photovoltaic characteristics were measured using a 150 W Xenon lamp (Model SF150B, SCIENCETECH Inc. Class ABA) solar simulator equipped with an AM 1.5 G filter for a less than 2% spectral mismatch. Prior to each measurement, the solar simulator output was calibrated with a KG5 filtered mono-crystalline silicon NREL calibrated reference cell from ABET Technologies (Model 15150-KG5). The current density-voltage characteristics of each cell was obtained with a Keithley digital source-meter (Model 2400). The incident photon-to-current conversion efficiency was measured with an

IPCE instrument manufactured by Dyenamo comprised of a 175 W Xenon lamp (CERMAX, Model LX175F), monochromator (Spectral Products, Model CM110, Czerny-Turner, dual-grating), filter wheel (Spectral Products, Model AB301T, fitted with filter AB3044 [440 nm high pass] and filter AB3051 [510 nm high pass]), a calibrated UV-enhanced silicon photodiode reference, and Dyenamo issued software.

Device Fabrication: For the photoanode, TEC 10 glass was purchased from Hartford Glass. Once cut into 2x2 cm squares, the substrate was submerged in a 0.2% Deconex 21 aqueous solution and sonicated for 15 minutes at room temperature. The electrodes were rinsed with water and sonicated in acetone 10 minutes followed by sonication in ethanol for 10 minutes. Finally, the electrodes were placed under UV/ozone for 15 minutes (UV-Ozone Cleaning System, Model ProCleaner by UVFAB Systems). A compact TiO_2 underlayer is then applied by pretreatment of the substrate submerged in a 40 mM $TiCl_4$ solution in water (prepared from 99.9% $TiCl_4$ between 0-5^oC). The submerged substrates (conductive side up) were heated for 30 minutes at 70^oC. After heating, the substrates were rinsed first with water then with ethanol. The photoanode consists of thin TiO_2 electrodes comprised of a 10 μm mesoporous TiO_2 layer (particle size, 20 nm, Dyesol, DSL 18NR-T) for **YZ7-YZ15** for devices using the iodine redox shuttle and a 5.0 μm TiO_2 scattering layer (particle size, 100 nm, Solaronix R/SP). Both layers were printed from a Sefar screen (54/137–64W). Between each print, the substrate was heated for 7 minutes at 125^oC and the thickness was measured with a profilometer (Alpha-Step D-500 KLA Tencor). The substrate was then sintered with progressive heating from 125^oC (5 minute ramp from r.t., 5 minute hold) to 325^oC (15 minute ramp from 125^oC, 5 minute hold) to 375^oC (5 minute ramp from 325^oC, 5 minute hold) to 450^oC (5 minute ramp from 375^oC, 15 minute hold) to 500^oC (5 minute ramp from 450^oC, 15 minute hold) using a programmable furnace (Vulcan® 3-Series Model 3-550). The cooled

sintered photoanode was soaked 30 min at 70°C in a 40 mM $TiCl_4$ water solution and heated again at 500°C for 30 minutes prior to sensitization. The complete working electrode was prepared by immersing the TiO_2 film into the dye solution overnight at room temperature. The solution is 0.3 mM of dye in different solvent mixtures (Table S2). For preparing counter electrodes, 2x2 cm squares TEC 7 FTO glass was drilled using a Dremel-4000 with Dremel 7134 Diamond Taper Point Bit with FTO side protected by tape. Electrodes were washed with water followed by a 0.1M HCl in EtOH wash and sonication in acetone bath for 10 minutes. These washed FTO electrodes were then dried at 400°C for 15 minutes. A thin layer of Pt-paste (Solaronix, Platisol T/SP) was slot printed on the FTO, and the printed electrodes were then heated at 450°C for 10 minutes. After allowing them to cool to room temperature, the working electrodes were then sealed to the Pt-FTO electrodes with a 25 μm thick hot melt film (Solaronix, "Meltonix", Surlyn) by heating the system at 130°C under 0.2 psi pressure for 1 minute. Devices were completed by filling the electrolyte through the pre-drilled holes in the counter electrodes, and finally the holes were sealed with a Surlyn circle and a thin glass cover by heating at 130°C under a pressure of 0.1 psi for 25 seconds. Finally, soldered contacts were added with a MBR Ultrasonic soldering machine (model USS-9210) with a solder alloy (Cerasolzer wire diameter 1.6 mm, item # CS186-150). A circular black mask (active area 0.15 cm^2) was punched from black tape and used in the subsequent photovoltaic studies. Film absorption was done using TEC 15 glass with 3 μm mesoporous TiO_2 film (particle size, 20 nm, Dyesol, DSL 18NR-T), and progressively heated as described previously.

SYNTHETIC DATA

2-ethynyl-1,3-bis(hexyloxy)benzene (2b): To a flame dried flask was added freshly prepared dibromomethyl-triphenylphosphonium bromide[76] (38.6 g, 75.3 mmol, 2.02 equiv.) and tetrahydrofuran (377 ml). In one portion, potassium *tert*-butoxide (7.93 g, 70.8 mmol, 1.90 equiv.)

was added and the mixture stirred at ambient temperature for 3 minutes. A solution of **1b**[69] (11.4 g, 37.3 mmol, 1.0 equiv.) in tetrahydrofuran (63.2 ml) was added to the reaction mixture via cannula, and the resulting mixture was stirred at room temperature for 10 minutes. The reaction was cooled to -78°C and potassium *tert*-butoxide (20.8 g, 187 mmol, 5.0 equiv.) was added in one portion following gradual warming to ambient temperature. After 1.5 hours, the reaction mixture was diluted with dichloromethane and rinsed with water, dried by Na_2SO_4 and evaporated. The crude mixture was purified through silica gel chromatography using 20% dichloromethane: hexane was the eluent to get clear oil. (8.51 g, 75%). ^{1}H NMR (500 MHz, $CDCl_3$) δ = 7.18 (t, *J* = 8.4 Hz, 1H), 6.50 (d, *J* = 8.5 Hz, 2H), 4.03 (t, *J* = 6.7 Hz, 4H), 3.48 (s, 1H), 1.95-1.70 (m, 4H), 1.60-.142 (m, 4H), 1.42-1.22 (m, 8H), 0.95-0.92 (ap t, 6H). ^{13}C NMR (125 MHz, $CDCl_3$) δ = 161.8, 129.9, 104.5, 101.4, 85.1, 76.3, 68.9, 31.6, 29.1, 25.6, 22.6, 14.0. IR (neat, cm^{-1}): 3324, 2936, 2918, 2852, 1583, 1453, 1391, 1289, 1251, 1092, 894, 771. HRMS (ESI) *m/z* calc'd (positive mode) for $C_{20}H_{31}O_2$ $[M+H]^+$ 303.2324, found 303.2304.

1-(2,6-bis((2,6-bis(hexyloxy)phenyl)ethynyl)phenyl)-1H-pyrrole (4b): To a flame dried N_2 filled flask was added 1-(2,6-dibromophenyl)-1H-pyrrole (**3**),[69] (3.53 g, 11.3 mmol, 1.0 equiv.), 2-ethynyl-1,3-bis(hexyloxy)benzene (**2b**) (8.51 g, 28.2 mmol, 2.4 equiv.), CuI (89.4 mg, 0.47 mmol, 0.04 equiv.), $Pd[P(tBu)_3]_2$ (359 mg, 0.70 mmol, 0.06 equiv.), dioxane (23.5 ml), and diisopropylamine (4.21 ml, 28.1 mmol, 2.4 equiv.). The mixture was stirred at room temperature overnight. The reaction mixture was then extracted with DCM and H_2O. The crude mixture was purified through silica gel chromatography using 5% ether: hexane as the eluent to give the pure product (7.22 g, 83%). ^{1}H NMR (500 MHz, $CDCl_3$) δ = 7.65 (d, *J* =7.7 Hz, 2H), 7.36 (br s, 2H), 7.27 (t, *J* = 7.7 Hz, 1H), 7.18 (t, *J* = 8.3 Hz, 2H), 6.51 (d, *J* = 8.3 Hz, 4H), 6.28 (br s, 2H), 4.02 (t, *J* = 6.4 Hz, 8H), 1.95-1.80 (m, 8H), 1.63-1.33 (m, 24H), 0.95-0.90 (ap t, 12H). ^{13}C NMR (125

MHz, $CDCl_3$) δ = 161.3, 141.4, 133.7, 129.9, 126.0, 122.8, 121.7, 108.2, 104.6, 102.4, 94.3, 87.5, 69.0, 31.8, 29.3, 25.9, 22.8, 14.2. IR (neat, cm^{-1}): 3098, 3057, 2925, 2860, 1578, 1454, 1383, 1297, 1251, 1093, 1012, 901. HRMS (ESI) *m/z* calc'd (positive mode) for $C_{50}H_{66}O_4N$ $[M+H]^+$ 744.4992, found 744.5026.

3,9-bis(2,6-bis(hexyloxy)phenyl)-4,4a1-dihydroindolizino[6,5,4,3-*ija*]quinolone (5b): To a flame dried, N_2 filled flask was added 1-(2,6-bis((2,6-bis(hexyloxy)phenyl)ethynyl)phenyl)-1H-pyrrole (**4b**), (6.90 mg, 9.27 mmol, 1.0 equiv.), $InCl_3$ (1.23 g, 5.58 mmol, 0.60 equiv.) and toluene (46.5 ml, 0.2 M). The mixture was stirred at 100°C overnight. The reaction mixture was filtered through a pad of silica gel with 5% ethylacetate: hexane as eluent to give the crude product after evaporation. Then, the mixture was purified through silica gel chromatography with 10% dichloromethane:hexanes to give the final pure product (1.99 g, 29%). ^{1}H NMR (500 MHz, $CDCl_3$) δ = 7.51-7.42 (m, 3H), 7.37 (t, *J* = 8.4 Hz, 2H), 7.20 (s, 2H), 6.76 (d, *J* =8.4 Hz, 4H), 6.60 (s, 2H), 4.10-3.88 (m, 8H), 1.70-1.49 (m, 8H), 1.32-1.05 (m, 24H), 0.79 (t, *J* = 6.7 Hz, 12H). ^{13}C NMR (75 MHz, $CDCl_3$) δ = 158.3, 132.9, 129.1, 127.0, 126.4, 126.1, 123.0, 121.0, 118.3, 117.2, 105.7, 105.2, 69.0, 31.4, 29.0, 25.6, 22.5, 13.9. IR (neat, cm^{-1}): 3585, 3174, 3055, 2920, 2855, 2334, 1585, 1452, 1410, 1365, 1244, 1091, 1030, 863. HRMS (ESI) *m/z* calc'd (positive mode) for $C_{50}H_{65}O_4NCs$ $[M+Cs]^+$ 876.3968, found 876.3904.

3,9-bis(2,6-bis(hexyloxy)phenyl)indolizino[6,5,4,3-*ija*]quinoline-5-carbaldehyde (6b): To a flame dried, N_2 filled round bottom flask was added 3,9-bis(2,6-bis(hexyloxy)phenyl)-4,4a1-dihydroindolizino[6,5,4,3-*ija*]quinolone (**5b**) (1.90 g, 2.6 mmol, 1.0 equiv.), dichloroethane (8.4 ml, 0.13 M), and anhydrous *N*,*N*-dimethylformamide (0.48 ml, 6.24 mmol, 2.4 equiv.). The mixture was stirred at room temperature while $POCl_3$ (0.60 ml, 6.24 mmol, 2.4 equiv.) was added dropwise via syringe. The reaction was stirred for 5 hours at room temperature to give a red

solution. The reaction mixture was then diluted with a 50 mL ~1:1 mixture of dichloromethane:NaOAc (sat. aq.) for 2 hours. The product was purified with silica chromatography using 10% dichloromethane:hexanes to give an orange oil (156 mg, 7.8 %) as the major side product. ^{1}H NMR (500 MHz, $CDCl_3$) δ = 10.32 (s, 1H), 8.95 (s, 1H), 7.89 (d, *J* =8.2 Hz, 1H), 7.53 (d, *J* =8.2 Hz, 1H), 7.44 (s, 1H), 7.41-7.32 (m, 2H), 6.91-6.96 (m, 2H), 6.73 (dd, *J* =2.9 Hz, *J* =2.9 Hz, 4H), 4.01-3.82 (m, 8H), 1.55-1.42 (m, 8H), 1.22-0.98 (m, 24H), 0.77-0.59 (m, 12H). ^{13}C NMR (75 MHz, $CDCl_3$) δ = 191.0, 158.1, 158.0, 131.9, 131.2, 130.8, 129.8, 129.6, 129.5, 128.4, 127.9, 126.6, 121.7, 121.2, 119.2, 116.7, 116.5, 115.9, 109.1, 108.7, 105.4, 105.3, 68.9, 68.8, 31.3, 31.3, 28.9, 28.9, 25.5, 25.5, 22.4, 22.4, 13.8, 13.8. IR (neat, cm^{-1}): 3489, 3284, 3186, 3111, 2922, 2855, 2714, 2337, 1664, 1582, 1453, 1350, 1297, 1245, 1185, 1092, 1028, 940. HRMS (ESI) *m/z* calc'd (positive mode) for $C_{51}H_{65}O_5NCs$ $[M+Cs]^+$ 904.3917, found 904.3705.

3,9-bis(2,6-bis(hexyloxy)phenyl)indolizino[6,5,4,3-*ija*]quinoline-4-carbaldehyde (7b): This material was formed as the major product during the formylation reaction to form 3,9-bis(2,6-bis(hexyloxy)phenyl)indolizino[6,5,4,3-*ija*]quinoline-5-carbaldehyde (**6b**). 3,9-bis(2,6-bis(hexyloxy)phenyl)indolizino[6,5,4,3-*ija*]quinoline-4-carbaldehyde (**7b**) was observed as a slightly lower R_f than 3,9-bis(2,6-bis(hexyloxy)phenyl)indolizino[6,5,4,3-*ija*]quinoline-5-carbaldehyde (**6b**) on TLC with 10% dichloromethane:hexane as eluent. The product was isolated by silica chromatography with 10% dichloromethane:hexanes to give a yellow solid (1.09 g, 55%). ^{1}H NMR (500 MHz, $CDCl_3$) δ = 9.44 (s, 1H), 7.59-7.50 (m, 3H), 7.46 (s, 1H), 7.64-7.49 (m, 2H), 7.23 (s, 1H), 7.08 (s, 1H), 6.71 (dd, *J* = 2.7 Hz, 2.7 Hz, 4H), 4.29-3.78 (m, 8H), 1.89-1.41 (m, 8H), 1.41-0.98 (m, 24H), 0.72 (ap t, 12H). ^{13}C NMR (125 MHz, $CDCl_3$) δ = 186.6, 158.1, 157.8, 131.9, 130.4, 130.3, 129.7, 128.2, 127.4, 126.7, 126.4, 125.8, 125.2, 124.4, 123.7, 120.9, 120.4, 120.4, 116.4, 115.4, 105.3, 105.3, 105.3, 104.7, 68.7, 68.7, 31.3, 31.2, 29.0, 28.9, 25.6, 25.5, 22.4, 22.4,

13.8, 13.8. IR (neat, cm^{-1}): 3311, 3180, 3057, 2924, 2858, 2335, 1648, 1587, 1523, 1454, 1386, 1290, 1245, 1194, 1093, 908, 879. HRMS (ESI) *m/z* calc'd (positive mode) for $C_{51}H_{65}O_5NCs$ $[M+Cs]^+$ 904.3917, found 904.3762.

5-ethynyl-3,9-bis(4-(hexyloxy)phenyl)indolizino[6,5,4,3-*ija*]quinoline (**8a**): To a flame dried flask was added freshly prepared dibromomethyl-triphenylphosphonium bromide[92] (2.01g, 4.04 mmol, 2.02 equiv.) and tetrahydrofuran (20.2 ml). In one portion, potassium *tert*-butoxide (426 mg, 3.80 mmol, 1.90 equiv.) was added and the mixture stirred at ambient temperature for 3 minutes. A solution of 3,9-bis(4-(hexyloxy)phenyl)indolizino[6,5,4,3-*ija*]quinoline-5-carbaldehyde (**6a**)[69] (1.149 g, 2.0 mmol, 1.0 equiv.) in tetrahydrofuran (3.4 ml) was added to the reaction mixture via cannula, and the resulting mixture was stirred at room temperature for 10 minutes. The reaction was cooled to negative 78°C and potassium *tert*-butoxide (426 mg, 3.80 mmol, 5.0 equiv.) was added in one portion following gradual warming to ambient temperature. After 1.5 hours, the reaction mixture was diluted with dichloromethane and rinsed with water, dried by Na_2SO_4 and evaporated. The crude product was filtered through a pad of silica gel, eluting with 50 % dichloromethane/hexanes to give the desired product as a yellow oil (1.08 g, 95%). ^{1}H NMR (500 MHz, $CDCl_3$) δ = 7.80 (d, *J* = 8.6 Hz, 2H), 7.75 (d, *J* = 8.6 Hz, 2H), 7.69 (s, 1H), 7.65 (d, *J* = 8.1 Hz, 1H), 7.44 (d, *J* = 8.1 Hz, 1H), 7.21 (s, 1H), 7.10 (d, *J* = 7.3 Hz, 2H), 7.08 (d, *J* = 7.3 Hz, 2H). 4.21-3.95 (m, 4H), 3.53 (s, 1H), 2.00-1.75 (m, 4H), 1.74-1.20 (m, 12H), 0.96 (t, *J* = 6.8 Hz, 6H). ^{13}C NMR (125 MHz, $CDCl_3$) δ = 159.5, 159.5, 133.9, 133.6, 131.4, 130.8, 130.6, 129.6, 129.6, 129.4, 128.2, 128.1, 127.5, 127.1, 127.0, 126.3, 118.5, 118.2, 117.3, 114.7, 114.7, 109.8, 107.2, 82.8, 81.7, 68.2, 31.7, 29.8, 29.4, 28.3, 25.9, 22.7, 14.2 IR (neat, cm^{-1}): 3312, 2925,

2855, 2334, 2093, 1602, 1503, 1493, 1389, 1299, 1276, 1240, 1171, 1110, 1032, 824, 792. HRMS (ESI) *m/z* calc'd (positive mode) for $C_{40}H_{41}O_2NCs$ $[M+Cs]^+$ 700.2192, found 700.2186.

3,9-bis(2,6-bis(hexyloxy)phenyl)-5-ethynylindolizino[6,5,4,3-*ija*]quinoline (8b): The synthesis follows the same procedure as 5-ethynyl-3,9-bis(4-(hexyloxy)phenyl)indolizino[6,5,4,3-*ija*]quinoline (**8a**) except 3,9-bis(2,6-bis(hexyloxy)phenyl)indolizino[6,5,4,3-*ija*]quinoline-5-carbaldehyde (**6b**, 64.3 mg) was used in place of 3,9-bis(4-(hexyloxy)phenyl)indolizino[6,5,4,3-*ija*]quinoline-5-carbaldehyde (**6a**). The reaction mixture was extracted by DCM and H_2O, dried with Na_2SO_4 and evaporated. The crude mixture was purified through silica gel chromatography using 50% dichloromethane:hexane as the eluent to give a pure yellow oil (54.3 mg, 85%). ^{1}H NMR (500 MHz, $CDCl_3$) δ = 7.67 (s, 1H), 7.63 (d, *J* = 8.0 Hz, 1H), 7.43-7.31 (m, 3H), 7.23 (s, 1H), 6.68-6.60 (m, 6H), 4.20-3.80 (m, 8H), 3.43 (s, 1H), 1.70-1.42 (m, 8H), 1.29-1.00 (m, 24H), 0.73 (ap t, 12H). ^{13}C NMR (75 MHz, $CDCl_3$) δ = 158.2, 158.2, 132.1, 129.3, 129.2, 127.8, 127.5, 127.4, 127.3, 127.2, 126.5, 120.9, 119.9, 117.5, 116.9, 116.7, 109.0, 106.5, 106.4, 105.5, 105.5, 105.5, 83.3, 80.6, 68.9, 68.9, 31.3, 31.3, 28.9, 28.9, 25.5, 25.5, 22.4, 22.4, 13.8, 13.8. IR (neat, cm^{-1}): 3307, 2927, 2862, 1591, 1457, 1421, 1395, 1366, 1297, 1247, 1098, 1027, 872. HRMS (ESI) *m/z* calc'd (positive mode) for $C_{51}H_{65}O_5NCs$ $[M+Cs]^+$ 900.3968, found 900.3716.

4-ethynyl-3,9-bis(4-(hexyloxy)phenyl)indolizino[6,5,4,3-*ija*]quinoline (9a): The synthesis follows the same procedure as 5-ethynyl-3,9-bis(4-(hexyloxy)phenyl)indolizino[6,5,4,3-*ija*]quinoline (**8a**) except 3,9-bis(4-(hexyloxy)phenyl)indolizino[6,5,4,3-*ija*]quinoline-4-carbaldehyde (**7a**, 280 mg)[69] was used in place of 3,9-bis(4-(hexyloxy)phenyl)indolizino[6,5,4,3-*ija*]quinoline-5-carbaldehyde (**6a**). The crude mixture was purified through silica gel chromatography using 50% dichloromethane:hexanes as the eluent to give the pure product (253 mg, 91%). ^{1}H NMR (300 MHz, Acetone-d_6) δ = 7.87 (d, *J* = 6.7 Hz, 1H), 7.70 (d, *J* = 8.5 Hz,

2H) , 7.67 (d, *J* = 8.4 Hz, 2H), 7.60 (d, *J* = 7.7 Hz, 1H), 7.52 (t, *J* = 7.7 Hz, 1H), 7.34 (s, 1H), 7.13-6.97 (m, 5H), 6.84 (d, *J* = 4.3 Hz, 1H), 4.13-4.00 (m, 4H), 3.99 (s, 1H), 1.90-1.71(m, 4H), 1.60-1.25 (m, 12H), 1.11-0.80 (m, 6H). ^{13}C NMR (75 MHz, acetone-d_6) δ = 159.6, 137.3, 132.6, 131.2, 130.9, 130.2, 129.2, 128.6, 127.5, 126.9, 125.7, 125.0, 124.1, 120.2, 119.3, 118.6, 114.7, 114.0, 109.1, 108.6, 107.0, 86.4, 80.2, 67.8, 67.8, 31.5, 25.6, 25.6, 22.4, 13.5. IR (neat, cm^{-1}): 3279, 2924, 2856, 1976, 1604, 1507, 1428, 1406, 1395, 1360, 1278, 1244, 1174, 1116, 1071, 1027, 830. HRMS (ESI) *m/z* calc'd (positive mode) for $C_{40}H_{41}O_2NCs$ $[M + Cs]^+$ 700.2192, found 700.2178.

3,9-bis(2,6-bis(hexyloxy)phenyl)-4-ethynylindolizino[6,5,4,3-*ija*]quinoline (9b): The synthesis follows the same procedure as 5-ethynyl-3,9-bis(4-(hexyloxy)phenyl)indolizino[6,5,4,3-*ija*]quinoline (**8a**) except 3,9-bis(2,6-bis(hexyloxy)phenyl)indolizino[6,5,4,3-*ija*]quinoline-4-carbaldehyde (**7b**, 466 mg) was used in place of 3,9-bis(4-(hexyloxy)phenyl)indolizino[6,5,4,3-*ija*]quinoline-5-carbaldehyde (**6a**). The reaction mixture was extracted by dichloromethane and H_2O, dried with Na_2SO_4 and evaporated. The crude mixture was purified through silica gel chromatography using 50% dichloromethane:hexanes as the eluent to give a yellow oil (153 mg, 33%). ^{1}H NMR (300 MHz, $CDCl_3$) δ = 7.44 (br s, 3H), 7.38-7.25 (m, 2H), 7.18 (d, *J* = 8.5 Hz, 2H), 6.70 (d, *J* = 8.3 Hz, 2H), 6.64 (ap d, 3H), 4.08-3.80 (m, 8H), 2.59 (s, 1H), 1.68-1.40 (m, 8H), 1.38-0.99 (m, 24H), 0.81-0.59 (m, 12H). ^{13}C NMR (125 MHz, $CDCl_3$) δ = 158.8, 158.1, 132.4, 129.3, 129.2, 128.4, 126.6, 126.1, 126.0, 126.0, 125.9, 123.6, 123.0, 122.3, 119.3, 119.1, 116.3, 116.2, 109.7, 105.4, 105.0, 99.2, 79.2, 77.6, 68.9, 68.9, 31.3, 31.3, 29.0, 28.9, 25.6, 25.5, 22.4, 22.4, 13.8, 13.8. IR (neat, cm^{-1}): 3310, 2926, 2861, 1589, 1457, 1388, 1296, 1247, 1097, 871. HRMS (ESI) *m/z* calc'd for (positive mode) $C_{52}H_{66}O_4N$ $[M+H]^+$ 768.4992, found 768.4495.

6-((3,9-bis(4-(hexyloxy)phenyl)indolizino[6,5,4,3-*ija*]quinolin-5-yl)ethynyl)-4,4-dihexyl-4H-cyclopenta[2,1-*b*:3,4-*b'*]dithiophene-2-carbaldehyde (11a): To a flame dried N_2 filled round bottom flask was added CuI (0.67 mg, 0.003 mmol, 0.04 equiv.), dioxane (0.18 ml), diisopropylamine (0.03 ml, 0.211 mmol, 2.4 equiv.), $Pd[P(t\text{-}Bu)_3]_2$ (2.69 mg, 0.005 mmol, 0.06 equiv.), 5-ethynyl-3,9-bis(4-(hexyloxy)phenyl)indolizino[6,5,4,3-*ija*]quinoline (**8a**) (60 mg, 0.106 mmol, 1.2 equiv.), and 6-bromo-4,4-dihexyl-4H-cyclopenta[2,1-b:3,4-b']dithiophene-2-carbaldehyde (**10**)[90] (40.0 mg, 0.088 mmol, 1.0 equiv.). The mixture was stirred at room temperature overnight. The reaction mixture was then diluted with dichloromethane and extracted with dichloromethane/H_2O, dried by Na_2SO_4 and evaporated. The product was then purified through silica gel chromatography with 50% diethyl ether:hexanes to give the desired product as a red solid (79 mg, 97%). ^{1}H NMR (300 MHz, $CDCl_3$) δ = 9.88 (s, 1H), 7.82 (d, *J* = 8.5 Hz, 2H), 7.76 (d, *J* = 8.6 Hz, 2H), 7.70 (s, 1H), 7.66 (d, *J* = 8.1 Hz, 1H), 7.59 (s, 1H), 7.46 (d, *J* = 8.0 Hz, 1H), 7.29 (d, *J* = 5.7 Hz, 1H), 7.22 (br. s, 3H), 7.11 (dd, *J* = 8.8 Hz, 8.7 Hz, 4H), 4.26-4.00 (m, 4H), 2.30-0.60 (m, 48H). ^{13}C NMR (125 MHz, $CDCl_3$) δ = 182.6, 161.8, 159.6, 159.5, 158.9, 147.2, 143.8, 136.7, 134.1, 133.8, 131.6, 130.7, 130.5, 129.8, 129.6, 129.5, 128.0, 127.5, 127.3, 127.2, 126.8, 126.4, 125.7, 118.8, 118.4, 117.4, 114.8, 114.8, 110.1, 107.4, 107.4, 95.5, 88.3, 68.2, 37.7, 31.6, 31.6, 29.7, 29.7, 29.3, 25.8, 24.6, 22.7, 22.6, 14.1, 14.0. IR (neat, cm^{-1}): 3303, 3051, 2926, 2856, 2179, 1657, 1604, 1503, 1393, 1369, 1246, 1176, 834. HRMS (ESI) *m/z* calc'd (positive mode) for $C_{62}H_{69}O_3NS_2$ $[M]^+$ 939.4719, found 939.4890.

6-((3,9-bis(2,6-bis(hexyloxy)phenyl)indolizino[6,5,4,3-*ija*]quinolin-5-yl)ethynyl)-4,4-dihexyl-4H-cyclopenta[2,1-*b*:3,4-*b'*]dithiophene-2-carbaldehyde (11b): The synthesis follows the same procedure as 6-((3,9-bis(4-(hexyloxy)phenyl)indolizino[6,5,4,3-*ija*]quinolin-5-yl)ethynyl)-4,4-dihexyl-4H-cyclopenta[2,1-*b*:3,4-*b'*]dithiophene-2-carbaldehyde (**11a**) except 3,9-bis(2,6-

bis(hexyloxy)phenyl)-5-ethynylindolizino[6,5,4,3-*ija*]quinoline (**8b**, 55.8 mg) was used in place of 5-ethynyl-3,9-bis(4-(hexyloxy)phenyl)indolizino[6,5,4,3-*ija*]quinoline (**8a**). The crude mixture was purified through silica gel chromatography using 50% dichloromethane:hexanes as the eluent to give a red solid (17.4 mg, 21%). ^{1}H NMR (500 MHz, $CDCl_3$) δ = 9.84 (s,1H), 7.65 (s,1H), 7.61 (d, *J* =8.1 Hz, 1H), 7.56 (s,1H), 7.45-7.29 (m, 3H), 7.21 (s,1H), 7.14 (s,1H), 6.81-6.64 (m, 6H), 4.05-3.90 (m, 8H), 2.00-1.80 (m, 4H), 1.70-0.79 (m, 54H), 0.79-0.61 (m, 12H). ^{13}C NMR (125 MHz, $CDCl_3$) δ = 182.5, 161.8, 158.7, 158.2, 158.1, 147.5, 143.5, 136.1, 132.2, 129.8, 129.4, 128.7, 127.6, 127.4, 127.4, 127.1, 126.6, 125.4, 121.2, 120.0, 117.8, 117.0, 116.6, 116.5, 109.2, 106.9, 106.7, 105.4, 105.4, 105.4, 96.4, 87.4, 69.0, 68.9, 54.1, 37.8, 31.6, 31.3, 31.3, 29.4, 28.9, 28.9, 25.6, 25.5, 24.6, , 22.6, 22.4, 22.3, 14.0, 13.0, 13.8. IR (neat, cm^{-1}): 3367, 3063, 2923, 2851, 1656, 1592, 1496, 1458, 1421, 1395, 1364, 1302, 1247, 1098. HRMS (ESI) *m/z* calc'd (positive mode) for $C_{74}H_{93}O_5NS_2Cs$ $[M+Cs]^+$ 1272.5550, found 1272.5785.

6-((3,9-bis(4-(hexyloxy)phenyl)indolizino[6,5,4,3-*ija*]quinolin-4-yl)ethynyl)-4,4-dihexyl-4H-cyclopenta[2,1-*b*:3,4-*b'*]dithiophene-2-carbaldehyde (12a): The synthesis follows the same procedure as 6-((3,9-bis(4-(hexyloxy)phenyl)indolizino[6,5,4,3-*ija*]quinolin-5-yl)ethynyl)-4,4-dihexyl-4H-cyclopenta[2,1-*b*:3,4-*b'*]dithiophene-2-carbaldehyde (**11a**) only 4-ethynyl-3,9-bis(4-(hexyloxy)phenyl)indolizino[6,5,4,3-*ija*]quinoline (**9a**, 41.3 mg) was used in place of 5-ethynyl-3,9-bis(4-(hexyloxy)phenyl)indolizino[6,5,4,3-*ija*]quinoline (**8a**). The crude mixture was purified through silica gel chromatography using 10% acetone: hexane as the eluent to give a red solid (39 mg, 57%). ^{1}H NMR (500 MHz, $CDCl_3$) δ = 9.88 (s, 1H), 7.96 (br t, 1H), 7.81 (d, *J* = 8.5 Hz, 2H), 7.74 (d, *J* = 8.4 Hz, 2H), 7.62-7.52 (m, 3H), 7.32 (s, 1H), 7.18-6.97 (m, 6H), 7.00 (d, *J* = 4.1 Hz, 1H), 4.13 (t, *J* = 6.4 Hz, 2H), 4.07 (t, *J* = 6.5 Hz, 2H), 2.00-1.80 (m, 8H), 1.69-1.49 (m, 8H), 1.49-0.89 (m, 21H), 0.86 (t, *J* = 6.8 Hz, 12H). ^{13}C NMR (125 MHz, $CDCl_3$) δ = 182.6, 161.8, 159.5,

159.4, 158.9, 147.1, 143.7, 136.9, 136.4, 132.8, 131.6, 131.2, 130.5, 129.8, 129.3, 128.9, 128.1, 127.9, 127.3, 125.8, 125.5, 124.6, 124.1, 120.0, 119.7, 118.7,114.8, 114.2, 109.4, 109.0, 107.3, 94.5, 91.6, 68.2, 68.2, 37.7, 32.0, 31.7, 31.6, 31.6, 31.6, 29.7, 29.6, 29.4, 29.3, 29.2, 25.8, 25.8, 24.6, 22.7, 22.7, 22.7, 22.6, 22.6, 14.1, 14.1, 14.0, 14.0. IR (neat, cm^{-1}): 3020, 2925, 2855, 2362, 2335, 1651, 1504, 1463, 1395, 1362, 1260, 1175, 1023, 892. HRMS (ESI) *m/z* calc'd (positive mode) for $C_{62}H_{69}O_3NS_2Cs$ $[M + Cs]^+$ 1072.3773, found 1072.3646.

6-((3,9-bis(2,6-bis(hexyloxy)phenyl)indolizino[6,5,4,3-*ija*]quinolin-4-yl)ethynyl)-4,4-dihexyl-4H-cyclopenta[2,1-*b*:3,4-*b'*]dithiophene-2-carbaldehyde (12b): To a flame dried, N_2 filled round bottom flask was added 6-bromo-4,4-dihexyl-4H-cyclopenta[2,1-*b*:3,4-*b'*]dithiophene-2-carbaldehyde (**10**)[90] (34 mg, 0.075 mmol, 1.0 equiv.), $Pd(PPh_3)_4$ (13.9 mg, 0.012 mmol, 0.16 equiv.) and dry N,N-dimethylformamide (10.8 ml, 0.007 M). A separate solution of 3,9-bis(2,6-bis(hexyloxy)phenyl)-4-((tributylstannyl)ethynyl)indolizino[6,5,4,3-*ija*]quinoline (**13b**) (158 mg, 0.15 mmol, 2.0 equiv.) in dry *N*,*N*-dimethylformamide (2.5 ml, 0.06 M) was added dropwise followed with stirring at 110°C and the mixture was stirred overnight. The reaction was cooled down to room temperature and extracted with diethylether and H_2O. The crude product was further purified by silica column chromatography with 10% ethyl acetate:hexanes to give a red solid (39 mg, 46%). ^1H NMR (300 MHz, $CDCl_3$) δ = 9.85 (s, 1H), 7.57 (s, 1H), 7.51-7.41 (m, 3H), 7.36 (dd, *J* = 9.1 Hz, *J* = 8.5 Hz, 2H), 7.23 (s, 1H), 7.19 (s, 1H), 6.72 (d, *J* = 8.2 Hz, 2H), 6.71 (d, *J* = 8.4 Hz, 2H), 6.67 (d, *J* = 4.7 Hz, 1H), 6.67 (d, *J* = 4.7 Hz, 1H), 4.10-3.79 (m, 8H), 2.00-1.75 (m, 4H), 1.75-1.42 (m, 8H), 1.42-0.80 (m, 46H), 0.80-0.60 (m, 12H). ^{13}C NMR (125 MHz, $CDCl_3$) δ = 182.4, 161.6, 158.5, 158.5, 158.3, 158.2, 158.2, 147.9, 143.0, 135.0, 132.4, 129.8, 129.6, 129.4, 127.9, 126.8, 126.6, 126.0, 125.4, 123.8, 123.6, 122.5, 119.6, 119.4, 116.2, 116.0, 109.0, 105.5, 105.5, 105.2, 105.2, 99.6, 93.6, 85.0, 68.9, 68.9, 37.7, 31.7, 31.3, 31.3, 29.7, 29.7, 29.0, 25.6,

25.5, 24.6, 22.6, 22.5, 22.4, 14.0, 13.9, 13.9. IR (neat, cm^{-1}): 3311, 3052, 2926, 2857, 1655, 1590, 1495, 1458, 1421, 1396, 1300, 1228, 1120, 1098, 870.6. HRMS (ESI) *m/z* calc'd (positive mode) for $C_{74}H_{93}O_5NS_2$ $[M]^+$ 1139.6495, found 1139.6481.

3,9-bis(2,6-bis(hexyloxy)phenyl)-4-((tributylstannyl)ethynyl)indolizino[6,5,4,3-*ija*]quinoline (13b): To a N_2 filled flame dried round bottom flask was added 3,9-bis(2,6-bis(hexyloxy)phenyl)-4-ethynylindolizino[6,5,4,3-*ija*]quinoline (**9b**) (100 mg, 0.13 mmol, 1.0 equiv.) and dry THF (4.4 ml, 0.03M). The solution was cooled to -78°C, then 2.5 M *n*-BuLi in hexane (0.06 ml, 0.15 mmol, 1.16 equiv.) was added at -78°C and stirred for 2.5 hours. Bu_3SnCl (0.04 ml, 0.14 mmol, 1.1 equiv.) was added and the whole reaction was stirred at room temperature for 2.5 hours. The reaction mixture was extracted with diethyl ether and H_2O, dried with Na_2SO_4 and evaporated to get the crude product that was used without further purification in the next step (137 mg, 100%). ^1H NMR (300 MHz, $CDCl_3$) δ = 7.45-7.24 (m, 5H), 7.10 (d, *J* = 2.7 Hz, 2H), 6.68 (d, *J* =8.4, 2H), 6.65-6.55 (m, 3H), 4.01-3.80 (m, 8H), 1.81-0.80 (m, 59H), 0.80-0.60 (m, 12H).

(*E*)-3-(6-((3,9-bis(4-(hexyloxy)phenyl)indolizino[6,5,4,3-*ija*]quinolin-5-yl)ethynyl)-4,4-dihexyl-4H-cyclopenta[2,1-*b*:3,4-*b'*]dithiophen-2-yl)-2-cyanoacrylic acid (YZ7): To a round bottom flask was added 6-((3,9-bis(4-(hexyloxy)phenyl)indolizino[6,5,4,3-*ija*]quinolin-5-yl)ethynyl)-4,4-dihexyl-4H-cyclopenta[2,1-*b*:3,4-*b'*]dithiophene-2-carbaldehyde (**11a**) (40 mg, 0.04 mmol, 1.0 equiv.) and $CHCl_3$ (0.17 ml). The mixture was degassed with N_2 for 30 minutes, then cyanoacetic acid (11 mg, 0.13 mmol, 3.0 equiv.) and piperidine (0.03 mL, 0.29 mmol, 7.0 equiv.) were added into the flask. The flask was sealed with a plastic stopper and electrical tape and stirred at 90°C for 10 hours. To the reaction mixture was added acetic acid, then the mixture was directly purified through a silica gel plug using first 100% dichloromethane, followed by 10% methanol:90% dichloromethane, and finally 10% methanol:2% acetic acid:88% dichloromethane.

Then the dye was again extracted with hexane and water to remove acetic acid and trace silica gel particles. The organic layer was concentrated under reduced pressure to give a purple solid. The product was suspended in hexane solvent then centrifuged five times to give the pure product (43 mg, 97%). ^{1}H NMR (400 MHz, $CDCl_3$/d6-DMSO, 85^{o}C) δ = 8.14 (s, 1H), 7.82 (d, *J* = 8.4 Hz, 2H), 7.77 (d, *J* = 8.4 Hz, 2H), 7.69 (s, 1H), 7.65 (d, *J* = 8.4 Hz, 1H), 7.60-7.55 (m, 2H), 7.44 (d, *J* = 6.4 Hz, 2H), 7.22 (s, 2H), 7.18-7.10 (m, 4H), 4.11 (ap dt, *J* = 6.4, 2.0 Hz, 4H), 1.95-1.90 (m, 4H), 1.81 (ap pent, *J* = 7.2 Hz, 4H), 1.55-1.46 (m, 4H), 1.40-1.36 (m, 8H), 1.18-1.13 (m, 12H), 0.95-0.90 (m, 10H), 0.81 (t, *J* = 6.8 Hz, 6H). ^{13}C NMR spectrum could not be obtained due to the sparing solubility of this dye. IR (neat, cm^{-1}): 3413, 2923, 2854, 2361, 2335, 1600, 1560, 1505, 1366, 1295, 1249, 1174, 1086, 1028, 799. HRMS (ESI) *m/z* calc'd (negative mode) for $C_{65}H_{69}O_4N_2S_2$ $[M-H]^-$ 1005.4699, found 1005.3744. UV-Vis (CH_2Cl_2): λ_{max} = 532 nm (ε = 29,000 M^{-1} cm^{-1}), λ_{onset} = 650 nm. CV (0.1 M Bu_4NPF_6 in CH_2Cl_2, sweep width 2.0-(-1.2.0), 0.1 Vs-1 scan rate) versus NHE: $E_{(S+/S)}$ = 0.90 V; E_g^{opt} = 1.88 eV. $E_{(S+/S*)}$ = –0.98 V [vs NHE, calculated from $E_{(S+/S*)} = (E_{(S+/S)} - E_g^{opt})$].

(*E*)-3-(6-((3,9-bis(4-(hexyloxy)phenyl)indolizino[6,5,4,3-*ija*]quinolin-4-yl)ethynyl)-4,4-dihexyl-4H-cyclopenta[2,1-*b*:3,4-*b'*]dithiophen-2-yl)-2-cyanoacrylic acid (YZ12): The synthesis follows the same procedure as (*E*)-3-(6-((3,9-bis(4-(hexyloxy)phenyl)indolizino[6,5,4,3-*ija*]quinolin-5-yl)ethynyl)-4,4-dihexyl-4H-cyclopenta[2,1-*b*:3,4-*b'*]dithiophen-2-yl)-2-cyanoacrylic acid (**YZ7**) except 6-((3,9-bis(4-(hexyloxy)phenyl)indolizino[6,5,4,3-*ija*]quinolin-4-yl)ethynyl)-4,4-dihexyl-4H-cyclopenta[2,1-*b*:3,4-*b'*]dithiophene-2-carbaldehyde (**12a**, 20.2 mg) was used in place of 6-((3,9-bis(4-(hexyloxy)phenyl)indolizino[6,5,4,3-*ija*]quinolin-5-yl)ethynyl)-4,4-dihexyl-4H-cyclopenta[2,1-*b*:3,4-*b'*]dithiophene-2-carbaldehyde (**11a**). Also, after the silica gel plug filtration, the crude

product was further purified by silica gel column chromatography with 60% DCM:10% methanol:30% hexane to give a pure purple solid (6.5 mg, 30%). ^{1}H NMR (400 MHz, d6-DMSO, 85^{o}C) δ = 8.00 (s, 1H), 7.91 (d, *J* = 7.2 Hz, 1H), 7.80-7.72 (m, 4H), 7.66 (t, *J* = 7.6 Hz, 1H), 7.61 (s, 1H), 7.48 (s, 1H), 7.31 (s, 1H), 7.19 (d, *J* = 8.4 Hz, 2H), 7.16-7.11 (m, 3H), 6.95 (d, *J* = 4.4 Hz, 1H), 6.09 (s, 1H), 4.15 (t, *J* = 6.8 Hz, 2H), 4.11-4.09 (t, *J* = 6.8 Hz, 2H), 1.94-1.76 (m, 8H), 1.54-1.48 (m, 4H), 1.48-1.13 (m, 20H), 0.95-0.77 (m, 16H) ^{13}C NMR spectrum could not be obtained due to the sparing solubility of this dye. IR (neat, cm^{-1}): 3400, 2955, 2921, 2852, 2335, 1729, 1580, 1569, 1509, 1461, 1360, 1290, 1254, 1170, 1087, 1019, 797. HRMS (ESI) *m/z* calc'd (negative mode) for $C_{65}H_{69}O_4N_2S_2$ $[M-H]^-$ 1005.4699, found 1005.4708. UV-Vis (CH_2Cl_2): λ_{max} = 543 nm (ε = 28,000 M^{-1} cm^{-1}), λ_{onset} = 690 nm. CV (0.1 M Bu_4NPF_6 in CH_2Cl_2, sweep width 2.0-(-1.2.0), 0.1 Vs-1 scan rate) versus NHE: $E_{(S+/S)}$ = 0.90 V; E_g^{opt} = 1.84 eV. $E_{(S+/S*)}$ = –0.94 V [vs NHE, calculated from $E_{(S+/S*)} = (E_{(S+/S)} - E_g^{opt})$].

(*E*)-3-(6-((3,9-bis(2,6-bis(hexyloxy)phenyl)indolizino[6,5,4,3-*ija*]quinolin-5-yl)ethynyl)-4,4-dihexyl-4H-cyclopenta[2,1-*b*:3,4-*b'*]dithiophen-2-yl)-2-cyanoacrylic acid (YZ14): The synthesis follows the same procedure as (*E*)-3-(6-((3,9-bis(4-(hexyloxy)phenyl)indolizino[6,5,4,3-*ija*]quinolin-5-yl)ethynyl)-4,4-dihexyl-4H-cyclopenta[2,1-*b*:3,4-*b'*]dithiophen-2-yl)-2-cyanoacrylic acid (**YZ7**) except 6-((3,9-bis(2,6-bis(hexyloxy)phenyl)indolizino[6,5,4,3-*ija*]quinolin-5-yl)ethynyl)-4,4-dihexyl-4H-cyclopenta[2,1-*b*:3,4-*b'*]dithiophene-2-carbaldehyde (**11b**, 17.0 mg) was used in place of 6-((3,9-bis(4-(hexyloxy)phenyl)indolizino[6,5,4,3-*ija*]quinolin-5-yl)ethynyl)-4,4-dihexyl-4H-cyclopenta[2,1-*b*:3,4-*b'*]dithiophene-2-carbaldehyde (**11a**). Also, after the silica gel plug filtration, the crude product was further purified by reverse phase column (C18 silica) with 80% MeOH:acetonitrile to give a red solid (11 mg, 61%). ^{1}H NMR (300 MHz, d6-DMSO, 40^{o}C) δ =

8.02 (s, 1H), 7.69-7.62 (m, 2H), 7.53 (d, *J* = 7.8 Hz, 1H), 7.49-7.35 (m, 3H), 7.25 (s, 1H), 7.11-7.08 (m, 1H), 6.83 (ap t, *J* = 7.8 Hz, 4H), 6.61-6.50 (m, 2H), 4.00-3.90 (m, 8H), 1.90-1.85 (m, 4H), 1.50-0.50 (m, 66H). ^{13}C NMR spectrum could not be obtained due to the sparing solubility of this dye. IR (neat, cm^{-1}): 3050, 2922, 2854, 1732, 1605, 1458, 1361, 1254, 1099, 843. HRMS (ESI) *m/z* calc'd (negative mode) for $C_{77}H_{93}O_6N_2S_2$ $[M-H]^+$ 1205.6475, found 1205.6469. UV-Vis (CH_2Cl_2): λ_{max} = 537 nm (ε = 28,000 M^{-1} cm^{-1}), λ_{onset} = 700 nm. CV (0.1 M Bu_4NPF_6 in CH_2Cl_2, sweep width 2.0-(-1.2.0), 0.1 Vs-1 scan rate) versus NHE: $E_{(S+/S)}$ = 0.71 V; E_g^{opt} = 1.79 eV; $E_{(S+/S^*)}$ = -1.08 V [vs NHE, calculated from $E_{(S+/S^*)} = (E_{(S+/S)} - E_g^{opt})$].

(*E*)-3-(6-((3,9-bis(2,6-bis(hexyloxy)phenyl)indolizino[6,5,4,3-*ija*]quinolin-4-yl)ethynyl)-4,4-dihexyl-4H-cyclopenta[2,1-*b*:3,4-*b'*]dithiophen-2-yl)-2-cyanoacrylic acid (YZ15): The synthesis follows the same procedure as (*E*)-3-(6-((3,9-bis(4-(hexyloxy)phenyl)indolizino[6,5,4,3-*ija*]quinolin-5-yl)ethynyl)-4,4-dihexyl-4H-cyclopenta[2,1-*b*:3,4-*b'*]dithiophen-2-yl)-2-cyanoacrylic acid (**YZ7**) except 6-((3,9-bis(2,6-bis(hexyloxy)phenyl)indolizino[6,5,4,3-*ija*]quinolin-4-yl)ethynyl)-4,4-dihexyl-4H-cyclopenta[2,1-*b*:3,4-*b'*]dithiophene-2-carbaldehyde (**12b**, 18.9 mg) was used in place of 6-((3,9-bis(4-(hexyloxy)phenyl)indolizino[6,5,4,3-*ija*]quinolin-5-yl)ethynyl)-4,4-dihexyl-4H-cyclopenta[2,1-*b*:3,4-*b'*]dithiophene-2-carbaldehyde (**11a**). Also, after the silica gel plug filtration, the crude product was further purified by silica gel chromatography with 5% MeOH:35% dichloromethane:60% hexanes to give a red solid (6.2 mg, 31%). ^{1}H NMR (300 MHz, d6-DMSO, 40 ^{o}C) δ = 7.64-7.35 (m, 5H), 7.18 (s, 2H), 6.85-6.74 (m, 5H), 6.66 (s, 1H), 6.52 (s, 1H), 6.43 (s, 1H), 3.94 (br s, 8H), 1.90-1.75 (m, 4H), 1.50-0.50 (m, 66H). ^{13}C NMR spectrum could not be obtained due to the sparing solubility of this dye. IR (neat, cm^{-1}): 3025, 2926, 2856, 1588, 1458, 1373, 1290, 1251, 1098, 1019, 869. HRMS (ESI) *m/z* calc'd (negative mode) for $C_{77}H_{93}O_6N_2S_2$

$[M - H]^+$ 1205.6475, found 1205.7507. UV-Vis (CH_2Cl_2): λ_{max} = 549 nm (ε = 26,000 M^{-1} cm^{-1}), λ_{onset} = 690 nm. CV (0.1 M Bu_4NPF_6 in CH_2Cl_2, sweep width 2.0-(-1.2.0), 0.1 Vs-1 scan rate) versus NHE: $E_{(S+/S)}$ = 0.84 V; E_g^{opt} = 1.89 eV; $E_{(S+/S^*)}$ = –1.05 V [vs NHE, calculated from $E_{(S+/S^*)} = (E_{(S+/S)} - E_g^{opt})$

CHAPTER 4

4.1 PANCROMATIC CROSS-CONJUGATED π-BRIDGE NIR DYES FOR DSCS

Adapted from **Yanbing Zhang**,; Hammad Cheema,; Alexander E. London,; Amber Morales,; Jason D. Azoulay,; Delcamp, J. H.; *Phys. Chem. Chem. Phys*. **2018**, *20*, 2438.

Reproduced by permission of The ROYAL SOCEITY OF CHEMISTRY.

(See appendix for permission license)

This project was a collaboration with Dr. Azoulay's group at the University of Southern Mississippi. Dr. Hammad Cheema contributed equally for making all the device and analyzing all the device data, Alexander London contributed to the project by synthesizing **C=CPhCPDT** building blocks and Amber Morales was a REU student who worked with me in synthesizing dyes.

ABSTRACT

Four organic sensitizers incorporating a cross-conjugated cyclopenta[2,1-b:3,4-b']dithiophene (CPDT) π-bridge have been synthesized. As a result of molecular engineering, broad high energy bands and red shifted absorption maxima and onset is observed relative to a benchmark analogue (**C218**) using a non-cross-conjugated CPDT π-bridge. The use of a cross-conjugated bridge allows a new strategy for tuning dye energetics and introduction of increased absorption uniformity by adding additional high-energy absorption bands. These dyes show solar-

to-electric conversion up to 800 nm with one derivative exceeding the performance of **C218** under identical conditions.

INTRODUCTION

Developing renewable energy conversion systems is important since worldwide power consumption is increasing dramatically. Research on dye-sensitized solar cells (DSCs) has been fuelled with the potential for affordable production, excellent tunability of device components and relatively high power conversion efficiencies (PCEs) from organic light absorbing materials.[63–65,93,94] DSCs operate by light absorption of a sensitizer which then transfers an electron to an inorganic semiconductor. The electron then traverses an external circuit before being collected at the counter electrode by a redox shuttle, which returns the electron back to the oxidized sensitizer. The sensitizer or dye plays several critical roles in this process concerning efficiency of electron transfers and the breadth of the absorption spectrum used. Recently, **SM315** and **ADEKA-1/LEG-4** based devices have achieved record PCEs of 13.0% and 14.3% for single-dye and co-sensitized DSC device efficiencies, respectively.[4–6] These exceptionally efficient dyes are designed based on three conjugated structural elements: a donor, a π-bridge and an acceptor (D-π-A). The π-bridge plays the critical role of both allowing the donor and acceptor regions to undergo intramolecular charge transfer (ICT) and to define the initial energy levels of the molecule prior to substituent addition. An appropriate π-bridge should: (1) ensure a minimal optical gap to extend the region where sunlight is converted to electricity,[95–99] (2) allow for properly positioned dye energetics for rapid electron transfers to TiO_2 and from the redox shuttle,[100,101] (3) suppress aggregation which lowers PCEs,[102] and (4) reduce non-productive electron transfers (recombination).[70,103]

Thiophene-based building blocks are ubiquitous π-bridges due to excellent ICT properties and synthetic accessability.[1,73,104–106] A thiophene-based π-bridge 4,4-dihexyl-4*H*-cyclopenta[2,1-*b*:3,4-*b'*] dithiophene (Hx_2CPDT) was employed in the design of an exceptionally successful organic dye (**C218**) with a triphenyl amine donor (TPA) and cyanoacrylic acid acceptor (CAA) with a high molar absorptivity, low recombination rate and wide absorption range.[8,107] The dialkylated CPDT bridge has now been incorporated into >125 dyes according to a SciFinder search, yet no conjugated alkene analogues have been evaluated. Herein, we have designed a new series of sensitizers with identical donor and acceptor to **C218** that include a solubilizing cross-conjugated bridgehead olefin substituent (*C*=CPh) substituent replacing the dialkyl chains on the CPDT π-bridge of **C218** to give *C*=CPhCPDT (Figure 18). We hypothesized that by introducing the extended conjugated system of *C*=CPhCPDT an increase in spectral response into the NIR region would be observed.[108]

RESULTS AND DISCUSSION

Two target dyes **YZ11** and **YZ13** directly replace the hexyl chains of Hx_2CPDT with a simple phenyl-alkene. These dyes differ in orientation of the phenyl group either toward the acceptor (**YZ11**) or toward the donor (**YZ13**). Since alkyl chains often contribute to DSC device photovoltage increases, we also prepared two 3,5- or meta-dialkylated phenyl derivatives, **YZ16** and **YZ17**, which differ at the alkene conformation.

The synthesis of **YZ11**, **YZ13**, **YZ16** and **YZ17** proceeded in 5-7 steps from commercial materials (Scheme 3). The cross-conjugated aryl group was synthesized via a Negishi coupling of dibromide **1**. Alcohol **2** was converted to the benzyl bromide **4** in high yield with the use of PBr_3.

Next, either commercial benzyl bromide **3** or **4** was converted to a phosphonium salt and a Wittig reaction with 4*H* -cyclopenta[2,1-*b* :3,4-*b′*]dithiophen-4-one **5** gave the *C*=CPhCPDT substituted intermediates **6** and **7**, respectively. Vilsmeier–Haack reaction on **6** or **7** gave two silica gel column separable *E/Z* alkene isomers in equal ratios. The isomers were assigned via ^{1}H NMR NOE (nuclear Overhauser effect) experiments (Figure 19). By irradiation of the proton on the CPDT ring adjacent to the aldehyde for isomers **8** and **10**, the two isomers could be differentiated. **10** shows a response from both the alkene proton and the aldehyde proton signaling that these protons are close enough for a through space interaction to be observed. This gave four separate C=CPhCPDT π-bridges, which smoothly underwent an NBS bromination, Suzuki coupling with TPABpin, and a Knoevenagel reaction to give **YZ11**, **YZ13**, **YZ16**, and **YZ17**.

UV-Vis absorption spectroscopy was performed with **YZ11**, **YZ13**, **YZ16**, **YZ17** and **C218** in dichloromethane to compare changing the π-bridge from Hx_2CPDT to *C*=CPhCPDT (Figure 20, right). The absorption maxima (λ_{max}) and absorption onsets (λ_{onset}) for all of the *C*=CPhCPDT dyes were red-shifted relative to **C218**. The molar absorptivities at λ_{max} for the *C*=CPhCPDT based dyes were measured to be very similar at 15,000 to 16,000 $M^{-1}cm^{-1}$; however, a high-energy band near 440 nm for the cross-conjugated π-bridge based dyes reached molar absorptivities substantially higher than **C218** in this region. The C=CPhCPDT based panchromatic dyes show a much more even molar absorptivity across the full

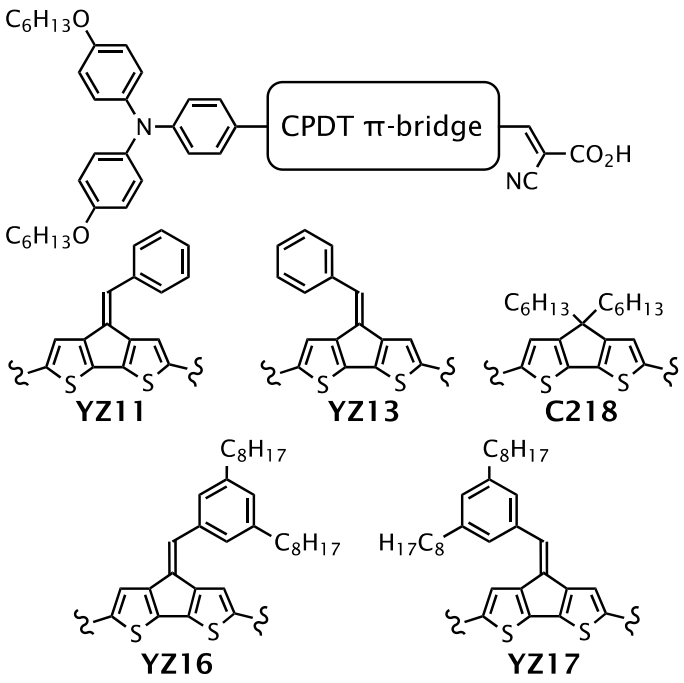

Figure 18. Cross-conjugated C=CPhCPDT π-bridge based D-π-A dyes and **C218.**

spectrum in solution than **C218**. Among the C=CPhCPDT based dyes, the octyl substituents on **YZ16** and **YZ17** led to slightly higher molar absorptivities than **YZ11** and **YZ13**. Interestingly, the dyes with the aryl groups oriented toward the donor region of the dye (**YZ13** and **YZ17**) have similar absorption spectrum with the high energy region being higher in molar absorptivity than the dyes with the aryl groups oriented toward the acceptor. Dye-TiO_2 film UV-Vis absorption spectrum were also measured and are compared with the solution measurements as well as correlated to device performances below (Figure 20, left).

Cyclic voltammetry was performed on **YZ11**, **YZ13**, **YZ16**, and **YZ17** to estimate the driving forces for electron transfer from the redox shuttle to the dye (ΔG_{reg}) and from the dye to the TiO_2 conduction band (ΔG_{inj}, Figure 21). The ground-state oxidation potentials (0.87-0.93 V versus NHE) of these dyes were more positive than the I^-/I_3^- redox

shuttle (0.35 V versus NHE), which favors electron transfer from I^- to the oxidized dye.[109,110] **YZ11**, **YZ13**, **YZ16**, **YZ17**, and **C218** have very similar $E_{(S+/S)}$ values, which indicate that the *C*=CPhCPDT bridge has minimal effects on ground-state state oxidation potential when compared with Hx_2CPDT. The excited-state oxidation potentials ($E_{(S+/S*)}$) for **YZ11**, **YZ13**, **YZ16**, and **YZ17** were calculated from the equation

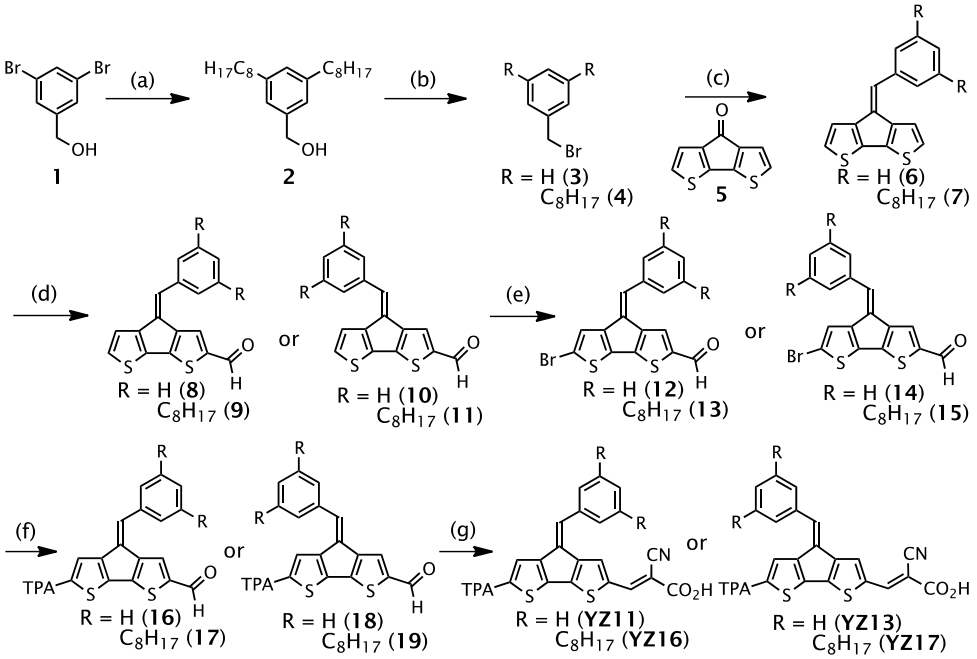

Scheme 3. Synthetic route to **YZ11**, **YZ13**, **YZ16** and **YZ17**.

(a) Pd-PEPPSI-IPr (cat.), n-octylzinc bromide, 62%. (b) PBr_3, 73% (c) PPh_3, **5**, NaOEt, **6:** 76%, **7:** 60%. (d) $POCl_3$, DMF, **8:** 40%, **10:** 41%, **9:** 50%, **11:** 59%. (e) NBS, **12:** 96%, **14:** 100%, **13:** 95%, **15:** 91%. (f) TPA-Bpin, $Pd(PPh_3)_4$ (cat.), **16:** 91%, **18:** 69%, **17:** 100%, **19:** 83%. (g) cyanoacetic acid, piperdine, **YZ11:** 87%, **YZ13:** 64%, **YZ16:** 20%, **YZ17:** 20%.

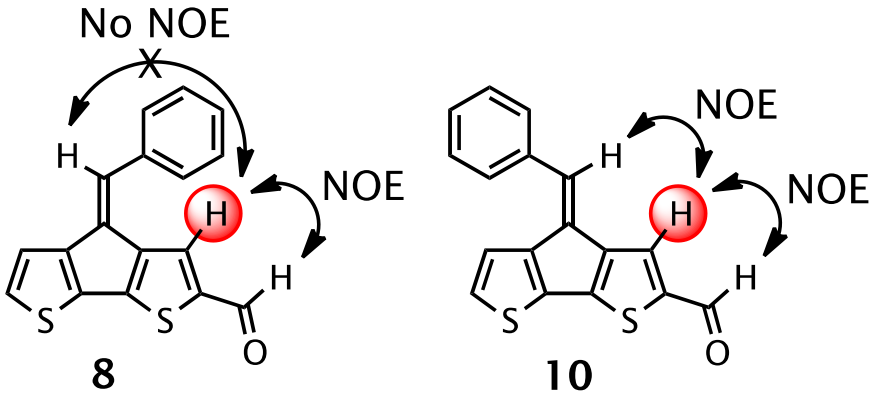

Figure 19. NOE responses for C=CPhCPDTCHO of Z (**8)** and E(**10)**. Irradiated proton is highlighted in red.

$E_{(S+/S^*)} = E_{(S+/S)} - E_g^{opt}$ and were found to range from -0.87 to -0.97 V versus NHE which is suitable for efficient electron injection to the TiO_2 CB.[111] This is significantly lower in energy than the -1.08 V value measured for **C218**. The energetically lower $E_{(S+/S^*)}$ values for the cross-conjugated *C*=CPhCPDT bridge when compared to the Hx_2CPDT suggested that the excited-state is stabilized to a greater extent with the extended conjugation bridge with minimal effect on the ground-state oxidation potentials. This provides a valuable method for independently tuning dye redox potentials.

Having established **YZ11, YZ13, YZ16,** and **YZ17** have suitable energetics to work efficiently in solar cell devices, we next evaluated the orbital position and involvement/electronic structure via density functional theory (DFT) and time-dependent density functional theory (TD-DFT) at the B3LYP/6-311G(d,p) level. For efficient DSC devices, the highest occupied molecular orbital (HOMO) of the dye should be oriented far from the TiO_2 surface to reduce the rate of back electron transfer from TiO_2 to the oxidized dye after an electron is injected. Also, the lowest unoccupied molecular orbital (LUMO) should be positioned near the TiO_2 surface to promote electron transfer upon photoexcitation. The HOMO and LUMO of **YZ17** are illustrated in Figure

22 with the remaining dye orbitals available in the SI (Figure 46, Appendix). The HOMO is primarily located on the donor and CPDT portion of the π-bridge with some contribution on the CAA (cyanoacrylic acid) acceptor and no contribution on the cross-conjugated phenyl substituent. This is consistent with the CV data which suggests that there is minimal effect on the ground state oxidation potential by introducing the cross-conjugated phenyl substituent onto CPDT. The LUMO is positioned primarily on the CPDT-CAA region with some delocalized to some extent on the cross-conjugated phenyl substituent. The HOMO and LUMO of **YZ17** are well positioned for devices based on **YZ7** to operate

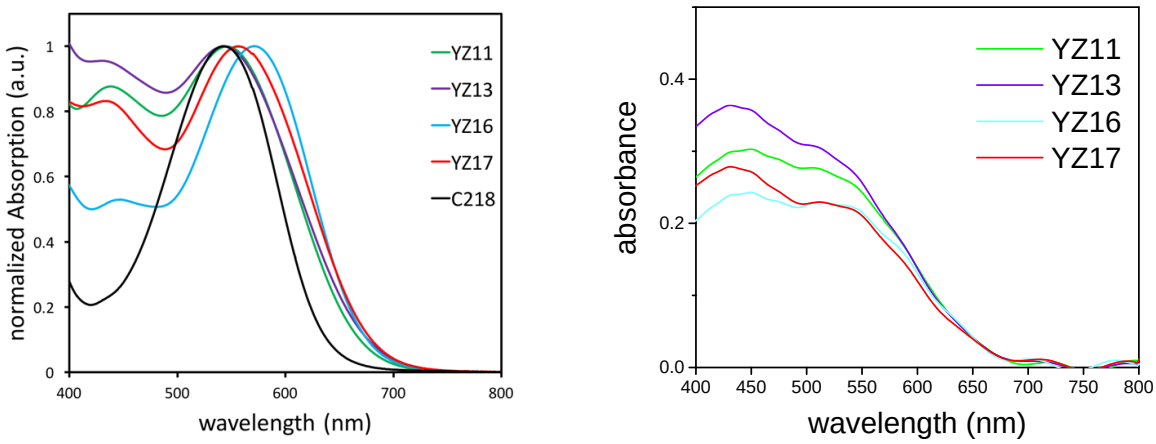

Figure 20. UV-Vis absorption spectra collected for **YZ11, YZ13, YZ16, YZ17** and **C218** in CH_2Cl_2 at 25°C (right) and on TiO_2 (left).

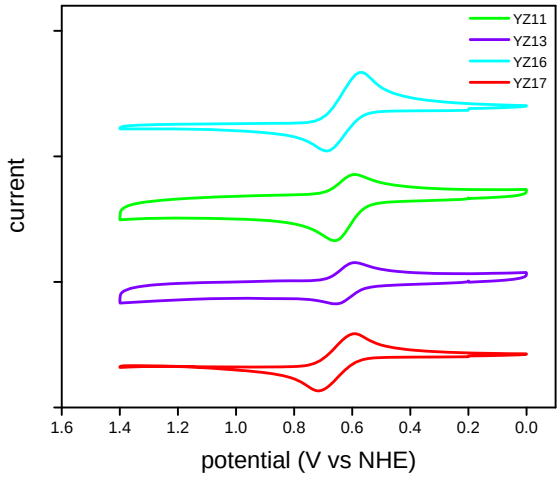

Figure 21. Cyclic voltammograms for **YZ11, YZ13, YZ16,** and **YZ17** in CH_2Cl_2 with 0.1 M tetrabutylammonium hexafluorphosphate electrolyte, glassy carbon working electrode, platinum counter electrode and Ag/AgCl reference electrode.

efficiently. TD-DFT was performed for each dye to better understand the broad charge transfer bands observed in the absorption spectra and the broad high energy bands (Table 16, Appendix). In each case, the HOMO-LUMO transition dominates the low-energy vertical transitions (96%), while both the HOMO-1 to LUMO (44%) and HOMO to LUMO+1 (51%) primarily contribute to the high-energy vertical transition. The HOMO-1 is delocalized across the entire dye with the exception of the cross-conjugated phenyl substituent, and the LUMO+1 is entirely localized on the cross-conjugated phenyl substituent and cyanoacrylic acid regions. This result shows that the cross-conjugated phenyl substituent plays a critical role in influencing in the LUMO and LUMO+1 resulting in strengthened high and low-energy charge transfer bands.

Table 6. Optical and electrochemical properties of **YZ11, YZ 13, YZ16, YZ17** and **C218** in CH_2Cl_2 at 25 °C[a]

dye	λ_{onset} (nm)	λ_{max} (nm)	ε ($M^{-1}cm^{-1}$)	$E_{(S+/S)}$ (V)	$E_{(S+/S^*)}$ (V)	E_g^{opt} (eV)
YZ11	675	546	15,000	0.87	-0.97	1.84
YZ13	690	553	15,000	0.89	-0.91	1.80
YZ16	690	572	16,000	0.89	-0.91	1.80
YZ17	690	557	16,000	0.93	-0.87	1.80
C218	630	550	20,000	0.89	-1.08	1.97

[a]See for Appendix 11 detailed energy measurements and calculations.

Solar cells were assembled and characterized according to the equation, PCE = (J_{sc}*V_{oc}*FF)/I_0 where PCE is power conversion efficiency, J_{sc} is the short circuit current, V_{oc} is the open circuit voltage, FF is the fill factor, and I_0 is the sun intensity. A range of PCE's were observed for devices prepared with **YZ11**, **YZ13**, **YZ16** and **YZ17** from 4.2% to 6.7% using the I^-/I_3^- redox couple (Table 7, Figure 23). The dialkylated *C*=CPhCPDT bridged dyes **YZ16** and **YZ17** gave higher open circuit voltages (622 and 671 mV, respectively) than the non-alkylated *C*=CPhCPDT bridged dyes **YZ11** and **YZ13**. For the dyes with the phenyl substituent oriented toward the acceptor (**YZ11** and **YZ16**), similar overall PCE values of 5.4% versus 5.1% were obtained, respectively, with a higher photocurrent observed for **YZ11**. A significant

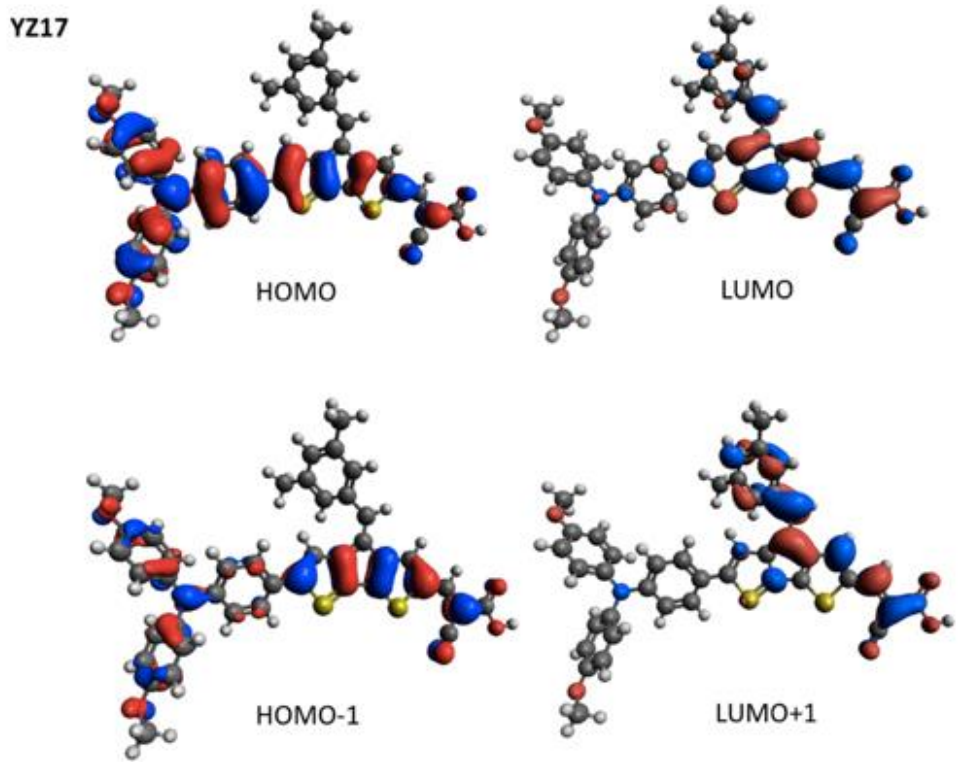

Figure 22. HOMO, LUMO, HOMO-1, LUMO+1 orbitals for dye **YZ17** as calculated by DFT at B3LYP/6-311G (d,p) level.

difference in PCE was observed for devices prepared with **YZ13** and **YZ17**, which have the phenyl substituent oriented toward the donor (4.2% versus 6.7%). This performance enhancement was the result of significant gains to both photocurrent and photovoltage for **YZ17** to give the highest performing dye of the series. Under identical device conditions, **YZ17** has a higher PCE than benchmark dye **C218** due to the panchromatic absorption of **YZ17** with a peak incident photon-to-current conversion efficiency (IPCE) of 67% and an IPCE onset of 800 nm (Figure 23). This broadened IPCE response translates into a high J_{sc} of 13.6 mA/cm^2 for **YZ17** compared to 13.2 mA/cm^2 for **C218**. Through the use of N_2 bubbling during electrode sensitization to accelerate dye infiltration throughout the TiO_2

film, the V_{oc} and J_{sc} of **YZ17** could be enhanced to give a 7.6% PCE device. The peak IPCE for this device reaches 77%, with a higher J_{sc} value of 14.7 mA/cm^2 although the IPCE spectrum onset is blue-shifted by approximately 20 nm relative to the **YZ17**-based electrodes prepared without gas flow.

Comparing phenyl group orientation with device performance, the non-alkylated phenyl group oriented toward the acceptor (*E*-isomer, dye **YZ11**) is higher performing by 1.2% PCE. However, for the heavily alkylated phenyls the phenyl group pointed toward the donor (*Z*-isomer, dye **YZ17**) is higher performing by 1.6% PCE. We reasoned the bulky chain alkylated phenyl group of *E*-isomer **YZ16** could result in a lower dye loading due to sterics near the surface. Dye loading studies reveal this is the case as **YZ17** has a nearly 2x higher dye loading on the TiO_2 surface (2.1 x 10^{-8} versus 3.7 x 10^{-8} mol/cm^2, (Table 17, Appendix). **YZ13** with the smaller phenyl group oriented away from the surface only shows a modestly higher dye loading than **YZ11** (4.6 x 10^{-8} versus 3.9 x 10^{-8} mol/cm^2). This suggests that if the dye loadings are similar, the phenyl group

Table 7. Photovoltaic parameters of devices for **YZ11, YZ13, YZ16, YZ17** and **C218**.[a]

dye	V_{oc} (mV)	J_{sc} (mA/cm^2) [IPCE J_{sc}][b]	FF	PCE (%)
YZ11	599	12.9 [12.5]	0.67	5.4
YZ13	577	9.8 [9.4]	0.72	4.2
YZ16	622	12.3 [11.8]	0.65	5.1
YZ17	671	13.6 [13.4]	0.71	6.7
YZ17[c]	683	14.7 [13.5]	0.74	7.6
C218	654	13.2 [12.6]	0.70	6.3

[a]The electrolyte is composed of guanadinium thiocyanate (GuNCS, 0.1 M), 1,3-dimethylimidazolium iodide (DMII, 1.0 M), I_2 (0.03 M), 4-*tert*-butyl pyridine (TBP, 0.5 M), LiI (1.0 M), and MeCN:valeronitrile (85:15) as solvent unless otherwise noted. The electrodes were dipped in 0.3 mM acetonitrile:*tert*-butanol:THF (1:1:1) with 20x CDCA overnight. [b]Calculated by integrating the area under the IPCE curves in Figure 22. [c]**YZ17** dipping in acetonitrile:*tert*-butanol:chlorobenzene (2.5:2.5:1) dye solution with N_2 passed over the dye solution for 30 minutes. Measurements were carried out under simulated 1 sun illumination (100 mW/cm^2), with active area of 0.15 cm^2 for the cells.

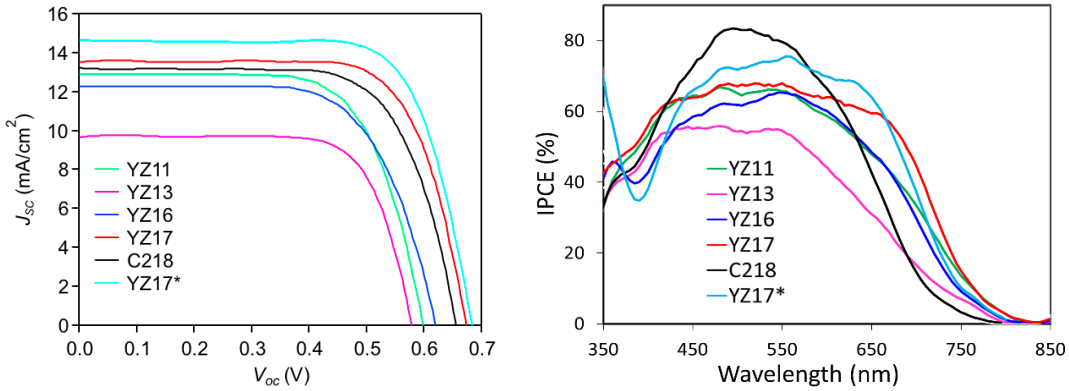

Figure 23. *J*-V curves (top) and IPCE (bottom) for DSC devices of **YZ11**, **YZ13**, **YZ16**, **YZ17**, and **C218**. * Dye deposition through bubbling N2 through dye solution during electrode sensitization.

oriented toward the surface is higher performing (*E*-isomer **YZ11**>*Z*-isomer **YZ13** in terms of PCE); however, if the phenyl group near the surface has significant steric bulk, the dye loading is significantly diminished and the phenyl group oriented away from the surface will be higher performing (*Z*-isomer **YZ17**> *E*-isomer **YZ16** in terms of PCE). Analysis of the film absorption compared to solution absorption reveals a substantial increase in the

high energy absorption band of the film (relative to solution) for the donor oriented phenyl groups (*Z*-isomer dyes **YZ13** and **YZ17**). This significant change could suggest either the dye planarity has changed at the surface significantly or the *Z*-isomers are more prone to aggregation. For the smaller non-alkylated phenyl group, we observe a correlation between keeping the solution curve shape with film measurements and high performance. However, this gain in performance is offset if the dye loadings are not similar as observed for the alkylated phenyl group dyes.

Electron lifetime studies were undertaken to better understand the higher V_{oc} values observed for the alkylated *C*=CPhCPDT bridged dyes versus the non-alkylated dyes and the higher V_{oc} values observed for **YZ17** relative to **C218** for devices prepared under identical conditions (Figure 24). A decrease in electron lifetimes was observed across the series in the following order: **YZ17** > **C218** > **YZ16** > **YZ11** > **YZ13**, which is identical to the order observed for the device V_{oc} values. This

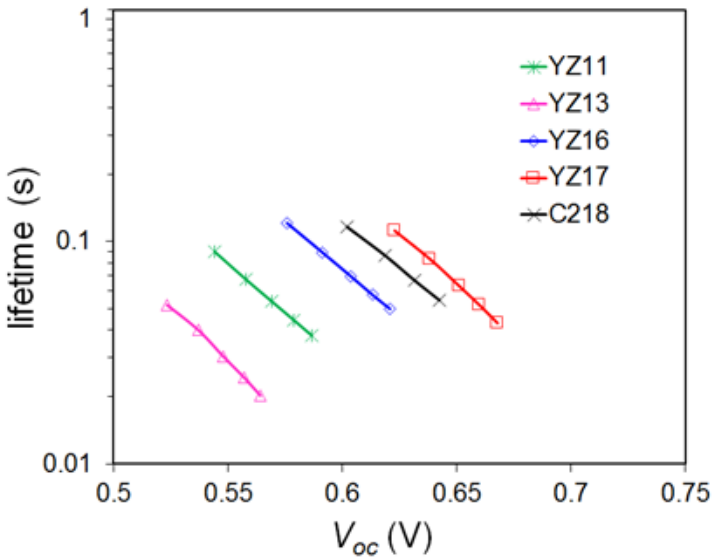

Figure 24. Electron lifetime versus open-circuit voltage plot.

suggests the long alkyl chains of **YZ17** oriented away from the surface are most effective at reducing the rate of recombination of electrons in TiO_2 with the redox shuttle. The broadened absorption and longer lifetime of electrons in TiO_2 of **YZ17** illustrate the utility of a cross-conjugated CPDT bridge relative to the commonly used Hx_2CPDT building block.

CONCLUSION

Four cross-conjugated CPDT-based organic sensitizers were designed and synthesized. Dye isomers were assigned based on ^{1}H NMR NOE studies, and the dyes were characterized via UV, CV, and computational studies to probe the effect of a cross-conjugated π-bridge on dye energetics. The *C*=CPhCPDT bridge leads to a red-shift of the absorption spectrum and an increase in the high-energy absorption to give a series of panchromatic dyes. The red-shift in the absorption spectrum was found to be due to a stabilization of the dye excited-state oxidation potential. The addition of long alkyl chains onto the cross-conjugated CPDT bridge oriented away from the TiO_2 surface was found to reduce recombination of electrons in TiO_2 with the oxidized redox shuttle. A peak PCE of 7.6% was observed for **YZ17**, which surpasses the benchmark **C218** under identical device conditions. This performance enhancement was in part due to an extended IPCE range reaching an 800 nm onset for **YZ17**. The cross-conjugated CPDT bridge approach offers a new strategy for tuning dye energetics to increase light absorption and increase device performance relative to the ubiquitous Hx_2CPDT bridge used in **C218**.

CHAPTER 5

5.1 IODINE BINDING WITH THIOPHENE AND FURAN BASED DYES FOR DSCS

Adapted with permission from Alexandra Baumann,; Hammad Cheema,; Md Abdus Sabuj,; Louis E. McNamara,; **Yanbing Zhang,;** Adithya Peddapuram,; Suong T. Nguyen,; Davita L. Watkins,; Nathan I Hammer,; Neeraj Rai,; Delcamp, J. H.; *Phys. Chem. Chem.Phys.* **2018**, *20*, 17895. Reproduced by permission of The ROYAL SOCEITY OF CHEMISTRY.

(See appendix for permission license.)

This is a collaborative project with Dr. Watkins, Dr. Delcamp, Dr. Hammer and Dr. Rai's group. Alexandra Baumann synthesized and characterized the dyes. Hammad Cheema and Yanbing Zhang fabricate and measured the data of the device. Adithya Paddapuram synthesized LD03 and LD04 two dyes. LouisE.Mc Namara measured Raman spectroscopy data. Md Abdus Sabuji performed computational studies. Suong T.Nguyen synthesized the Br-TF-COH intermediate.

ABSTRACT

Iodine binding to thiophene rings in dyes for dye-sensitized solar cells (DSCs) has been hypothesized to be performance degrading in a number of literature cases. Binding of iodine to dyes near the semiconductor surface can promote undesirable electron transfers and lower the overall efficiency of devices. Six thiophene or furan containing dye analogs were synthesized to analyze iodine binding to the dyes via Raman spectroscopy, UV-Vis studies, device performance

metrics and density functional theory (DFT) based computations. Evidence suggests I_2 binds thiophene-based dyes stronger than furan-based dyes. This leads to higher DSC device currents and voltages from furan analogues, and longer electron lifetimes in DSC devices using furan based dyes. Raman spectra of the TiO_2 surface-bound dyes reveals additional and more instense peaks for thiophene dyes in the presense of I_2 relative to no I_2. Additionally, broader and shifted UV-Vis peaks are observed for thiophene dyes in the presence of I_2 on TiO_2 films suggesting significant interaction between the dye molecules and I_2. These observations are also supported by DFT and TD-DFT calculations which indicate the absence of a key geometric energy minimum in the dye-I_2 ground state for furan dyes which are readily observed for the thiophene based analogues.

INTRODUCTION

The need for an energy source that is both sustainable and renewable is apparent. One viable option that is cost-effective and potentially aesthetically appealing are dye-sensitized solar cells (DSCs).[1,63] DSC devices operate by: (1) photoexcitation of a dye molecule, (2) injection of excited electrons into a semiconductor conduction band (e.g. TiO_2 CB), (3) an electron traversing an external circuit to the counter electrode, (4) collection of the electron at the counter electrode by a redox shuttle, and finally (5) transfer of the electron from the redox shuttle to the oxidized dye molecule.[6] Organic dye based DSCs have been able to reach power conversion efficiencies (PCEs) for this process in excess of 14%, but there is still room for improvement by minimizing non-productive electron transfers such as from TiO_2 to the dye (back electron transfer) or from TiO_2 to the redox shuttle (recombination).[6,103,111] Undesirable charge recombinations are thought to increase when the iodine (I_2) redox shuttle binds with a dye near the TiO_2 surface (Figure

25).[112–115] Minimizing recombination events which prevent electrons from completing an external circuit is critical to developing higher efficiency DSC devices.

Isothiocyanates (NCS) bound to transition metals, amine, cyano, halide and thioether groups have been demonstrated to bind iodine and iodide through prior spectroscopic, computational and device studies.[107,114,116–126] Despite good evidence of sulfur-based NCS groups and aromatic 5-member heterocycle selenophenes[113] interacting with iodine, experimental evidence of thiophenes binding I_2 is lacking. However, thiophene is commonly implicated in promoting recombination by binding I_2 near the semiconductor surface.[127,128] Several computational reports suggest thiophene-based dyes binding I_2 may be favorable and likely has device performance implications.[126,129–132] The possibility of thiophene binding I_2 is concerning since thiophenes have become ubiquitous in DSC organic-dye design. To probe the ongoing hypothesis that I_2 in DCSs is binding to the sulfur atom present in thiophene stronger than the oxygen atom present in furan rings, we have systematically studied a series of six thiophene or furan based-dye analogs experimentally via Raman spectroscopy, UV-Vis absorption, and DSC device performance properties, as well as computationally via geometry analysis, binding strength comparisons, and analysis of vertical transition events. The results put forward in this manuscript offer strong evidence of thiophenes binding I_2 which leads to lower DSC device performances.

We hypothesized sulfur would bind I_2 stronger than oxygen due to the higher polarizability of sulfur which is more similar to iodine.[133] Additionally, the widened C-S-C angle of thiophene relative to the C-O-C angle of furan could play an important role in accessibility of the S atom to I_2. To test this, we employed dyes in our studies which replace a thiophene ring with a furan ring to give a single atom change within the larger dye

structure. Donor and π-bridge functionality was examined for three sets of dyes which all employ the ubiquitous cyanoacrylic acid acceptor within the donor-π bridge-acceptor (D-π-A) framework. Specifically, **LD03** (thiophene) and **LD04** (furan) have a simple alkyl ether donor group as part of the D-π-A conjugated system (Figure 26). This limits the heteroatom (non-carbon or hydrogen) binding positions relative to more complex dye systems. Hagfeldt's triarylamine donor was used to compare dyes varying π-bridges from one thiophene (**D35**), one furan (**AB3**), two thiophenes (**AB1**), and one thiophene with one furan (**AB2**) (Figure 25). This donor was selected as **D35** has been extensively studied and allows for a

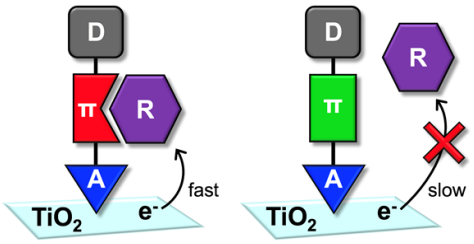

Figure 25. Example of a D-π-A dye binding a redox shuttle "R" near the TiO_2 surface (left) and a dye with no redox shuttle binding (right).

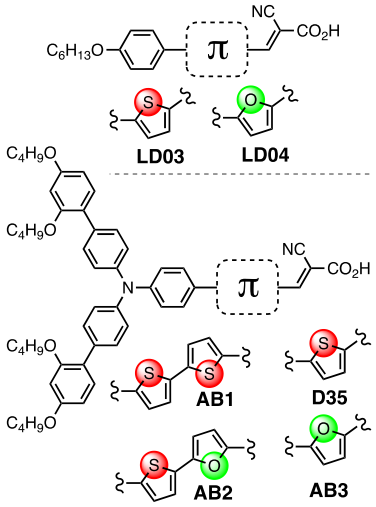

Figure 26. Target structures of **AB1, AB2, AB3, D35, LD03** and **LD04** dyes.

comparison to an established dye. The target dyes were known (**AB1**, **LD03** and **LD04**),[134,135] commercially available (**D35** via Dyenamo), or prepared through analogous routes to the thiophene analogues[134,136] for the unknown furan dyes (**AB2** and **AB3**, see Figure 47 in Appendix for synthetic route).

RESULTS AND DISCUSSION

Raman Spectroscopy. First, we examined the vibrational spectrum of the dyes with and without I_2 present on TiO_2 films in acetonitrile (MeCN) via Raman spectroscopy. Raman spectroscopy provides a sensitive spectroscopic method for evaluation of dye vibrational modes under conditions similar to those in devices for the neutral ground-state dye at a surface in the presence of MeCN with and without I_2. If iodine binding were to occur to the sulfur atom stronger than oxygen, we reasoned a change in the vibrational spectra of the dye molecules would be expected due to new vibrational peaks resulting from new vibrational modes associated with a S-I_2 binding or a change in the relative intensity of already existing peaks by perturbation of ring breathing/stretching modes of thiophene through introduction of an S-I_2 bond.[137,138] To compare thiophene versus furan dyes binding I_2, TiO_2-dye films were prepared with **D35** (thiophene), **AB3** (furan), **LD03** (thiophene) and **LD04** (furan). **AB1** (thiophene) and **AB2** (furan) were not studied via Raman spectroscopy since they suffer from decomposition on films in the presence of I_2 alone. Notably, **AB1** and **AB2** were stable in operational DSC devices presumably due to the full electrolyte stabilizing the dyes. For the other 4 dyes, Raman spectra were collected on the TiO_2-dye films with and without I_2 in the common DSC device electrolyte solvent MeCN.

D35 (thiophene) and **AB3** (furan) both show an increase in the relative intensity of the peaks seen between 1000-1600 cm^{-1} when compared with the 300-1000 cm^{-1} region; however, the increase is substantially greater for **D35** (thiophene) (Figure 27a and 27b). Initial pure dye peaks and new peaks associated with I_2 addition can be seen around 950 cm^{-1}, 1025 cm^{-1}, 1060 cm^{-1}, and 1400-1600 cm^{-1} for **AB3** (furan) (Figure 27b), but **D35** (thiophene) shows few original dye peaks after I_2 addition with numerous intense signals being added from 1000-1600 cm^{-1} (Figure 27a). This points to the presence of iodine binding in both dyes, however the presence of the sulfur atom in **D35** (thiophene) has resulted in a larger change in the Raman spectrum relative to **AB3** (furan). This larger change in the **D35** (thiophene) Raman spectrum is the result of a single atom change from oxygen in **AB3** (furan) to a sulfur. Given that the experimental conditions were held constant, this single atom is responsible for the large change in the Raman spectrum when I_2 is present. The changes are consistent with a sulfur-halogen bonding event to I_2 as discussed in the computational section below.

To reduce the possible influence of the nitrogen atom of the amine donor during these studies, the simple alkoxy donor-based dyes, **LD03** (thiophene) and **LD04** (furan), were examined in an identical study. Changes in the Raman spectra were subtler for these two derivatives which could be due to the absence of nitrogen-I_2 interactions or due to a less electron rich thiophene binding weaker to I_2 when only a relatively weak ether donor is used. A larger difference in the relative intensity of the peaks between 1000-1600 cm^{-1} with and without I_2 present is observed for **LD03** (thiophene, Figure 27c) when compared with the 300-1000 cm^{-1} region, while the change for **LD04** (furan, Figure 27d) is less dramatic when these regions are compared. These results indicate a difference in the

influence of I_2 on the Raman spectrum of **LD03** (thiophene) when compared to **LD04** (furan) which may be attributed to the stronger binding of I_2 by thiophene. This observation is consistent with Raman spectroscopy studies performance on films of **D35** (thiophene) and **AB3** (furan).

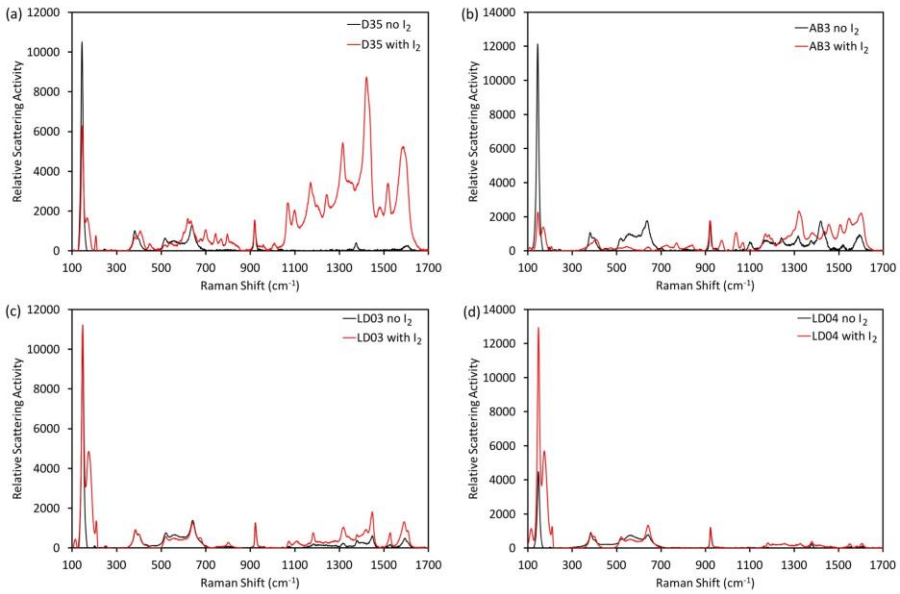

Figure 27. Raman spectra for (a) **D35**, (b) **AB3**, (c) **LD03** and (d) **LD04** on TiO_2 films under acetonitrile with and without I_2 present. Background spectrum were subtracted in each case without the dye present but all other components were present.

Computational Analysis. To gain insight into the changes observed experimentally in the Raman spectra, the interactions of **AB1** (thiophene), **AB2** (furan), **D35** (thiophene) and **AB3** (furan) with I_2 were probed computationally to examine the hypothesis of thiophene interacting non-covalently with I_2 more strongly than furan. **AB1** (thiophene) and **AB2** (furan) were also of interest since spectroscopic film studies in the presence of I_2 could not be conducted. Since **LD03** (thiophene) and **LD04** (furan) displayed similar Raman spectra trends to **D35** (thiophene) and **AB3** (furan), the more common benchmark dye **D35**

(thiophene) was chosen for computational studies to compare with analogue **AB3** (furan). First, geometries of the dyes were optimized in two different conformations (referred to as *cis* and *trans* based on the orientation of the CN group of the cyanoacrylic acid relative to the thiophene sulfur or furan oxygen atoms, Figure 28) in isolation without I_2 present at the wB97XD/6-31+G* level of theory. On TiO_2 film surfaces the exact dye geometry is challenging to predict, thus two geometries were analyzed for the four dyes examined. Calculations were conducted in the absence of solvent and the TiO_2 surface to reduce the complexity in trying to evaluate vibrational changes induced by non-covalent bonding with a large number of atoms present.

To examine the dye interactions of I_2 at the thiophene or furan rings, I_2 was positioned near the heterocycles of the geometry optimized dyes in space with a linear orientation of I_2 and the S/O atom all in the same plane as the heterocycle. The geometries were then optimized to the lowest energy conformation. It is noteworthy that a number of binding sites are evident on each dye with stronger binding at the nitrogen atoms of the triarylamine and cyanoacrylic acid; however, these binding events are present in all dyes. We have focused on the heterocycles as these binding events differentiate the thiophene and furan dyes. A close interaction for sulfur and iodine of ~3.45 Å is observed for *cis*- or *trans*-**AB1** (thiophene) with an end-on binding to I_2 at the presumed sigma-hole location (Figure 29, Table 8). When comparing these results to **AB2** (furan) it is interesting that only one conformer (*trans*) binds I_2 to give a linear O-I_2 geometry orientation. The *cis*-**AB2** (furan) conformer does not show an energy minimum with a linear geometry, but instead the I_2 shifts to above the π-face of the system as the nearest energy minimum (Table 8, Figure 29). This result supports our experimental finding that sulfur of thiophene the oxygen

of furan, since one of the potential binding sites for furan is non-active in the *cis* conformation. For the cases where I_2 adopts a linear orientation relative to the sulfur and oxygen atoms, the I_2 molecule adopts a 65° to 81° dihedral angle with the π-system of the heterocycle (Figure 29, Table 8). Similar results are observed when the *trans* and *cis* isomers of **D35** (thiophene) and **AB3** (furan) are compared. For the comparable *trans* isomers, the location of the highest occupied molecular orbital (HOMO) and the lowest unoccupied molecular orbital (LUMO) offer some insight into the nature of this binding event. The HOMO of *trans*-**D35** (thiophene) and *trans*-**AB3** (furan) is delocalized

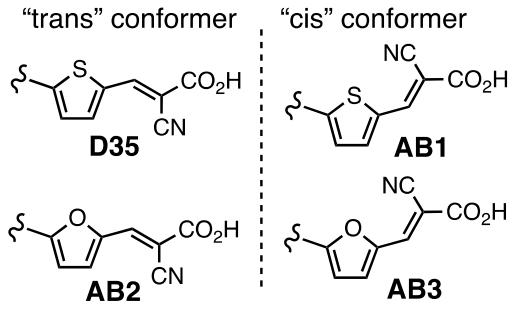

Figure 28. Illustration of the *trans* and *cis* conformer of **D35, AB1, AB2,** and **AB3** assignments

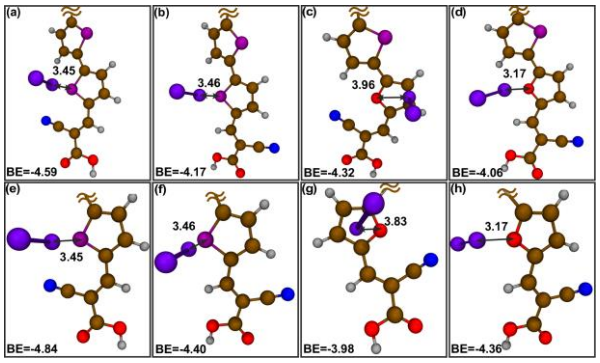

Figure 29. Illustration of the closest I_2 binding energy minima at the heterocycle near that CAA acceptor for *cis*-**AB1**, *trans*-**AB1**, *cis*-**AB2**, *trans*-**AB2**, *cis*-**D35**, *trans*-**D35**, *cis*-**AB3**, and *trans*-**AB3**. Calculations were done at wB97XD/6-31+G* level of theory and basis set.

onto the heterocycles (Figure 30, see Figure 48-51in Appendix for **AB1** and **AB2** orbitals). In both cases the LUMO is heavily localized on the I_2 molecule suggesting an intermolecular charge transfer event may be possible. This interaction is indicative of a halogen bonding event in a conformation that would be predicted by a first principle approximation.

Binding energies were analyzed for these dyes to I_2 by summing the energies of the dye and I_2 separately optimized in isolation, then comparing with the system energy having both the dye and I_2 present. Again, only the *trans* isomers could be compared as no *cis*-**AB2** (furan)-I_2 optimized geometry could be located which was comparable to thiophene analogue (Table 8). The *trans*-**AB1** (thiophene)-I_2 binding energy was found to be stronger than that of the *trans*-**AB2** (furan)-I_2 binding energy by a 0.11 kcal difference. A very similar analysis can be made comparing **D35** (thiophene) and **AB3** (furan), with **AB3** (furan) again showing no binding in a linear orientation to I_2 for the *cis* conformer and the *trans* conformer showing weaker binding relative to the *trans*-**D35** (thiophene) analogue (Figure 30, Table 8). When the *cis* and *trans* isomers are compared for the thiophene based dyes **AB1** and **D35**, a 0.42-0.44 kcal/mol greater binding energy is present for the *cis* isomers. Thus, not only do thiophene-based dyes have a stronger analogue binding mode than the furans in the *trans* conformation, but they also bind even stronger in the *cis* conformation which is exclusive to thiophene. These results suggest that an I_2 binding event may not be completely absent from furan heterocycles, but thiophene analogues exhibit much stronger halogen bonding interactions in multiple conformations.

Having found optimized geometries for **D35** (thiophene) and **AB3** (furan) with and without I_2, we simulated Raman spectra from DFT calculations at the wB97XD/6-31+G* level of theory to better understand the vibrational modes in the 1400-1800 cm^{-1} range of

Table 8. Computational results of **AB1, AB2, D35** and **AB3** for I_2 binding distance, binding energies and dihedral angles at wB97XD/6-31+G* level.

dye	S/O-I_2 distance (Å)	Binding energy (kcal/mol)	S/O-I_2 dihedral (°)
cis-**AB1** (thiophene)	3.45	-4.59	81
trans-**AB1** (thiophene)	3.46	-4.17	71
cis-**AB2** (furan)	no minimum	no minimum	---
trans-**AB2** (furan)	3.17	-4.06	65
cis-**D35** (thiophene)	3.45	-4.84	81
trans-**D35** (thiophene)	3.46	-4.40	70
cis-**AB3** (furan)	no minimum	no minimum	---
trans-**AB3** (furan)	3.17	-4.36	70

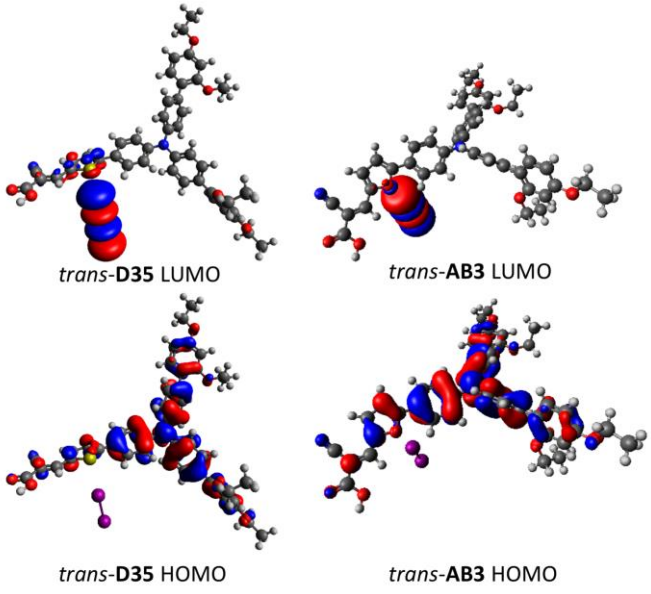

Figure 30. HOMO and LUMO orbitals of trans **D35** and **AB3**. Calculations were done at wB97XD/6-31+G* level of theory and basis set. Iso values are set to 0.2.

the experimental Raman spectrum which were changing much more dramatically for **D35** (thiophene) in the presence of I_2 relative to **AB3** (furan, Figures 27 and Figure 52 in

Appendix). Two different geometries for each dye were analyzed with and without I_2 present. While the simulated spectra can be used to help understand the experimental spectra, a direct comparison cannot be made since the simulated Raman spectra is obtained in the gas phase with only one I_2 molecule present and under harmonic approximations while the experimental data was collected on the surface with acetonitrile solvent present with a large excess of I_2 molecules. Thus, the comparison of the data is restricted to broad wavenumber ranges rather than to wavenumber peaks. It could be seen that in both the *cis* and *trans* conformations for **AB3** (furan) no shift or emergence of new peaks can be seen when I_2 is present and only a slight change in intensities for 2-3 peaks between 1500-1700 cm^{-1} is observed (Figure 52 in Appendix). However, in terms of **D35** (thiophene), the *cis* conformation shows a slight change in intensity along with a shifting of peaks between 1500-1600 cm^{-1} by 3-5 cm^{-1} toward higher energy, while the *trans* conformation shows intensity changes and some shifting of peaks near 1100 and 1600 cm^{-1} with a new peak at ~1250 cm^{-1} evident (Figure 52 in Appendix). For the DFT Raman spectra, the 1500-1600 cm^{-1} region where the most significant changes are occurring corresponds to ring breathing and stretching modes for both thiophene and furan. Experimentally, the largest changes in the Raman spectrum are occurring near this region as well. Given that the experimental changes when I_2 is present were significantly more pronounced for the thiophene based dyes, this suggests that I_2 is interacting stronger with thiophene resulting in significant changes in ring breathing/stretching modes for this heterocycle but to a lesser extent for furan. It is reasonable that the presence of this interaction for thiophene is due to halogen bonding from the sulfur atom to I_2.

UV-Vis Absorption Spectroscopy. To further evaluate our hypothesis that the sulfur of thiophene binds I_2 more strongly than the oxygen of furan, we measured film UV-Vis absorption spectra for **D35** (thiophene), **AB3** (furan), **LD03** (thiophene) and **LD04** (furan). We reasoned that if I_2 binding were occurring with thiophene effects should also be visible in the UV-Vis spectrum. A S-I_2 halogen bond would be predicted to red-shift the dye absorption spectrum since the I_2 serves as an electron acceptor which would lower the LUMO energy based on first approximations. Therefore, we predict significant observable changes in dye absorption transition energies for the thiophene-based dyes **D35** and **LD03** due to S-I_2 binding and relatively minor changes for the furan-based dyes **AB3** and **LD04** due to a weaker O-I_2 interaction. To probe this prediction, we prepared TiO_2 films of each of the dyes and submerged them in solutions of acetonitrile with and without I_2 present. The UV-Vis spectra were analyzed by comparing the shift in the λ_{max} and shape of the normalized absorption curves. On TiO_2 films submerged in acetonitrile with and without I_2, the λ_{max} of **D35** (thiophene) shifts about 10 nm, while the λ_{max} of **AB3** (furan) shows no shift (Figure 31). For the simple alkoxy donor dyes, **LD03** (thiophene) shows a 7 nm shift in the λ_{max} value, while **LD04** (furan) shows a smaller 3 nm shift (Figure 31). The larger shift in λ_{max} for the thiophene based dyes can be attributed to a halogen bonding event due to the presence of I_2 binding stronger with the sulfur atom in thiophene than the oxygen of furan. Additionally, the shift toward lower energy photon absorption (red-shift) in the presence of I_2 occurs as predicted. This is consistent with the hypothesis that halogen bonding with thiophene and I_2 is occurring by donation of electron density from the sulfur to I_2.

To computationally probe the experimentally observed changes in the UV-Vis spectrum in the presence of I_2, time dependent-density functional theory (TD-DFT) calculations were undertaken to evaluate which orbitals were contributing to the observed red-shift and to identify

the position of these orbitals. If I_2 binding is causing the red-shift, a low energy transition of electron density from the dye to I_2 is predicted. To evaluate this prediction, the first 10 states were examined using the previously optimized geometries (both *cis* and *trans* for each dye) for **AB1** (thiophene), **AB2** (furan), **D35** (thiophene), and **AB3** (furan) with TD-DFT calculations at the wB97XD/6-31+G* level of theory. For all of the dyes, in the presence of I_2 the first two states have very low oscillator strengths (*f* of ~0.0005) ranging from 0.3 to 0.5 eV lower in energy than

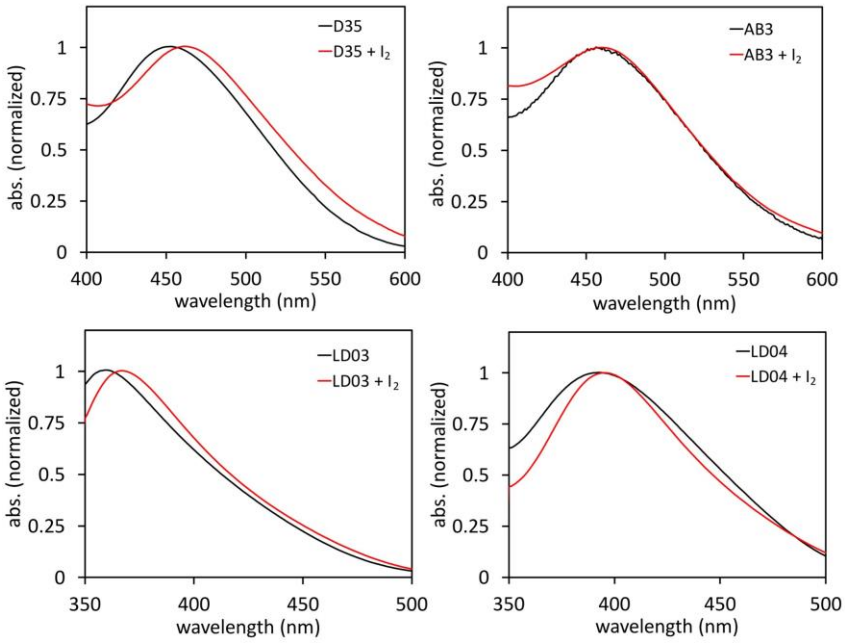

Figure 31. UV-Vis absorption spectra for dyes **D35, AB3**, **LD03,** and **LD04** in acetonitrile with and without I_2 present on films. Background spectrum were subtracted in each case without the dye present but all other components were present. the first major transition (Table 18-25 in Appendix). The transitions for the first two states also involve a large number of orbitals (up to five occupied to unoccupied transitions). The first strong transition (state 3, *f* of 0.99) for *cis* **AB1** (thiophene) is made up of several transitions from occupied orbitals centered on the dye with no significant concentration on I_2 to unoccupied orbitals localized on I_2. Among the transitions involved in this state, the HOMO-LUMO transition is the strongest contributor at 27%

followed by the HOMO-1 to LUMO at 15% with 9 total transitions (Table 18 and Figure 48 in Appendix). Compared to the first state (f = 1.7, primarily HOMO to LUMO and HOMO-1 to LUMO) of *cis* **AB1** (thiophene) in the absence of I_2, state 3 of *cis* **AB1** (thiophene) with I_2 is

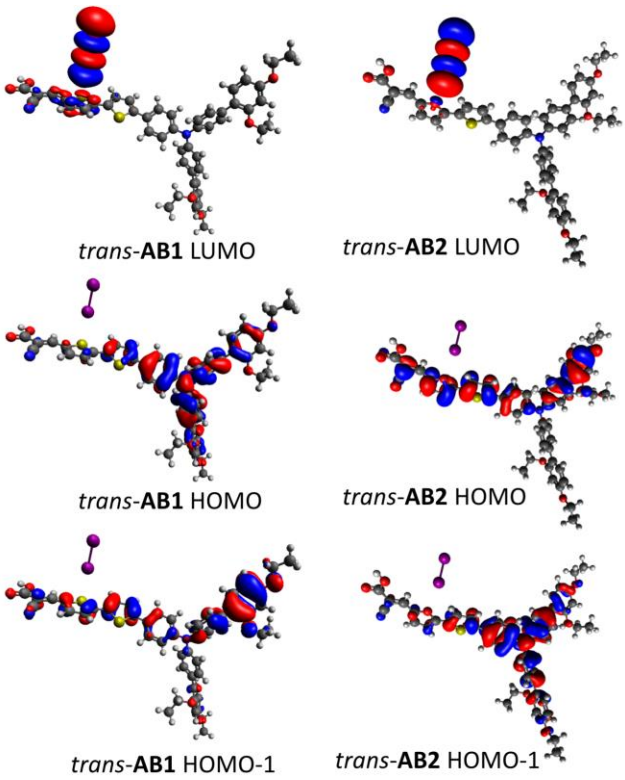

Figure 32. Orbitals contributing to the first strong oscillator strength state for trans **AB3** and **D35**. Calculations were done at wB97XD/6-31+G* level of theory and basis set.

0.14 eV lower in energy. Analysis of *trans* **AB1** (thiophene) with and without I_2 reveals a very similar set of observations (Figures 31, Table 19 and Figure 49 in Appendix). As noted previously, the geometry minima for *cis* **AB2** (furan) is significantly different. However, for both *cis* and *trans* isomers of **AB2** (furan), the first two states show very weak oscillator strengths, and the first major oscillator strength observed is for state 3 when I_2 is present. State 3 for *cis* **AB2** (furan) is still comprised of the same dominate orbital transitions as *cis* **AB1** (thiophene) (HOMO to LUMO and HOMO-1 to LUMO, Table 20, Figure 50 in Appendix) and a similar magnitude red-shift, but with

fewer transition (5 versus 9). Interestingly, the oscillator strength for this third state is significantly lower in strength for *cis* **AB2** (furan) than for *cis* **AB1** (thiophene) (0.15 versus 0.99). This again suggests a significantly stronger interaction of I_2 with thiophene than furan and supports a S-I_2 halogen bonding hypothesis. *Trans* **AB2** (furan) follows the same analysis as *cis* **AB2** (furan) only with a dramatically lower oscillator strength for state 3 (f = 0.02, Table S5, Figure 8 and S5). This data suggests a very weak interaction between the furan heterocycle and I_2 presumably due to the lack of a significant halogen bonding event between O and I_2. These weak red-shifted transition oscillator strengths for **AB2** (furan) in the presence of I_2 are consistent with the relatively minor changes observed by experimental UV-Vis spectroscopy for the furan-based dyes (**AB3** and **LD04**). Computationally, **AB1** (thiophene) shows a much stronger red-shifted transition oscillator strength in the presence of I_2 which is consistent with the experimental data for the thiophene dyes (**D35** and **LD03**) showing a significant red-shift of the UV-Vis spectrum in the presence of I_2. Computationally, both cis and trans isomers of **D35** (thiophene) and **AB3** (furan) follow a similar trend to that described above for **AB1** (thiophene) and **AB2** (furan) (Tables S6-S9). The experimental and computational data is again consistent with a stronger S-I_2 halogen bonding event than O-I_2.

Device Data. Given the spectroscopic observations from the surface Raman studies and film UV-Vis studies, several predictions about the performance of the furan-based and thiophene-based dyes in DSC devices can be made based on the cascade of electron transfer events after photoexcitation of the dye. After the injection of an electron from the photoexcited dye into the TiO_2 CB (equation 1), the ground-state dye can be regenerated with iodide (equation 2). Although a number of possible electron transfer pathways exist concerning the iodide redox shuttle,[34] a commonly cited pathway suggests the I_2^- product from equation 2 can then undergo

disproportionation to give I_3^- and I^- via equation 3. I_3^- represents the fully oxidized redox shuttle species in DSC devices and is involved with an equilibrium reaction to give I_2 and I^- via equation 4. Thus, I_2 is both continuously being generated within the DSC cell under operational conditions and is explicitly added to the electrolyte to generate a concentration of the triiodide species in solution needed for rapid electron collection at the counter electrode. The electrons injected into the TiO_2 CB can either traverse an external circuit to the counter electrode as desired before following the reverse reactions equation 3 and the reduction of I_2^- via equation 5 to give the original iodide reductant, or these electrons can be transferred to an oxidizing species directly from the TiO_2 CB undesirably (equation 6). Specifically, the recombination rate of electrons in the TiO_2 semiconductor conduction band (CB) with the redox shuttle should be slower for the furan-based dyes compared with the thiophene-based analogues if the sulfur of thiophene is halogen bonding to I_2 near the TiO_2 surface. The rate of this recombination is a function of distance for the through-space electron transfer, and sulfur halogen bonding with I_2 will increase the local concentration of I_2 near the TiO_2 surface to promote the undesirable electron transfer shown in equation 6:

$$dye^* + TiO_2 \rightarrow dye^+ + TiO_2(e^-) \quad (1)$$

$$dye^+ + 2\ I^- \rightarrow dye + I_2^- \quad (2)$$

$$2\ I_2^- \rightarrow I_3^- + I^- \quad (3)$$

$$I_3^- \rightleftharpoons I_2 + I^- \quad (4)$$

$I_2^- + e^- \rightarrow 2\ I^-$ (5)

$I_2 + TiO_2(e^-) \rightarrow I_2^- + TiO_2$ (6)

Since equation 6 represents a non-productive DSC device electron transfer pathway, it will lower photocurrent because fewer electrons are traveling the external circuit. Additionally, the electron transfer event represented by equation 6 will also lower photovoltage since electrons are being transferred out of TiO_2 more rapidly leading to a depletion of the number of electrons in the TiO_2 CB and lowering the TiO_2 fermi level. These predictions can all be tested through a series of DSC device measurements including current-voltage (*J-V*) curve, incident photon-to-current conversion efficiency (IPCE), and small modulation photovoltage transient measurements.

First device performances were analyzed for all of the dyes via *J-V* curve measurements (Figure 33, Table 9). In all cases, the furan-based dyes (**AB2**, **AB3**, **LD04**) gave both higher current and voltage than the thiophene analogues (**AB1**, **D35**, **LD03**) as is predicted if a S-I_2 halogen bonding event were occurring. The open-circuit voltage (V_{oc}) values averaged 28 mV higher and the short-circuit current density (J_{sc}) values averaged 0.5 mA/cm^2 higher for the furan derivatives. Via the equation PCE = (V_{oc} x J_{sc} x *FF*)/I_0, where *FF* is fill-factor and I_0 is the sun intensity (set to 1 for this study), the furan-based dyes were found to average 0.6 % higher in PCE. This equates to a >10% overall gain in performance for the furan-based dyes when compared with the thiophene-based dyes. Upon analysis of the IPCE spectrum, thiophene based dyes **AB1** and **D35** are significantly red-shifted relative to the furan analogues (**AB2** and **AB3**, respectively); however, the peak IPCE value for the furan analogues is significantly higher which explains the observed photocurrents via the *J-V* curve measurements (Figure 34). The red-shift of the IPCE spectrum is similar to that observed in the UV-Vis measurements for **D35** (thiophene) when I_2 was

added. It is noteworthy, that there is little change in the dye-film absorption spectrum under pure acetonitrile when **D35** (thiophene) and **AB3** (furan) absorption spectrum are compared (Figure 31). As hypothesized for the UV- Vis data explanation, the IPCE red-shift for the

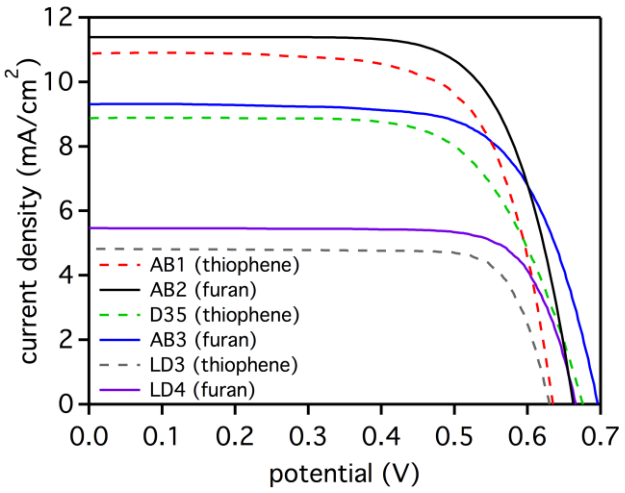

Figure 33. J-V curve comparison for **AB1**, **AB2**, **AB3**, **D35**, **LD03** and **LD04**.

furan dyes can be rationalized as I_2 binding to the thiophene containing dyes to remove electron density from the π-system and lowering the LUMO energy of the system. Having I_2 coordinate to the sulfur in thiophene results in electron density being pulled out of the system, effectively lowering the LUMO of the dye and shrinking the HOMO-LUMO gap as was shown via TD-DFT above. This causes the thiophene-based dyes IPCE's to be

Table 9. Device parameters for **AB1**, **AB2**, **AB3**, **D35**, **LD03** and **LD04**.

dye	V_{oc} (mV)	J_{sc} (mA/cm^2)	*FF*	PCE (%)	dye loading (mol/cm^2)
AB1 (T)	631	11.0	0.65	4.6	2.49×10^{-7}
AB2 (F)	659	11.4	0.71	5.5	2.50×10^{-7}
D35 (T)	675	8.9	0.64	3.9	3.53×10^{-8}

AB3 (F)	696	9.4	0.67	4.5	4.62×10^{-8}
LD03 (T)	630	4.8	0.77	2.4	1.87×10^{-7}
LD04 (F)	664	5.5	0.76	2.8	1.20×10^{-7}

See device fabrication section for TiO_2 thicknesses and compositions. Dyes were deposited from a THF:EtOH (1:4) solution with a dye concentration of 0.3 mM and a 40:1 CDCA:dye ratio overnight in the dark at room temperature. The electrolyte was composed of 0.1 M GuCNS, 1.0 M DMII, 0.03 M I_2, 0.5 M TBP and 0.05 M LiI in 85:15 MeCN:valeronitrile. T = thiophene. F = furan.

selectively red-shifted relative to the film absorption spectrum. For the **LD03** (thiophene)/**LD04** (furan) comparison, the IPCE onset values are similar, but the furan derivative again shows a higher peak performance. The relative increased peak IPCE performance is consistent with the S of thiophene halogen bonding to I_2 to promote unwanted recombination, while a significantly weaker interaction (if any) is present for the O of furan with I_2 which does not promote recombination.

To better understand the rate of recombination of electrons in the TiO_2 CB with I_2 (equation 6), electron lifetime measurements were made via small modulated photovoltage transient studies (Figure 35). Given the larger V_{oc} and J_{sc} values for the furan-based dyes, longer electron lifetimes are expected for **AB2** (furan), **AB3** (furan), and **LD04** (furan) than the thiophene analogues. This is indeed the case, with **AB2** (furan) and **LD04** (furan) showing dramatically longer electron lifetimes than **AB1** (thiophene) and **LD03** (thiophene) (Figure 35). Even for the case of the exceptionally long electron lifetime benchmark dye **D35** (thiophene), the furan analogue **AB3**

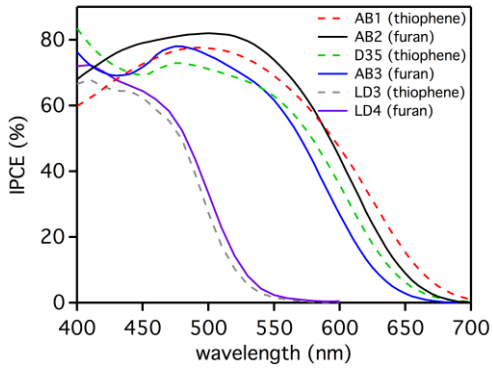

Figure 34. IPCE curves for **AB1**, **AB2**, **D35**, **AB3**, **LD03**, and **LD04**.

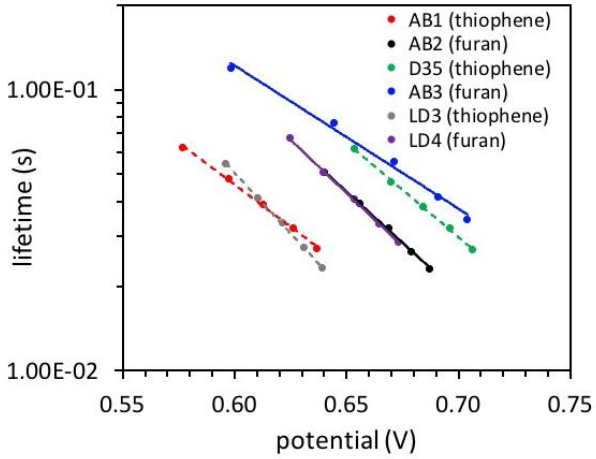

Figure 35. Electron lifetime measurements for dyes **AB1**, **AB2**, **AB3**, **D35**, **LD03** and **LD04** using small modulation photovoltage transient measurements.

shows a longer electron lifetime. These results add further evidence that the sulfur of thiophene is halogen bonding with I_2 near the TiO_2 surface to promote a faster electron recombination event.

Since V_{oc} and J_{sc} device performance metrics are often correlated to dye loadings, dye desorption studies were conducted to probe if dye loading could have had a significant influence in the device data results in addition to the stronger halogen bonding of thiophene relative to furan (Table 9). While the dye analogues only differ by a single atom, the atom used in the heterocycle has a significant influence on the geometry of the substituents at the 2 and 5 positions of furan or

thiophene. The O-C bond lengths are shorter for furan which leads to more of a "U" shape, while the S-C bonds are longer in the case of thiophene which leads to more of a linear geometry. The variation in geometry could result in a difference in dye loading despite the seemingly subtle change of a single atom. However, the dye loadings were all found to be similar between the analogues. Specifically, the dye loadings for **AB1** (thiophene) and **AB2** (furan) were found to be near identical at 2.5 x 10^{-7} mol/cm^2, and **D35** (thiophene) was found to have a dye loading within 25% of the value of **AB3** (furan). Interestingly, the dye loading varied the most between **LD03** (thiophene) and **LD04** (furan) with about 55% more **LD03** (thiophene) in the devices, yet despite the higher dye loadings for the thiophene based dye, the furan-based dye still has a higher photocurrent, photovoltage, and electron lifetime within DSC devices. This highlights that the factors controlling the recombination rate for these systems is certainly more than just a simple surface blocking model dominated by dye loadings. These observations further suggest that the halogen bonding of S to I_2 is a primary factor in the uniformly lower V_{oc} and J_{sc} values of thiophene dyes relative to furan.

CONCLUSION

Overall, evidence for stronger binding of I_2 to thiophene containing dyes versus furan containing dyes is observed. Raman spectroscopy on TiO_2 surface bound dyes shows a much more dramatic change in the intensity and shifting of vibrational peaks in the presence of iodine for thiophene-based dyes **LD03** and **D35** relative to the furan-based analogues **LD04** and **AB3**, respectively. UV-Vis analysis again lends evidence of I_2 binding **LD03** (thiophene) and **D35** (thiophene) on TiO_2 showing a red shift in the λ_{max}. Indirect evidence of I_2 binding could be seen for **AB1** (thiophene) and **AB2** (furan) where device V_{oc} and J_{sc} measurements show a higher value for the furan-based dye despite identical dye

loadings. This suggests a lower recombination rate which was confirmed via electron lifetime studies through small modulated photovoltage transient measurements for **AB1** and **AB2**. IPCE measurements also showed a red-shift and decrease in IPCE for thiophene based dyes **AB1** and **D35** similar to the addition of an electron withdrawing group, hinting toward the coordination of I_2 to sulfur lowering the LUMO energy. Computational studies lend further evidence to these experimental observations as the thiophene based dyes **AB1** and **D35** were both found to have a stronger influence from an I_2 binding mode at the sulfur atom of thiophene than at the oxygen atom of furan for **AB2** and **AB3**, respectively. TD-DFT results reveal that the thiophene based dyes more readily transfer electron density (have a higher oscillator strength) from the dye to I_2 via the HOMO centered on the dye and LUMO centered on I_2. The oscillator strengths were significantly lower for the analogues charge transfer event with furan-based dyes. This study shows substantial evidence for I_2 binding to the sulfur atoms of thiophene which means dyes should be carefully designed to reduce S and I_2 interactions near the TiO_2 surface for higher device performances.

EXPERIMENTAL

General Experimental Details. All commercially obtained regents were used as received. 2',4'-dibutoxy-N-(2',4'-dibutoxy-[1,1'-biphenyl]-4-yl)-N-(4-(4,4,5,5-tetramethyl-1,3,2-dioxaborolan-2-yl)phenyl)-[1,1'-biphenyl]-4-amine and (*E*)-3-(5-(4-(bis(2',4'-dibutoxy-[1,1'-biphenyl]-4-yl)amino)phenyl)thiophen-2-yl)-2-cyanoacrylic acid (D35) were purchased from Dyenamo. 5-bromofuran-2-carbaldehyde was purchased from ArkPharm. Thin-layer chromatography (TLC) was conducted with Sorbtech silica XHL TLC plates and visualized with UV. Flash column chromatography was performed with

Sorbent Tech P60, 40-63 um (230-400 mesh). Reverse phase column chromatography was performed with Sorbent Tech C18 P60, 40-63 um (230-400 mesh). ^{1}H and ^{13}C NMR spectra were recorded on a Bruker Avance-300 (300 MHz) spectrometer and a Bruker Avance-500 (500 MHz) spectrometer and are reported in ppm using solvent as an internal standard ($CDCl_3$ at 7.26 and Acetone-d_6 at 2.09). Data reported as s = singlet, d = doublet, t = triplet, q = quartet, p = pentet, m = multiplet, br = broad, ap = apparent, dd = doublet of doublets; coupling constant(s) in Hz. UV spectra were measured with a Cary 5000 UV-Vis-NIR spectrometer with either dichloromethane or 0.1 M Bu_4NOH in DMF solution. Cyclic voltammetry curves were measured with a C-H Instruments electrochemical analyzer CHI600E. (*E*)-3-(5'-(4-(bis(2',4'-dibutoxy-[1,1'-biphenyl]-4-yl)amino)phenyl)-[2,2'-bithiophen]-5-yl)-2-cyanoacrylic acid (AB1), (*E*)-2-cyano-3-(5-(4-(hexyloxy)phenyl)thiophen-2-yl)acrylic acid (LD03) and (*E*)-2-cyano-3-(5-(4-(hexyloxy)phenyl)furan-2-yl)acrylic acid (LD04) were synthesized according to literature procedures.[134,135]

Raman Experimental Details. A Horiba Scientific LabRAM HR Evolution Raman Spectroscopy system was used for the acquisition of Raman spectra. The 633 nm line from a HeNe laser was focused onto solid samples using a 100x objective with a 0.9 NA and a 1800 grooves/mm grating and CCD camera were used for detection.

Computational Details. All geometry optimization and binding energy calculations were completed with Gaussian 16 package.[139] *w*B97XD functional[140] was used to include long-range corrections with D2 dispersion model.[141] Tight optimization criteria were used for both force and density matrix convergence along with ultrafine grid for numerical integration. We used a 6-31+G* basis set for all atoms except for I, where we used

LANL2DZdp[142,143] basis set and associated effective core potential. Each dye molecules consists of two different configurations; *cis*- and *trans*-, which are defined as whether the S (for thiophene ring) and O (for furan ring) were on the same or on the different side of N (for nitrile functional group). For the binding energy calculations, 5 (five) different sites were considered for **AB1** and **AB2**; however, in case of **AB3** and **D35**, 4 (four) different sites were considered. In each of these sites, the I_2 molecule was placed at 4 different locations around the considered sites to account for the variations in binding energy. Frequency calculations indicate all geometries are in their corresponding local minima's.

SYNTHETIC PROTOCOLS

5-(5-(4-(bis(2',4'-dibutoxy-[1,1'-biphenyl]-4-yl)amino)phenyl)thiophen-2-yl)furan-3-carbaldehyde: In a 8.0 mL glass vial, 2',4'-dibutoxy-*N*-(2',4'-dibutoxy-[1,1'-biphenyl]-4-yl)-*N*-(4-(4,4,5,5-tetramethyl-1,3,2-dioxaborolan-2-yl)phenyl)-[1,1'-biphenyl]-4-amine (75 mg, 0.092 mmol), 5-(5-bromothiophen-2-yl)furan-2-carbaldehyde[144] (22 mg, 0.084 mmol) and potassium phosphate (53 mg, 0.25 mmol) were dissolved in 1.68 mL of toluene and 0.073 mL of water. The solution was then degassed for about 10 minutes under nitrogen, after which $Pd_2(dba)_3$ (3.0 mg, 0.003 mmol) and XPhos (6.0 mg, 0.013 mmol) were added together. The reaction was then sealed, and brought to 80 ^oC for 15 hours. The reaction was then removed from heat and cooled to room temperature. The mixture was then extracted with ethyl acetate and water and dried with magnesium sulfate. The crude product was purified with silica gel chromatography with a gradient from 10% ethyl acetate/hexanes to 20% ethyl acetate/hexanes (0.076 g; 95% yield). ^1H NMR (500 MHz, Acetone-d_6) δ 9.66 (s, 1H), 7.71 (d, *J* = 8.7 Hz, 2H), 7.66 (d, *J* = 3.9 Hz, 1H), 7.60-7.55 (m, 5H), 7.51 (d, *J* = 3.9 Hz, 1H), 7.32 (d, *J* = 8.4 Hz, 2H), 7.21 (d, *J* = 8.6 Hz, 4H), 7.18 (d, *J*

= 8.7 Hz, 2H), 7.03 (d, *J* = 3.8 Hz, 1H), 6.68 (d, *J* = 2.3 Hz, 2H), 6.64 (dd, *J* = 2.4, 2.4 Hz, 2H), 4.13-4.04 (m, 8H), 1.85-1.73 (m, 8H), 1.62-1.46 (m, 8H), and 1.05-0.95 (m, 12H) ppm. ^{13}C NMR (500 MHz, $CDCl_3$) δ 176.9, 159.7, 157.1, 155.2, 151.5, 148.4, 147.1, 145.5, 133.7, 131.0, 130.4, 129.4, 127.5 (appears broad, assumed 2 signals), 126.9, 126.7, 124.3, 123.3, 123.1, 123.0, 107.3, 105.4, 100.6, 68.3, 67.9, 31.5, 31.3, 19.5, 19.4, 14.0, and 14.0 ppm. IR (neat) ν = 3190, 3073, 3030, 2955, 2926, 2868, 2330, 2117, 1730, 1670, 1599 cm^{-1}. HRMS *m/z* calc'd for $C_{55}H_{59}NO_6SCs$ $[M + Cs]^+$: calculated 994.3118, found 994.3125.

(E)-3-(5-(5-(4-(bis(2',4'-dibutoxy-[1,1'-biphenyl]-4 yl)amino)phenyl)thiophen-2-yl)furan-3-yl)-2-cyanoacrylic acid (AB2): In a 8 mL vial, compound 5-(5-(4-(bis(2',4'-dibutoxy-[1,1'-biphenyl]-4-yl)amino)phenyl)thiophen-2-yl)furan-3-carbaldehyde (0.040 g, 0.047 mmol) was dissolved in 0.94 mL chloroform. The mixture was then degassed with N_2 for approximately 30 minutes. Cyanoacetic acid (0.012 g, 0.14 mmol) and piperidine (0.032 mL, 0.33 mmol) were added to vial, which was then sealed, heated to 90 °C and allowed to stir for 16 hours. The reaction mixture was diluted with dichloromethane and purified through a plug of silica gel with 100% dichloromethane to 10% methanol/dichloromethane to 12% methanol/3% acetic acid/dichloromethane. The solvent of the third fraction was evaporated under reduced pressure. The dye was then extracted with hexanes and water to give the final dye (**AB2**, 0.040 g, 91% yield). ^{1}H NMR (500 MHz, Acetone-d_6) δ 8.07 (s, 1H), 7.73-7.69 (m, 4H), 7.57 (d, *J* = 8.6 Hz, 4H), 7.55 (d, *J* = 3.9 Hz, 1H), 7.32 (d, *J* = 8.4 Hz, 2H), 7.22-7.17 (m, 6H), 7.11 (d, *J* = 3.7 Hz, 1H), 6.69 (d, *J* = 2.3 Hz, 2H), 6.64 (dd, *J* = 2.4, 2.4 Hz, 2H), 4.11-4.00 (m, 8H), 1.85-1.70 (m, 8H), 1.60-1.46 (m, 8H), and 1.05-0.95 (m, 12H) ppm. IR (neat) ν = 3050, 2952, 2924, 2854, 2360,

2340, 1699, 1602 cm^{-1}. ESI HRMS *m/z* calc'd for $C_{58}H_{59}N_2O_7S$ $[M - H]^-$: calculated 927.4043, found 927.4072.

5-(4-(bis(2',4'-dibutoxy-[1,1'-biphenyl]-4-yl)amino)phenyl)furan-2-carbaldehyde: In a 8.0 mL glass vial, 2',4'-dibutoxy-*N*-(2',4'-dibutoxy-[1,1'-biphenyl]-4-yl)-*N*-(4-(4,4,5,5-tetramethyl-1,3,2-dioxaborolan-2-yl)phenyl)-[1,1'-biphenyl]-4-amine (100 mg, 0.12 mmol), 5-bromofuran-2-carbaldehyde (20 mg, 0.11 mmol) and potassium phosphate (71 mg, 0.34 mmol) were dissolved in 2.24 mL of toluene and 0.097 mL of water. The solution was then degassed for about 10 minutes under nitrogen, after which $Pd_2(dba)_3$ (4.0 mg, 0.005 mmol) and XPhos (8.5 mg, 0.018 mmol) were added together. The reaction was then sealed, and brought to 80°C for 15 hours. The reaction was then removed from heat and cooled to room temperature. The mixture was then extracted with ethyl acetate and water and dried with magnesium sulfate. The crude product was purified with silica gel chromatography with 10% ethyl acetate/hexanes (0.092 g; 96% yield). ^{1}H NMR (500 MHz, $CDCl_3$) δ 9.59 (s, 1H), 7.67 (d, *J* = 8.9 Hz, 2H), 7.47 (d, *J* = 8.6 Hz, 4H), 7.30 (d, *J* = 3.8 Hz, 1H), 7.28 (s, 2H), 7.20-7.10 (m, 6H), 6.71 (d, *J* = 3.7 Hz, 1H), 6.65-6,45 (m, 4H), 4.05-3.85 (m, 8H), 1.85-1.70 (m, 8H), 1.50-1.45 (m, 8H), 1.05-0.90 (m, 12H) ppm.^{13}C NMR (500 MHz, $CDCl_3$) δ 177.1, 160.4, 160.0, 157.3, 151.9, 149.8, 145.3, 134.4, 131.2 (signal appears larger than expected, assumed 2 signals), 130.7, 126.7, 124.9, 123.1, 122.4, 122.1, 106.6, 105.7, 100.8, 68.5, 68.1, 31.7, 31.5, 19.7, 19.6, 14.2, 14.2 ppm. IR (neat) ν = 3200, 3037, 2957, 2931, 2870, 2360, 2333, 2115, 1672, 1602, 1600 cm^{-1}. ESI HRMS *m/z* calc'd for $C_{51}H_{57}NO_6Cs$ $[M + Cs]^+$: calculated 912.3240, found 912.3235.

(E)-3-(5-(4-(bis(2',4'-dibutoxy-[1,1'-biphenyl]-4-yl)amino)phenyl)furan-2-yl)-2-cyanoacrylic acid (AB3): In a 8.0 mL vial, 5-(4-(bis(2',4'-dibutoxy-[1,1'-biphenyl]-4-

yl)amino)phenyl)furan-2-carbaldehyde (0.056 g, 0.072 mmol) was dissolved in 1.50 mL chloroform. The mixture was then degassed with N_2 for approximately 30 minutes. Cyanoacetic acid (0.018 g, 0.217 mmol) and piperidine (0.050 mL, 0.507 mmol) were added to vial, which was then sealed, heated to 90°C and allowed to stir for 16 hours. The reaction mixture was diluted with dichloromethane and purified through a plug of silica gel with 100% dichloromethane to 10% methanol/dichloromethane to 12% methanol/3% acetic acid/dichloromethane. The solvent of the third fraction was evaporated under reduced pressure. The dye was then extracted with hexanes and water to give **AB3** with trace impurities. The product was then purified using reverse phase column chromatography with a gradient from 10% methanol/acetonitrile to 50% methanol/acetonitrile, then with a CombiFlash R_f^+ chromatography system (RediSep R_f Gold high performance silica gel, 0% methanol/dichloromethane → 10% methanol/dichloromethane) to give the final pure dye (0.014 g, 23%). ^{1}H NMR (500 MHz, $CDCl_3$) δ7.94 (s, 1H), 7.72 (d, *J* = 8.8 Hz, 2H), 7.47 (d, *J* = 8.7 Hz, 4H), 7.28-7.25 (m, 3H), 7.21-7.16 (m, 6H), 6.81 (d, *J* = 3.8 Hz, 1H), 6.60-6.52 (m, 4H), 4.05-3.95 (m, 8H), 1.85-1.70 (m, 8H), 1.50-1.45 (m, 8H), 1.05-0.90 (m, 12H) ppm. IR (neat) ν = 3340, 2944, 2923, 2854, 2333, 2114, 1602, 1593 cm^{-1}. ESI HRMS *m/z* calc'd for $C_{54}H_{59}N_2O_7$ $[M + H]^+$: calculated 847.4323, found 847.4347.

Photovoltaic Device Characterization. Photovoltaic characteristics were measured using a 150 W xenon lamp (Model SF150B, SCIENCETECH Inc. Class ABA) solar simulator equipped with an AM 1.5 G filter for a less than 2% spectral mismatch. Prior to each measurement, the solar simulator output was calibrated with a KG5 filtered mono-crystalline silicon NREL calibrated reference cell from ABET Technologies (Model 15150-KG5). The current density-voltage characteristic of each cell was obtained with a

Keithley digital source-meter (Model 2400). The incident photon-to-current conversion efficiency was measured with an IPCE instrument manufactured by Dyenamo comprised of a 175 W xenon lamp (CERMAX, Model LX175F), monochromator (Spectral Products, Model CM110, Czerny-Turner, dual-grating), filter wheel (Spectral Products, Model AB301T, fitted with filter AB3044 [440 nm high pass] and filter AB3051 [510 nm high pass]), a calibrated UV-enhanced silicon photodiode reference and Dyenamo issued software.

Photovoltaic Device Fabrication. For the photoanode, TEC 10 glass was purchased from Hartford Glass. Once cut into 2x2 cm squares, the substrate was submerged in a 0.2% Deconex 21 aqueous solution and sonicated for 15 minutes at room temperature. The electrodes were rinsed with water and sonicated in acetone 10 minutes followed by sonication in ethanol for 10 minutes. Finally, the electrodes were placed under UV/ozone for 15 minutes (UV-Ozone Cleaning System, Model ProCleaner by UVFAB Systems). A compact TiO_2 underlayer is then applied by treatment of the substrate submerged in a 40 mM $TiCl_4$ solution in water (prepared from 99.9% $TiCl_4$ between 0-5^oC). The submerged substrates (conductive side up) were heated for 30 minutes at 70^oC. After heating, the substrates were rinsed first with water then with ethanol. The photoanode consists of thin TiO_2 electrodes comprised of a 10 μm mesoporous TiO_2 layer (particle size: 20 nm, Dyesol, DSL 18NR-T) for iodine cells with a 5 μm TiO_2 scattering layer (particle size: >100 nm, Solaronix R/SP). Both layers were screen printed from a Sefar screen (54/137–64W) resulting in 5 μm thickness for each print. Between each print, the substrate was heated for 7 minutes at 125^oC and the thickness was measured with a profilometer (Alpha-Step D-500 KLA Tencor). The substrate was then sintered with progressive heating from 125^oC (5

minute ramp from r.t., 5 minute hold) to 325°C (15 minute ramp from 125°C, 5 minute hold) to 375°C (5 minute ramp from 325°C, 5 minute hold) to 450°C (5 minute ramp from 375°C, 15 minute hold) to 500°C (5 minute ramp from 450°C, 15 minute hold) using a programmable furnace (Vulcan® 3-Series Model 3-550). The cooled, sintered photoanode was soaked 30 minutes at 70°C in a 40 mM $TiCl_4$ water solution and heated again at 500°C for 30 minutes prior to sensitization. The complete working electrode was prepared by immersing the TiO_2 film into the dye solution for 16 hours. The solution for all the dyes consists of 0.3 mM dye, with 40x of CDCA (chenodeoxycholic acid) (i.e. 40:1, CDCA:dye ratio) in (4:1) EtOH:THF. For preparing the counter electrode, 2x2 cm squares of TEC 7 FTO glass were drilled using Dremel-4000 with a Dremel 7134 Diamond Taper Point Bit from the back side to a taped FTO side. After the tape was removed, the electrodes were washed with water followed by a 0.1 M HCl in EtOH wash and sonication in acetone bath for 10 minutes. The washed electrodes were then dried at 400°C for 15 minutes. A thin layer of Pt-paste (Solaronix, Platisol T/SP) on TCO was slot printed though a punched tape and the printed electrodes were then cured at 450°C for 10 minutes. After allowing them to cool to room temperature, the working electrodes were then sealed with a 25 μm thick hot melt film (Meltonix 1170-25, Solaronix) by heating the system at 130°C under 0.2 psi pressure for 1 minute. Devices were completed by filling the electrolyte through the pre-drilled holes in the counter electrodes and finally the holes were sealed with a Meltonix 1170-25 circle and a thin glass cover slip by heating at 130°C under pressure 0.1psi for 25 seconds. Finally, soldered contacts were added with a MBR Ultrasonic soldering machine (model USS-9210) with solder alloy (Cerasolzer wire dia 1.6mm item # CS186-150). A

circular black mask (active area 0.15 cm^2) punched from black tape was used in the subsequent photovoltaic studies.

Electron Lifetime Measurements. Electron lifetime measurements via small modulated photovoltage transient measurements, were carried out with a Dyenamo Toolbox (DN-AE01) instrument and software. The intensity of the LED light source (Seoul Semiconductors, Natural White, S42182H, 450 to 750 nm emission) is varied to modulate the device open-circuit voltage. The biased light intensity was modulated by applied voltages of 2.80, 2.85, 2.90, 2.95, and 3.00 V applied to the LED with the 3.0 V bias approaching 1 sun intensity (97%). The direction of illumination was from the photoanode to the counter electrode, and the device was positioned 5 cm from the LED light source. The voltage rise and decay times are fitted with a Levenberg-Marquardt fitting algorithm via LabView, and the electron lifetime was obtained from the averaging of rise and decay time.

CHAPTER 6

6.1 QUINOXALINE-BASED DUAL DONOR, DUAL ACCEPTOR ORGANIC DYES FOR DYE-SENSITIZED SOLAR CELSS

Adithya Peddapuram,; Hammad Cheema,; Louis E. McNamara,; **Yanbing Zhang,**; Nathan I. Hammer,; Delcamp, J. H. *Appl. Sci*. **2018**, *8*, 1421. Adapted from permission of the MDPI

(See appendix for permission license.)

This is a collaborative project with Dr. Hammer group. Adithya Paddapuram is in charge of the synthesis and characterizing of all the dyes, Hammad Chemma and Yanbing Zhang measured all the photovoltaic data from Dr.Delcamp's group. Louis E. McNamara performed all excited-state fluorescence lifetime measurements and calculated electron injection efficiencies for all target molecules from Dr. Hammer's group.

ABSTRACT

A novel metal-free quinoxaline-based molecular framework with a dual donor and dual acceptor (DD-π-AA) motif has been introduced. Four sensitizers (**AP6**, **AP8**, **AP9**, and **AP12**) have been synthesized and fully characterized via UV–Vis absorption, cyclic voltammetry, density functional theory (DFT) calculations, time-correlated single photon counting (TCSPC), and in dye-sensitized solar cell (DSC) devices. Structural modifications to both the donor and acceptor/anchor

regions were evaluated via structure–property relationships without altering the quinoxaline π-bridge. Through careful dye design, a broadly absorbing near-infrared (NIR) sensitizer extending electricity production to 800 nm is realized in DSC devices. Ground- and excited-state oxidation potentials were measured to show energetically favorable charge transfer events. Importantly, the dye structure was found to have a strong influence on dye energetics in different environments with structural elements allowing for either similar or dramatically different solution versus film measurements. The DSC device electrolyte was also found to have a significant influence on dye energetics as well. Electron transfer events were probed for each dye with DSC device measurements and with TCSPC studies. The results are correlated to the dye structures.

INTRODUCTION

Dye-sensitized solar cells (DSCs) remain a promising and intensely studied area of research after two decades of exploration.[1,62-63,71,102–104,107,142–146] In typical n-type DSC devices, dye molecules are first photoexcited followed by the transfer of electrons to the conduction band (CB) of TiO_2. The electrons then traverse an external circuit before travelling back to the oxidized dye via a redox shuttle after collection at a counter electrode. The dye is one of the most important components of DSC devices for determining which photon energies are useable. Broad UV–Vis–near-infrared (NIR) absorption properties are crucial for realizing the highest efficiency DSC devices possible.[87] A DSC device employing organic dyes surpassing 14% power conversion efficiency (PCE) has been reported owing to well-positioned energy levels, high extinction coefficients, and strong binding properties.[6] However, in order to further improve DSC device performances, dyes with NIR absorption (>750 nm) are required. In this work, structure–property relationships of quinoxaline-based dual donor and dual acceptor (DD-π-AA) dyes are explored with absorptions extending to 800 nm.

Donor-π bridge-acceptor (D-π-A) and D-A′-π-A (where A′ is an auxiliary acceptor) dye constructs have become increasingly popular in DSC research.[1,73,104,150,151] Fueled by PCEs in excess of 13%, this direction remains heavily pursued.[4,6,152] Additionally, tightly bound anchors are crucial in achieving higher efficiencies, because they allow co-sensitization and co-deposition of insulators to facilitate panchromatic absorption and to protect against the transfer of electrons from the TiO_2 CB to the oxidized redox shuttle (recombination), respectively. As a key example, **ADEKA-1**-based devices have used these strategies to set the current record for DSC device efficiency at 14.3%.[6]

The silanol anchoring group is regarded as both one of the strongest anchoring groups, with efficient electron transfers to TiO_2, and as a very challenging functional group to synthesize and employ in devices.[153] In this regard, sensitizers with panchromatic absorption and strong binding through multiple carboxylic acid anchors, such as with the DD-π-AA design, are highly attractive.[154] Quinoxaline-based dyes employing the DD-π-AA molecular framework have demonstrated broad absorptions and TiO_2 dissociation rates up to 180 times slower than dyes employing a traditional D-π-A structure.[155] Thienopyrazine (TPz)-based DD-π-AA dye, **AP3**, has shown a PCE of 5.5% (>10% under low light when co-sensitized) with panchromatic absorption.[72,156] Energetically, the PCE of devices made with **AP3** could be increased by destabilizing the low-energy excited-state to facilitate faster electron injection into the TiO_2 CB by forgoing the need for excessive lithium iodide (LiI), which is known to lower DSC device photovoltages.[156] We reasoned that the use of a benzene in place of the thiophene group of TPz could broaden the dye optical energy gap enough to raise the dye excited-state energy without fully sacrificing panchromatic absorption properties.[157–159] Dyes **AP6**, **AP8**, **AP9**, and **AP12** were selected as target dyes, which vary at the donor and acceptor regions. **AP6** and **AP8** have been

previously reported to have strong binding to TiO_2 and only differ at the dual carboxylic acid anchors, with **AP6** having a phenyl space between the anchors and the quinoxaline group (Figure 36).[155] Both **AP6** and **AP8** had yet to be evaluated in DSC devices prior to this study, and both dyes require photons higher in energy than are present in the NIR region. Dye designs strategies for overcoming this limited absorption focus on extending conjugation, planarization of the π-conjugated system, and the increasing of the electron-donating/accepting group strengths. **AP9** directly compares to **AP8** with the addition of a thiophene spacer between the triphenyl amine (TPA) donors and the quinoxaline π-bridge. The added thiophene groups are selected to increase conjugation and to minimize the dihedral angle between the quinoxaline and donor region for efficient electron transfer from donor to acceptor upon photoexcitation. **AP12** compares to **AP6** with the same number of π-electrons in the conjugated dye system, but **AP12** differs in the planarization of the spacer groups between the carboxylic acids and at the quinoxaline π-bridge with the introduction of two nitrogen atoms in place of two C–H groups to reduce sterics at the TiO_2 surface. The planarization and introduction of two electron-accepting nitrogen groups is expected to broaden the absorption of **AP6**.

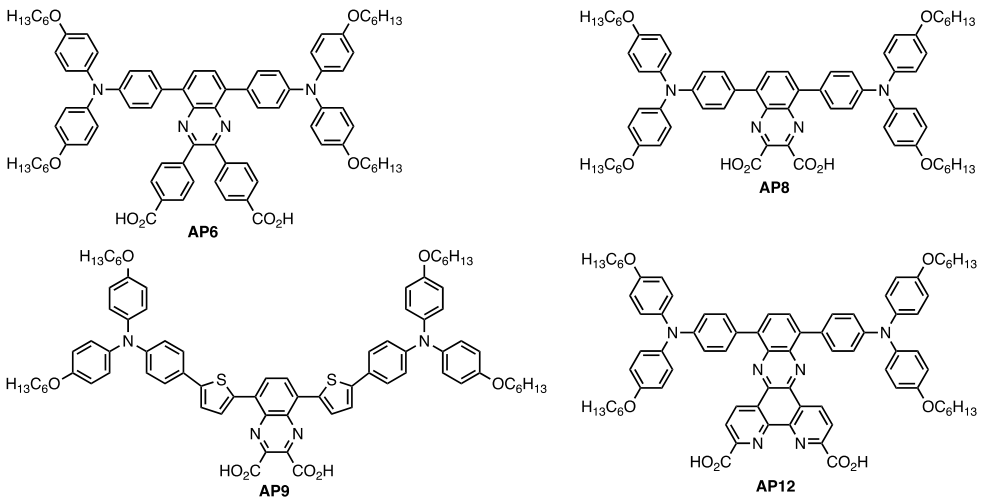

Figure 36. Target structures of **AP6**, **AP8**, **AP9**, and **AP12**.

Materials and Methods

Known Synthetic Intermediates

Diethyl 5,8-dibromo-4*a*,8*a*-dihydroquinoxaline-2,3-dicarboxylate (**1**),[155] 4-(hexyloxy)-*N*-(4-(hexyloxy)phenyl)-*N*-(4-(5-(tributylstannyl)thiophen-2-yl)phenyl)aniline (**2**),[160] 4,7-dibromobenzo[*c*][1,2,5]thiadiazole (**4**),[161] 4-(hexyloxy)-*N*-(4-(hexyloxy)phenyl)-*N*-(4-(4,4,5,5-tetramethyl-1,3,2-dioxaborolan-2-yl)phenyl)aniline (**5**),[162] and diethyl 5,6-dioxo-5,6-dihydro-1,10-phenanthroline-2,9-dicarboxylate (**8**)[163] were synthesized according to literature procedures (Scheme 4).

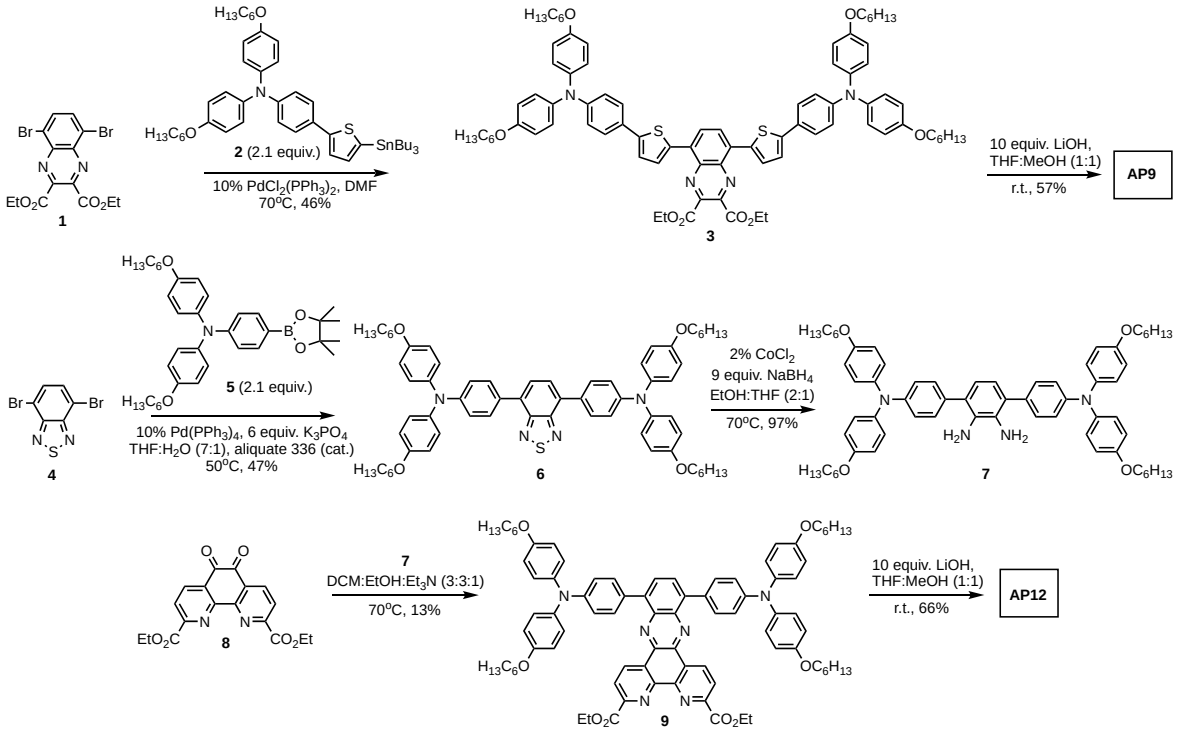

Scheme 4. Synthetic route to target dyes **AP9** and **AP12.**

RESULT AND DISCUSSION

*3.1. **AP9** and **AP12** Synthesis Discussion*

AP6 and **AP8** were synthesized according to the literature.[155] **AP9** was synthesized beginning with a Stille coupling of diester intermediate **1** with TPA-thiophene tin reagent **2** to give the diester precursor to **AP9** in 46% yield (Scheme 4, Figure 53 and 54 in Appendix). Basic hydrolysis of **3** with LiOH afforded **AP9** in high yield in two steps from known materials (Figure 55 in Appendix). The synthesis of **AP12** began with a Suzuki coupling of a TPA-boronic ester derivative (**5**) with dibromobenzothiadiazole **4** to give a *bis*TPA substituted benzothiadiazole derivative **6** in good yield (Figure 56 and 57 in Appendix). A sodium borohydride reduction of **6** yielded *bis*TPA-substituted phenyl diamine **7** in excellent yield (Figure 58 in Appendix). Upon condensation of **7** with known dione diester intermediate **8**, the diester precursor to **AP12** was synthesized (Figure 59 and 60 in Appendix). This diester intermediate **9** underwent basic hydrolysis to give the desired **AP12** dye (Figure 61 in Appendix).

3.2. UV–Vis Absorption Properties

After synthesis, the dyes were first evaluated by UV–Vis absorption spectroscopy to analyze the effects each structural modification had on the dye optical energy gaps (Figure 36, Table 10). All four dyes showed a single, broad charge transfer absorption band as the lowest energy transition in solution. Absorption maxima values were observed in the following order **AP6** < **AP8** < **AP9** ≈ **AP12** in dichloromethane (479, 531, 590, and 588 nm, respectively). While the absorption maxima of **AP9** and **AP12** were similar in energy, the absorption onset values varied significantly due to a broader absorption from **AP9** in solution. Because DSC devices typically produce electricity until a dye onset, these values are more representative of the energies relevant

to DSC devices. The dye λ_{onset} values were estimated from both solution measurements in dichloromethane (DCM) and on TiO_2 films. The comparison with TiO_2 films is critical for dual anchor dyes, because the carboxylic acid is part of the charge transfer system, and the carboxylic acid conformation relative to the dye π-system can be dramatically affected by surface binding orientations.[72] **AP6** showed an absorption onset of 560 nm in DCM and only a slight red-shift on TiO_2 to 585 nm. The removal of the π-spacer phenyl groups between the quinoxaline and the carboxylic acids red-shifted the solution onset by 80 nm to give an onset of 640 nm for **AP8** in DCM. This red-shift was rationalized by the phenyl groups having significant steric influence on the dye conformation, which prohibited the carboxylic acids of **AP6** from being completely planar with the dye π-system as is needed for maximal influence on the charge transfer band. The carboxylic acid groups of **AP8** can access a completely planar orientation leading to a red-shift in absorption despite **AP8** having fewer π-electrons. Interestingly, **AP8** showed a 70 nm λ_{onset} blue-shift on TiO_2. We attributed this to a significantly different film conformation being accessed relative to that observed in the DCM solution, which was potentially due to both anchors binding the TiO_2 surface leading to a dye conformation with a reduced π-system overlap between the carboxylic acids and the quinoxaline group. This highlights the need for careful assessment of the dyes on TiO_2 films rather than just from the solution when estimating dye energetics, as the change in the dye optical energy gap was 240 mV for the case of **AP8**. This was a substantial change, especially at longer wavelengths as there is little room in this spectral region for non-ideal energetics.

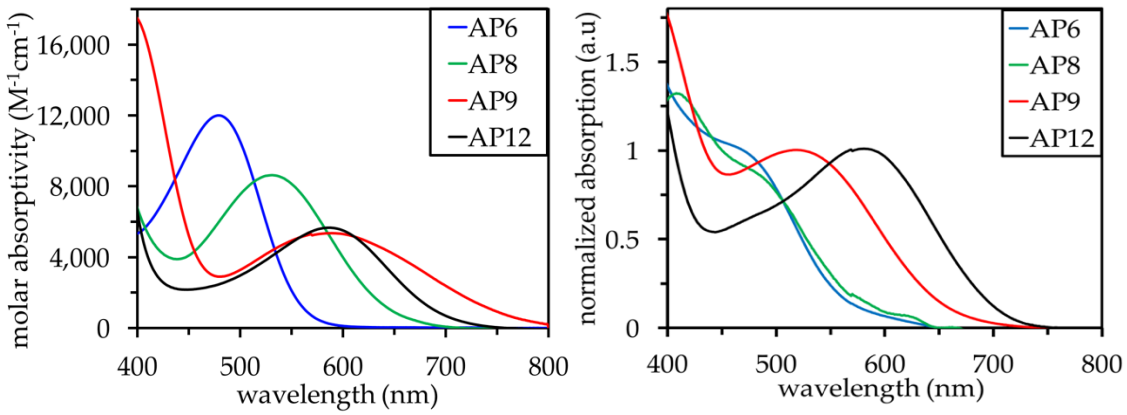

Figure 37. Molar absorptivities of **AP6**, **AP8**, **AP9**, and **AP12** in DCM and normalized absorption on TiO_2.

Table 10. Optical and electrochemical data of **AP6**, **AP8, AP9**, and **AP12**.

Absorbance Data [a]						Electrochemical Data				
Dye	**λ_{max} (nm)**	**λ_{onset}^{DCM} (nm)**	**$\lambda_{onset}^{TiO_2}$ (nm)**	**$IPCE_{onset}$ (nm)**	**ε (M^{-1} cm^{-1})**	**$E_{(S+/S)}$ DCM**	**E_g^{opt} (eV) [b]**	**$E_{(S+/S^*)}$ DCM [c]**	**$E_{(S+/S^*)}$ TiO_2 [c]**	**$E_{(S+/S^*)}$ IPCE [c]**
AP6	479	560	585	590	12,000	0.88	2.21	−1.33	−1.24	−1.22
AP8	531	640	570	675	8,000	0.90	1.94	−1.04	−1.28	−0.94
AP9	590	770	660	680	5,500	0.88	1.61	−0.73	−1.00	−0.94
AP12	588	720	720	800	5,600	0.89	1.72	−0.83	−0.83	−0.66

[a] Onset values are taken as the x-intercept of a downward tangent line on the absorption curves on the low-energy side; [b] Calculated from the equation $E_g^{opt} = 1240/\lambda_{onset}$; [c] Calculated from the equation $E_{(S+/S^*)} = E_{(S+/S)} - E_g^{opt}$.

AP9 showed a dramatic shift in the absorption curve onset in solution to 770 nm when compared with **AP8**, where the only difference in the two dyes was a thiophene spacer between the quinoxaline and TPA groups. This could be due to both extending the conjugation of the dye π-system and to reducing the steric interactions between the quinoxaline π-bridge and donor region

by the introduction of a 5-member ring at the quinoxaline bridge. The anchor group spacing is identical to that of **AP8**, and a significant shift in the absorption onset would again be expected on TiO_2. Indeed, a 110 nm blue-shift was observed for **AP9** on TiO_2. **AP12** compares most directly to **AP6**, and **AP12** had a solution absorption onset of 720 nm. This was a 160-nm red-shift in the absorption onset relative to **AP6**, where **AP12** differed by only the linking of the phenyl π-spacers between the quinoxaline and carboxylic acid to force planarity of this group and the addition of two nitrogen atoms to reduce sterics at the TiO_2 surface. Both changes likely influenced the absorption onset. Because the anchor spacing of **AP12** is similar to **AP6**, which did not show a significant shift of absorption onset on TiO_2 relative to in solution, no significant change was expected for **AP12** on the TiO_2 films. As predicted, the onset for **AP12** on TiO_2 was very similar to that in solution. Additionally, it is particularly noteworthy that all of these dyes suffered from poor molar absorptivities ranging from 12,000 to 5,500 M^{-1} cm^{-1}. **AP8**, **AP9**, and **AP12** all had molar absorptivities ≤8,000 M^{-1} cm^{-1}. Low molar absorptivities can be problematic in DSC devices.

3.3 *Electrochemical Properties*

For dyes to function efficiently in DSC devices, the dye energy levels should be thermodynamically well positioned relative to the TiO_2 CB for efficient electron injection and the redox shuttle for efficient dye regeneration. Thus, electrochemical measurements were carried out in dichloromethane solutions and on TiO_2 electrodes to evaluate the suitability of these dyes to work in DSC devices based on TiO_2 and I^-/I_3^-. The ground-state oxidation potentials ($E_{(S+/S)}$) of the dye should be lower in energy than the redox shuttle (0.35 V vs. normal hydrogen electrode (NHE)). All of the dyes had similar $E_{(S+/S)}$ values within 20 mV ranging from 0.88 to 0.90 V both in DCM and on TiO_2 (Table 10, Figures 38, and Figure 53, Appendix). Thus, all the dyes can

undergo thermodynamically favorable electron transfers from I^- to regenerate the neutral dye after electron injection into TiO_2. This suggests that despite the dye conformation change when the solution and film absorption spectrum were compared, no significant effect was seen for any of the dyes via the $E_{(S+/S)}$ value measurements. Therefore, all of the energetic changes with regard to the narrowing or widening of the optical energy gap on film relative to solution is due to changes in the excited-state oxidation potentials ($E_{(S+/S^*)}$). This observation is somewhat intuitive, because the $E_{(S+/S^*)}$ values are primarily controlled by the dye acceptor groups anchored to the TiO_2 surface.

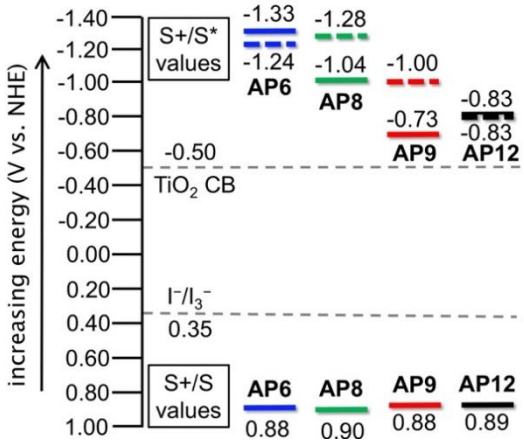

Figure 38. Energy level diagram for **AP6**, **AP8**, **AP9**, and **AP12** in DCM (solid bars) and on TiO_2 (dashed bars). The S+/S values change by <0.02 V on TiO_2 when compared with the solution values shown in the figure.

The $E_{(S+/S^*)}$ values were estimated via the equation $E_{(S+/S^*)} = E_{(S+/S)} - E_g^{opt}$ for the **AP** dyes both on TiO_2 and in solution. Because the dye structural modifications had little effect on the $E_{(S+/S)}$ values, and the dye E_g^{opt} values were found to vary broadly via UV–Vis spectroscopy in solution, a broad range of $E_{(S+/S^*)}$ values are observed for this series ranging from −0.73 to −1.33 V vs. NHE. All of these values indicate a thermodynamically favorable electron transfer to the TiO_2 CB from a photoexcited dye. **AP9** with thiophene spacers extending conjugation between the quinoxaline

and TPA groups was found to have the lowest energy $E_{(S+/S^*)}$ value of −0.73 V in DCM. The removal of the thiophene groups gave dye **AP8** an $E_{(S+/S^*)}$ value of −1.04 V. **AP12** with the planarized acceptor region gave the second lowest energy $E_{(S+/S^*)}$ value of −0.83 V, which was significantly lower than that of the non-planarized **AP6** (−1.33 V). Because film energetic values are more relevant to DSC devices, each of the dyes were energetically analyzed on TiO_2 films. On the TiO_2 films, the $E_{(S+/S^*)}$ values for **AP8** and **AP9** both upshifted significantly by ≥240 mV. This was likely due to the spacing of the dual anchors resulting in a dramatically different conformation on TiO_2 than in solution. Based on the energetic changes, a significant twist angle was introduced between the carboxylic acid and quinoxaline groups for these dyes on film relative to in solution. After this change in **AP9** energetics on TiO_2 compared with the solution measurements, **AP12** had the lowest energy excited-state on films, as no change was observed when solution and TiO_2 excited-states were compared. The modest-to-no change in excited-states for **AP6** and **AP12** on films compared with solution suggests a similar conformation in both environments indicating solution measurements were a reasonable approximation of energy levels for this dual anchor spacing in DSC devices. This observation has also been reported for thienopyrazine-based dual anchor DSC dyes with similar carboxylic acid anchor spacings, where the phenyl spacer-based systems showed similar solution and film energetics, while the dyes with no phenyl spacer showed significantly altered energetics on the TiO_2 films.[72] In all cases, the dye thermodynamics on film indicated that a facile electron transfer event to TiO_2 is possible.

3.4 Computational Analysis

In addition to thermodynamically favorable energy levels, molecular orbital positions are critical for facile, productive electron transfers in DSC devices. Ideally, the highest occupied molecular orbital (HOMO) of the dye should be located away from the TiO_2 surface to avoid back

electron transfers after electron injection, and the lowest unoccupied molecular orbital (LUMO) of the dye should be localized closer to the TiO_2 surface for efficient electron injection to TiO_2 after photoinduced intramolecular charge transfer (ICT). Density functional theory (DFT) calculations at the B3LYP/6-311G(*d,p*) level were carried out in Gaussian09 to visualize the frontier orbital distribution of the target structures.[164] The HOMO was found to be distributed across both donors on each dye with some presence on the quinoxaline benzene ring. This HOMO location is well positioned to be far from the TiO_2 surface, as desired. The LUMO was localized on the quinoxaline bridge and carboxylic acid anchors at the TiO_2 surface (Figure 38). The LUMO is ideally positioned for electron transfer to TiO_2. Significant HOMO–LUMO overlap was observed at the quinoxaline (primarily at the benzene ring), which shows the role of this group as a π-bridge. Thus, efficient ICT from donor to acceptor in the DD-π-AA molecular framework is possible, which is critical to absorbing lower energy light with reasonable molar absorptivities.

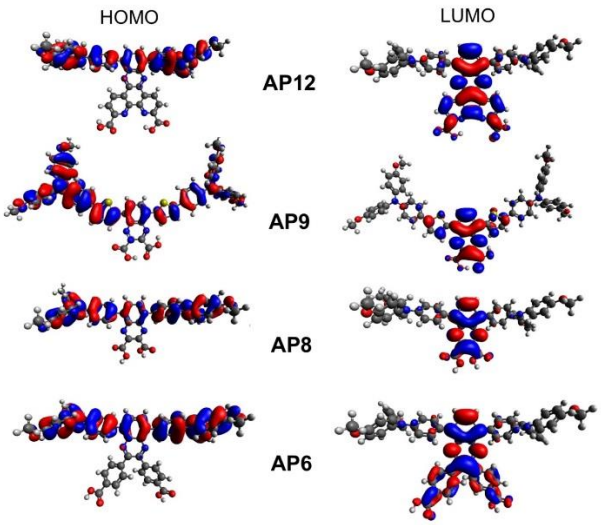

Figure 39. Frontier molecular orbital distributions of **AP6**, **AP8**, **AP9**, and **AP12**.

3.5 Photovoltaic Analysis

Based on optical, electrochemical, and computational data, all of the dyes studied can perform well in $I^-/I_3^-/TiO_2$-based DSCs. The devices were analyzed under AM 1.5 G incident solar simulation with PCEs calculated according to the equation, PCE = $(J_{SC} \times V_{OC} \times FF)/I_0$, where J_{SC} is the short-circuit current density, V_{OC} is the open-circuit voltage, *FF* is the fill factor, and I_0 is the incident light intensity equal to 1 sun in this study. The highest PCE of the series was measured for **AP6** at 3.7% with a J_{SC} value of 7.0 mA/cm^2 (Figure 40 and Table 11). **AP6** also had the highest observed *V*oc value of 694 mV, with the remaining dyes having very similar V_{OC} values of 591–615 mV, which also contributed to **AP6** showing the highest PCE of the series. **AP6**-based devices have the highest J_{SC} value for the series followed by **AP12** > **AP9** > **AP8**. Interestingly, the J_{SC} trend followed the same trend for absorption onsets on TiO_2, with the longest wavelength absorbing dyes producing the highest J_{SC} values except for **AP6**. **AP6** had the narrowest absorption of the series yet had the highest photocurrent in DSC devices. This was likely the result of a significantly higher molar absorptivity for **AP6** relative to the other dyes in the series. **AP6** also showed the highest peak incident photon-to-current conversion efficiency (IPCE) value of the dyes in this series at >70%. **AP8**, **AP9**, and **AP12** reached a peak IPCE of ~40%, which was roughly half that of **AP6**. This observation correlates to the observed molar absorptivities for **AP8**, **AP9**, and **AP12** being roughly half that of **AP6**. The J_{SC} values for **AP8**, **AP9**, and **AP12** ranged from 3.8 to 6.1 mA/cm^2, which was significantly closer to the J_{SC} value of **AP6** due to the broader absorption of these dyes. It is noteworthy that the broadest IPCE spectrum was observed for **AP12**, which reached 800 nm. Very few organic dyes produce electricity from such a low-energy wavelength.[66] Importantly, through this double donor, double anchor design strategy, the IPCE breadth can be increased relative to a more traditional D-A-π-A dye design using the same TPA

donor, quinoxaline auxiliary acceptor, thiophene π-bridge, and the stronger-accepting cyanoacrylic acid, and, for the case of **AP12**, the IPCE breadth exceeds that observed for even metal-based dyes such as **N719.**[165] Given this improvement on DSC device electricity production wavelength range and the observed slow desorption from TiO_2 surfaces for DD-π-AA structures (similar to dual anchors popularized with heteroleptic-Ru dyes), this organic design is attractive.[166,167] Molecular engineering strategies to improve the molar absorptivity are important to improve the peak IPCE value, and the focus of future designs should be on maintaining or extending this exceptional IPCE breadth. Interestingly, both **AP8** and **AP12** showed a dramatic red-shift in the IPCE onset relative to the film absorption on TiO_2 of ≥80 nm (Table 10). This change was likely due in part to the interaction of the dyes with the electrolyte, whereas if this were the result of a solid-state ordering on film (such as *J*-aggregates) this shift would have presented during the TiO_2 film absorption studies.[168] Accounting for these interactions energetically when rationally designing DSC dyes is not straightforward, but these interactions can have profound effects on dye energetics. Directly measuring how the electrolyte is affecting the dye energy levels is challenging; however, if the assumption that the dye $E_{(S+/S)}$ energy level remains unchanged, as it does when comparing solution and TiO_2 film measurements for these dyes, then the excited state energy levels are shifting dramatically upon the addition of the electrolyte. For example, in the case of **AP12**, a driving force for electron injection (ΔG_{inj}) into the TiO_2 CB of 330 mV is estimated from both solution and film measurements when the TiO_2 CB is taken as −0.50 V vs. NHE (Table 10). However, using the IPCE onset value to calculate the excited-state energy level of **AP12** gives a ΔG_{inj} value of only 160 mV. This lower ΔG_{inj} value could have a dramatic influence on electron injection efficiencies and may also contribute to lower peak IPCE values. *Methods to both predict and control dye energetics within a full DSC cell environment are critical to move toward rational*

dye design and away from pseudo-empirical dye design protocols where the energetics within a DSC device only mirror that of the solution or film estimates on an unpredictable case-by-case basis. The inability to directly account for the dye–electrolyte energetic changes has rendered a very promising broad absorbing dye (**AP12**) as estimated energetically from the solution and film measurements, low performing in DSC devices (2.9% PCE).

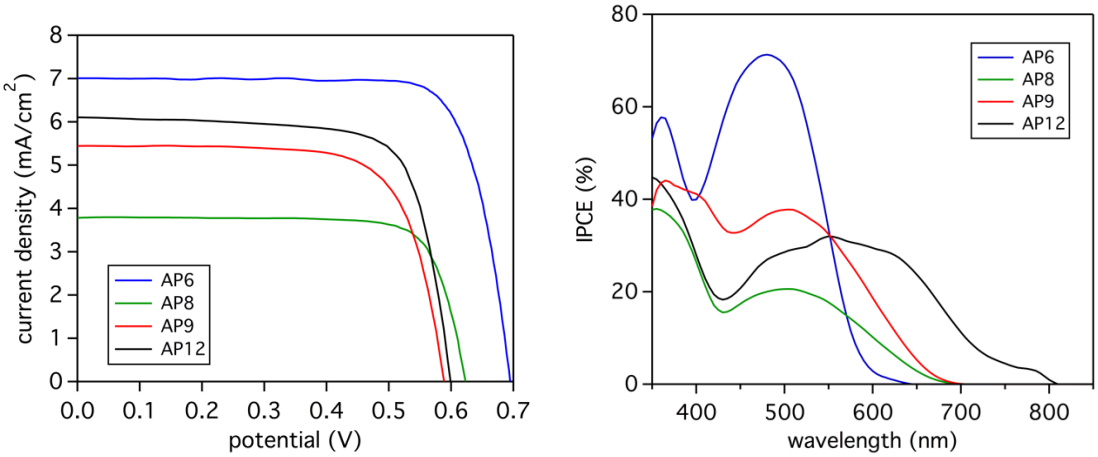

Figure 40. Left: *J*–*V* curves for DSC devices with **AP6**, **AP8**, **AP9**, and **AP12**. Right: IPCE curves for **AP6**, **AP8**, **AP9**, and **AP12**-based DSC devices.

Table 11. Summary of photovoltaic parameters for **AP** dyes.

Dye	J_{SC} (mA/cm^2)	V_{OC} (mV)	*FF*	PCE (%)
AP6	7.0	694	0.76	3.7
AP8	3.8	615	0.71	1.7
AP9	5.4	591	0.72	2.3
AP12	6.1	599	0.74	2.8

All devices were prepared with an I^-/I_3^- electrolyte comprised of 0.1 M guanidinium thiocyanate (GuNCS), 1.0 M 1,3-dimethylimidazolium iodide (DMII), 30 mM I_2, 0.5 M 4-*tert*butylpyridine (TBP), and 0.05 M lithium iodide (LiI) in acetonitrile/valeronitrile (85:15).

3.6 Time-Correlated Single Photon Counting (TCSPC) Studies

Electron injection efficiencies were estimated from time-correlated single photon counting (TCSPC) studies with **AP9** and **AP12** to compare with the reported values for **AP6** and **AP8.**[155] The experiments were conducted for each dye in DCM solution, on TiO_2, on TiO_2 with chenodeoxycholic acid (CDCA) as a deaggregating agent, and on TiO_2 with CDCA and LiI.[2,68,72] Due to the short excited-state lifetimes of the dyes in solution combined with instrument response function limitations (>150 ps timescale), injection efficiencies can only be reported as a lower limit and are likely faster than that reported. The equation $\eta_{eff} = 1 - (\tau_{TiO2}/\tau_{sol})$ is used to estimate the photoinduced dye electron injection efficiency to the TiO_2 CB where the overall efficiency (η_{eff}) is calculated based on the fluorescence decay lifetime (τ) of the dye in different environments. The solution lifetimes of the dyes ranged from 0.34 to 0.79 ns in the following order: **AP12** > **AP9** > **AP6** > **AP8** (Figure 6 and Table 3).

Table 12. Fluorescence lifetime and charge injection efficiencies of **AP6**, **AP8**, **AP9**, and **AP12** in different environments.

Dye	τ_{sol} (ns) [a]	τ_{TiO2} (ns) [b]	η_{eff} (%) [b]	τ_{TiO2} (ns)[c]	η_{eff} (%) [c]	τ_{TiO2} (ns) [d]	η_{eff} (%) [d]
AP6	0.38	0.30	29	0.29	24	<0.15	>61
AP8	0.34	0.29	27	0.27	21	<0.15	>54
AP9	0.77	0.44	42	0.32	58	<0.15	>80
AP12	0.79	0.55	30	0.25	68	<0.15	>81

[a] In dichloromethane (DCM); [b] On TiO_2; [c] On TiO_2 with chenodeoxycholic acid (CDCA); [d] On TiO_2 with CDCA and LiI.

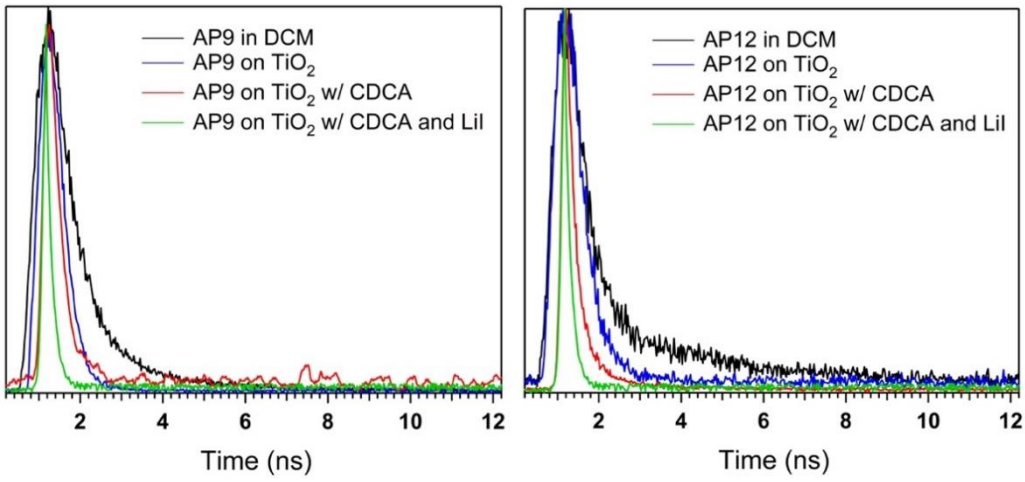

Figure 41. Fluorescence lifetimes of **AP9** and **AP12** in different environments.

The lifetimes of the π-extended **AP9** and the fused ring **AP12** were significantly longer than that of derivatives **AP8** and **AP6**, respectively (~0.78 ns vs. ~0.36 ns). On TiO_2 with no additives, an emission can still be observed, but lifetimes were shorter than observed in solution ranging from 0.29–0.55 ns with η_{eff} values of 27–42%. In this environment, **AP9** showed the highest injection efficiency, with **AP6** and **AP8** showing the lowest η_{eff} values of ~28%. The addition of the deaggregating agent CDCA to the dyeing solution resulted in significantly increased charge injection efficiencies for **AP9** and **AP12** from 42% to 58% and 30% to 68%, respectively. **AP6** and **AP8** remained relatively unchanged, which suggests these dyes have fewer dye–dye energy transfer pathways and excited-state deactivation pathways than **AP9** and **AP12**. **AP9** and **AP12** inject best in isolation from other dye molecules when the CDCA insulator is added. The addition of LiI resulted in fluorescence lifetimes shorter than the response function of the instrument, leading to the highest injection efficiencies observable for each dye ranging from >54% (**AP8**) to >81% (**AP12**). Given that the dye excited-state lifetimes exceeded the response time of the instrument with the LiI additive, no further additives were evaluated. This does suggest that the low peak IPCE observed for **AP12** was not due to electron injection into TiO_2 and was

more likely a combination of results from a low molar absorptivity and possibly a relatively slow regeneration event, as has been previously observed for DD-π-AA dyes.[72] However, the >81% electron injection efficiency from the novel **AP12** anchor/acceptor group with a very low driving force for electron transfer (160 mV) strongly suggests this group is valuable for the future design of NIR organic dyes for DSCs.

It is noteworthy that the excited-state lifetimes for the dyes evaluated in this series are short relative to typical D-π-A dye designs, which are often ≥1–2 ns. This may be an inherent limitation to the DD-π-AA design, as short lifetimes have also been observed for a thienopyrazine-based DD-π-AA dye **AP3** (0.36 ns in DCM).[72] However, **AP3** gave DSC devices with >10% PCE and >80% peak IPCE values in low light in the prior study. **AP6** also showed a reasonable peak IPCE of ~70% despite having one of the shortest excited-state lifetimes of the series. Thus, despite the short lifetimes, electron transfer to TiO_2 may still be facile.

CONCLUSIONS

Quinoxaline was successfully employed and studied as a π-bridge for four dyes using the dual donor, dual acceptor (DD-π-AA) construct. The effect of structural modifications was studied via UV–Vis absorption spectroscopy, electrochemical analysis, computational DFT analysis, TCSPC spectroscopy, and DSC device analysis. With this design, dyes could be rationally designed, which absorb light beyond 750 nm in solution. The evaluation of the dye energetics on film showed that the dye anchor spacing plays a critical role in the validity of using solution measurements to approximate dye–TiO_2 film energetics. The anchor group spacing using two benzoic acid groups *ortho* substituted on a 6-member ring provides a reliable group arrangement for rational dye energy level translation from solution to TiO_2 films. Additionally, the IPCE spectrum onset shifts dramatically in some cases further exacerbating the challenge of trying to

reliably predict dye energetics within a working DSC device regardless of if the estimates for dye energetics were made on film or in solution. **AP12** has the widest IPCE response reaching beyond 800 nm. This is an exceptional IPCE onset for an organic dye and was presumably due in part to dye–electrolyte interaction as the dye–TiO_2 absorption onset was 80 nm blue-shifted compared with the IPCE onset. TCSPC studies revealed short excited-states for all of the dyes in this series, but with the addition of Li ions, dye-emission became unobservable, indicating that electron transfer from the dye to TiO_2 upon photoexcitation was facile. These results suggest that the primary drawback for this dye design is the poor molar absorptivities, such as 5,600 M^{-1} cm^{-1} for **AP12**. Future dye designs will focus on bolstering the dye molar absorptivities while retaining good electron transfer kinetics with properly spaced dual anchor groups.

CHAPTER 7

7.1 OVERALL CONCLUSION

Dye-sensitized solar cells are being developed with the goal of replacing non-renewable energy sources such as coal or natural gas. The most intriguing parts of the DSCs are the tunable energy gap through optimizing the molecular structure and low cost of the application compared to the regular silicon solar cells. The research in this thesis is focused on the design and synthesis of organic molecules to extend the absorption range up to 800 nm or above while maintaining the desired energy level for the devices. **YZ7, YZ12, YZ14** and **YZ15** have been designed and synthesized based on the Ullazine structure which is a nitrogen containing peri-fused heterocyclic system with strong electron donating properties combined with a π-bridge and acceptor groups. All of these four dyes have a narrowed optical band by 140 mV to 240 mV compared to **JD21**, which has only donor-acceptor structure. The device data shows that **YZ7** has reached 5.6% power conversion efficiency with an IPCE onset of 800 nm and the current has increased relative to a comparison dye with up to 14.1 mA/cm^{-2} observed. Increasing the electron density on the linking π-bridge is another common strategy to extend the absorption range. **YZ11, YZ13, YZ16** and **YZ17** use a cross-conjugated phenyl group to optimize the optical gap instead of a linear conjugation method to increase the absorption range. The device data shows that these dyes have successfully red shifted UV-vis absorption 50 nm compared to a benchmark dye, **C218**, under the same condition. **YZ17** shows the highest efficiency at 7.6 % which is better than **C218** under the same condition. This project has opened a new strategy for organic dye design in extending the absorption range. Molecular recognition approaches are critical to low energy use systems, and

this work has analyzed devices using iodide/iodine as the redox shuttle system to probe rates of electron transfers within solar cell devices, finding that sulfur functionality near the inorganic interface in solar cells should be avoided. Many of these dyes have applications as NIR dyes for biological imaging detectors. The TPzPh series and TTD series discussed herein have been designed, synthesized, and have successfully shown absorption and emission window in the therapeutic window (700-1000 nm) while maintaining reasonable quantum yields. The strategy of applying strong acceptor and strong electron rich donor to tune the absorption and emission range is successfully shown in this study. The stability of the dyes is better than the clinically used indocyanine green (ICG) when exposed to the air.

LIST OF REFERENCES

REFERENCES

1. Hagfeldt, A., Boschloo, G., Sun, L., Kloo, L. & Pettersson, H. Dye-Sensitized Solar Cells. *Chem. Rev.* **110**, 6595–6663 (2010).
2. Zhang, Y. *et al.* Ullazine Donor–π bridge-Acceptor Organic Dyes for Dye-Sensitized Solar Cells. *Chem. – A Eur. J.* **24**, 5939–5949 (2018).
3. Chen, C.-Y. *et al.* Highly Efficient Light-Harvesting Ruthenium Sensitizer for Thin-Film Dye-Sensitized Solar Cells. *ACS Nano* **3**, 3103–3109 (2009).
4. Mathew, S. *et al.* Dye-sensitized solar cells with 13% efficiency achieved through the molecular engineering of porphyrin sensitizers. *Nat. Chem.* **6**, 242 (2014).
5. Kakiage, K. *et al.* An achievement of over 12 percent efficiency in an organic dye-sensitized solar cell. *Chem. Commun.* **50**, 6379–6381 (2014).
6. Kakiage, K. *et al.* Highly-efficient dye-sensitized solar cells with collaborative sensitization by silyl-anchor and carboxy-anchor dyes. *Chem. Commun.* **51**, 15894–15897 (2015).
7. Yao, Z. *et al.* Donor/Acceptor Indenoperylene Dye for Highly Efficient Organic Dye-Sensitized Solar Cells. *J. Am. Chem. Soc.* **137**, 3799–3802 (2015).
8. Wang, H. *et al.* Kinetics of electron recombination of dye-sensitized solar cells based on TiO2 nanorod arrays sensitized with different dyes. *Phys. Chem. Chem. Phys.* **13**, 17359–17366 (2011).
9. Zhang, Y. *et al.* Panchromatic cross-conjugated π-bridge NIR dyes for DSCs. *Phys. Chem. Chem. Phys.* **20**, 2438–2443 (2018).
10. Zhang, Y. *et al.* Near-Infrared Fluorescent Thienothiadiazole Dyes with Large Stokes Shifts and High Photostability. *J. Org. Chem.* **82**, 5597–5606 (2017).
11. Keereweer, S. *et al.* Optical Image-Guided Cancer Surgery: Challenges and Limitations. *Clin. Cancer Res.* **19**, 3745–3754 (2013).
12. Pretel, H., Lizarelli, R. F. Z. & Ramalho, L. T. O. Effect of low-level laser therapy on bone repair: Histological study in rats. *Lasers Surg. Med.* **39**, 788–796 (2007).
13. Smith, A. M., Mancini, M. C. & Nie, S. Bioimaging: second window for in vivo imaging. *Nat. Nanotechnol.* **4**, 710–711 (2009).
14. Guo, Z., Park, S., Yoon, J. & Shin, I. Recent progress in the development of near-infrared fluorescent probes for bioimaging applications. *Chem. Soc. Rev.* **43**, 16–29 (2014).
15. Yi, X., Wang, F., Qin, W., Yang, X. & Yuan, J. Near-infrared fluorescent probes in cancer imaging and therapy: an emerging field. *Int. J. Nanomedicine* **9**, 1347–1365 (2014).
16. Nani, R. R., Shaum, J. B., Gorka, A. P. & Schnermann, M. J. Electrophile-Integrating Smiles Rearrangement Provides Previously Inaccessible C4′-O-Alkyl Heptamethine Cyanine Fluorophores. *Org. Lett.* **17**, 302–305 (2015).
17. Peng, X. *et al.* Heptamethine Cyanine Dyes with a Large Stokes Shift and Strong Fluorescence: A Paradigm for Excited-State Intramolecular Charge Transfer. *J. Am. Chem. Soc.* **127**, 4170–4171 (2005)..

18. Luo, S., Zhang, E., Su, Y., Cheng, T. & Shi, C. A review of NIR dyes in cancer targeting and imaging. *Biomaterials* **32**, 7127–7138 (2011)
19. Li, X., Gao, X., Shi, W. & Ma, H. Design Strategies for Water-Soluble Small Molecular Chromogenic and Fluorogenic Probes. *Chem. Rev.* **114**, 590–659 (2014).
20. Kaur, M. & Choi, D. H. Diketopyrrolopyrrole: brilliant red pigment dye-based fluorescent probes and their applications. *Chem. Soc. Rev.* **44**, 58–77 (2015).
21. Berezin, M. Y. & Achilefu, S. Fluorescence Lifetime Measurements and Biological Imaging. *Chem. Rev.* **110**, 2641–2684 (2010).
22. Sun, Y. *et al.* Novel benzo-bis(1,2,5-thiadiazole) fluorophores for in vivo NIR-II imaging of cancer. *Chem. Sci.* **7**, 6203–6207 (2016).
23. Zhang, X.-D. *et al.* Traumatic Brain Injury Imaging in the Second Near-Infrared Window with a Molecular Fluorophore. *Adv. Mater.* **28**, 6872–6879 (2016).
24. Zhang, X., Yu, H. & Xiao, Y. Replacing Phenyl Ring with Thiophene: An Approach to Longer Wavelength Aza-dipyrromethene Boron Difluoride (Aza-BODIPY) Dyes. *J. Org. Chem.* **77**, 669–673 (2012).
25. Yamazawa, S., Nakashima, M., Suda, Y., Nishiyabu, R. & Kubo, Y. 2,3-Naphtho-Fused BODIPYs as Near-Infrared Absorbing Dyes. *J. Org. Chem.* **81**, 1310–1315 (2016).
26. Alander, J. T. *et al.* A review of indocyanine green fluorescent imaging in surgery. *Int. J. Biomed. Imaging* **2012**, 940585 (2012).
27. Ren, L. *et al.* Developing Quinoidal Fluorophores with Unusually Strong Red/Near-Infrared Emission. *J. Am. Chem. Soc.* **137**, 11294–11302 (2015).
28. Avirah, R. R., Jayaram, D. T., Adarsh, N. & Ramaiah, D. Squaraine dyes in PDT: from basic design to in vivo demonstration. *Org. Biomol. Chem.* **10**, 911–920 (2012).
29. Yan, F. *et al.* Molecular imaging-guided photothermal/photodynamic therapy against tumor by iRGD-modified indocyanine green nanoparticles. *J. Control. Release* **224**, 217–228 (2016).
30. Lee, H., Mason, J. C. & Achilefu, S. Heptamethine Cyanine Dyes with a Robust C−C Bond at the Central Position of the Chromophore. *J. Org. Chem.* **71**, 7862–7865 (2006).
31. Hirata, T. *et al.* Synthesis and reactivities of 3-Indocyanine-green-acyl-1,3-thiazolidine-2-thione (ICG-ATT) as a new near-infrared fluorescent-labeling reagent. *Bioorg. Med. Chem.* **6**, 2179–2184 (1998).
32. Landsman, M. L., Kwant, G., Mook, G. A. & Zijlstra, W. G. Light-absorbing properties, stability, and spectral stabilization of indocyanine green. *J. Appl. Physiol.* **40**, 575–583 (1976).
33. Han, J., Engler, A., Qi, J. & Tung, C.-H. Ultra Pseudo-Stokes Shift Near Infrared Dyes Based on Energy Transfer. *Tetrahedron Lett.* **54**, 502–505 (2013).
34. Davydenko, I. *et al.* Facile Incorporation of Pd(PPh3)2Hal Substituents into Polymethines, Merocyanines, and Perylene Diimides as a Means of Suppressing Intermolecular Interactions. *J. Am. Chem. Soc.* **138**, 10112–10115 (2016).
35. Kim, J. S., Kodagahally, R., Strekowski, L. & Patonay, G. A study of intramolecular H-complexes of novel bis(heptamethine cyanine) dyes. *Talanta* **67**, 947–954 (2005).
36. Antaris, A. L. *et al.* A small-molecule dye for NIR-II imaging. *Nat. Mater.* **15**, 235 (2015).
37. McNamara, L. E. *et al.* Donor–Acceptor–Donor Thienopyrazines via Pd-Catalyzed C–H Activation as NIR Fluorescent Materials. *J. Org. Chem.* **81**, 32–42 (2016).
38. Tam, T. L., Li, H., Lam, Y. M., Mhaisalkar, S. G. & Grimsdale, A. C. Synthesis and Characterization of [1,2,5]Chalcogenazolo[3,4-f]benzo[1,2,3]triazole and

[1,2,3]Triazolo[3,4-g]quinoxaline Derivatives. *Org. Lett.* **13**, 4612–4615 (2011).
39. Schwiderski, R. L. & Rasmussen, S. C. Synthesis and Characterization of Thieno[3,4-b]pyrazine-Based Terthienyls: Tunable Precursors for Low Band Gap Conjugated Materials. *J. Org. Chem.* **78**, 5453–5462 (2013).
40. Céron-Carrasco, J. P., Siard, A. & Jacquemin, D. Spectral signatures of thieno[3,4-b]pyrazines: Theoretical interpretations and design of improved structures. *Dye. Pigment.* **99**, 972–978 (2013).
41. Xia, Y. *et al.* Novel Random Low-Band-Gap Fluorene-Based Copolymers for Deep Red/Near Infrared Light-Emitting Diodes and Bulk Heterojunction Photovoltaic Cells. *Macromol. Chem. Phys.* **207**, 511–520 (2006).
42. Kitamura, C., Tanaka, S. & Yamashita, Y. Design of Narrow-Bandgap Polymers. Syntheses and Properties of Monomers and Polymers Containing Aromatic-Donor and o-Quinoid-Acceptor Units. *Chem. Mater.* **8**, 570–578 (1996).
43. Steinberger, S. *et al.* Synthesis and characterizations of red/near-IR absorbing A–D–A–D–A-type oligothiophenes containing thienothiadiazole and thienopyrazine central units. *J. Mater. Chem.* **22**, 2701–2712 (2012).
44. Hwang, Y.-J., Kim, F. S., Xin, H. & Jenekhe, S. A. New Thienothiadiazole-Based Conjugated Copolymers for Electronics and Optoelectronics. *Macromolecules* **45**, 3732–3739 (2012).
45. Mikroyannidis, J. A., Tsagkournos, D. V, Sharma, S. S., Vijay, Y. K. & Sharma, G. D. Low band gap conjugated small molecules containing benzobisthiadiazole and thienothiadiazole central units: synthesis and application for bulk heterojunction solar cells. *J. Mater. Chem.* **21**, 4679–4688 (2011).
46. Kmínek, I., Výprachtický, D., Kříž, J., Dybal, J. & Cimrová, V. Low-band gap copolymers containing thienothiadiazole units: Synthesis, optical, and electrochemical properties. *J. Polym. Sci. Part A Polym. Chem.* **48**, 2743–2756 (2010).
47. Bower, J. D. & Schlessinger, R. H. Synthesis of two nonclassical thienothiadiazoles. *J. Am. Chem. Soc.* **91**, 6891–6892 (1969).
48. Pericles_109906902012.
49. Luo, J., Zhao, B., On Chan, H. S. & Chi, C. Synthesis, physical properties and self-assembly of star-shaped oligothiophenes-substituted and fused triphenylenes. *J. Mater. Chem.* **20**, 1932–1941 (2010).
50. Lambert, C., Scherpf, T., Ceymann, H., Schmiedel, A. & Holzapfel, M. Coupled Oscillators for Tuning Fluorescence Properties of Squaraine Dyes. *J. Am. Chem. Soc.* **137**, 3547–3557 (2015).
51. Siebrand, W. Radiationless Transitions in Polyatomic Molecules. I. Calculation of Franck—Condon Factors. *J. Chem. Phys.* **46**, 440–447 (1967).
52. Siebrand, W. Radiationless Transitions in Polyatomic Molecules. II. Triplet-Ground-State Transitions in Aromatic Hydrocarbons. *J. Chem. Phys.* **47**, 2411–2422 (1967).
53. Caspar, J. V, Sullivan, B. P., Kober, E. M. & Meyer, T. J. Application of the energy gap law to the decay of charge transfer excited states, solvent effects. *Chem. Phys. Lett.* **91**, 91–95 (1982).
54. Englman, R. & Jortner, J. The energy gap law for radiationless transitions in large molecules. *Mol. Phys.* **18**, 145–164 (1970).
55. Wilson, J. S. *et al.* The Energy Gap Law for Triplet States in Pt-Containing Conjugated Polymers and Monomers. *J. Am. Chem. Soc.* **123**, 9412–9417 (2001).

56. Cekli, S., Winkel, R. W., Alarousu, E., Mohammed, O. F. & Schanze, K. S. Triplet excited state properties in variable gap π-conjugated donor–acceptor–donor chromophores. *Chem. Sci.* **7**, 3621–3631 (2016).
57. Chen, X. *et al.* Photostabilities of novel heptamethine 3H-indolenine cyanine dyes with different N-substituents. *J. Photochem. Photobiol. A Chem.* **181**, 79–85 (2006).
58. Song, F. *et al.* Syntheses, spectral properties and photostabilities of novel water-soluble near-infrared cyanine dyes. *J. Photochem. Photobiol. A Chem.* **168**, 53–57 (2004).
59. Su, D. *et al.* The development of a highly photostable and chemically stable zwitterionic near-infrared dye for imaging applications. *Chem. Commun.* **51**, 3989–3992 (2015).
60. Kirkus, M. *et al.* Synthesis and Optical Properties of Pyrrolo[3,2-b]pyrrole-2,5(1H,4H)-dione (iDPP)-Based Molecules. *J. Phys. Chem. A* **117**, 2782–2789 (2013).
61. Crosby, G. A. & Demas, J. N. Measurement of photoluminescence quantum yields. Review. *J. Phys. Chem.* **75**, 991–1024 (1971).
62. Vincett, P. S., Voigt, E. M. & Rieckhoff, K. E. Phosphorescence and Fluorescence of Phthalocyanines. *J. Chem. Phys.* **55**, 4131–4140 (1971).
63. O'Regan, B. & Grätzel, M. A low-cost, high-efficiency solar cell based on dye-sensitized colloidal TiO2 films. *Nature* **353**, 737–740 (1991).
64. Fakharuddin, A., Jose, R., Brown, T. M., Fabregat-Santiago, F. & Bisquert, J. A perspective on the production of dye-sensitized solar modules. *Energy Environ. Sci.* **7**, 3952–3981 (2014).
65. Zhang, S., Yang, X., Numata, Y. & Han, L. Highly efficient dye-sensitized solar cells: progress and future challenges. *Energy Environ. Sci.* **6**, 1443–1464 (2013).
66. Brogdon, P., Cheema, H. & Delcamp, J. H. Near-Infrared-Absorbing Metal-Free Organic, Porphyrin, and Phthalocyanine Sensitizers for Panchromatic Dye-Sensitized Solar Cells. *ChemSusChem* **11**, 86–103 (2018).
67. Dualeh, A., Humphry-Baker, R., Delcamp, J. H., Nazeeruddin, M. K. & Grätzel, M. Solid-State Dye-Sensitized Solar Cells Using a Novel Class of Ullazine Dyes as Sensitizers. *Adv. Energy Mater.* **3**, 496–504 (2013).
68. Huckaba, A. J. *et al.* Indolizine-Based Donors as Organic Sensitizer Components for Dye-Sensitized Solar Cells. *Adv. Energy Mater.* **5**, 1401629 (2015).
69. Delcamp, J. H., Yella, A., Holcombe, T. W., Nazeeruddin, M. K. & Grätzel, M. The Molecular Engineering of Organic Sensitizers for Solar-Cell Applications. *Angew. Chemie Int. Ed.* **52**, 376–380 (2013).
70. Huckaba, A. J. *et al.* A low recombination rate indolizine sensitizer for dye-sensitized solar cells. *Chem. Commun.* **52**, 8424–8427 (2016).
71. Huckaba, A. J. *et al.* Molecular Design Principles for Near-Infrared Absorbing and Emitting Indolizine Dyes. *Chem. – A Eur. J.* **22**, 15536–15542 (2016).
72. Cheema, H. *et al.* Molecular Engineering of Near Infrared Absorbing Thienopyrazine Double Donor Double Acceptor Organic Dyes for Dye-Sensitized Solar Cells. *J. Org. Chem.* **82**, 12038–12049 (2017).
73. Mishra, A., Fischer, M. K. R. & Bäuerle, P. Metal-Free Organic Dyes for Dye-Sensitized Solar Cells: From Structure: Property Relationships to Design Rules. *Angew. Chemie Int. Ed.* **48**, 2474–2499 (2009).
74. Wan, D. *et al.* Palladium-Catalyzed Annulation of Internal Alkynes: Direct Access to π-Conjugated Ullazines. *Org. Lett.* **18**, 2876–2879 (2016).
75. Qiao, H. *et al.* Effect of π-spacers and anchoring groups on the photovoltaic performances

of ullazine-based dyes. *RSC Adv.* **6**, 70046–70055 (2016).
76. Mathew, S. *et al.* Synthesis, characterization and ab initio investigation of a panchromatic ullazine–porphyrin photosensitizer for dye-sensitized solar cells. *J. Mater. Chem. A* **4**, 2332–2339 (2016).
77. Feng, J. *et al.* First Principles Design of Dye Molecules with Ullazine Donor for Dye Sensitized Solar Cells. *J. Phys. Chem. C* **117**, 3772–3778 (2013).
78. Zhou, J., Yang, W., Wang, B. & Ren, H. Friedel–Crafts Arylation for the Formation of C□C Bonds: A Route to Unsymmetrical and Functionalized Polycyclic Aromatic Hydrocarbons from Aryl Triazenes. *Angew. Chemie Int. Ed.* **51**, 12293–12297 (2012).
79. Boldt, S., Parpart, S., Villinger, A., Ehlers, P. & Langer, P. Synthesis and Properties of Aza-ullazines. *Angew. Chemie Int. Ed.* **56**, 4575–4578 (2017).
80. Berger, R., Wagner, M., Feng, X. & Müllen, K. Polycyclic aromatic azomethine ylides: a unique entry to extended polycyclic heteroaromatics. *Chem. Sci.* **6**, 436–441 (2015).
81. Drigo, N. A. *et al.* Approaches for Selective Synthesis of Ullazine Donor–Acceptor Systems. *Chem. – A Eur. J.* **23**, 17209–17212 (2017).
82. Balli, H. & Zeller, M. Neue Heteroarene: Synthese und spektrale Daten von Indolizino[6,5,4,3-aij]chinolin («Ullazin») und einigen Derivaten. *Helv. Chim. Acta* **66**, 2135–2139 (1983).
83. Aspinall, H. C., Greeves, N. & Valla, C. Samarium Diiodide-Catalyzed Diastereoselective Pinacol Couplings. *Org. Lett.* **7**, 1919–1922 (2005).
84. Brogdon, P. *et al.* A Computational and Experimental Study of Thieno[3,4-b]thiophene as a Proaromatic π-Bridge in Dye-Sensitized Solar Cells. *Chem. – A Eur. J.* **22**, 694–703 (2016).
85. Pei, K. *et al.* Cosensitization of D-A-π-A Quinoxaline Organic Dye: Efficiently Filling the Absorption Valley with High Photovoltaic Efficiency. *ACS Appl. Mater. Interfaces* **7**, 5296–5304 (2015).
86. Seo, K. D., Choi, I. T. & Kim, H. K. Organic Dyes with Well-Defined Structures for Highly Efficient Dye-Sensitised Solar Cells Based on a Cobalt Electrolyte. *Chem. – A Eur. J.* **21**, 14804–14811 (2015).
87. Hardin, B. E., Snaith, H. J. & McGehee, M. D. The renaissance of dye-sensitized solar cells. *Nat. Photonics* **6**, 162 (2012).
88. Liu, J., Zhou, D., Xu, M., Jing, X. & Wang, P. The structure–property relationship of organic dyes in mesoscopic titania solar cells: only one double-bond difference. *Energy Environ. Sci.* **4**, 3545–3551 (2011).
89. Delcamp, J. H. *et al.* The Role of π Bridges in High-Efficiency DSCs Based on Unsymmetrical Squaraines. *Chem. – A Eur. J.* **19**, 1819–1827 (2013).
90. Sutter, A. & Ziessel, R. A Versatile Synthesis of Long-Wavelength-Excitable BODIPY Dyes from Readily Modifiable Cyclopenta[2,1-b:3,4-b′]dithiophenes. *Synlett* **25**, 1466–1472 (2014).
91. di Nunzio, M. R. *et al.* Spectroscopy and Dynamics of YD2-o-C8 in Solution and Interacting with Alumina Nanoparticles Electrode. *J. Phys. Chem. C* **118**, 11365–11376 (2014).
92. Dolhem, F., Lièvre, C. & Demailly, G. Synthesis of glyco-1-ynitols via 1,1-dibromo-1-alkenes from partially and unprotected aldoses. *Tetrahedron* **59**, 155–164 (2003).
93. The greener grid. *Nature* **454**, 551 (2008).
94. Jelle, B. P. & Breivik, C. The Path to the Building Integrated Photovoltaics of Tomorrow.

Energy Procedia **20**, 78–87 (2012).
95. Gao, P., Tsao, H. N., Yi, C., Grätzel, M. & Nazeeruddin, M. K. Extended π-Bridge in Organic Dye-Sensitized Solar Cells: the Longer, the Better? *Adv. Energy Mater.* **4**, 1301485 (2014).
96. Holcombe, T. W. *et al.* A structural study of DPP-based sensitizers for DSC applications. *Chem. Commun.* **48**, 10724–10726 (2012).
97. Yum, J.-H. *et al.* Towards high-performance DPP-based sensitizers for DSC applications. *Chem. Commun.* **48**, 10727–10729 (2012).
98. Yao, Z. *et al.* Dithienopicenocarbazole as the kernel module of low-energy-gap organic dyes for efficient conversion of sunlight to electricity. *Energy Environ. Sci.* **8**, 3192–3197 (2015).
99. Ooyama, Y. & Harima, Y. Photophysical and Electrochemical Properties, and Molecular Structures of Organic Dyes for Dye-Sensitized Solar Cells. *ChemPhysChem* **13**, 4032–4080 (2012).
100. Delcamp, J. H., Yella, A., Nazeeruddin, M. K. & Grätzel, M. Modulating dyeE(S+/S*) with efficient heterocyclic nitrogen containing acceptors for DSCs. *Chem. Commun.* **48**, 2295–2297 (2012).
101. Zhang, M. *et al.* Design of high-efficiency organic dyes for titania solar cells based on the chromophoric core of cyclopentadithiophene-benzothiadiazole. *Energy Environ. Sci.* **6**, 2944–2949 (2013).
102. Yella, A. *et al.* Porphyrin-Sensitized Solar Cells with Cobalt (II/III)–Based Redox Electrolyte Exceed 12 Percent Efficiency. *Science (80-.).* **334**, 629 LP-634 (2011).
103. Cheema, H. & Delcamp, J. H. Harnessing Photovoltage: Effects of Film Thickness, TiO2 Nanoparticle Size, MgO and Surface Capping with DSCs. *ACS Appl. Mater. Interfaces* **9**, 3050–3059 (2017).
104. Ahmad, S., Guillén, E., Kavan, L., Grätzel, M. & Nazeeruddin, M. K. Metal free sensitizer and catalyst for dye sensitized solar cells. *Energy Environ. Sci.* **6**, 3439–3466 (2013).
105. Sun, Z., Liang, M. & Chen, J. Kinetics of Iodine-Free Redox Shuttles in Dye-Sensitized Solar Cells: Interfacial Recombination and Dye Regeneration. *Acc. Chem. Res.* **48**, 1541–1550 (2015).
106. Yum, J.-H., Baranoff, E., Wenger, S., Nazeeruddin, M. K. & Grätzel, M. Panchromatic engineering for dye-sensitized solar cells. *Energy Environ. Sci.* **4**, 842–857 (2011).
107. Li, R., Liu, J., Cai, N., Zhang, M. & Wang, P. Synchronously Reduced Surface States, Charge Recombination, and Light Absorption Length for High-Performance Organic Dye-Sensitized Solar Cells. *J. Phys. Chem. B* **114**, 4461–4464 (2010).
108. London, A. E. *et al.* Donor–acceptor polymers with tunable infrared photoresponse. *Polym. Chem.* **8**, 2922–2930 (2017).
109. Boschloo, G. & Hagfeldt, A. Characteristics of the Iodide/Triiodide Redox Mediator in Dye-Sensitized Solar Cells. *Acc. Chem. Res.* **42**, 1819–1826 (2009).
110. Anderson, A. Y., Barnes, P. R. F., Durrant, J. R. & O'Regan, B. C. Quantifying Regeneration in Dye-Sensitized Solar Cells. *J. Phys. Chem. C* **115**, 2439–2447 (2011).
111. Listorti, A., O'Regan, B. & Durrant, J. R. Electron Transfer Dynamics in Dye-Sensitized Solar Cells. *Chem. Mater.* **23**, 3381–3399 (2011).
112. Reynal, A. *et al.* Interfacial Charge Recombination Between e−−TiO2 and the I−/I3− Electrolyte in Ruthenium Heteroleptic Complexes: Dye Molecular Structure−Open Circuit Voltage Relationship. *J. Am. Chem. Soc.* **130**, 13558–13567 (2008).

113. Hu, K. *et al.* Direct Spectroscopic Evidence for Constituent Heteroatoms Enhancing Charge Recombination at a TiO2−Ruthenium Dye Interface. *J. Phys. Chem. C* **118**, 17079–17089 (2014).
114. Mazloum-Ardakani, M. & Khoshroo, A. Enhanced performance of dye-sensitized solar cells with dual-function coadsorbent: reducing the surface concentration of dye–iodine complexes concomitant with attenuated charge recombination. *Phys. Chem. Chem. Phys.* **17**, 22985–22990 (2015).
115. Li, X. *et al.* Measured binding coefficients for iodine and ruthenium dyes; implications for recombination in dye sensitised solar cells. *Phys. Chem. Chem. Phys.* **14**, 15421–15428 (2012).
116. Robson, K. C. D., Hu, K., Meyer, G. J. & Berlinguette, C. P. Atomic Level Resolution of Dye Regeneration in the Dye-Sensitized Solar Cell. *J. Am. Chem. Soc.* **135**, 1961–1971 (2013).
117. Gu, D.-M., Zhang, J.-Z., Zhang, M., Geng, Y. & Su, Z.-M. Dye regeneration mechanisms of dye sensitized solar cells: Quantum chemical studies on the interaction between iodide and O/S-containing organic dyes. *Dye. Pigment.* **132**, 136–141 (2016).
118. Asghar, M. I. *et al.* Intriguing Photochemistry of the Additives in the Dye-Sensitized Solar Cells. *J. Phys. Chem. C* **120**, 27768–27781 (2016).
119. O'Regan, B. C. *et al.* Structure/Function Relationships in Dyes for Solar Energy Conversion: A Two-Atom Change in Dye Structure and the Mechanism for Its Effect on Cell Voltage. *J. Am. Chem. Soc.* **131**, 3541–3548 (2009).
120. Liu, T. & Troisi, A. Theoretical evidence of multiple dye regeneration mechanisms in dye-sensitized solar cells. *Chem. Phys. Lett.* **570**, 159–162 (2013).
121. Jeanbourquin, X. A. *et al.* Rediscovering a Key Interface in Dye-Sensitized Solar Cells: Guanidinium and Iodine Competition for Binding Sites at the Dye/Electrolyte Surface. *J. Am. Chem. Soc.* **136**, 7286–7294 (2014).
122. Swords, W. B. *et al.* Evidence for Interfacial Halogen Bonding. *Angew. Chemie Int. Ed.* **55**, 5956–5960 (2016).
123. Simon, S. J. C. *et al.* Halogen Bonding Promotes Higher Dye-Sensitized Solar Cell Photovoltages. *J. Am. Chem. Soc.* **138**, 10406–10409 (2016).
124. Kusama, H., Funaki, T., Koumura, N. & Sayama, K. Intermolecular interactions between a Ru complex and organic dyes in cosensitized solar cells: a computational study. *Phys. Chem. Chem. Phys.* **16**, 16166–16175 (2014).
125. Kusama, H. & Sayama, K. A comparative computational study on the interactions of N719 and N749 dyes with iodine in dye-sensitized solar cells. *Phys. Chem. Chem. Phys.* **17**, 4379–4387 (2015).
126. Pastore, M., Mosconi, E. & De Angelis, F. Computational Investigation of Dye–Iodine Interactions in Organic Dye-Sensitized Solar Cells. *J. Phys. Chem. C* **116**, 5965–5973 (2012).
127. Aghazada, S. *et al.* Unraveling the Dual Character of Sulfur Atoms on Sensitizers in Dye-Sensitized Solar Cells. *ACS Appl. Mater. Interfaces* **8**, 26827–26833 (2016).
128. Cariello, M. *et al.* An investigation of the roles furan versus thiophene π-bridges play in donor–π-acceptor porphyrin based DSSCs. *Dalt. Trans.* **47**, 6549–6556 (2018).
129. Xie, M. *et al.* Theoretical description of dye regeneration on the TiO2–dye–electrolyte model. *Comput. Mater. Sci.* **111**, 239–246 (2016).
130. Li, H.-B. *et al.* Theoretical studies on organic D-π-A sensitizers with planar triphenylamine

donor and different π-linkers for dyes-sensitized solar cells. *J. Mol. Model.* **20**, 2309 (2014).
131. Zhang, J. *et al.* A promising anchor group for efficient organic dye sensitized solar cells with iodine-free redox shuttles: a theoretical evaluation. *J. Mater. Chem. A* **1**, 14000–14007 (2013).
132. Balanay, M. P. & Kim, D. H. Theoretical study on the correlations between dye–iodine interactions and open-circuit voltages in dyes containing furan and thiophene. *Comput. Theor. Chem.* **1029**, 1–12 (2014).
133. Metrangolo, P., Meyer, F., Pilati, T., Resnati, G. & Terraneo, G. Halogen Bonding in Supramolecular Chemistry. *Angew. Chemie Int. Ed.* **47**, 6114–6127 (2008).
134. Gabrielsson, E. *et al.* Convergent/Divergent Synthesis of a Linker-Varied Series of Dyes for Dye-Sensitized Solar Cells Based on the D35 Donor. *Adv. Energy Mater.* **3**, 1647–1656 (2013).
135. Luo, J., Wan, Z., Jia, C., Wang, Y. & Wu, X. A co-sensitized approach to efficiently fill the absorption valley, avoid dye aggregation and reduce the charge recombination. *Electrochim. Acta* **215**, 506–514 (2016).
136. Feldt, S. M. *et al.* Design of Organic Dyes and Cobalt Polypyridine Redox Mediators for High-Efficiency Dye-Sensitized Solar Cells. *J. Am. Chem. Soc.* **132**, 16714–16724 (2010).
137. Deplano, P. *et al.* On the Use of Raman Spectroscopy in the Characterization of Iodine in Charge-Transfer Complexes. *Appl. Spectrosc.* **46**, 1625–1629 (1992).
138. Asseily, G. A., Davies, R. P., Rzepa, H. S. & White, A. J. P. A solid-state structural and theoretical study on the 1 : 1 addition compounds of thioethers with dihalogens and interhalogens I–X (X = I, Br, Cl). *New J. Chem.* **29**, 315–319 (2005).
139. M. J. Frisch, G. W. Trucks, H. B. Schlegel, G. E. Scuseria, M. A. Robb, J. R. Cheeseman, G. Scalmani, V. Barone, G. A. Petersson, H. Nakatsuji, X. Li, M. Caricato, A. V. Marenich, J. Bloino, B. G. Janesko, R. Gomperts, B. Mennucci, H. P. Hratchian, J. V., J. B. F. and D. J. F. *Gaussian 16, Revision A.03,*. (2016).
140. Chai, J.-D. & Head-Gordon, M. Long-range corrected hybrid density functionals with damped atom–atom dispersion corrections. *Phys. Chem. Chem. Phys.* **10**, 6615–6620 (2008).
141. Grimme, S. Semiempirical GGA-type density functional constructed with a long-range dispersion correction. *J. Comput. Chem.* **27**, 1787–1799 (2006).
142. Feller, D. The role of databases in support of computational chemistry calculations. *J. Comput. Chem.* **17**, 1571–1586 (1996).
143. Schuchardt, K. L. *et al.* Basis Set Exchange: A Community Database for Computational Sciences. *J. Chem. Inf. Model.* **47**, 1045–1052 (2007).
144. Kim, S.-H. & Rieke, R. D. 5-Substituted-2-furaldehydes: A Synthetic Protocol Utilizing an Organozinc Route. *J. Org. Chem.* **78**, 1984–1993 (2013).
145. Ardo, S. & Meyer, G. J. Photodriven heterogeneous charge transfer with transition-metal compounds anchored to TiO2 semiconductor surfaces. *Chem. Soc. Rev.* **38**, 115–164 (2009).
146. Bella, F., Gerbaldi, C., Barolo, C. & Grätzel, M. Aqueous dye-sensitized solar cells. *Chem. Soc. Rev.* **44**, 3431–3473 (2015).
147. Hamann, T. W. & Ondersma, J. W. Dye-sensitized solar cell redox shuttles. *Energy Environ. Sci.* **4**, 370–381 (2011).
148. O'Regan, B. C. & Durrant, J. R. Kinetic and Energetic Paradigms for Dye-Sensitized Solar Cells: Moving from the Ideal to the Real. *Acc. Chem. Res.* **42**, 1799–1808 (2009).
149. Wu, J. *et al.* Electrolytes in Dye-Sensitized Solar Cells. *Chem. Rev.* **115**, 2136–2173 (2015).
150. Wu, Y., Zhu, W.-H., Zakeeruddin, S. M. & Grätzel, M. Insight into D–A−π–A Structured

Sensitizers: A Promising Route to Highly Efficient and Stable Dye-Sensitized Solar Cells. *ACS Appl. Mater. Interfaces* **7**, 9307–9318 (2015).
151. Liang, M. & Chen, J. Arylamine organic dyes for dye-sensitized solar cells. *Chem. Soc. Rev.* **42**, 3453–3488 (2013).
152. Eom, Y. K. *et al.* Significant light absorption enhancement by a single heterocyclic unit change in the π-bridge moiety from thieno[3,2-b]benzothiophene to thieno[3,2-b]indole for high performance dye-sensitized and tandem solar cells. *J. Mater. Chem. A* **5**, 2297–2308 (2017).
153. Sobuś, J. *et al.* Factors Affecting the Performance of Champion Silyl-Anchor Carbazole Dye Revealed in the Femtosecond to Second Studies of Complete ADEKA-1 Sensitized Solar Cells. *Chem. – A Eur. J.* **22**, 15807–15818 (2016).
154. Manfredi, N., Cecconi, B. & Abbotto, A. Multi-Branched Multi-Anchoring Metal-Free Dyes for Dye-Sensitized Solar Cells. *European J. Org. Chem.* **2014**, 7069–7086 (2014).
155. Brogdon, P., McNamara, L. E., Peddapuram, A., Hammer, N. I. & Delcamp, J. H. Toward tightly bound carboxylic acid-based organic dyes for DSCs: relative TiO2 binding strengths of benzoic acid, cyanoacrylic acid, and conjugated double carboxylic acid anchoring dyes. *Synth. Met.* **222**, 66–75 (2016).
156. Peddapuram, A., Cheema, H., Adams, R. E., Schmehl, R. H. & Delcamp, J. H. A Stable Panchromatic Green Dual Acceptor, Dual Donor Organic Dye for Dye-Sensitized Solar Cells. *J. Phys. Chem. C* **121**, 8770–8780 (2017).
157. Liyanage, N. P., Yella, A., Nazeeruddin, M., Grätzel, M. & Delcamp, J. H. Thieno[3,4-b]pyrazine as an Electron Deficient π-Bridge in D–A−π–A DSCs. *ACS Appl. Mater. Interfaces* **8**, 5376–5384 (2016).
158. Lee, K., Park, S. W., Ko, M. J., Kim, K. & Park, N.-G. Selective positioning of organic dyes in a mesoporous inorganic oxide film. *Nat. Mater.* **8**, 665 (2009).
159. Cheng, P. & Zhan, X. Stability of organic solar cells: challenges and strategies. *Chem. Soc. Rev.* **45**, 2544–2582 (2016).
160. Chang, Y. J., Watanabe, M., Chou, P.-T. & Chow, T. J. [2.2]Paracyclophane as a bridging unit in the design of organic dyes for sensitized solar cells. *Chem. Commun.* **48**, 726–728 (2012).
161. Wang, B., Tsang, S.-W., Zhang, W., Tao, Y. & Wong, M. S. Naphthodithiophene-2,1,3-benzothiadiazole copolymers for bulk heterojunction solar cells. *Chem. Commun.* **47**, 9471–9473 (2011).
162. Mátravölgyi, B. *et al.* Synthesis and Investigation of Solar-Cell Photosensitizers Having a Fluorazone Backbone. *European J. Org. Chem.* **2017**, 1843–1854 (2017).
163. Gislason, K. & Sigurdsson, S. T. Rigid 5′-6-locked phenanthroline-derived nucleosides chelated to ruthenium and europium ions. *Bioorg. Med. Chem. Lett.* **23**, 264–267 (2013).
164. MJ., Frisch. Frisch, M.J.; Trucks, G.W.; Schlegel, H.B.; Scurseria, G.E.; Robb, M.A.; Cheeseman, J.R.; Scalmani, G.; Barone, V.; Mennucci, B.; Petersson, A. *Gaussian09 Revision D.01; Gaussian Inc.: Wallingford, CT,*. (2009).
165. Li Sie-Rong A4 - Lee, Chuan-Pei A4 - Liao, Chia-Wei A4 - Su, Wei-Lin A4 - Li, Chun-Ting A4 - Ho, Kuo-Chuan A4 - Sun, Shih-Sheng, S.-R. A.-L. Structural engineering of dipolar organic dyes with an electron-deficient diphenylquinoxaline moiety for efficient dye-sensitized solar cells. *Tetrahedron* **v. 70**, 6276-6284–2014 v.70 (2014).
166. Falgenhauer, J., Richter, C., Miura, H. & Schlettwein, D. Stable Sensitization of ZnO by Improved Anchoring of Indoline Dyes. *ChemPhysChem* **13**, 2893–2897 (2012).

167. Aghazada, S. & Nazeeruddin, K. M. Ruthenium Complexes as Sensitizers in Dye-Sensitized Solar Cells. *Inorganics* **6**, (2018).
168. Baumann, A. *et al.* Iodine binding with thiophene and furan based dyes for DSCs. *Phys. Chem. Chem. Phys.* **20**, 17859–17870 (2018).

APPENDIX

APPENDIX A: FIGURES AND TABLES

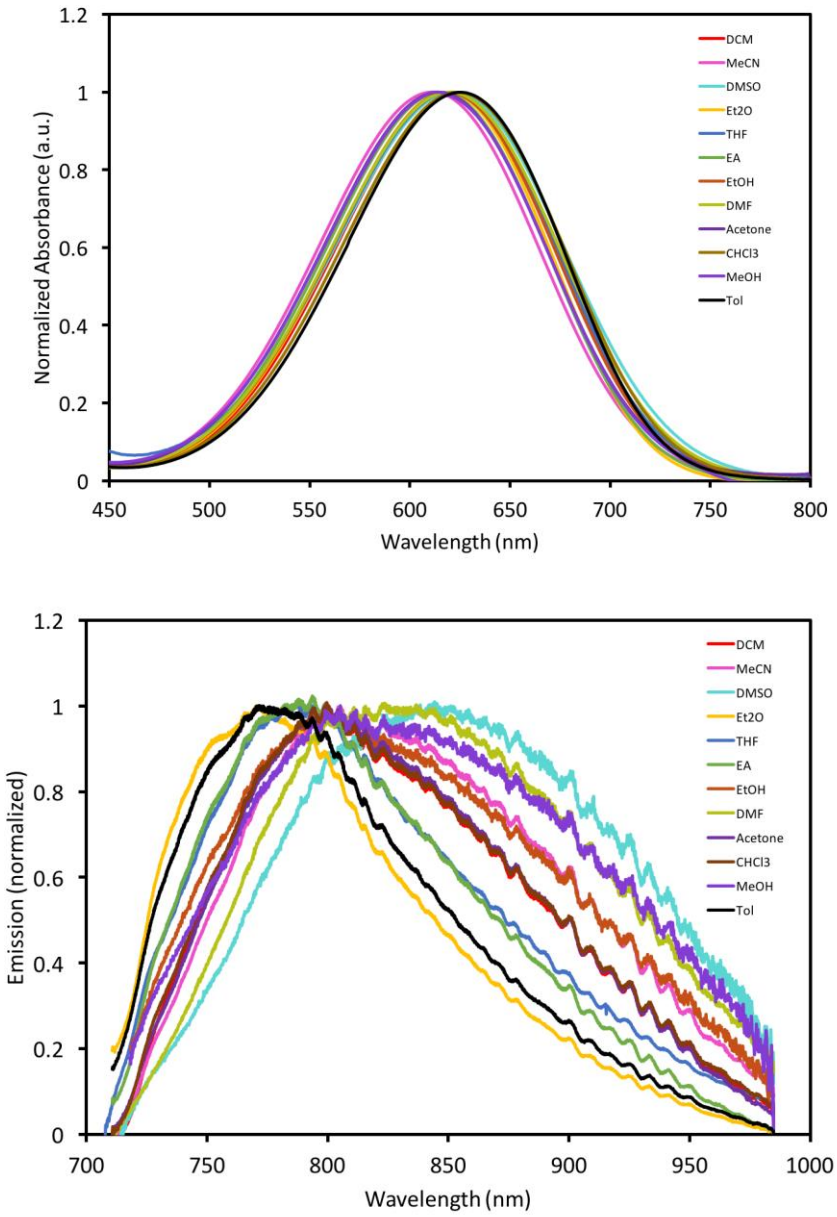

Figure 42. UV-vis absorption and emission spectra for $TTD(T)_2$ in various solvent.

YZ12

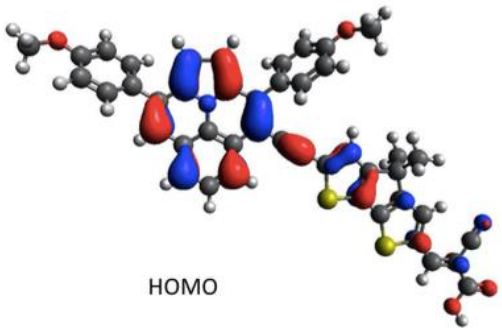

HOMO

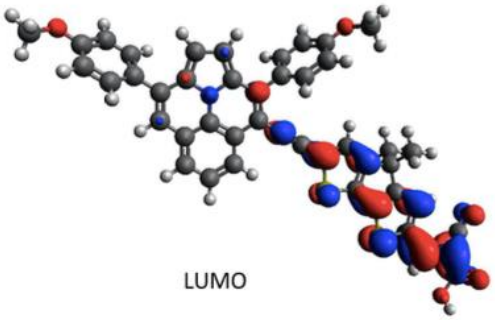

LUMO

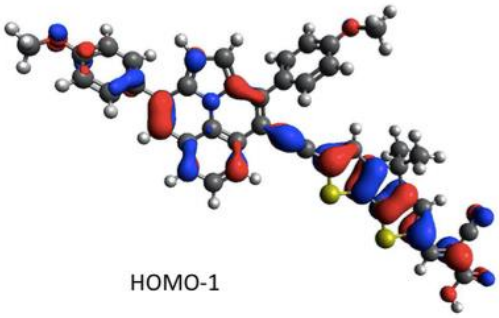

HOMO-1

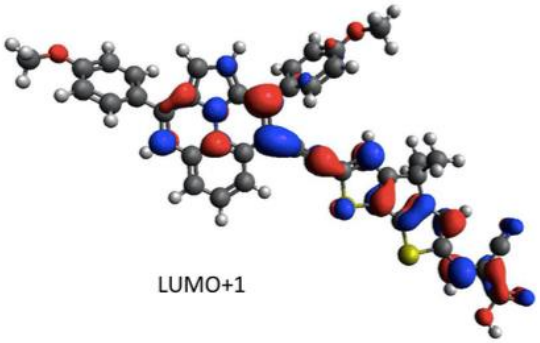

LUMO+1

YZ14

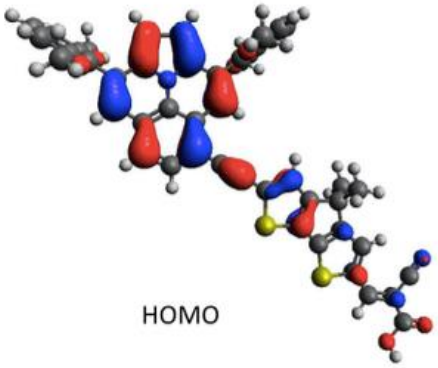

HOMO

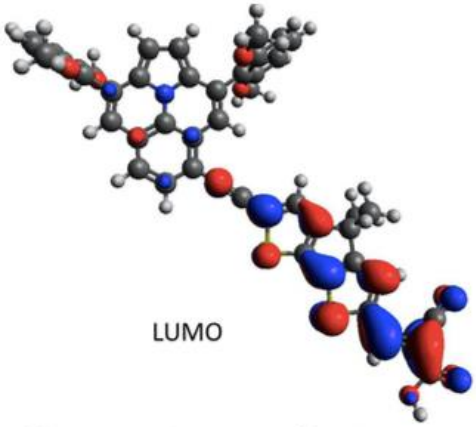

LUMO

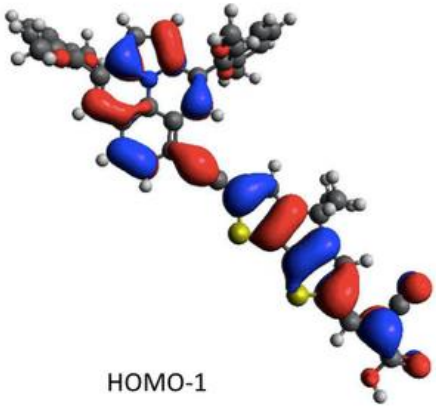

HOMO-1

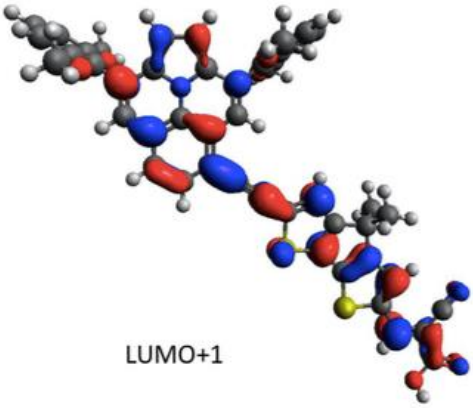

LUMO+1

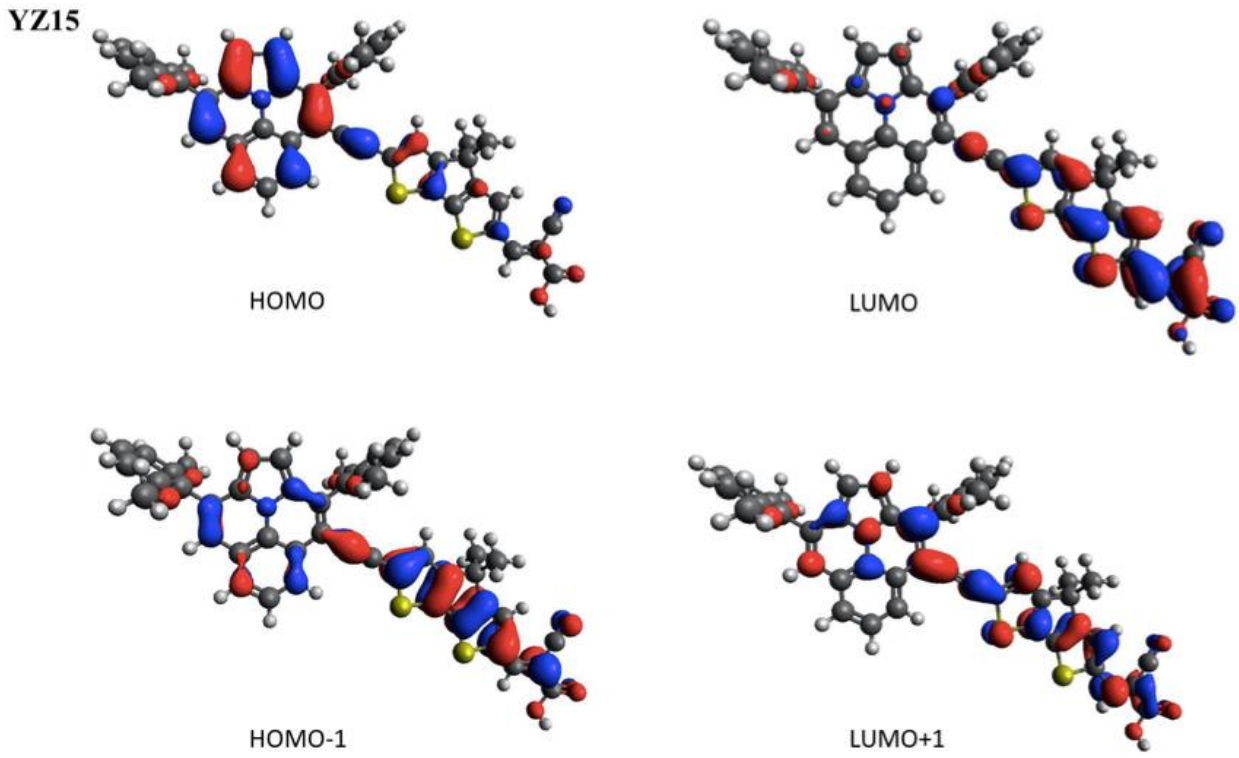

Figure 43. HOMO, LUMO, HOMO-1 and LUMO+1 orbitals for dyes **YZ12-YZ15** given by DFT calculations at the B3LYP/6- 311G(d,p) level with isovalues of 0.30. Long alkyl chains were truncated to methyls on the aryl amines and phenyl ring.

Table 13. Summary table of **YZ7, YZ12, YZ14** and **YZ15** for computational results: dihedral angles, orbital contributions to vertical transitions, vertical transition energies and oscillator strengths computed with DFT and TD-DFT analysis at the B3LYP/6-311(d,p) level

dye	transition	contrib. (%)	vert. trans. (nm/eV)	oscillator strength	energy (Hartrees)
YZ7	H → L	99%	665/1.87	1.1337	-2940.1266378
	H^{-1} → L	62%	476/2.61	1.0546	
	H → L^{+1}	36%			
YZ12	H → L	98%	670/1.85	0.8859	-2940.1361627
	H^{-1} → L	58%	480/2.58	0.7240	
	H → L^{+1}	40%			
YZ14	H → L	99%	689/1.80	1.0385	-3169.2360226
	H^{-1} → L	66%	477/2.59	1.1125	
	H → L^{+1}	33%			
YZ15	H → L	99%	707/1.75	0.8662	-3169.2338538
	H^{-1} → L	45%	480/2.58	0.7997	
	H → L^{+1}	53%			

Table 14. YZ7 devices under different LiI concentration.

Dye	Concentration of LiI (mM)	V_{oc} (mV)	J_{sc} (mA/cm^2)	FF	PCE (%)
YZ7	1	584	10.5	0.69	4.4
	0.05	609	8.0	0.74	3.7

Note: All the devices were applied E2I, with 20x CDCA inside, DMF as dipping solvent, and the film thickness is 10 µm active layer and 5 µm scattering layer.

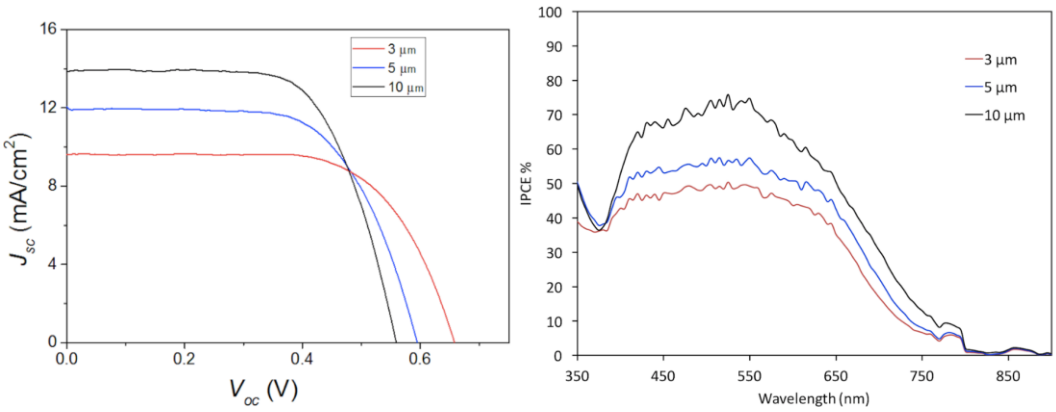

Figure 44. IPCE (right) and I-V (left) curves of **YZ7** with different active layer thickness. Note: All the devices were applied E2I, with 10:1 CDCA:dye.

Table 15. DSC devices of **YZ7** under various deposition solvents conditions.

Dye	electrode variables	V_{oc} (mV)	J_{sc} (mA/cm^2)	FF	PCE (%)
YZ7	CB	531	12.9	0.70	4.9
	EtOH:THF	507	10.0	0.69	3.7
	EtOH:DCM	531	8.50	0.71	3.4
	tBuOH:MeCN:CB	563	11.5	0.70	4.8

Note: For the concentration of dipping solution, CB (0.2 mM), EtOH:THF (1.2:1, 0.18 mM), EtOH:DCM (1:1.3, 0.18 mM), tBuOH: MeCN: CB (1:1:1.2, 0.13 mM). Note: All the devices were applied E2I, with no CDCA inside, and the film thickness is 10 µm active layer and 5 µm scattering layer.

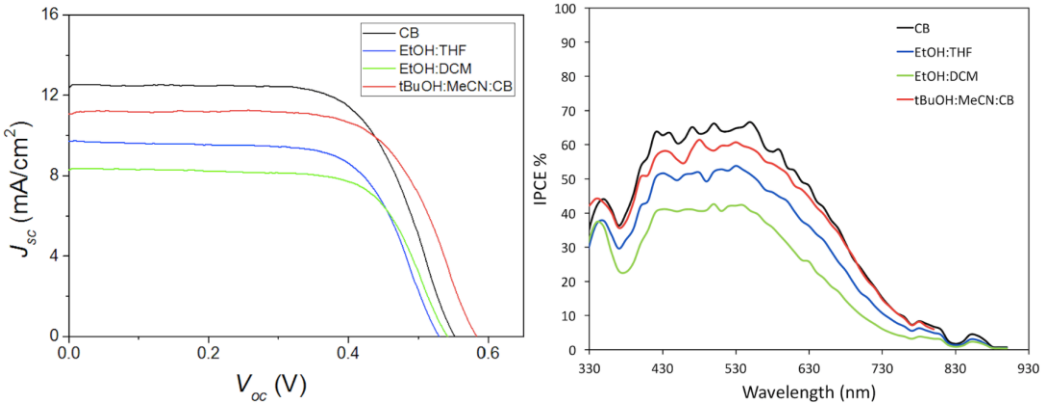

Figure 45. IPCE (right) and I-V (left) curves of **YZ7** under different dipping solvents. Note: All the devices were applied E2I, with no CDCA inside, and the film thickness is 10 µm active layer and 5 µm scattering layer.

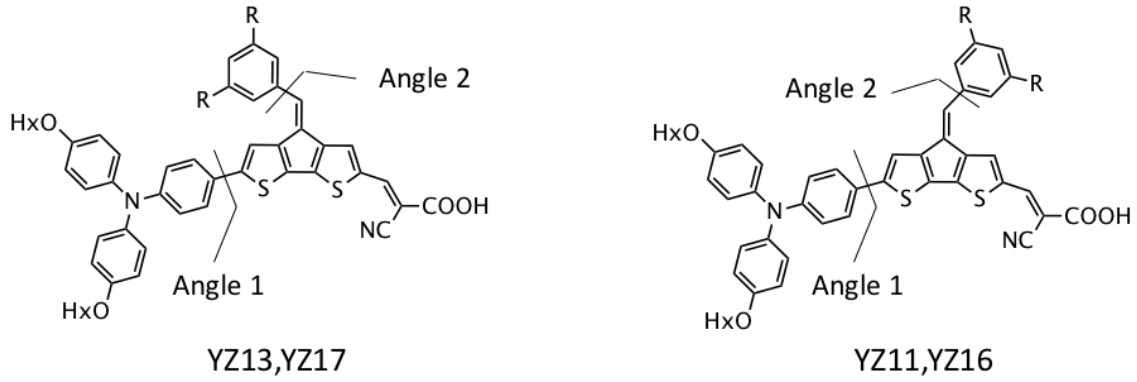

Figure 46. Position for dihedral angles of **YZ11, YZ13, YZ16 and YZ17**.

Table 16. Summary table of **YZ11, YZ13, YZ16** and **YZ17** for computational results: dihedral angles, orbital contributions to vertical transitions, vertical transition energies and oscillator strengths computed with DFT and TD-DFT analysis at the B3LYP/6-311(d,p) level.

dye	angle 1 (°)	angle 2 (°)	transition	contrib. (%)	vert. trans. (nm/eV)	oscillator strength	energy (Hartrees)
YZ11	24.5	35.2	$H \rightarrow L$	96%	640/1.93	0.5506	-2748.3620869
			$H^{-1} \rightarrow L$	44%	458/2.71	0.5275	
			$H \rightarrow L^{+1}$	51%			
YZ13	23.7	36.0	$H \rightarrow L$	96%	654/1.89	0.5146	-2748.3619642
			$H^{-1} \rightarrow L$	45%	462/2.68	0.6078	
			$H^{-1} \rightarrow L^{+1}$	2%			
			$H \rightarrow L^{+1}$	50%			
YZ16	25.8	38.5	$H \rightarrow L$	96%	631/1.97	0.5895 0.5264	-2827.0179941
			$H^{-1} \rightarrow L$	45%	453/2.74		
			$H \rightarrow L^{+1}$	50%			
YZ17	24.7	35.6	$H \rightarrow L$	96%	642/1.93	0.5379	-2827.0174338
			$H^{-1} \rightarrow L$	44%	455/2.72	0.6317	
			$H \rightarrow L^{+1}$	51%			

Table 17. Dye desorption study results for **YZ11, YZ13, YZ16** and **YZ17**. All films were prepared according to the conditions for devices reported in **Table 7** of the manuscript.

dye film	molar absorptivity ($M^{-1}cm^{-1}$)	λ_{max} (nm)	dye loading density (mol/cm^2)
YZ11	25,000	503	3.9×10^{-8}
YZ13	28,000	509	4.6×10^{-8}
YZ16	24,000	504	2.1×10^{-8}
YZ17	23,000	505	3.7×10^{-8}

Molar absorptivity values and absorption maximum were measured in 0.1 M TBAOH (tetrabutylammonium hydroxide) DMF solutions. Dye was desorbed by submerging sensitized films in a 0.1 M TBAOH (tetrabutylammonium hydroxide) DMF solution until the film showed no more dye present.

Appendix 11. Photovoltaic Measurements and Device Fabrication

DSC Device Fabrication: For the photoanode, TEC 10 glass was purchased from Hartford Glass. Once cut into 2x2 cm squares, the substrate was submerged in a 0.2% Deconex 21 aqueous solution and sonicated for 15 minutes at room temperature. The electrodes were rinsed with water and sonicated in acetone for 10 minutes followed by sonication in ethanol for 10 minutes. Finally, the electrodes were placed under UV/ozone for 15 minutes (UV-Ozone Cleaning System, Model ProCleaner by UVFAB Systems). A compact TiO_2 underlayer is then applied by pretreatment of the substrate submerged in a 40 mM $TiCl_4$ solution in water (prepared from 99.9% $TiCl_4$ between 0-5 ^oC). The submerged substrates (conductive side up) were heated for 30 minutes at 70 ^oC. After heating, the substrates were rinsed first with water then with ethanol. The photoanode consists of thin TiO_2 electrodes comprised of a 10 μm mesoporous TiO_2 layer (particle size, 20 nm, Dyesol, DSL 18NR-T) for iodine cells and 5 μm mesoporous TiO_2 layer (particle size, 30 nm, Dyenamo,

DN-GPS-30TS) for cobalt cells. All the photoanodes had 5.0 μm TiO_2 scattering layer (particle size, 100 nm, Solaronix R/SP). All the layers were screen printed from a Sefar screen (54/137–64W). Between each print, the substrate was heated for 7 minutes at 125 ^oC and the thickness was measured with a profilometer (Alpha-Step D-500 KLA Tencor). After all layers were deposited, the substrate was then sintered with progressive heating from 125^oC (5-minute ramp from r.t., 5 minute hold) to 325 ^oC (15 minute ramp from 125^oC, 5 minute hold) to 375 ^oC (5 minute ramp from 325 ^oC, 5 minute hold) to 450 ^oC (5 minute ramp from 375 ^oC, 15 minute hold) to 500 ^oC (5 minute ramp from 450 ^oC, 15 minute hold) using a programmable furnace (Vulcan® 3-Series Model 3-550). The cooled sintered photoanode was soaked 30 min at 70 ^oC in a 40 mM $TiCl_4$ water solution and heated again at 500 ^oC for 30 minutes prior to sensitization. The complete working electrode was prepared by immersing the TiO_2 film into the dye solution overnight. The solution is 0.3 mM of dye in MeCN:t-BuOH:THF mixture (1:1:1) with a 20:1 CDCA:dye ratio unless otherwise indicated. For preparing counter electrodes, 2x2 cm squares TEC 7 FTO glasses were drilled using Dremel-4000 with Dremel 7134 Diamond Taper Point Bit from the conductive and taped FTO side. The electrodes were washed with water followed by 0.1 M HCl in EtOH rinse and sonication in acetone bath for 10 minutes. The washed FTO electrodes were then dried at 400 ^oC for 15 minutes. A thin layer of Pt-paste (Solaronix, Platisol T/SP) was slot printed on the FTO and the printed electrodes were then cured at 450 ^oC for 10 minutes. After allowing them to cool to room temperature, the working electrodes were then sealed with a 25 μm thick hot melt film (Surlyn, Solaronix, “Meltonix 1170-25”) by heating the system at 130 ^oC under 0.2 psi pressure for 1 minute. Devices were completed by filling the electrolyte by pre-drilled holes in the counter electrodes and finally the holes were sealed with a Surlyn pre-cut circle and a thin glass cover by heating at 130 ^oC under pressure 0.1 psi for 25 seconds. Finally, soldered contacts were added with

a MBR Ultrasonic soldering machine (model USS-9210) with solder alloy (Cerasolzer wire dia 1.6 mm item # CS186-150). A circular black mask (active area 0.15 cm^2) punched from black tape was used in the subsequent photovoltaic studies.

Photovoltaic Measurements: Current-Voltage Curves: Photovoltaic characteristics were measured using a 150 W Xenon lamp (Model SF150B, SCIENCETECH Inc. Class ABA) solar simulator equipped with an AM 1.5 G filter for a less than 2% spectral mismatch. Prior to each measurement, the solar simulator output was calibrated with a KG5 filtered mono-crystalline silicon NREL calibrated reference cell from ABET Technologies (Model 15150-KG5). The current density-voltage characteristic of each cell was obtained with Keithley digital source meter (Model 2400). Device performances under AM 1.5G irradiation were analyzed based on the equation PCE = (J_{sc}*V_{oc}*FF)/I_0. The incident photon-to-current conversion efficiency was measured with an IPCE instrument manufactured by Dyenamo comprised of a 175 W Xenon lamp (CERMAX, Model LX175F), monochromator (Spectral Products, Model CM110, Czerny-Turner, dual-grating), filter wheel (Spectral Products, Model AB301T, fitted with filter AB3044 [440 nm high pass] and filter AB3051 [510 nm high pass]), a calibrated UV-enhanced silicon photodiode reference and Dyenamo issued software.

Electron lifetime measurements: Also known as small modulation photovoltage transient measurements, were carried out with a Dyenamo Toolbox (DN-AE01) instrument and software. The intensity of the LED light source (Seoul Semiconductors, Natural White, S42182H, 450 nm to 750 nm emission) is varied to modulate the device open-circuit voltage. The base light intensity was modulated by applied voltages of 2.80, 2.85, 2.90, 2.95 and 3.00 V applied to the LED with the 3.0 V bias approaching 1 sun intensity (97%). The direction of illumination was from the photoanode to the counter electrode, and the device was positioned 5 cm from the LED light source.

The voltage rise and decay times are fitted with a Levenberg-Marquardt fitting algorithm via LabView, and the electron lifetime was obtained from the averaging of rise and decay times.

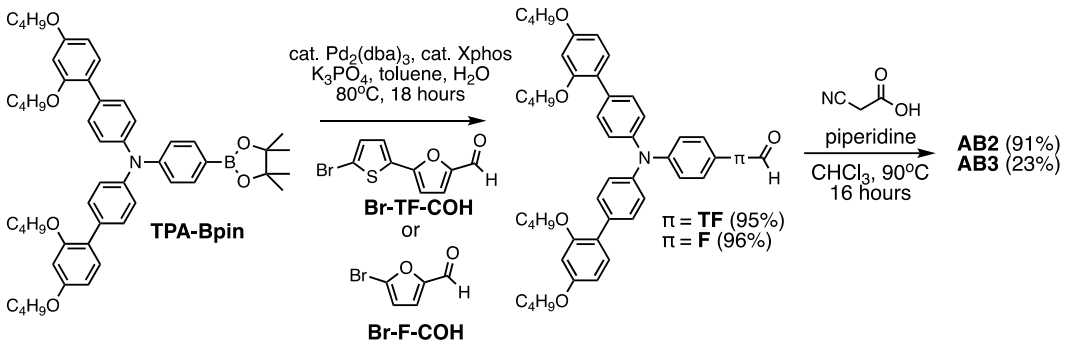

Figure 47. Synthetic route to **AB2** and **AB3**.

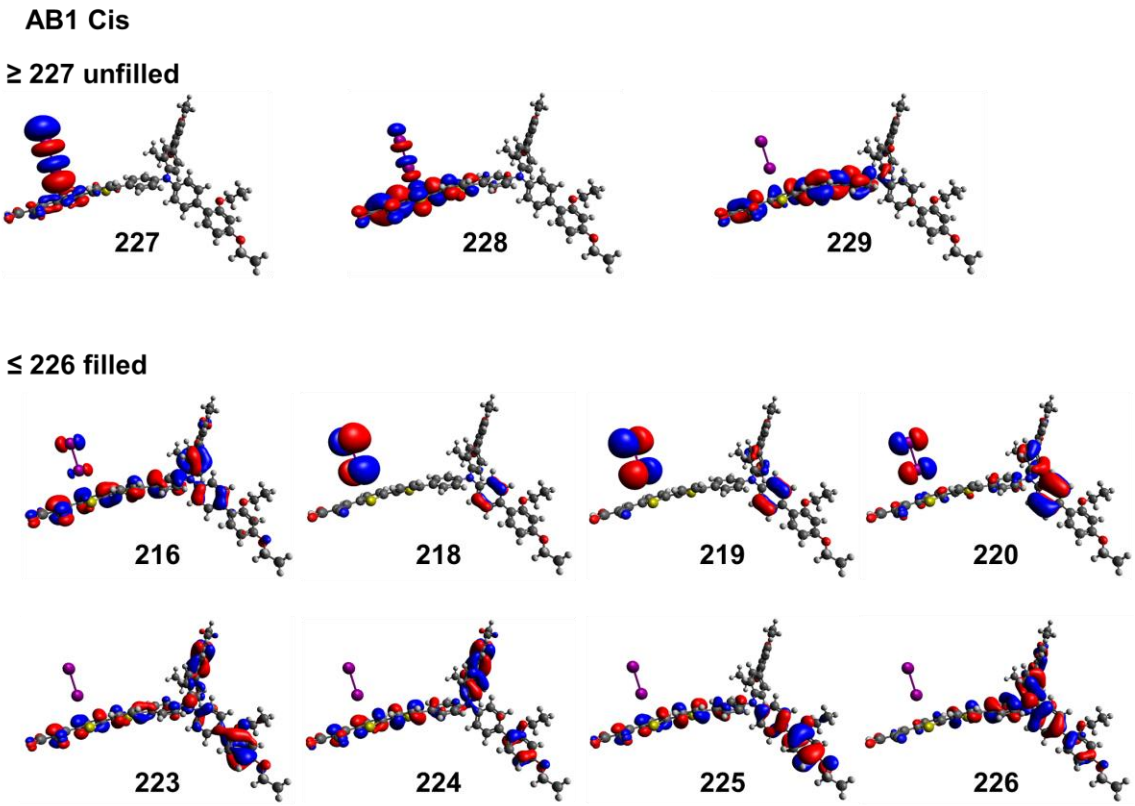

Figure 48. Orbitals contributing to TD-DFT predicted transitions for **AB1**. Calculations were done at wB97XD/6-31+g* level of theory and basis set.

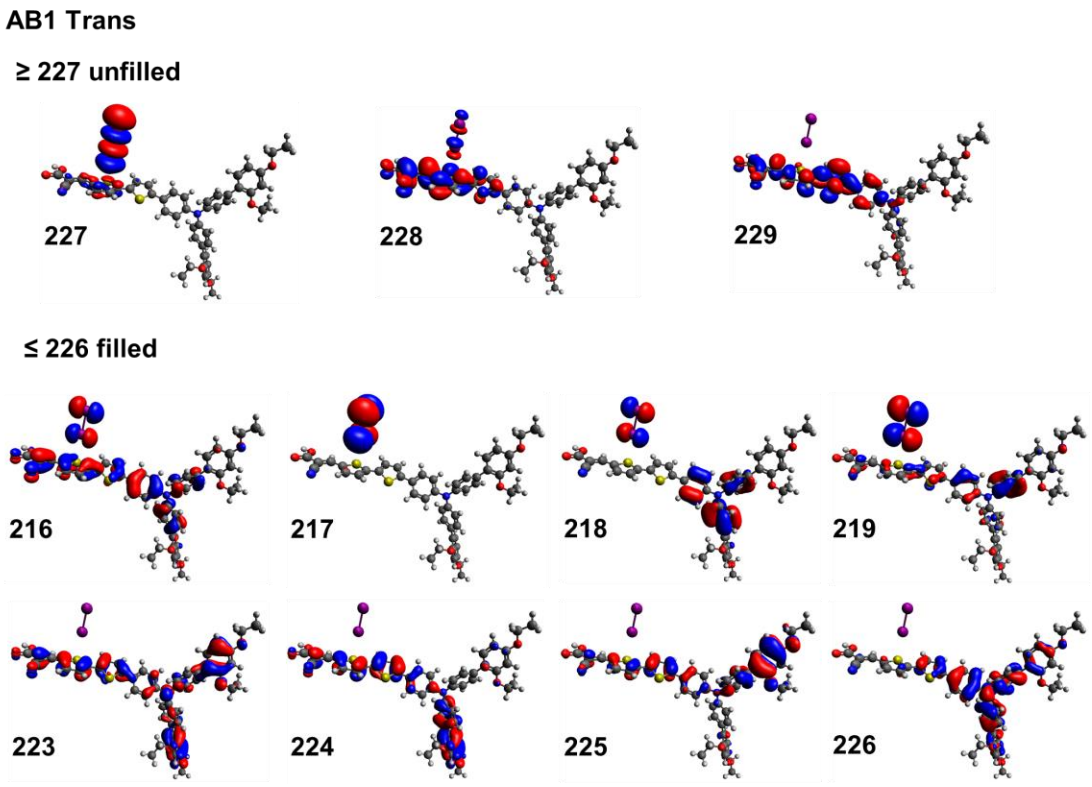

Figure 49. Orbitals contributing to TD-DFT predicted transitions for trans **AB1**. Calculations were done at wB97XD/6-31+g* level of theory and basis set.

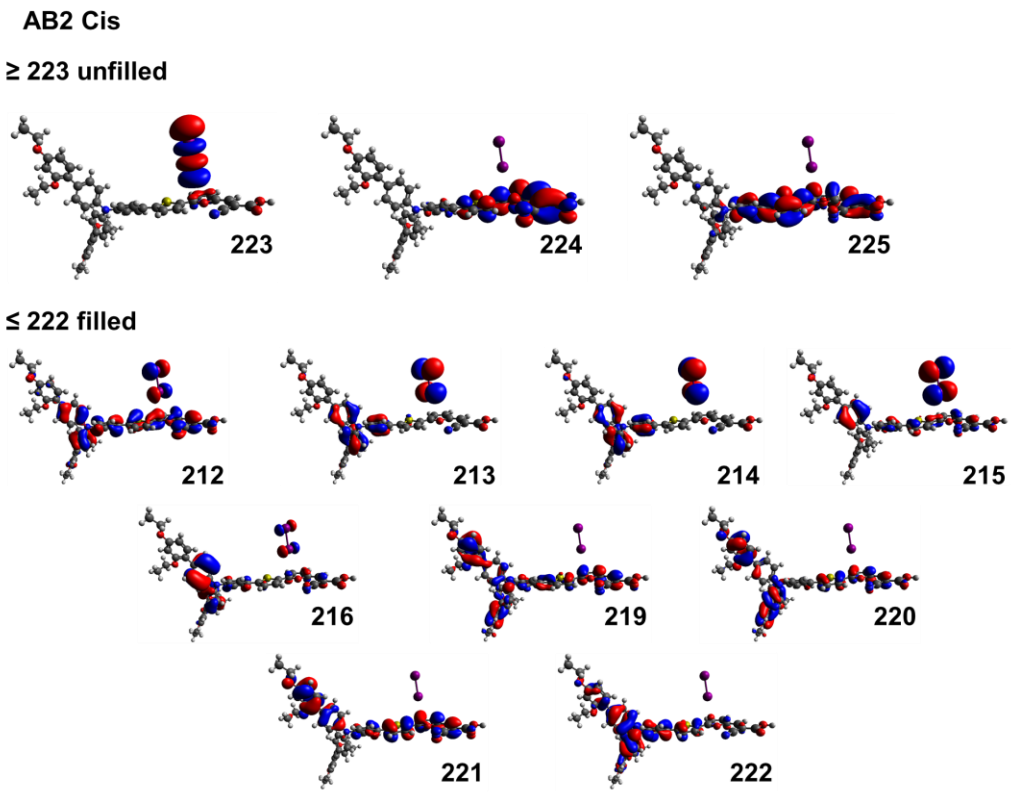

Figure 50. Orbitals contributing to TD-DFT predicted transitions for cis **AB2**. Calculations were done at wB97XD/6-31+g* level of theory and basis set.

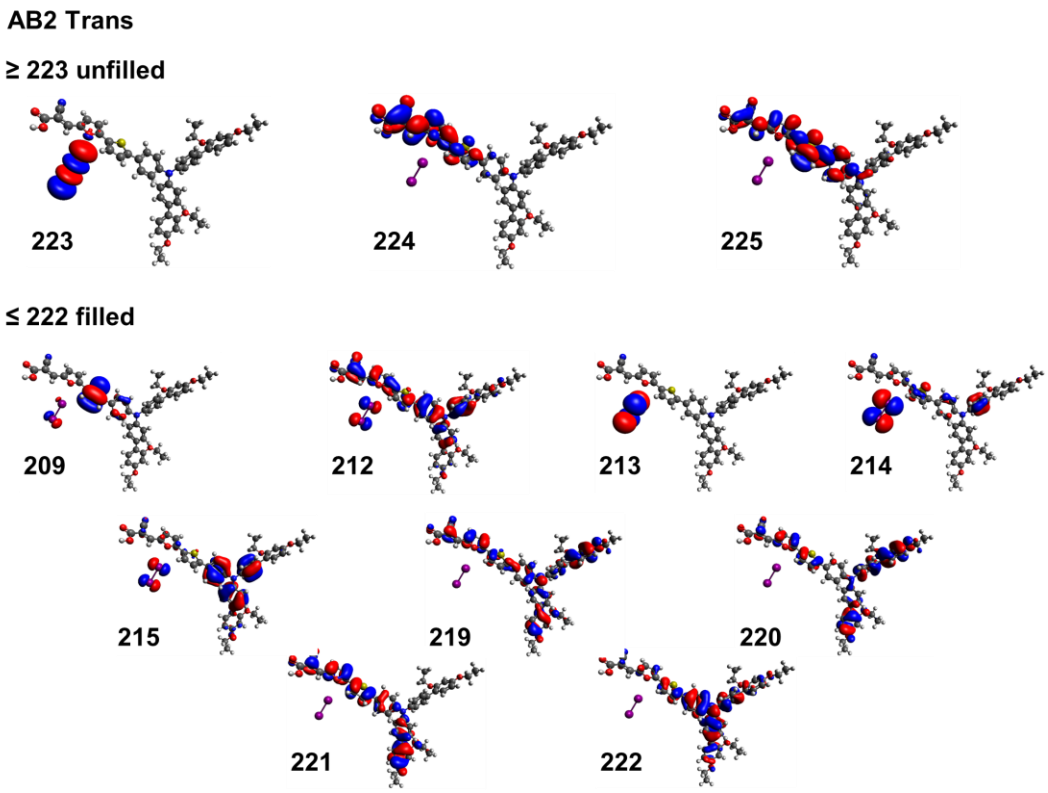

Figure 51. Orbitals contributing to TD-DFT predicted transitions for **AB2**. Calculations were done at wB97XD/6-31+g* level of theory and basis set.

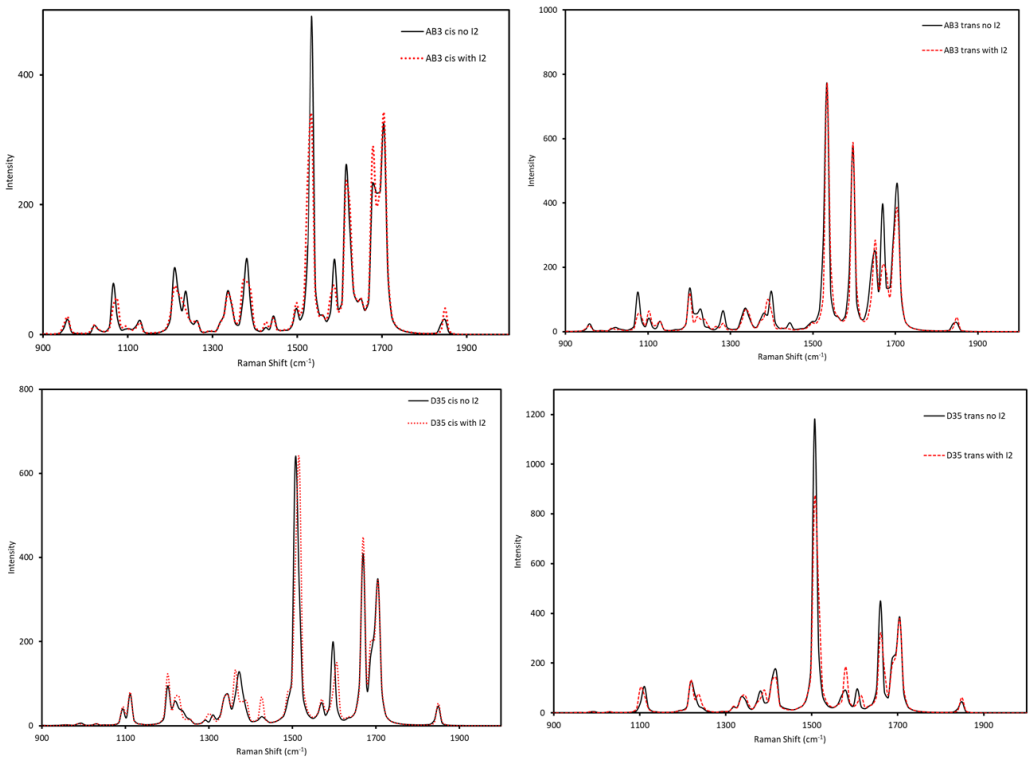

Figure 52. Simulated Raman spectra for cis and trans states of dyes **AB3** and **D35.** Calculations were done at wB97XD/6-31+g* level of theory and basis set.

Table 18. Excited state orbital transitions for cis **AB1**. Calculations were done at wB97XD/6-31+g* level of theory and basis set.

dye	State	transition orbitals	contribution (%)	vert. trans. (nm | eV)	oscillator strength	energy (Hatrees)
AB1 cis	1	219 (I_2) → 227 (I_2) 219 (I_2) → 228 (dye/I_2) 220 (dye/I_2) → 227 (I_2)	66 4 27	523 | 2.37	0.0004	-3310.9
AB1 cis	2	216 (dye/I_2) → 227 (I_2) 218 (I_2) → 227 (I_2) 218 (I_2) → 228 (dye/I_2) 219 (I_2) → 227 (I_2) 220 (dye/I_2) → 227 (I_2)	2 77 4 2 12	518 | 2.39	0.0004	-3310.9
AB1 cis	3	223 (dye) → 227 (I_2) 223 (dye) → 228 (dye/I_2) 224 (dye) → 227 (I_2) 224 (dye) → 228 (dye/I_2) 225 (dye) → 227 (I_2) 225 (dye) → 228 (dye/I_2) 226 (dye) → 227 (I_2) 226 (dye) → 228 (dye/I_2) 226 (dye) → 229 (dye)	6 3 14 7 15 7 27 12 4	423 | 2.93	0.9905	-3310.9
AB1 cis (no I_2)	1	216 (dye) → 220 (dye) 217 (dye) → 220 (dye) 218 (dye) → 220 (dye) 219 (dye) → 220 (dye) 219 (dye) → 221 (dye)	6 9 36 35 7	404 | 3.07	1.6582	-3288.1

Table 19. Excited state orbital transitions for trans **AB1**. Calculations were done at wB97XD/6-31+g* level of theory and basis set.

dye	State	transition orbitals	contribution (%)	vert. trans. (nm | eV)	oscillator strength	energy (Hatrees)
AB1 trans	1	216 (dye/I_2) → 227 (I_2) 217 (I_2) → 227 (I_2) 218 (I_2) → 227 (dye/I_2) 219 (dye/I_2) → 227 (I_2)	11 19 11 53	522 | 2.37	0.0005	-3310.9
AB1 trans	2	216 (dye/I_2) → 227 (I_2) 217 (I_2) → 227 (I_2) 217 (I_2) → 228 (dye/I_2) 219 (dye/I_2) → 227 (I_2)	4 77 3 14	520 | 2.38	0.0003	-3310.9
AB1 trans	3	223 (dye) → 227 (I_2) 223 (dye) → 228 (dye/I_2) 224 (dye) → 227 (I_2) 224 (dye) → 228 (dye/I_2) 225 (dye) → 227 (I_2) 225 (dye) → 228 (dye/I_2) 226 (dye) → 227 (I_2) 226 (dye) → 228 (dye/I_2) 226 (dye) → 229 (dye)	8 2 20 6 13 4 32 7 3	426 | 2.91	0.7251	-3310.9
AB1 trans (no I_2)	1	216 (dye) → 220 (dye) 217 (dye) → 220 (dye) 218 (dye) → 220 (dye) 219 (dye) → 220 (dye) 219 (dye) → 221 (dye)	8 13 31 34 8	401 | 3.09	1.7475	-3288.1

Table 20. Excited state orbital transitions for cis **AB2**. Calculations were done at wB97XD/6-31+g* level of theory and basis set.

dye	**State**	**transition orbitals**	**contribution (%)**	**vert. trans. (nm | eV)**	**oscillator strength**	**energy (Hatrees)**
AB2 cis	1	212 (dye/I_2) → 223 (I_2) 213 (I_2) → 223 (I_2) 215 (dye/I_2) → 223 (I_2) 216 (dye/I_2) → 223 (I_2)	12 5 72 8	522 | 2.37	0.0003	-2987.9
AB2 cis	2	214 (I_2) → 223 (I_2)	98	519 | 2.39	0.0007	-2987.9
AB2 cis	3	219 (dye) → 223 (I_2) 220 (dye) → 223 (I_2) 221 (dye) → 223 (I_2) 222 (dye) → 223 (I_2) 222 (dye) → 224 (dye)	5 10 32 44 2	429 | 2.89	0.1524	-2987.9
AB2 cis (no I_2)	1	212 (dye) → 216 (dye) 213 (dye) → 216 (dye) 214 (dye) → 216 (dye) 215 (dye) → 216 (dye) 215 (dye) → 217 (dye)	4 3 45 35 7	407 | 3.07	1.4447	-2965.1

Table 21. Excited state orbital transitions for trans **AB2**. Calculations were done at wB97XD/6-31+g* level of theory and basis set.

dye	**State**	**transition orbitals**	**contribution (%)**	**vert. trans. (nm | eV)**	**oscillator strength**	**energy (Hatrees)**
AB2 trans	1	209 (dye/I_2) → 223 (I_2) 212 (dye/I_2) → 223 (I_2) 214 (I_2) → 223 (I_2) 215 (I_2) → 223 (I_2)	3 7 57 33	522 | 2.38	0.0001	-2987.9
AB2 trans	2	213 (I_2) → 223 (I_2)	98	517 | 2.40	0.0003	-2987.9
AB2 trans	3	219 (dye) → 223 (I_2) 220 (dye) → 223 (I_2) 221 (dye) → 223 (I_2) 222 (dye) → 223 (I_2)	6 11 35 43	430 | 2.88	0.0248	-2987.9
AB2 trans (no I_2)	1	212 (dye) → 216 (dye) 213 (dye) → 216 (dye) 214 (dye) → 216 (dye) 215 (dye) → 216 (dye) 215 (dye) → 217 (dye)	5 4 43 34 8	400 | 3.10	1.8967	-2965.1

Table 22. Excited state orbital transitions for cis **D35**. Calculations were done at wB97XD/6-31+g* level of theory and basis set.

dye	State	transition orbitals	contribution (%)	vert. trans. (nm | eV)	oscillator strength	energy (Hatrees)
D35 cis	1	199 (I_2) → 206 (I_2) 199 (I_2) → 207 (dye/I_2)	94 3	523 | 2.37	0.0004	-2759.2
D35 cis	2	197 (I_2) → 206 (I_2) 198 (I_2) → 206 (I_2) 198 (I_2) → 207 (dye/I_2)	9 83 3	519 | 2.39	0.0007	-2759.2
D35 cis	3	202 (dye) → 206 (I_2) 203 (dye) → 206 (I_2) 203 (dye) → 207 (dye/I_2) 205 (dye) → 206 (I_2) 205 (dye) → 207 (dye/I_2) 205 (dye) → 208 (dye)	4 12 2 66 8 2	431 | 2.88	0.4107	-2759.2
D35 cis (no I_2)	1	195 (dye) → 199 (dye) 196 (dye) → 199 (dye) 198 (dye) → 199 (dye) 198 (dye) → 200 (dye)	8 18 61 7	393 | 3.16	1.2567	-2736.3

Table 23. Excited state orbital transitions for trans **D35**. Calculations were done at wB97XD/6-31+g* level of theory and basis set.

dye	**State**	**transition orbitals**	**contribution (%)**	**vert. trans. (nm | eV)**	**oscillator strength**	**energy (Hatrees)**
D35 trans	1	196 (I_2) → 206 (I_2) 197 (I_2) → 206 (I_2) 198 (I_2) → 206 (dye/I_2) 199 (dye/I_2) → 206 (I_2)	13 46 30 5	521 | 2.38	0.0009	-2759.2
D35 trans	2	197 (I_2) → 206 (I_2) 198 (I_2) → 206 (I_2)	32 64	520 | 2.38	0.0004	-2759.2
D35 trans	3	202 (dye) → 206 (I_2) 203 (dye) → 206 (I_2) 205 (dye) → 206 (I_2) 205 (dye) → 207 (dye/I_2)	4 12 74 4	437 | 2.84	0.2797	-2759.2
D35 trans (no I_2)	1	195 (dye) → 199 (dye) 196 (dye) → 199 (dye) 198 (dye) → 199 (dye) 198 (dye) → 200 (dye)	9 19 59 8	390 | 3.18	1.4418	-2736.3

Table 24. Excited state orbital transitions for cis **AB3**. Calculations were done at wB97XD/6-31+g* level of theory and basis set.

dye	**State**	**transition orbitals**	**contribution (%)**	**vert. trans. (nm | eV)**	**oscillator strength**	**energy (Hatrees)**
AB3 cis	1	192 (I_2) → 202 (I_2) 193 (I_2) → 202 (I_2)	2 93	528 | 2.35	0.0021	-2436.2
AB3 cis	2	192 (I_2) → 202 (I_2) 193 (I_2) → 202 (I_2)	97 3	523 | 2.37	0.0003	-2436.2
AB3 cis	3	193 (I_2) → 202 (I_2) 198 (dye) → 202 (I_2) 199 (dye) → 202 (I_2) 201 (dye) → 202 (I_2) 201 (dye) → 203 (dye)	3 5 14 67 4	447 | 2.77	0.1710	-2436.2
AB3 cis (no I_2)	1	191 (dye) → 195 (dye) 192 (dye) → 195 (dye) 193 (dye) → 195 (dye) 194 (dye) → 195 (dye) 194 (dye) → 196 (dye)	5 15 3 66 6	407 | 3.04	1.0472	-2413.4

Table 25. Excited state orbital transitions for trans **AB3**. Calculations were done at wB97XD/6-31+g* level of theory and basis set.

dye	**State**	**transition orbitals**	**contribution (%)**	**vert. trans. (nm | eV)**	**oscillator strength**	**energy (Hatrees)**
AB3 trans	1	190 (dye/I_2) → 202 (I_2) 192 (I_2) → 202 (I_2) 193 (I_2) → 202 (I_2) 194 (I_2) → 202 (I_2) 195 (dye) → 202 (I_2)	3 18 3 72 4	521 | 2.38	0.0004	-2436.2
AB3 trans	2	192 (I_2) → 202 (I_2) 193 (I_2) → 202 (I_2)	3 96	516 | 2.40	0.0003	-2436.2
AB3 trans	3	198 (dye) → 202 (I_2) 199 (dye) → 202 (I_2) 201 (dye) → 202 (I_2)	6 11 35	458 | 2.71	0.0042	-2436.2
AB3 trans (no I_2)	1	191 (dye) → 195 (dye) 192 (dye) → 195 (dye) 194 (dye) → 195 (dye) 194 (dye) → 196 (dye)	6 19 64 7	397 | 3.12	1.5510	-2413.4

Figure 53. ^{1}H NMR spectrum of TPA-T-Q-T-TPA (3) (CDCl3, 500 MHz).

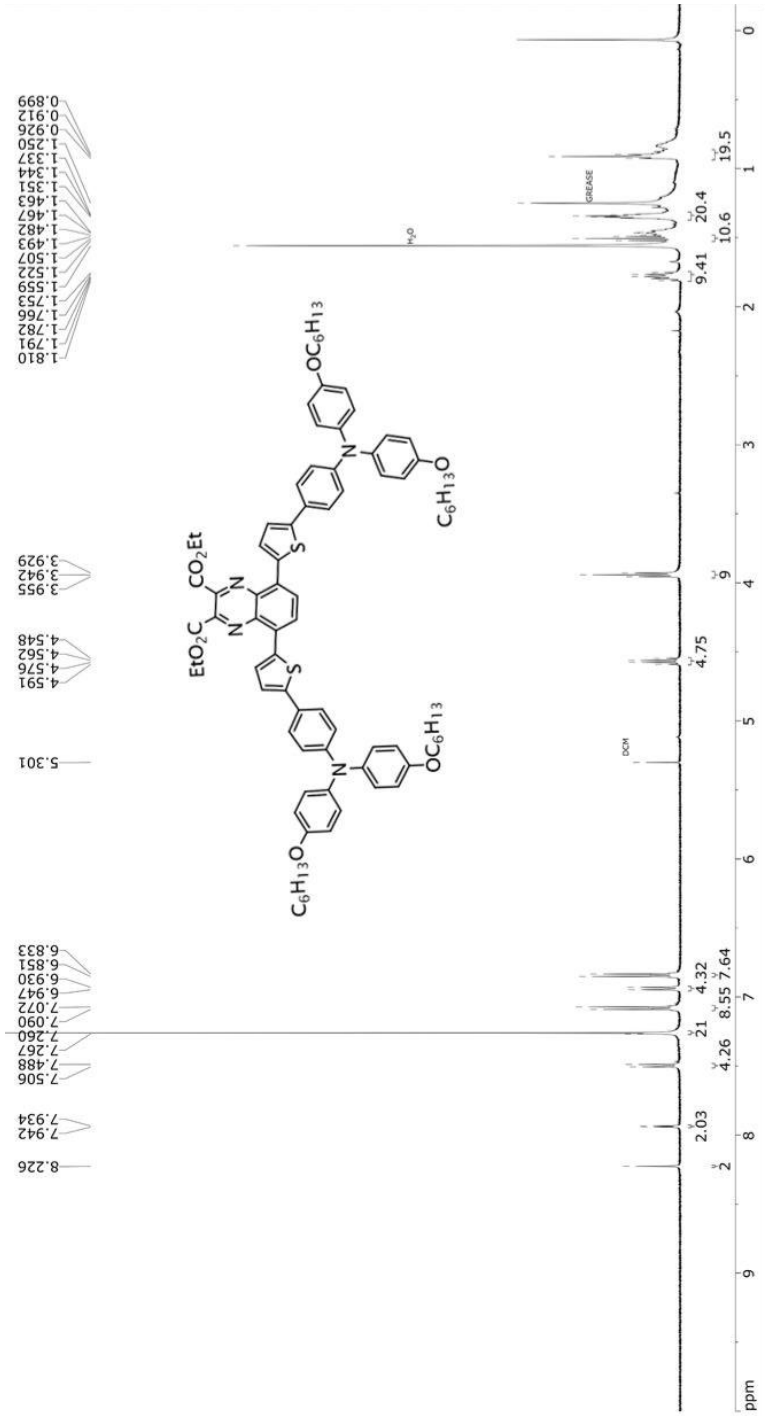

Figure 54. ^{13}C NMR spectrum of TPA-T-Q-T-TPA (3) (CDCl3, 75 MHz).

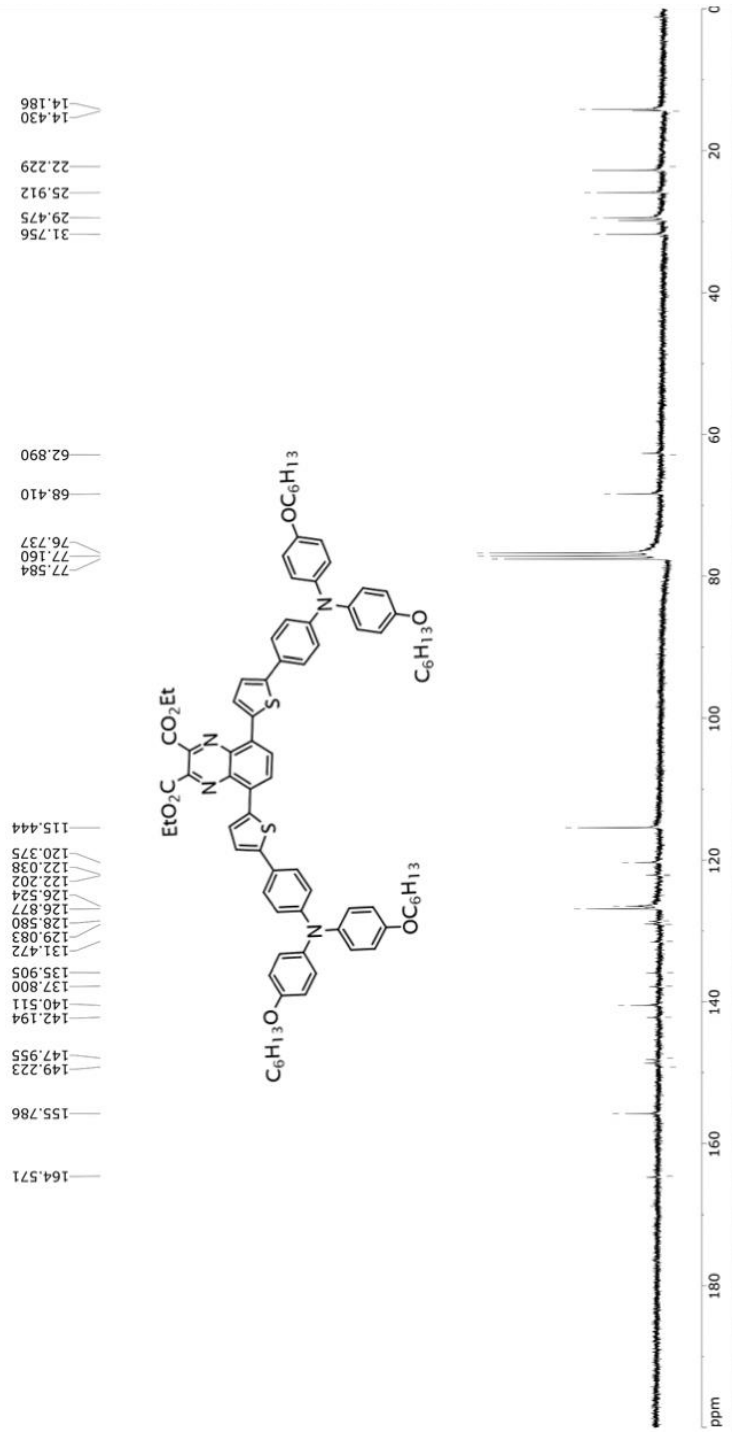

Figure 55. ^{1}H NMR spectrum of compound AP9 (DMSO-d6, 500 MHz).

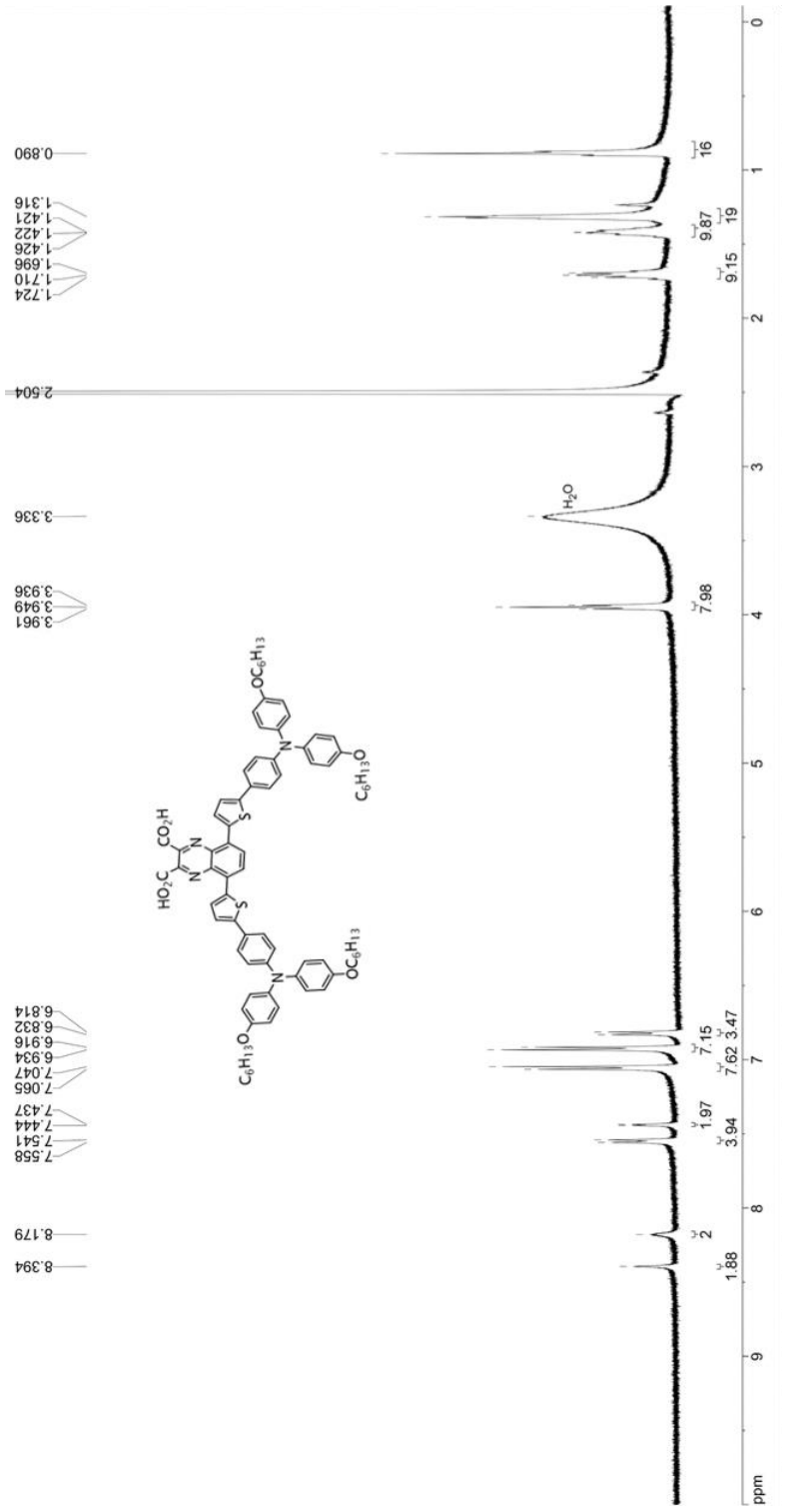

Figure 56. ^{1}H NMR spectrum of TPA-BT-TPA (6) (CDCl3, 500 MHz).

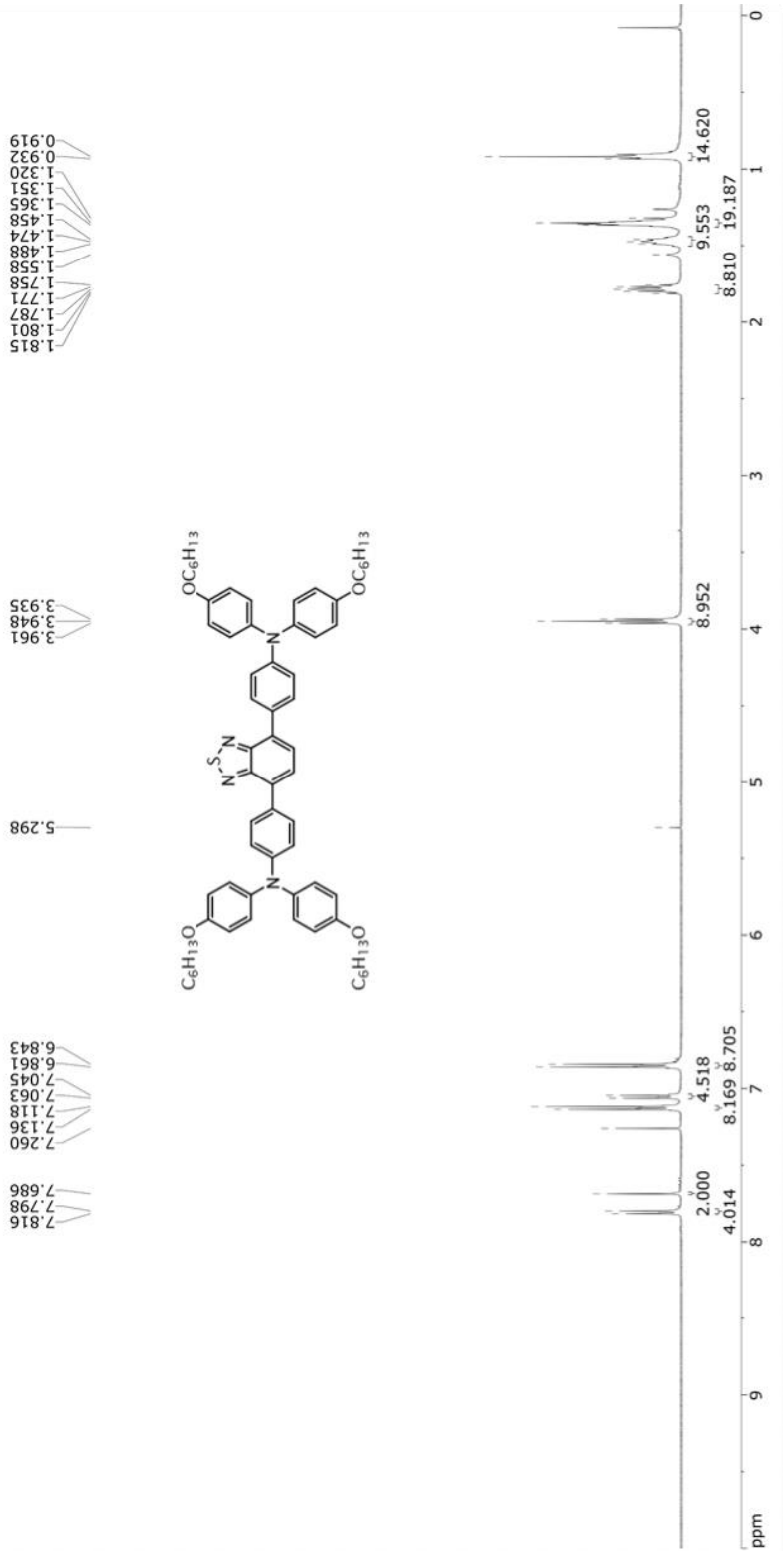

Figure 57. ^{13}C NMR spectrum of TPA-BT-TPA (6) (CDCl3, 125 MHz).

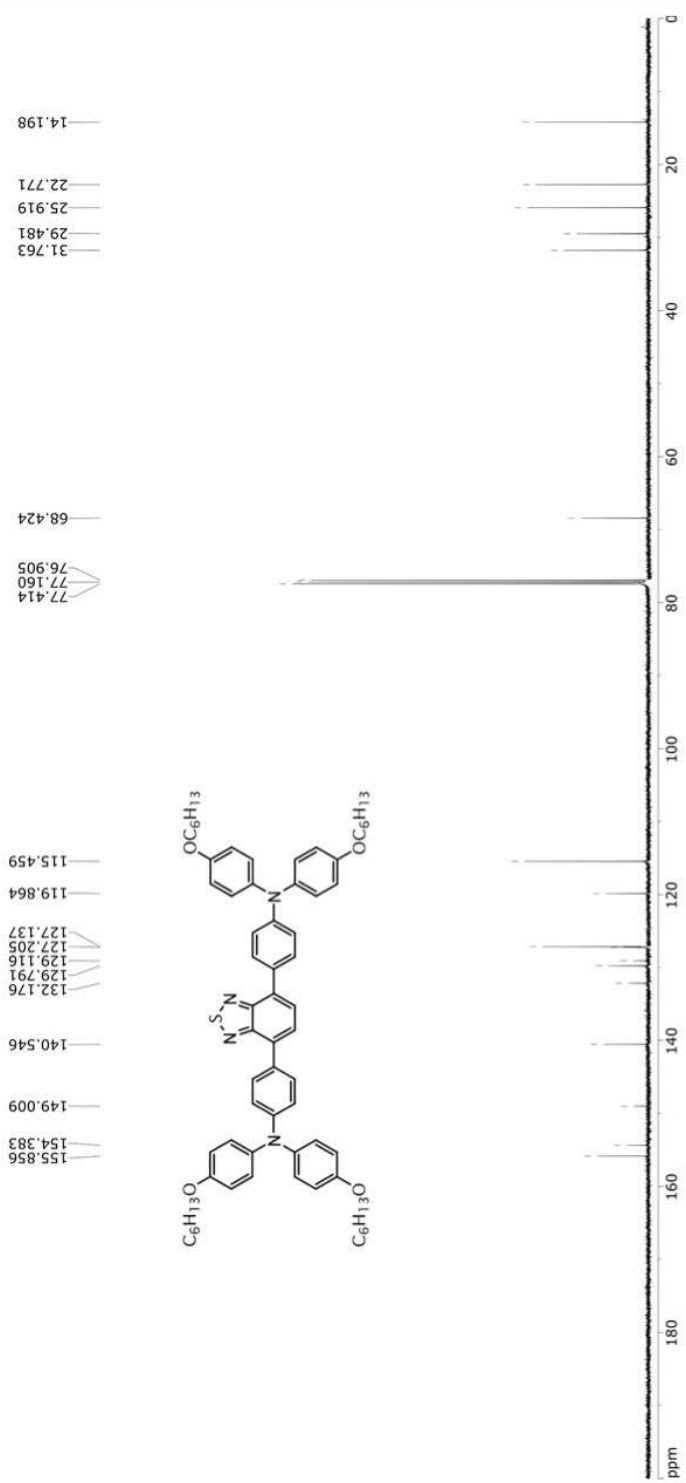

Figure 58. ^{1}H NMR spectrum of TPA-BA-TPA (7) ($CDCl_3$, 300 MHz).

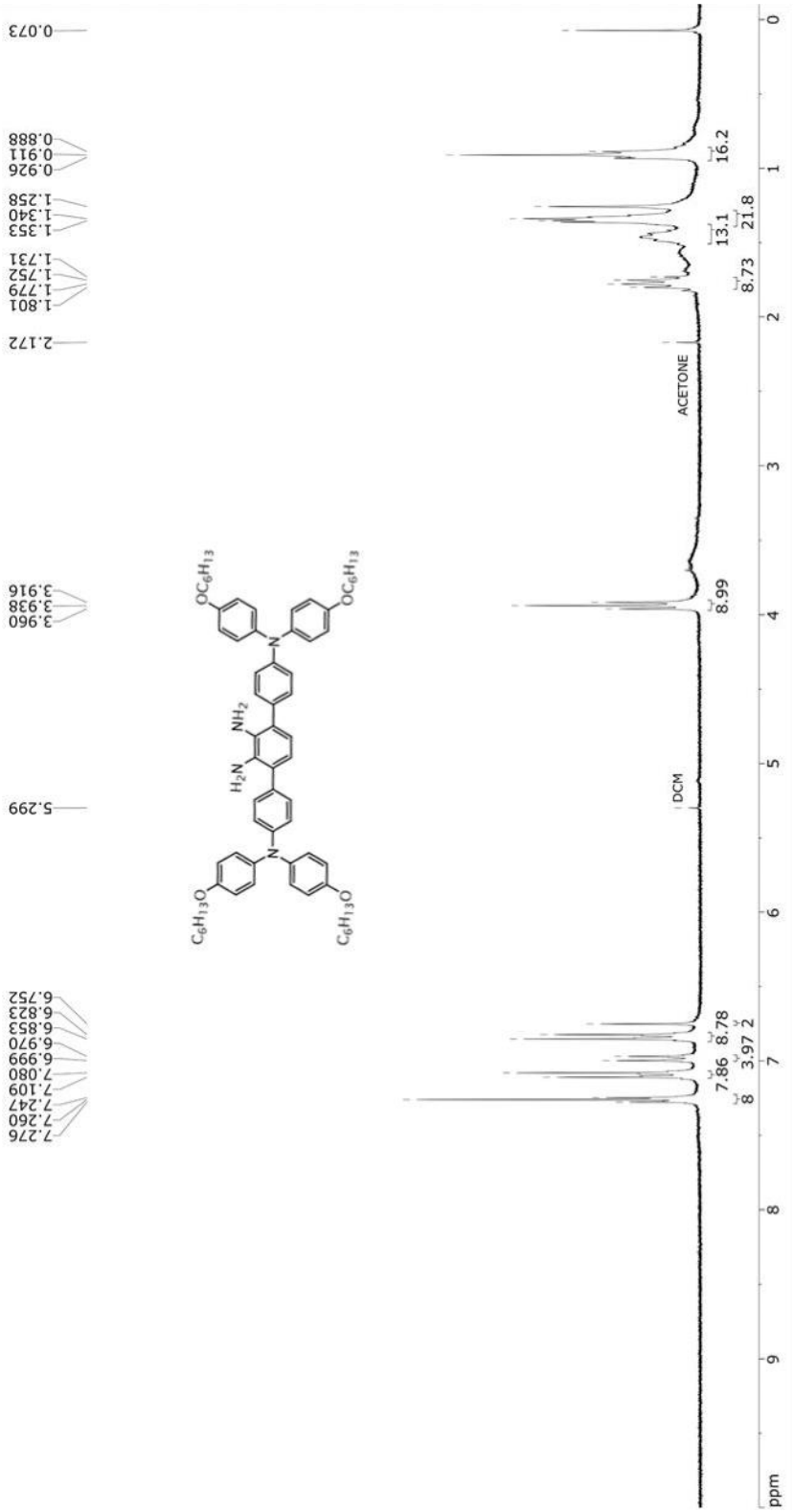

Figure 59. ^{1}H NMR spectrum of TPA-DP-TPA (9) (CDCl3, 300 MHz).

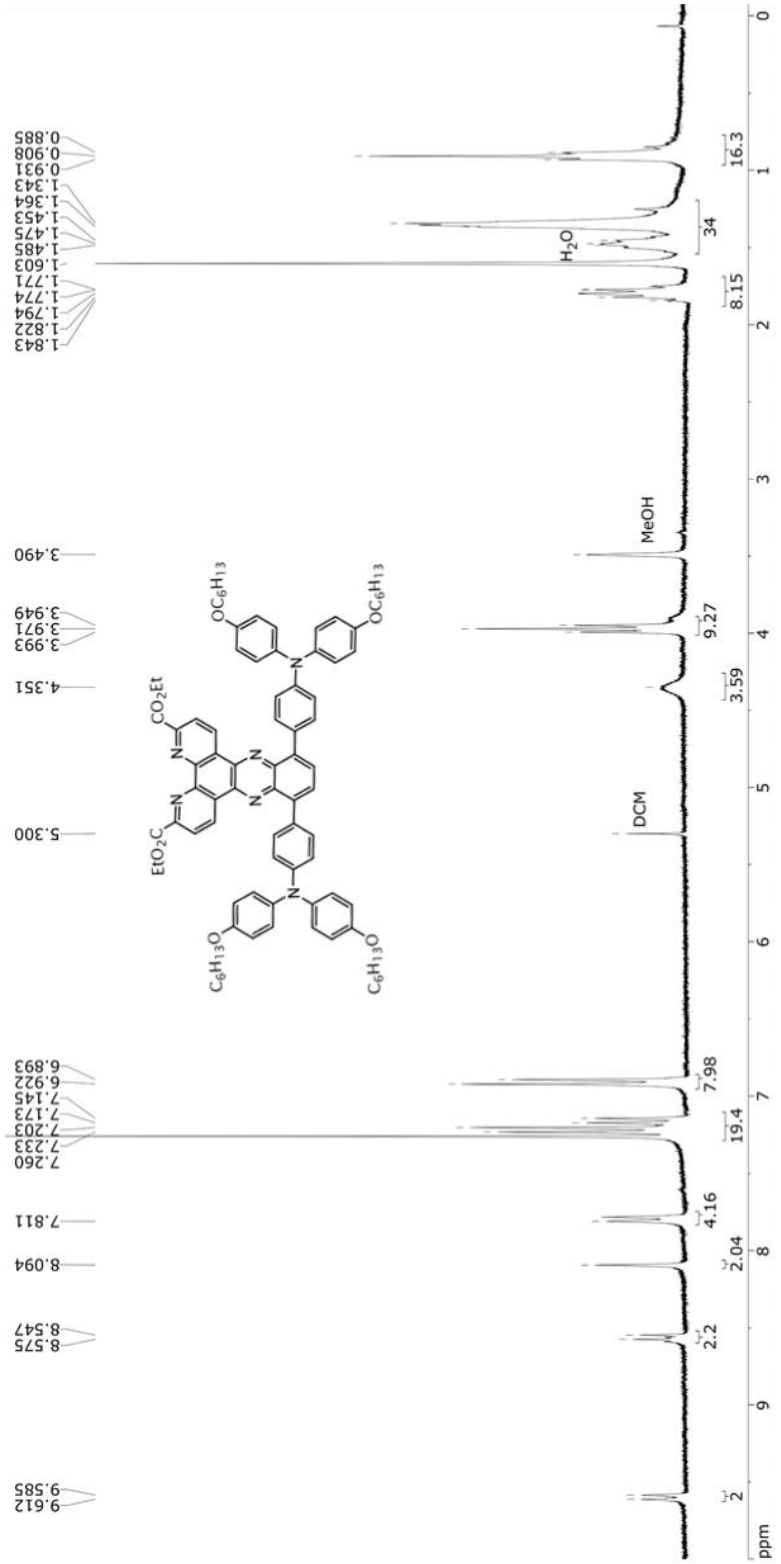

Figure 60. ^{13}C NMR spectrum of TPA-DP-TPA (9) (CDCl3, 75 MHz).

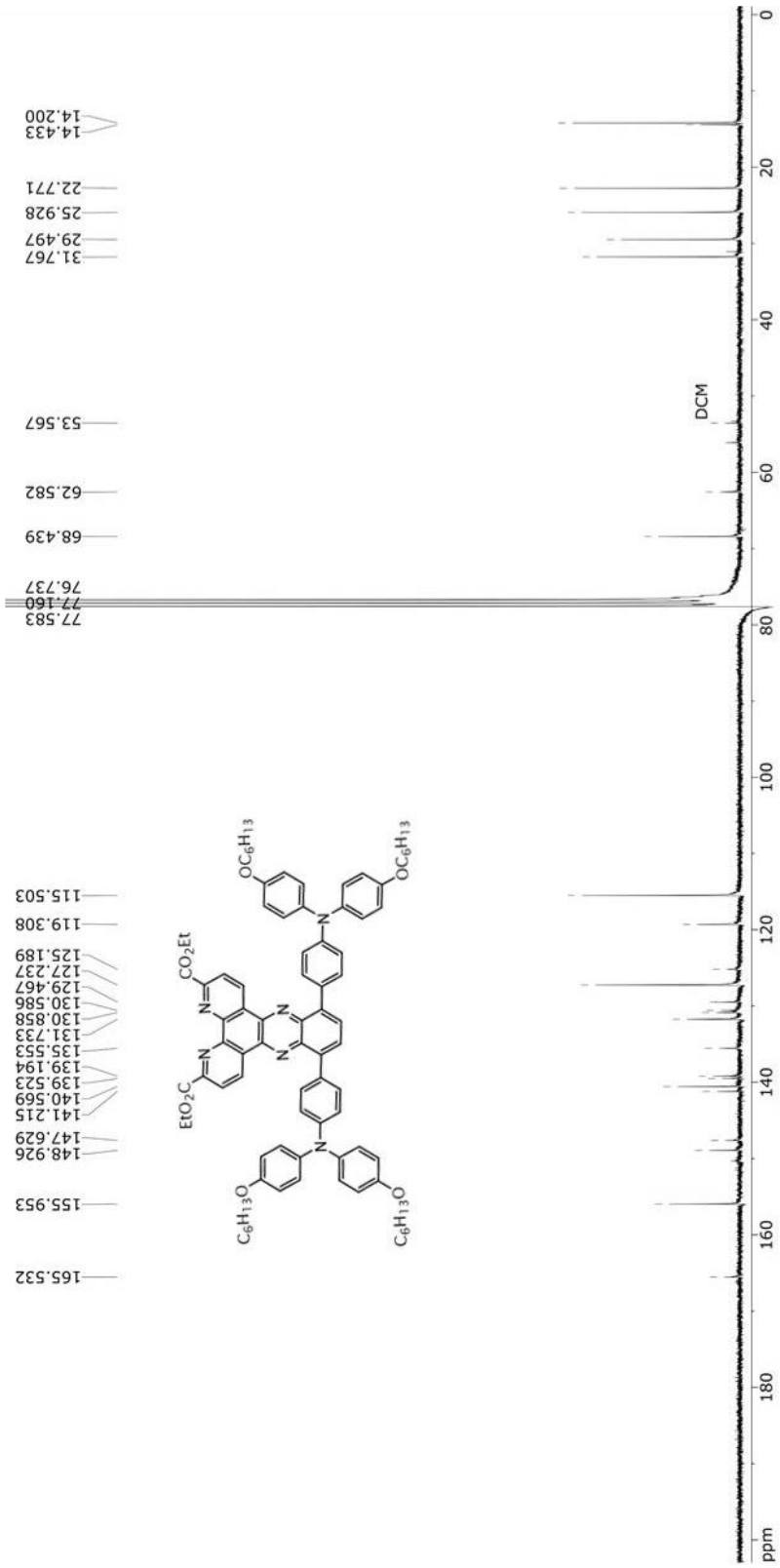

Figure 61. ^{1}H NMR spectrum of compound AP12 (DMSO-d6, 500 MHz, 80^{o}C).

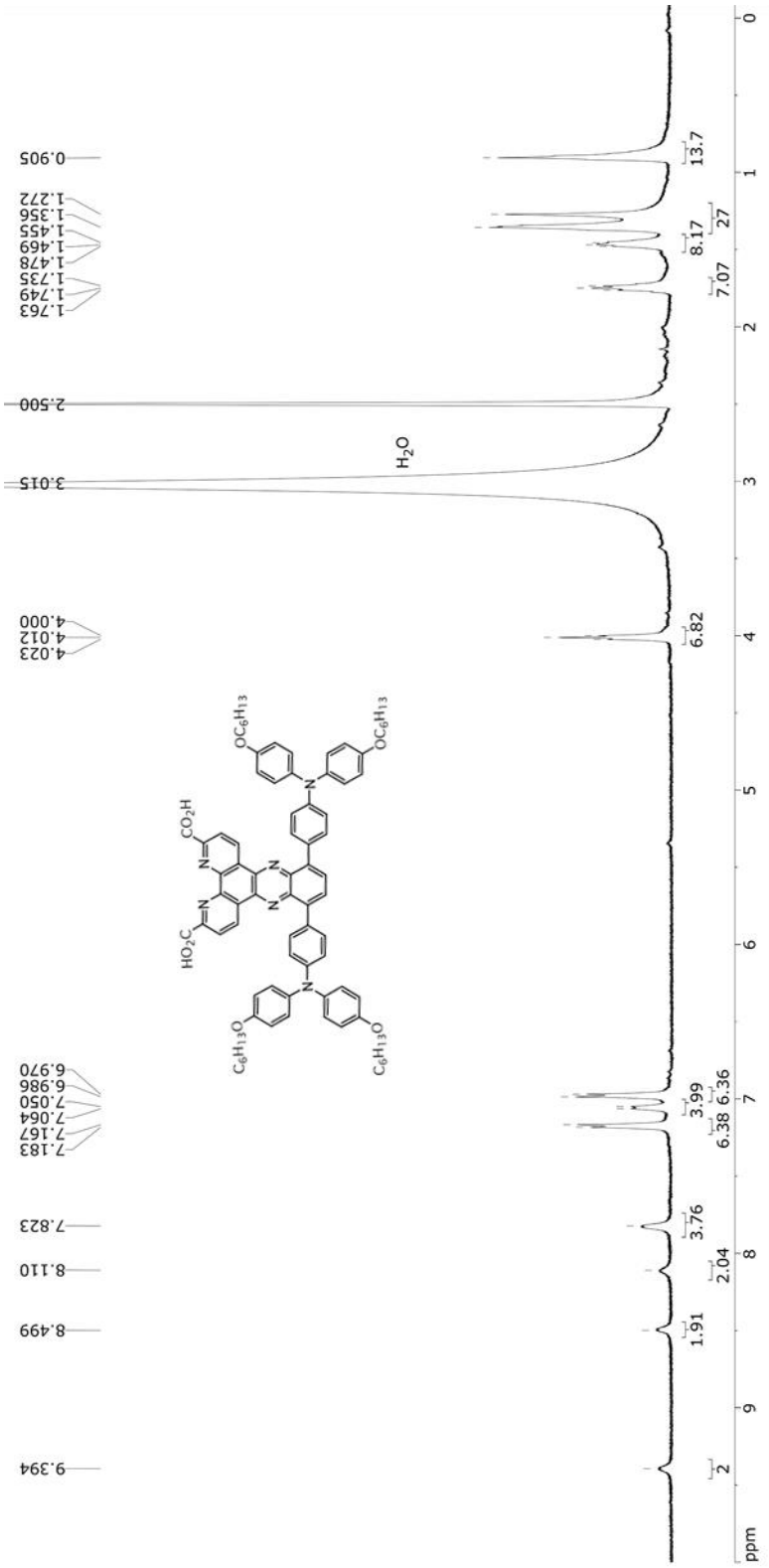

APPENDIX B: JOURNAL PERMISSION FOR REPRODUCED MANUSCRIPTS

1.Journal permission for Chapter 2.1

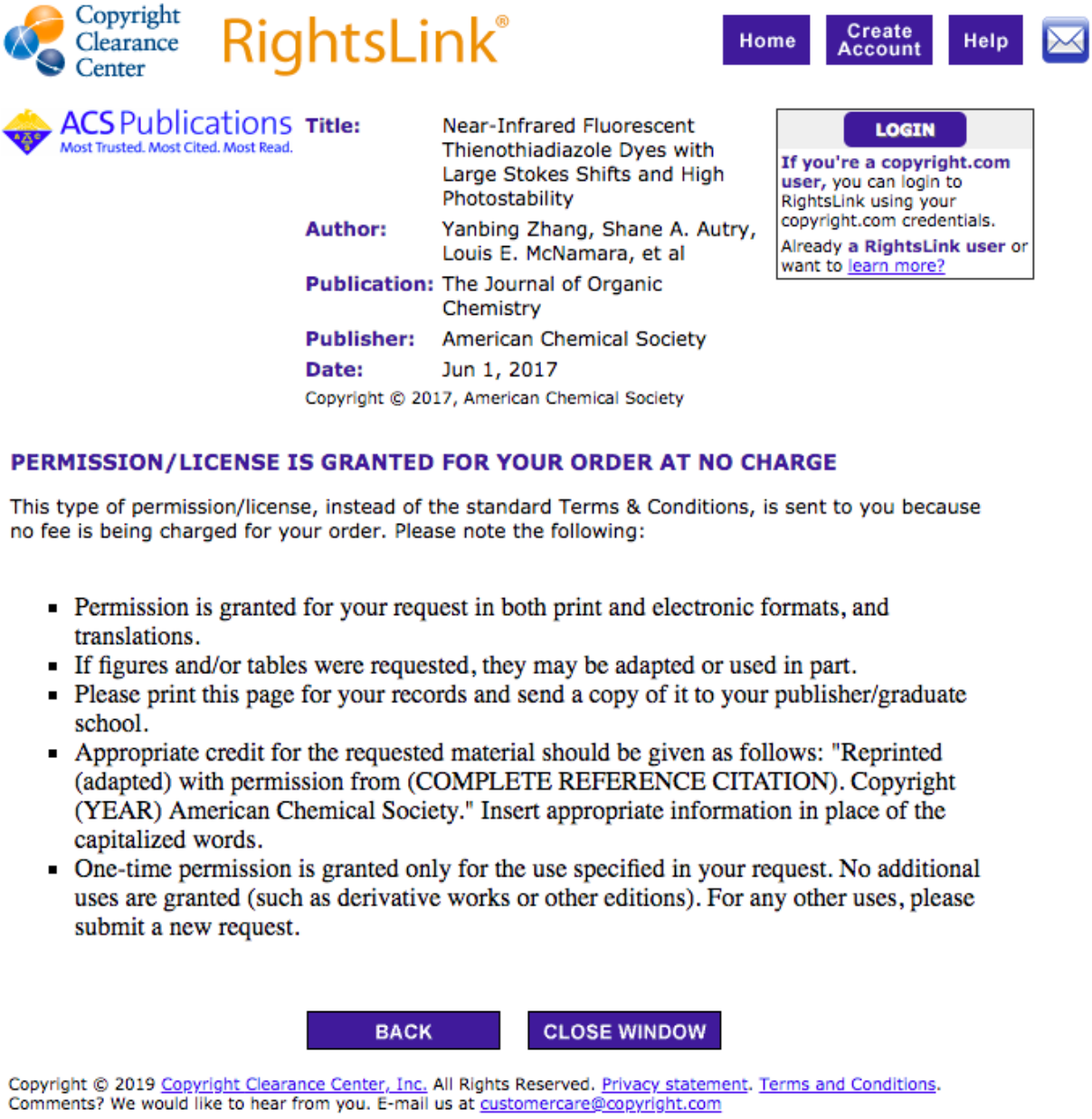

Copyright Clearance Center RightsLink®

Home | Create Account | Help

ACS Publications
Most Trusted. Most Cited. Most Read.

Title: Near-Infrared Fluorescent Thienothiadiazole Dyes with Large Stokes Shifts and High Photostability

Author: Yanbing Zhang, Shane A. Autry, Louis E. McNamara, et al

Publication: The Journal of Organic Chemistry

Publisher: American Chemical Society

Date: Jun 1, 2017

Copyright © 2017, American Chemical Society

LOGIN

If you're a copyright.com user, you can login to RightsLink using your copyright.com credentials.

Already **a RightsLink user** or want to learn more?

PERMISSION/LICENSE IS GRANTED FOR YOUR ORDER AT NO CHARGE

This type of permission/license, instead of the standard Terms & Conditions, is sent to you because no fee is being charged for your order. Please note the following:

- Permission is granted for your request in both print and electronic formats, and translations.
- If figures and/or tables were requested, they may be adapted or used in part.
- Please print this page for your records and send a copy of it to your publisher/graduate school.
- Appropriate credit for the requested material should be given as follows: "Reprinted (adapted) with permission from (COMPLETE REFERENCE CITATION). Copyright (YEAR) American Chemical Society." Insert appropriate information in place of the capitalized words.
- One-time permission is granted only for the use specified in your request. No additional uses are granted (such as derivative works or other editions). For any other uses, please submit a new request.

BACK | CLOSE WINDOW

Copyright © 2019 Copyright Clearance Center, Inc. All Rights Reserved. Privacy statement. Terms and Conditions.
Comments? We would like to hear from you. E-mail us at customercare@copyright.com

2.Journal permission for Chapter 3.1

JOHN WILEY AND SONS LICENSE TERMS AND CONDITIONS

Mar 19, 2019

This Agreement between 1100 Augusta Dr Unit 1103 ("You") and John Wiley and Sons ("John Wiley and Sons") consists of your license details and the terms and conditions provided by John Wiley and Sons and Copyright Clearance Center.

License Number	4552520339016
License date	Mar 19, 2019
Licensed Content Publisher	John Wiley and Sons
Licensed Content Publication	Chemistry - A European Journal
Licensed Content Title	Ullazine Donor–π bridge-Acceptor Organic Dyes for Dye-Sensitized Solar Cells
Licensed Content Author	Yanbing Zhang, Hammad Cheema, Louis McNamara, et al
Licensed Content Date	Mar 24, 2018
Licensed Content Volume	24
Licensed Content Issue	22
Licensed Content Pages	11
Type of use	Dissertation/Thesis
Requestor type	Author of this Wiley article
Format	Print and electronic
Portion	Full article
Will you be translating?	No
Title of your thesis / dissertation	NEAR-INFRARED HIGH EFFICIENCY ORGANIC DYE SENSITIZED SOLAR CELLS (DSCS) AND BIOLOGICAL FLUORESCENT IMAGING DYES
Expected completion date	May 2019
Expected size (number of pages)	200

3.Journal permission for Chapter 4.1

Panchromatic cross-conjugated π-bridge NIR dyes for DSCs

Y. Zhang, H. Cheema, A. E. London, A. Morales, J. D. Azoulay and J. H. Delcamp, *Phys. Chem. Chem. Phys.*, 2018, **20**, 2438
DOI: 10.1039/C7CP06703H

4.Journal permission for Chapter 5.1

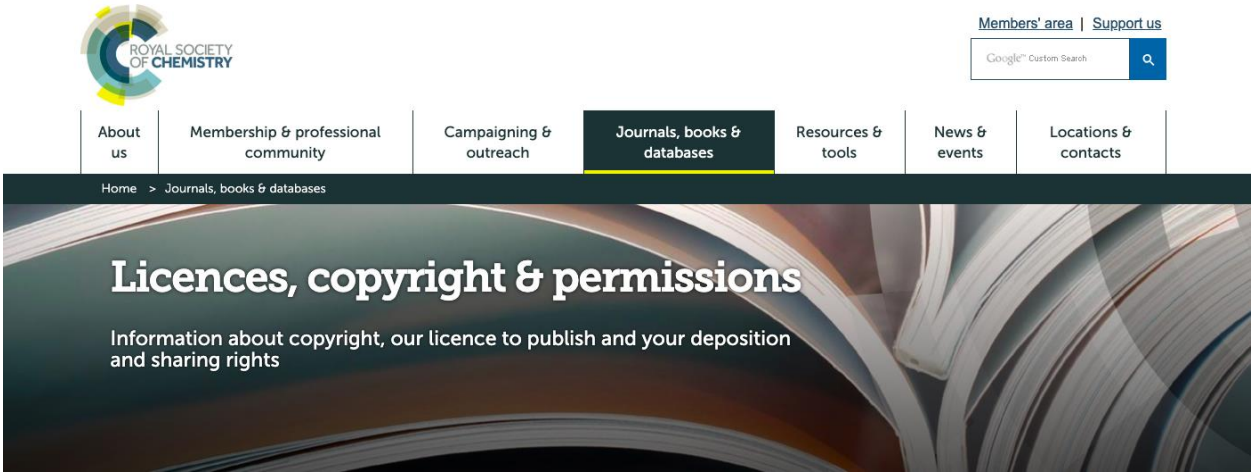

Author reusing their own work published by the Royal Society of Chemistry

You do not need to request permission to reuse your own figures, diagrams, etc, that were originally published in a Royal Society of Chemistry publication. However, permission should be requested for use of the whole article or chapter except if reusing it in a thesis. If you are including an article or book chapter published by us in your thesis please ensure that your co-authors are aware of this.

Reuse of material that was published originally by the Royal Society of Chemistry must be accompanied by the appropriate acknowledgement of the publication. The form of the acknowledgement is dependent on the journal in which it was published originally, as detailed in 'Acknowledgements'.

5.Journal permission for Chapter 6.1

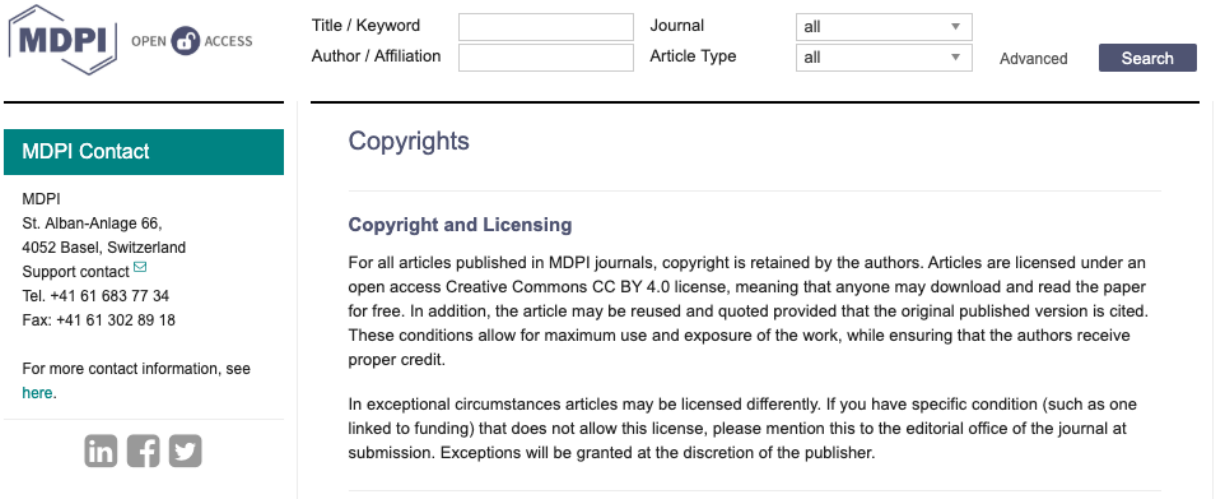

VITA

YANBING ZHANG

University of Mississippi, Department of Chemistry and Biochemistry, 478 Coulter Hall, University, MS 38677 ; Email: yzhang3@go.olemiss.edu, yanbinzhangedu@gmail.com

EDUCATION

University of Mississippi: Department of Chemistry and Biochem., University, MS, 2013-2018

Advisor: Prof. Jared H. Delcamp; Degree: Chemistry, Ph.D.

Shenyang Pharmaceutical University: Department of Pharmaceutical Engineering, Shenyang, China, 2010-2014

Advisors: Prof.Chun Hu and Prof. Yongxue Guo; Degree: B.S. Chemistry

WORK HISTORY

Research and Teaching Assistant: University of Mississippi, University, MS, 2014-2019

RESEARCH EXPERIENCE

- Near-IR absorbing organic dye design, synthesis, and characterization.
- Solar cells devices manufacturing and data analysis

PUBLICATIONS

1) **Zhang, Y.**; Autry, S. A.; McNamara, L. E.; Nguyen, S. T.; Le, N.; Brogdon, P.; Watkins, D. L.; Hammer, N. I.; Delcamp, J. H. "Near-Infrared Fluorescent Thienothiadiazole Dyes with Large Stokes Shifts and High Photostability" *J. Org. Chem*. **2017**, *82*, 5597.

2) **Zhang, Y.**; Cheema, H.; London, A. E.; Morales, A.; Azoulay, J. D.; Delcamp, J. H. "Panchromatic Cross-Conjugated π-Bridge NIR Dyes for DSCs" *Phys. Chem. Chem. Phys.* **2018**, *20*, 2438.

3) **Zhang, Y.**; Cheema, H.; Delcamp, J. H. "Novel Ullazine-Based Organic Dyes for Dye-Sensitized Solar Cells" *Chem. Eur. J.* **2018**, *24*, 5939.

4) Baumann, A.; Cheema, H.; Sabuj, M. A.; McNamara, L. E.; Peddapuram, A.; **Zhang, Y.**; Nguyen, S. T.; Watkins, D. L.; Hammer, N. I.; Delcamp, J. H. "Iodine Binding with Thiophene Versus Furan Based Dyes for DSCs" *Phys. Chem. Chem. Phys*. **2018**, *20*, 17859.

5) Peddapuram A.; Cheema H.; McNamara, L. E.; **Zhang, Y.**; Hammer, N. I.; Delcamp, J. H. "Quinoxaline-based Dual Donor, Dual Acceptor Organic Dyes for Dye-Sensitized Solar Cells" *Appl. Sci.,* **2018**, *8*,1421.

ORAL PRESENTATIONS

3) November 2017. "Panchromatic Cross-Conjugated π-Bridge NIR Dyes for DSCs"
Southeast Regional Meeting of the American Chemical Society, Charlotte, NC.

2) July 2016. "Design and Characterization of the New Series of Near-Infrared Imaging Dyes in Living System", Feeding and Powering the World, University of Mississippi, University, MS.

1) June 2016. "Near-Infrared Charge Transfer Dyes"
Physical Chemistry REU Program, University, MS.

POSTER PRESENTATIONS

2) March 2018. “Novel Ullazine-Based Organic Dyes for Dye-Sensitized Solar Cells”

National Meeting of the American Chemical Society, New Orleans, LA.

1) April 2016. “Near-Infrared Fluorescent Imaging Dyes in Living System”

Graduate Student Council Research Day Symposium, University of Mississippi, University, MS